MODELING AND CHARACTERIZATION OF A MONOENERGETIC γ-RAY IMAGING SYSTEM FOR ACTIVE INTERROGATION APPLICATIONS

A Dissertation
Presented to
The Academic Faculty

By

Joseph Harms

In Partial Fulfillment
of the Requirements for the Degree
Doctor of Philosophy in the
School of Mechanical Engineering
Department of Nuclear and Radiological Engineering and Medical Physics

Georgia Institute of Technology

August 2018

MODELING AND CHARACTERIZATION OF A MONOENERGETIC γ-RAY IMAGING SYSTEM FOR ACTIVE INTERROGATION APPLICATIONS

Approved by:

Dr. Anna S. Erickson, Advisor
Nuclear and Radiological Engineering
Georgia Institute of Technology

Dr. Nolan Hertel
Nuclear and Radiological Engineering
Georgia Institute of Technology

Dr. Paul Rose, Jr.
Nuclear and Radiological Engineering
Georgia Institute of Technology

Dr. C-K Chris Wang
Nuclear and Radiological Engineering
Georgia Institute of Technology

Dr. Cameron Geddes
Accelerator Technology and Applied Physics Division
Lawrence Berkeley National Laboratory

Date Approved: May 31, 2018

ACKNOWLEDGEMENTS

The work presented in this thesis would not have been possible without contributions from several people throughout the course of my graduate work. First, I would like to thank my advisor Dr. Anna Erickson. Your guidance and help throughout my graduate years has been invaluable. I would also like to thank the members of my doctoal advisory committee, Dr. Cameron Geddes, Dr. Nolan Hertel, Dr. Paul Rose, Jr., and Dr. C-K Chris Wang.

I would also like to thank the multiple members of the LANNS-Detection group, Wesley Gillis, Luke Maloney, and Arith Rajapakse. The conversations we have had in the lab over the last few years have led to several ideas which appear in this thesis, and I never would have finished all of this work without your help.

I would like to thank my family, my brother Scot for always encouraging me to pursue a career in the sciences, my sister Lauren for proofreading my written work throughout my academic career, and my brothers Jack and Caleb for dredging through the waters of graduate school with me. I am especially grateful to my parents, who instilled in me the work ethic that made this possible and who have always helped my studies in every way they could. Finally, I would like to thank my wife, Kelsey, who has always been there to motivate me through tough times and inspires me to strive for perfection.

I gratefully acknowledge the support from the U.S. Department of Homeland Security under Grant Award Numbers 2014-DN-077-ARI079-02 and 2015-DN-077-ARI096. The views and conclusions contained in this document are mine and should not be interpreted as necessarily representing the official policies, either expressed or implied, of the U.S. Department of Homeland Security.

TABLE OF CONTENTS

LIST OF TABLES

LIST OF FIGURES

SUMMARY

The goal of this thesis is to develop an understanding of the benefits of using a monoenergetic photon source for imaging of cargo containers, as opposed to polyenergetic bremsstrahlung beams which are currently used. Monoenergetic beams can reduce dose to both the cargo and any potential stowaways within a container while increasing penetration and image contrast. In this work, imaging beams are tested for beam penetration, dose, and scatter within the container. It is found that higher energy beams scatter less widely, and can offer dose reductions to the cargo on the order of 40-60% while enhancing image quality. This is confirmed through simulation studies in Geant4 on both small-scale and full-scale cargo containers. Radiation detectors specifically targeted for imaging in this high-intensity environment are optimized and characterized, Cherenkov-based quartz detectors and LYSO scintillating detectors are used in the final imaging system. Imaging simulations include fully validated quartz detector response models. Dual-energy acquisition techniques, based on differences in attenuation coefficient as a function of energy, are developed and characterized for material-specific radiography. It is found that the monoenergetic sources offer better material specificity and higher contrast. Finally, tomographic image reconstruction algorithms are developed to take advantage of the isotropic nature of nuclear-reaction driven imaging beams. The incorporation of images taken at multiple views of the container can allow for unfolding of the cargo composition in 3D, enhancing operator safety if a container was found to hold suspicious material.

CHAPTER 1
INTRODUCTION AND BACKGROUND

Imaging in Active Interrogation

Cargo container shipping accounts for movement of 95% of all manufactured goods[1], moving 4 trillion US dollars of goods every year[2]. Since 2012, the ports of Long Beach and Los Angeles have averaged nearly 4% growth from year to year in total cargo imported[3]. As the amount of cargo moving across international borders increases, the risk of proliferation of special nuclear material (SNM) increases. This threat has been recognized by the Domestic Nuclear Detection Office (DNDO) of the U.S. Department of Homeland Security. Specifically, the detection of shielded SNM has been listed as one of DNDO's engineering grand challenges of the 21st century[4].

Cargo containers can be passively screened for presence of SNM with the use of radiation detectors at ports. Containers can also be probed for presence of SNM by bombarding the cargo with γ rays, x-rays, or neutrons, with a goal of imaging the cargo or inducing fission in SNM[5, 6, 7, 8]. These active interrogation methods can be more robust than passive interrogation for detection of SNM, especially in the presence of shielding[9, 10]. However, active interrogation methods are rarely performed on cargo containers. The challenge in scanning every container stems from high throughput requirements at most ports, the challenge of irradiating a large volume and processing the data rapidly, and limitations due to radiation doses both to radiation workers and potential stowaways in the containers ($<$500 mrem per scan)[11]. These factors lead to a relatively low active interrogation rate, around 5%[7]. Technological advances in both the interrogation source and detection systems are needed before active interrogation can be widely implemented.

Fundamental to active interrogation techniques is the use of high-intensity beams of

radiation. Both neutrons[12, 13, 14] and photons have been successfully used for imaging in laboratory environments, although this work will focus of photon imaging. High-energy, high-intensity beams are typically produced via electron linear accelerators (linacs). Electrons are accelerated by high voltages (from 3-9 MV), and stopped in a high-Z target, such as tungsten. As the electrons traverse the target, they lose their energy in bremsstrahlung interactions, creating x-rays which are released with a continuous energy spectrum. These x-ray spectra, although they can be very intense, are low-energy peaked. Previous investigators have reported that photons with energies greater than 2 MeV account for only 20% and 30% of 6 MV and 9 MV unfiltered bremsstrahlung spectra[15]. This relatively low energy means these sources are less penetrating than monoenergetic beams with similar peak energies. Many of the low-energy photons in a bremsstrahlung spectrum impart dose to the cargo while never making it to the detector, increasing the dose without contributing usable signal to the detection system. In addition, the low-energy photons scatter more widely than higher energy photons, degrading quality in imaging-based systems[16]. To alleviate the negative impacts of low-energy photons, bremsstrahlung spectra are sent through high-Z materials before reaching the cargo. This filtration increases the mean energy of the beam but can drastically reduce the flux. While multiple vendors have systems that can image containers, the dose and time requirements for cargo radiography pose a problem for bremsstrahlung-based systems[17, 18, 19].

One alternative to these systems is to use high-energy, monoenergetic beams. For example, inverse Compton scattering can produce bursts of high-energy photons by colliding laser pulses with relativistic electrons[15, 20, 21]. Inverse Compton scattering sources provide narrow divergence beams which are tunable in energy. These sources are attractive for use in an imaging system, but are still in a development phase. Another production method for high-energy photons is via low-energy nuclear reactions (LENR), such as $^{11}B(d, n\gamma)^{12}C$[22, 23, 24]. Nuclear reactions also provide a source with an on/off switch. Although the energy is not tunable, multiple energy acquisitions can be acquired at once,

for example with the 4.4 MeV and 15.1 MeV γ-rays produced by $^{11}B(d, n\gamma)^{12}C$. These sources are also nearly isotropic, and advanced collimation and acquisition schemes could be used to take near-tomographic images.

Downstream from the source, the detectors used in the imaging system will have a large impact on final image quality. Quartz Chernkov-based detectors are well suited for this imaging array because they are relatively inexpensive, which means several can be used to allow for large areal coverage. Since quartz detectors rely on Cherenkov radiation emission, they have an energy threshold, which means they will not see low-energy scattered radiation. In a large-scale imaging system, several detectors will need to be packed in order to optimize spatial resolution. However, spacing between detectors is decreased, radiative cross talk can become an issue. Quartz can alleviate these cross talk issues because of the Cherenkov threshold present in the detectors.

Objectives and Structure

This thesis work is part of a project with an objective of analyzing performance of an active interrogation imaging system based on a monoenergetic γ-ray source for cargo scanning. While any of the aforementioned monoenergetic photon sources could be used, this work will focus primarily on a reaction-driven imaging beam. The low-energy nuclear reaction $^{11}B(d, n\gamma)^{12}C$ produces multiple γ-rays and neutrons, including intense 4.4 MeV and 15.1 MeV photons. A diagram can be seen in Fig. 1.1. This thesis will focus primarily on the quantitative improvements such an imaging system can achieve by moving from a bremsstrahlung-driven imaging beam to a monoenergetic beam.

Much of this work will rely on simulated data in Geant4[25]. Much of the imaging work will be compared to the industry standard high-energy imaging source, bremsstrahlung. In order to compare between the low-energy nuclear reaction (LENR) and bremsstrahlung beams, a method for calculating beam dose to a generic cargo container will be developed. By equating the dose between acquisitions, image quality between can be compared

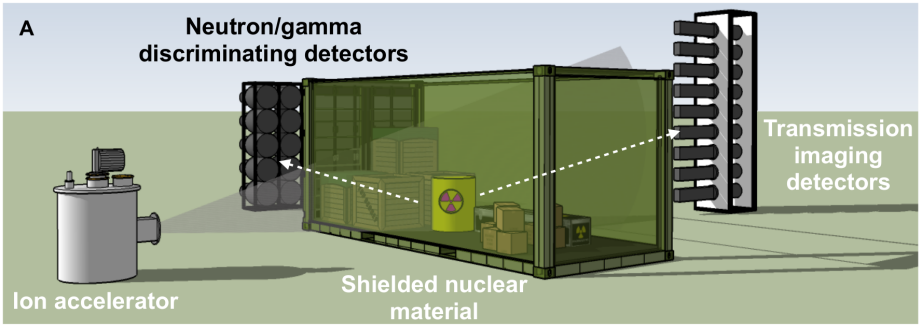

Figure 1.1: Conceptual design of the active interrogation imaging system. This work will focus on optimization of the array of transmission imaging detectors and data analysis algorithms. Figure reproduced with permission from [22].

between beam sources.

Another feature of the LENR source is that its γ-ray emissions are nearly isotropic. While this can be seen as a negative quality, as most beams are collimated down to only the forward direction, isotropic source can be utilized for tomographic image reconstruction. Iterative methods for x-ray CT and nuclear medicine imaging have been around since the 1970s, garnering more interest recently as available computational power continues to grow. Iterative reconstruction techniques are intriguing for this application because they allow for under-sampling of an object for tomographic reconstruction. Using the principles of compressed sensing, limited-angle, limited-view tomography is possible for this application, and a reconstruction algorithm will be developed and compared to other methods reported in the literature.

This work can be summarized by three focus areas:

1. Establishment and characterization of imaging requirements

2. Detector array optimization and modeling in Geant4

3. Image reconstruction and data processing algorithms.

Collectively, these three areas test the feasibility of this imaging system. Detector development is essential to data processing and image quality in the final system. Detectors must

operate in high-flux fields with little to no pulse pileup or detector dead time. Furthermore, these detectors must be relatively robust to detector-to-detector scatter, or cross talk, as several detectors will be placed close together in an imaging array. In an effort to minimize spatial resolution, the detectors must be small as well. As part of this thesis, the effects of array design on image qAuality will be characterized and quantified.

The dose calculation is necessary to show that imaging with monoenergetic sources can truly decrease the dose necessary for adequate image quality. Using monoenergetic beams, it will be shown that not only can the dose to cargo be decreased, but material discrimination can be enhanced. In development of imaging requirements, the detector array and imaging beam will be evaluated by the spatial resolution standard test outlined in ANSI standard N42.46-2008. Geant4 small-scale and full-scale cargo containers will be modeled to the penetration and contrast sensitivity of the imaging array with both the $^{11}B(d,n\gamma)^{12}C$ beam source and bremsstrahlung sources.

Achievable image characteristics for material-dependent, or Z_{eff}, image reconstruction will be characterized. This will be done both with the quartz detectors and independent of detector type so that the results may be made more general. Finally, image reconstruction and data processing algorithms will be developed to take advantage of the multidirectional beam source.

There are four specific research questions this work will set out to answer:

1. Can an active interrogation imaging system utilizing a monoenergetic photon source (specifically, the $^{11}B(d,n\gamma)^{12}C$ reaction), rather than a bremsstrahlung source, reduce imaging dose while maintaining comparable image quality? By how much can the total dose be decreased, assuming the same imaging geometry, and how will this affect image quality and material discrimination?

2. Is it feasible to produce an array for transmission imaging which can achieve a pixel size of 5 mm $\times$ 5 mm or less?

- How will reductions in vertical spatial resolution (i.e. detector packing) impact the detector response? Where is the balance of best spatial resolution vs. minimal cross talk?

3. Via dual-energy methods, what is the quantitative gain in material discrimination that can be attained with an imaging array comprised mainly of quartz Cherenkov detectors, as opposed to typical energy-integrating detectors?

4. With multiple arrays of detectors at different angles, can tomographic images be reconstructed? How few detector arrays, or views, can be used for this reconstruction?

As mentioned above, answering these questions will lead to a better understanding of cargo imaging and the impact monoenergetic photon sources can have on the field. Below is the outline of this thesis. It is laid out in a logical flow that starts with the beam source and detector design, explaining the impact these have on image quality. Later, radiographic and tomographic images are simulated in Geant4 and evaluated.

- Various beam sources for cargo radiography are discussed, both in place now and under development. Various beams are generated in Geant4 and these will be discussed and compared to results that others have reported in the literature.

- Moving down from the imaging source, discuss detector array optimization is discussed in detail. Cross talk, optical output, and efficiency of the quartz detectors to be used in the final imaging array are characterized.

- Using dose as a backbone, multiple images are generated via Monte Carlo simulation. These images will serve as phantoms, which are completely known, and will allow for comparison of the impact of imaging beam on final quality. It should be noted that in this work, images will always be created using a specific detector model and processing framework which may be different from methods used in industry or

by other authors. A consistent methodology is used to allow for a fair comparison between bremsstrahlung and LENR imaging.

- The use of an isotropic radiation source for tomography will be evaluated. Modified algorithms from medical computed tomography literature have been used for this application and evaluated.

CHAPTER 2

BEAM SOURCES

Implementation of active interrogation is hindered by multiple factors. A primary concern is the radiation dose involved, both to any radiation workers and to the cargo itself, especially in the presence of stowaways. A limit of 500 mrem per scan has been proposed by the National Council on Radiation Protection (NCRP) and DNDO[11]. Additionally, DNDO reports that an imaging system should take less than 2 minutes to scan an entire container to keep up with throughput requirements imposed at most ports. While multiple vendors produce interrogation systems, the dose and time requirements have proved difficult to satisfy, and these inhibit widespread implementation of active interrogation. In the context of cargo imaging, most systems use bremsstrahlung-generated x-ray sources. These exhibit a continuous energy distribution with maximum energies up to 9 MeV, yet average energies are typically less than 3 MeV. Many of the low-energy photons in a bremsstrahlung spectrum impart dose to the cargo while never making it to the detection system, increasing the dose without contributing usable signal to the imaging system.

If a high-energy monoenergetic beam source could be used instead, each source photon would have a higher probability of penetrating through the cargo and reaching the detector, increasing system efficiency and reducing the dose. Figure 2.1 shows the work-flow of an active interrogation system from a radiation detection standpoint. An interrogation beam bombards the container, and some portion of the beam is stopped in the container, while other components of the beam are transmitted. When using photons as the interrogation source, higher energy sources have better penetration. The black circles shown on the spectra showcase the difference in the energy distribution before and after the transmission through the container. The low-energy portions of the bremsstrahlung spectra are absorbed by the container, increasing dose to the cargo without contributing information to

Figure 2.1: Work-flow of a cargo scanning system from a radiation detection standpoint. The left shows the energy distribution of various interrogation beams and the right shows the energy distribution of those beams after penetration through the container. The black circle highlights the differences in the low-energy end of the spectrum. These photons are preferentially absorbed in the cargo container, imparting dose while not contributing to image quality. The LENR beam is relatively robust to this effect since it has a higher-energy, discrete distribution.

the detection system. Additionally, the shift in the mean energy of the spectra can lead to inaccuracies when measuring material attenuation.

There are two main methods of producing a high-energy monoenergetic photon source currently under investigation, namely inverse Compton scattering (also called Thomson scattering) and low-energy nuclear reactions. Inverse Compton scattering produces bursts of high-energy photons by up-scattering optical photons with relativistic electrons[15, 20, 21, 26]. Such a system would also allow for pencil beam scanning with higher control of the dose imparted to the cargo.

LENR beams, such as $^{11}B(d,n\gamma)^{12}C$[22, 27] can be produced using compact ion accelerators. Previous studies have investigated various LENRs as active interrogation beam sources[28, 29]. The prominent γ-ray energies coming from the $^{11}B(d,n\gamma)^{12}C$ reaction are at 4.4 and 15.1 MeV, yielding a relatively high energy beam. The presence of multiple γ-ray lines allows for calculation of effective atomic number (Z_{eff}) via dual-energy methods[30, 31, 32]. Previous work has shown feasibility of imaging with a LENR source in a proof-of-concept system[22, 33].

A prime advantage of using a nuclear-reaction based beam is that if energy-resolving detectors are used, the high- and-low energy images are acquired simultaneously, potentially leading to shorter image acquisition times. The images will be perfectly registered,

meaning the pixels in both images correspond to the exact same point in position and time. Although the pixel values between the low and high energy images will be different, their structures will be constant. From an imaging perspective, this redundant structural information can be utilized to reduce noise. Reducing final image noise allows for a potentially larger reduction in dose as the two quantities are correlated.

Bremsstrahlung Beam Production

As mentioned above, bremsstrahlung beams are typically produced using electron linear accelerators (linacs). These radiation sources are widely used because they are well understood and they can attain high fluxes, up to 10^{11} photons/s for imaging[15]. Varex Imaging, Rapiscan, and Nuctech are all industry leaders in bremsstrahlung-based cargo radiography, producing systems with maximum energies from 3 MeV to 9 MeV[17, 18, 19] that are capable dual-energy acquisition, achieving some form of material discrimination. Passport Systems uses a Rhodotron electron accelerator that can be run at multiple energies, producing even higher fluxes than conventional linacs, and their EZ-3D reconstruction technique can produce material-specific maps via backscatter imaging[34, 35, 36].

In order to compare monoenergetic photon beams against bremsstrahlung imaging sources, a Geant4 simulation to emulate these systems was developed. The Geant4 geometry can be seen in Figure 2.2. The parameters for the simulation were taken from both [15] and [37]. The electrons are incident on a tungsten target which is 3 mm in diameter, and electron position is sampled from a 2-D Gaussian distribution, with the standard deviation (σ) set to 1.18 mm. Downstream, the x-rays go through a filter which is varied from simulation to simulation. Finally, the tungsten collimators (blue) accept photons within a 2 degrees horizontally and 30 degrees vertically, creating a tight cone-beam. Rather than simulating the bremsstrahlung generation process with every simulation, the x-ray energy distribution is collected downstream from the target, filter, and collimator. This energy distribution is then compiled into a probability distribution function and sampled from in subsequent simula-

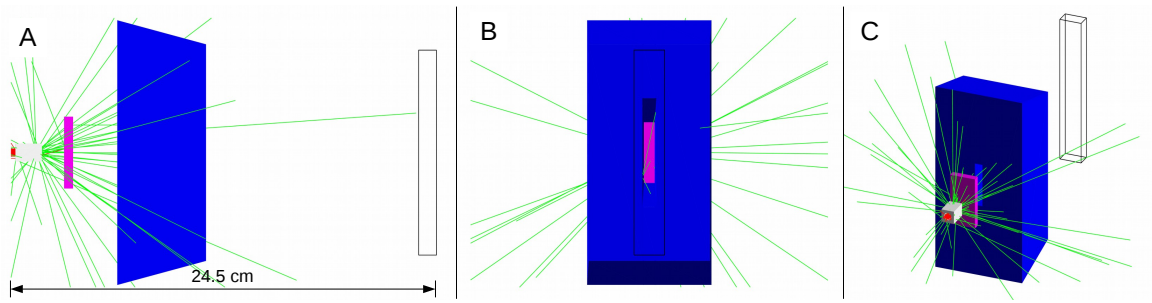

Figure 2.2: Geant4 geometry for simulating the generation of bremsstrahlung spectra. The electrons (red) are accelerated in vacuum to the target (gray), generating x-rays in a forward-directed cone in the target. The blue block is the collimation system which accepts photons within a cone that is $2°$ horizontally and $30°$ vertically. The magenta block is a 1 cm thick tungsten beam-hardening filter, although the filter can be changed between simulations. Photon energy distribution is collected in the black-outlined box downstream from the collimator. This energy distribution is then sampled from in future simulations.

tions, saving the computational cost of electron transport in the target in each simulation.

Three beam filters were tested for the bremsstrahlung simulations: 0.5 cm of copper, 1 cm of tungsten, and a combination of the two. All three filters were tested with incident electron energies of 3, 6, and 9 MeV. The effects of filtration on flux and energy distribution were tested, and these results are summarized in Figure 2.3 and Table 2.1. Figure 2.3 shows the collected spectra in the detector volume shown in Figure 2.2. Beam filtration can help reduce the dose imparted to the cargo in imaging, but at the cost of reduced flux.

Linac filter design is a non-trivial task. The optimal amount of filtration would be set such that the flux on the far side of a container would be minimally impacted while reducing the low-energy photons at the source as much as possible. Previous work has shown that low-Z filters with equivalent areal densities to those presented here can provide a high-energy spectral shift[32]. In this work, the filtration was not optimized in either of these ways. For all beam simulations later in this thesis, 1 cm of tungsten filtration was used. This was chosen as a compromise between high flux and high mean energy, and it allows for more direct to comparison to previous work. Table 2.1 shows that this increases the mean energies of 6-MV and 9-MV spectra to 1.65 MeV and 1.97 MeV. Similarly, 77.24% and 83.03% of the 6-MV and 9-MV spectra lie above 1 MeV. These results are similar

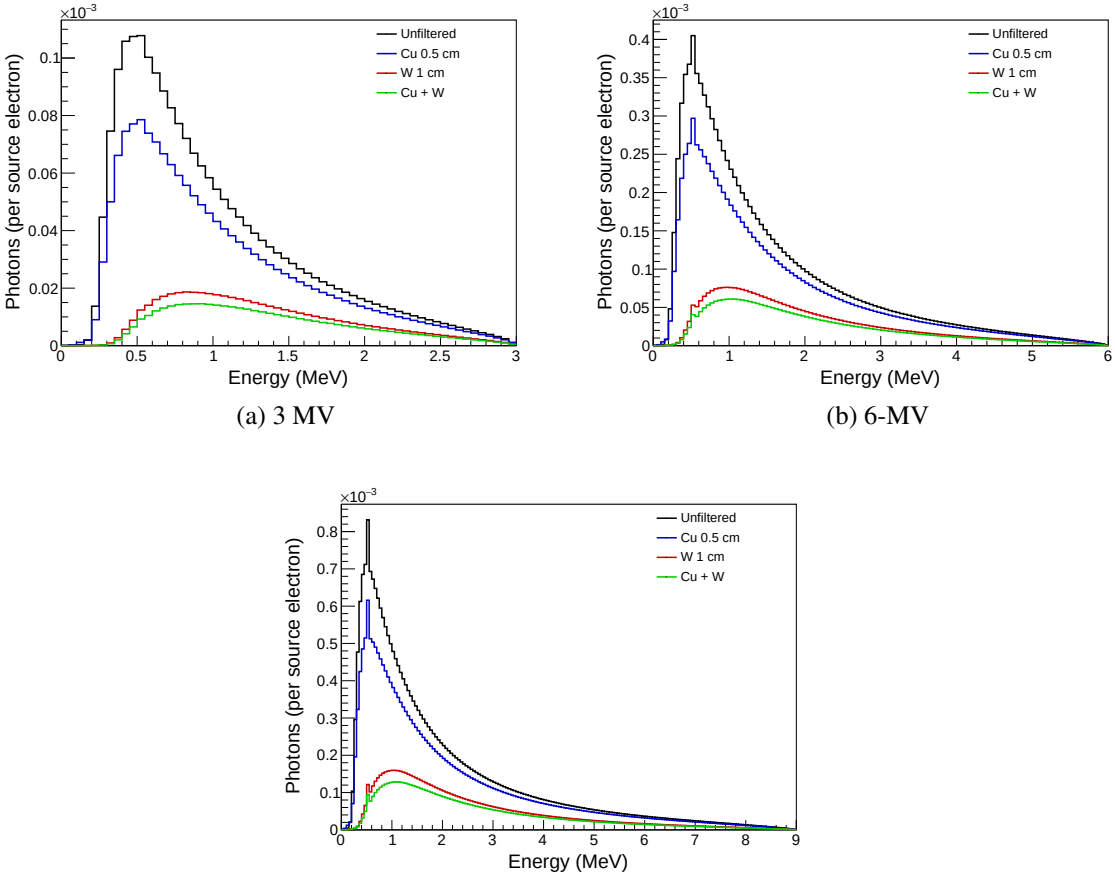

(a) 3 MV

(b) 6-MV

(c) 9-MV

Figure 2.3: Bremsstrahlung spectra from the simulation shown in Figure 2.2. As beam filtration is increased, the mean energy increases at the cost of reduced flux. Additionally, increasing electron energy leads to increased contibution of 511 keV photons from positron production and annihilation in the target and filters.

to the findings reported in [15], and use of the tungsten-filtered beam should allow for extrapolation from the data presented in that report.

Low Energy Nuclear Reactions

LENRs are typically induced by accelerating light ions into targets of a given material. This form of beam production has been widely used in the physics community, for example in deuteron-deuteron (D-D) or deuteron-triton (D-T) neutron generators. For photon imaging, the ideal reaction will involve light ions, such as protons or deuterons, have a relatively high

Table 2.1: Statistics from advanced bremsstrahlung simulations. Yields are calculated as (photons collected / electrons emitted). The final column shows the fraction of the detected photon spectrum above 1 MeV.

Electron Energy	Filter	Mean Energy (MeV)	Yield (%)	Above 1 MeV (%)
3-MeV	None	0.82	0.21	38.71
	0.5 cm Cu	0.86	0.16	41.41
	1 cm W	1.20	0.05	63.03
	Cu + W	1.22	0.04	64.73
6-MeV	None	1.14	1.04	55.88
	0.5 cm Cu	1.22	0.83	58.96
	1 cm W	1.65	0.33	77.24
	Cu + W	1.70	0.27	78.73
9-MeV	None	1.39	2.47	63.10
	0.5 cm Cu	1.49	2.00	66.06
	1 cm W	1.97	0.84	81.75
	Cu + W	2.04	0.70	83.03

Table 2.2: Candidate low-energy nuclear reactions for imaging.

Reaction	Reported γ-ray energies (MeV)	Reference(s)
$^{11}B(d,n\gamma)^{12}C$	4.4, 15.1	[22, 23, 27]
$^{11}B(p,\gamma)^{12}C$	11.7,12.13, 12.79, 17.23	[28, 29]
$^{12}C(p,p\gamma)^{12}C$	4.44, 12.79, 15.1	[38]
$^{16}O(p,p\gamma)^{16}O$	2.74, 6.13, 6.92, 7.12	[39]
$^{19}F(p,\gamma\alpha)^{16}O$	6.13, 6.92, 7.12	[28, 40, 41]
$^{27}Al(p,\gamma)^{28}Si$	9.8, 11.5	[28, 40, 42]

cross section, and produce γ-rays with energies greater than 3-MeV. Table. 2.2 lists a few candidate reactions and their resulting γ-ray energies. Additionally, like bremsstrahlung, these sources are nearly isotropic, potentially allowing for advanced imaging techniques like tomography given the beam can be collimated into views of the container at multiple angles.

Many of the reactions presented in Table. 2.2 could be used as an imaging source. An ideal monoenergetic beam produces multiple γ-ray lines so that material atomic number can be calculated from the transmission data. Additionally, these γ-ray lines should be well

separated so that they can be easily distinguished by the detector. Larger energy separation also can lead to enhanced material identification due to different mechanisms of photon interaction in matter. Ideally, the reaction would have a relatively high cross section and need a low energy light ion to ease constraints on the particle accelerator. Following these considerations, this work will use the $^{11}B(d, n\gamma)^{12}C$ reaction. The difference between the primary energies, 4.4 and 15.1 MeV, is great enough to ensure change in material attenuation coefficients. The reaction also provides neutrons, which could be leveraged to provide complementary imaging information, or filtered out if neutron dose is of concern.

Previous work has shown that it is possible to produce an imaging beam using the $^{11}B(d, n\gamma)^{12}C$ reaction[22, 23, 33, 43]. In order simulate an imaging acquisition system with this beam, the energy distribution of the beam must be understood. Although Geant4 is capable of modeling LENRs, experimental data are used to generate the beam source in an effort to keep these results consistent with those that have been previously reported.

To create an energy distribution function, measurements were first taken at MIT's Bates Accelerator facility with both LaBr and HPGe detectors by another member of the research group. The details of the experiment and characterization of the beam can be found in Reference [44]. To create the source input for Geant4, a γ-ray unfolding code was used to unfold the measured LaBr spectrum[45]. The unfolding code accounts for detector efficiency and can be used to measure the relative ratio between the γ-ray lines. The HPGe data was used to adjust the γ-ray energies output by the unfolding code. In the experimental studies, 35.56 cm of borated polyethylene was used to filter out the neutrons. The resulting energy distribution of the LENR source is shown in Figure 2.4.

The 4.4 MeV and 15.1 MeV γ-rays seen in Figure 2.4 are known to come from decay of the excited ^{12}C nucleus, and the lines at 6.5 MeV and 8.95 MeV are believed to come from other reactions in the head of the accelerator. While any of these lines could be leveraged in an imaging acquisition scheme, this work will focus only on the use of the 4.4 MeV and 15.1 MeV lines. Additionally, as mentioned above, $^{11}B(d, n\gamma)^{12}C$ produces neutrons of

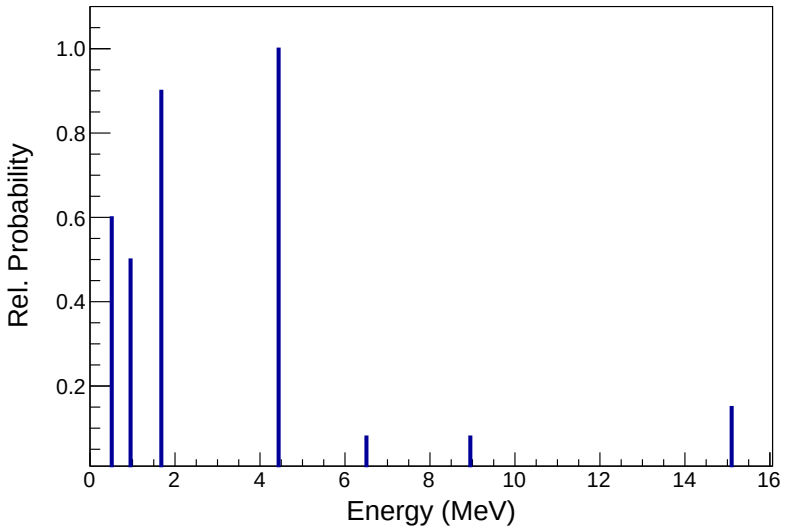

Figure 2.4: Energy distribution for the γ rays coming from the low energy nuclear reaction $^{11}B(d, n\gamma)^{12}C$, unfolded from experimental data taken at MIT's Bates Accelerator Laboratory. The 4.4 MeV and 15.1 MeV γ rays are known to come from decay of the excited ^{12}C nucleus, and the lines at 6.5 MeV and 8.95 MeV come from other reactions in the head of the accelerator.

up to 16.5 MeV, and these could be leveraged to provide complementary information to the γ-ray images, but that will not be discussed in this work. The γ-ray fluxes measured during the experiment were 5.3×10^7 photons/s/μA of beam current and 6.2×10^6 photons/s/μA for the 4.4 MeV and 15.1 MeV photons, respectively[22]. The fluxes produced in this experiment are lower than those produced by electron linacs. However, it should be noted that the primary limiting factor on fluxes in the experiment was the neutron dose rate in the facility. Better shielding or use of reactions which do not produce neutrons, such as $^{12}C(p, p\gamma)^{12}C$, could allow for increased fluxes. Furthermore, $^{16}O(p, p\gamma)^{16}O$ results in γ-rays with energy below 10 MeV, which may be desirable to diminish photoneutron generation in the accelerator or container.

Table 2.3: Effects of tuning the energy spread on MPS sources. Table recreated with permission from [15]. Energy spread is the full-width at half the maximum (FWHM) of the photon spectrum. Beam divergence is given in milliradians (mrad).

Parameter	2% Energy Spread	10% Energy Spread	30% Energy Spread
Photon energy	Continuously tunable from $<$ 1 MeV to $>$ 20 MeV		
Divergence	0.5 mrad at 2 MeV 0.25 mrad at 8 MeV	2.5 mrad at 2 MeV 1.25 mrad at 8 MeV	7 mrad at 2 MeV 3.5 mrad at 8 MeV
Emission spot size	few μm	0.1 μm-few μm	0.1 μm-few μm
Photon yield	$\leq 10^7$ photons/shot	$\leq 10^8$ photons/shot	$\leq$ few 10^8 photons/shot
Pulse length	microseconds to femtosecond		

Inverse Compton Scattering

As mentioned previously, inverse Compton scattering, also known as Compton backscattering or Thomson scattering, is a promising emerging technology to produce near-monoenergetic photons. In this report, these sources will be referred to as monoenergetic photon sources (MPS). Although reaction based sources are also monoenergetic, they will be referred to with the abbreviation LENR. Photons are produced when relativistic electrons collide with intense laser pulses. The electrons then oscillate, releasing synchrotron-like radiation[46]. There are various methods to produce the electrons and laser pulses, but they are trending smaller and more intense due to advancements in technology on both the electron acceleration side and the laser side[15, 47, 48, 49]. These sources are especially attractive for imaging because they are nearly monoenergetic, have μm-scale emission spot sizes, and are tunable in energy. These sources are commonly termed quasi-monoenergetic, because although they can produce nearly monoenergetic photons, there is some energy spread. The variation in energy will effect multiple characteristics of the beam, and Table 2.3 displays some of these effects.

For general radiography, it is not anticipated that a somewhat large energy spread (i.e. 20%) would have a tremendous impact on image quality. This would still be a large improvement in spectral shape over bremsstrahlung beams. Although not yet a fieldable tech-

nology for cargo radiography, these sources have a promising future. In this thesis, imaging characteristics of MPS beams at 3, 6, and 9-MeV, all with energy spreads of 10%, will be investigated.

Dose to the Cargo

Radiation dose, although inherently easy to define, can have multiple meanings when it comes to imaging. In cargo scanning, dose to the cargo, dose to operators running the scanning system, or dose to the detectors can all be limitations. The dose directly coming out of the accelerator head can also be a concern. Dose is typically defined as energy depostied per unit mass, so if detectors or cargo are changed, so is dose. One of the goals of this project is to maintain or improve image quality using a monoenergetic photon source while decreasing the imaging dose. In order to adequately compare images accurate dose calculations are necessary. While the NCRP has released dose guidelines for cargo imaging, the methods which are used to calculate that dose are not specifically listed.

For dose calculations, the imaging beams will be modeled according to the characteristics described above. Although the LENR beam produces neutrons, the neutron spectrum is not included in these calculations. In previous experiments the neutrons have been filtered using borated polyethylene, and other reactions, such as $^{12}C(p,p\gamma)^{12}C$ can produce the same states of carbon as $^{11}B(d,n\gamma)^{12}C$ but without the neutrons. The MPS beams are produced in a different manner from bremsstrahlung and LENR sources, resulting in a narrow-angle pencil beam, and they will have to be rastered across the cargo for imaging. For simplicity, the MPS sources were modeled in the same angular distribution as the other beams (i.e. the narrow divergence of the beam was not accounted for). This may be an over-representation of the dose due to these sources because a live system will use a pencil beam that reduces scatter contributions and hence the number of photons needed to form an image, and it may be able actively modulate dose[15]. These simulations show a baseline level dose for the MPS sources. All dose simulations were carried out in Geant4 using the

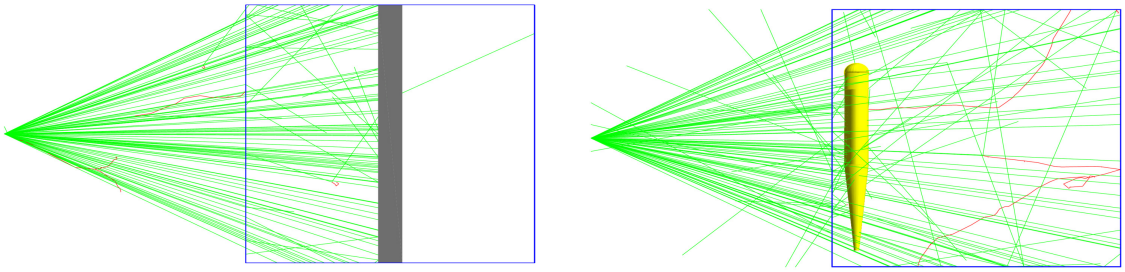

(a) Steel Plate (b) Human Phantom

Figure 2.5: Geant4 geometries used for dose calculation. (a) is meant to emulate an average cargo container and (b) is simulating dose to a possible stowaway in the container. A third simulation was run with the plate and human phantom in place. The imaging source is 40 cm wide and has a vertical fan half-angle of $30°$.

standard physics list QGSP_BERT_HP. This physics list includes photo-neutron generation, a potential concern for the high energy LENR beam, and energy deposition measurements were made for all particles. Dose is defined as energy deposited per unit mass. To mitigate the differences due to masses when looking at different geometries, dose will be defined in both relative and absolute terms below.

Three different dose measurement scenarios are tested, Figure 2.5 shows two of the configurations. Previous studies have reported that 80% of cargoes have an average areal density equivalent to 20 cm of steel, and the first dose scenario reflects the imaging dose to an average container using a 20-cm steel plate[11, 30, 50]. The plate has the same cross sectional area as the interior of the container, 1.19 m $\times$ 2.39 m. Dose to a possible stowaway in the container is then simulated by placing the MIRD human phantom in an empty container[51]. In the final dose measurement, the human phantom is placed in the container with the steel plate to determine the effects of scatter from the cargo. Only dose to the human phantom was tallied in this simulation. In all simulations, the radiation source was 40 cm wide, replicating acquisition of multiple image slices. This width was determined so that the human phantom was fully irradiated. Vertically, the source was sampled as a fan beam with a half-angle of $30°$, matching the imaging beam which will be used in later simulations. Each geometry was run with 10^{10} particle histories.

Table 2.4: Results of the dose simulations. Absolute doses are listed in Gy per source photon and relative doses are normalized to the 6-MV bremsstrahlung beam. The fourth and fifth columns are dose to the human phantom in the empty container while the sixth and seventh columns are dose to the human phantom with the steel plate inside the container.

Beam	Steel Plate		Human Phantom		Both	
	Absolute	Relative	Absolute	Relative	Absolute	Relative
6-MV Brem.	4.31E-15	1.00	4.72E-14	1.00	4.73E-14	1.00
9-MV Brem.	5.53E-15	1.28	5.59E-14	1.18	5.61E-14	1.18
3-MeV MPS	6.71E-15	1.56	6.18E-14	1.31	6.20E-14	1.31
6-MeV MPS	1.36E-14	3.16	9.31E-14	1.97	9.34E-14	1.97
9-MeV MPS	2.06E-14	4.77	1.18E-13	2.50	1.19E-13	2.51
LENR	6.90E-15	1.60	6.36E-14	1.35	6.37E-14	1.35

The results of the three dose simulations are summarized in Table 2.4. In the third configuration, with both the human phantom and the steel plate, only dose to the human phantom was tallied. As anticipated the monoenergetic beams deliver more dose per incident photon to the human phantom and steel plate than the bremsstrahlung beams. The advantage of the monoenergetic beams with regards to dose does not come from raw measurement of energy deposition, but of the higher penetration capabilities. Final noise on reconstructed images is dependent on the dose to the detectors, which will be discussed in later chapters. These effects will both be discussed later in this thesis.

Beam Quality Tests

Three different beam types have been evaluated for three characteristics relating to imaging performance. The first test is characterization of the scatter within a given cargo container, which can not only effect the final image quality, but will also f the dose to the cargo. Finally, the beams have been evaluated for dual-energy reconstruction. The capability of a beam to be used for a dual-energy acquisition is a property of both the detector and the imaging beam, and here the beams will be evaluated involving a generic detector response. Finally, beam penetration will be characterized, showing how the beam is effected by the presence of cargo and the impact this will have on noise characteristics of reconstructed

images.

Scatter in Cargo

The energy distribution of each imaging beam will not only effect the total beam penetration, but will also impact the scattering within the container. A Geant4 simulation of a homogeneously filled cargo container was used to study this effect. The filling material of the container is water, but with artificially lower density (0.6 g/cm^3), corresponding to the maximum container fill weight. In these simulations, flux and energy deposition in a voxelized sensitive detector within the container were measured. These simulations are meant to show how scattering affects the dose distribution within the container. Previous authors have shown that in addition to reduced cargo dose, reduced scattering due to the narrow-angle pencil beam of MPS sources can enhance image quality, further reducing the dose required to form an image of equal quality to bremsstrahlung sources[15]. These effects were not studied in this simulation. Figure 2.6 shows the simulation geometry with a fan beam acquisition. For all imaging beams, the source was a fan beam. In each simulation, the beam was fired into the center of the container in x. The volume was 101 $\times$ 101 $\times$ 201 voxels in x, y, and z. Each pixel is a cube with an edge length of 1.19 cm.

The resulting dose maps are shown in Figure 2.7. The maps are normalized such that the same number of photons would penetrate through an average cargo container (20 cm of steel). The maps show that the higher energy MPS and LENR beams deposit their dose more centrally than the bremsstrahlung beams. They are also more penetrating, which leads to more secondary scatter at deeper depths. Figure 2.8a shows the dose to each pixel on the central axis as a function of depth. This is just a projection of the primary beam line for each sub-figure shown in Figure 2.7. A strongly penetrating beam will show a relatively flat curve here. Note that this is shown on a logarithmic scale so all beams experience large amounts of attenuation, but the high-energy monoenergetic beams show the strongest

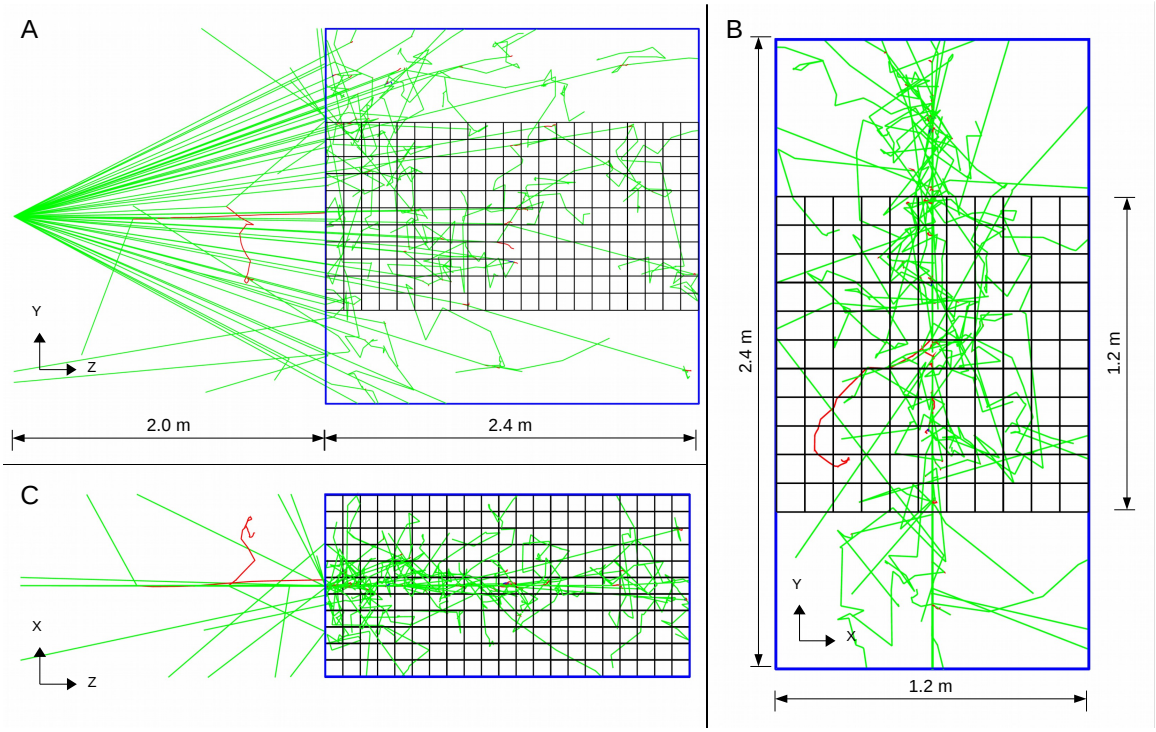

Figure 2.6: Simulation geometry for scattering measurements in a uniform container. (A) and (B) show the same simulation geometry looking from behind the source, and (C) shows the geometry looking from the top down. For this figure, the voxelized region is reduced to $11 \times 11 \times 21$ voxels. The full simulation has a voxel space of $101 \times 101 \times 201$ (1.2 m $\times$ 1.2 m $\times$ 2.4m). The fan half-angle for these simulations is $30°$.

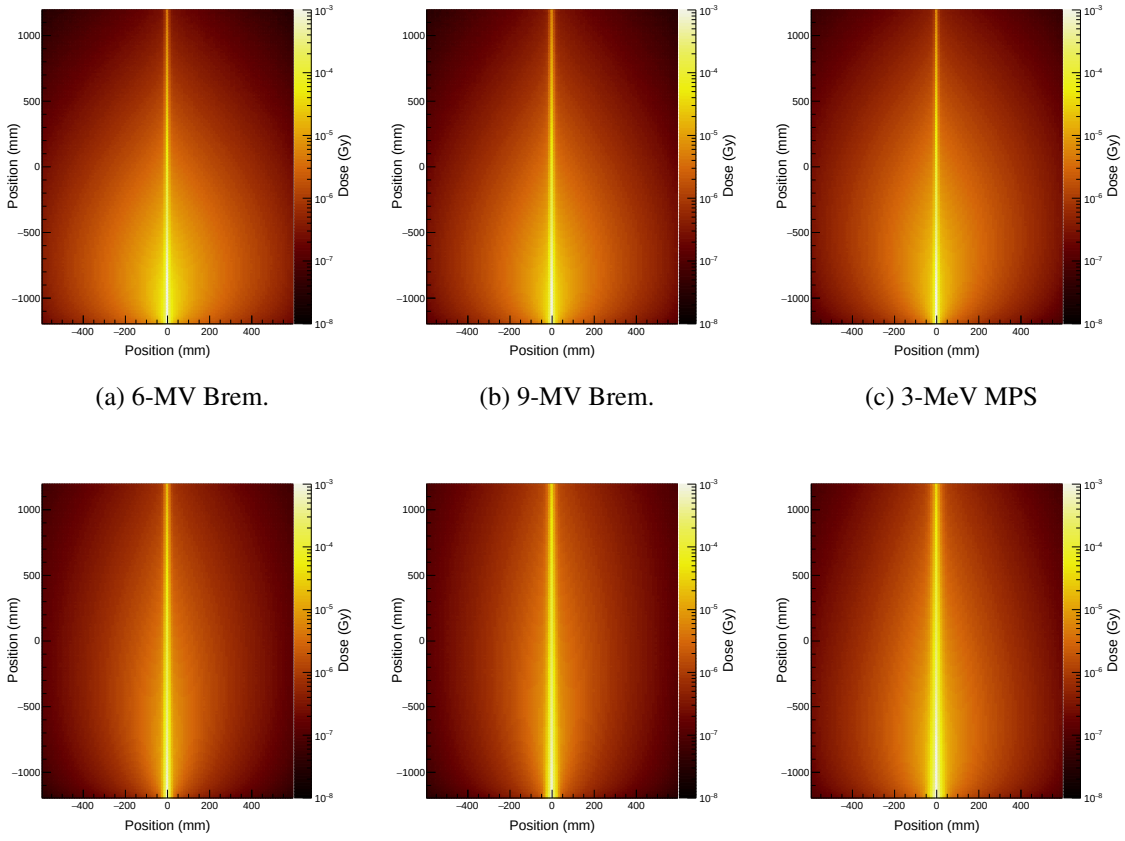

(a) 6-MV Brem. (b) 9-MV Brem. (c) 3-MeV MPS

(d) 6-MeV MPS (e) 9-MeV MPS (f) LENR

Figure 2.7: Energy deposition heat maps from image acquisitions of a homogeneously filled container with density 0.6 g/cm^3 (total areal density of 151 g/cm^2 including the 5 mm stainless steel walls). It should be noted that while these dose values can be compared to each other, the total value could be scaled up or down depending on scan time, image quality desired, etc. The higher-energy monoenergetic beams provide less off-axis dose, reducing cumulative dose to the cargo for an entire scan.

penetration. Figure 2.8b shows the off-axis ratio (OAR) which is defined as

$$OAR = \frac{\sum E_{secondary}}{\sum E_{primary}} \tag{2.1}$$

where $E_{scattered}$ is the secondary energy, i.e. energy given to all voxels outside of the beam. The 9-MeV MPS and LENR beams perform best with regards to OAR, delivering a lower portion of their dose to the parts of the cargo container that are not being imaged.

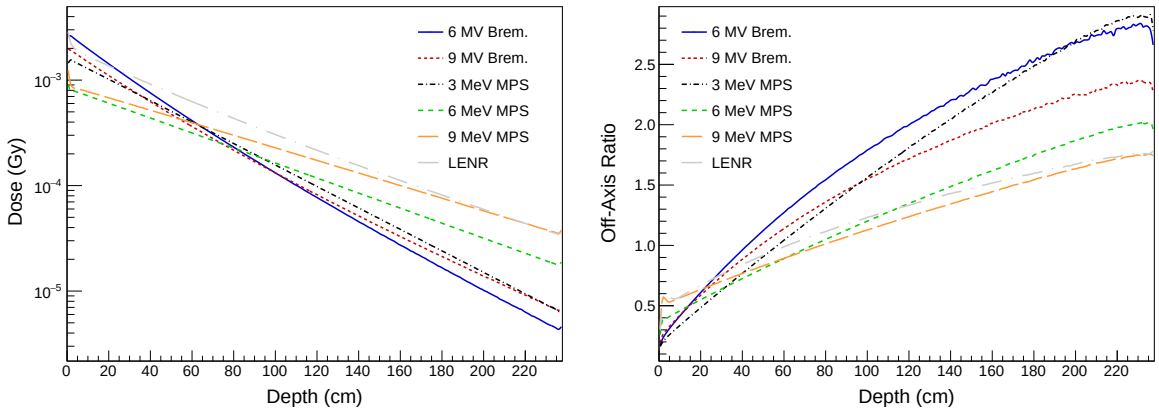

(a) (b)

Figure 2.8: Energy deposition profiles measured in a homogeneously filled container. (a) shows the dose in each pixel in the imaging beamline. (b) shows the off-axis ratio which measures the secondary dose relative to the beam-line. The LENR and 9-MeV MPS beams outperform the other beams, showing the smallest OAR at depth.

Dual-Energy Performance

Transmission radiography allows for sampling of the linear attenuation coefficient, μ, of a given material. The specific type of interaction a photon undergoes in a material is a function of both the material atomic number (Z) and the photon energy. Figure 2.9 shows reduced mass attenuation coefficient, μ/ρ (where ρ is the material density), for three materials in the energy domain used for cargo radiography. The attenuation coefficient can be broken up into components based on the interaction type, Compton scattering is the dominant interaction type shown in Figure 2.9, but as energy and atomic number increase, the probability of pair production increases. In the $^{11}B(d,n\gamma)^{12}C$ beam, most of the 4.4 MeV photons will undergo Compton scattering, while a significant amount of 15.1 MeV photons will undergo pair production, especially in high-Z materials such as uranium. This difference in interaction type can be leveraged to back out atomic number from transmission measurements. In the case of any monoenergetic beam, the transmission of each γ-ray is mapped to the attenuation coefficient

$$T(E) = \frac{I}{I_0} = e^{-\mu(E)x} \tag{2.2}$$

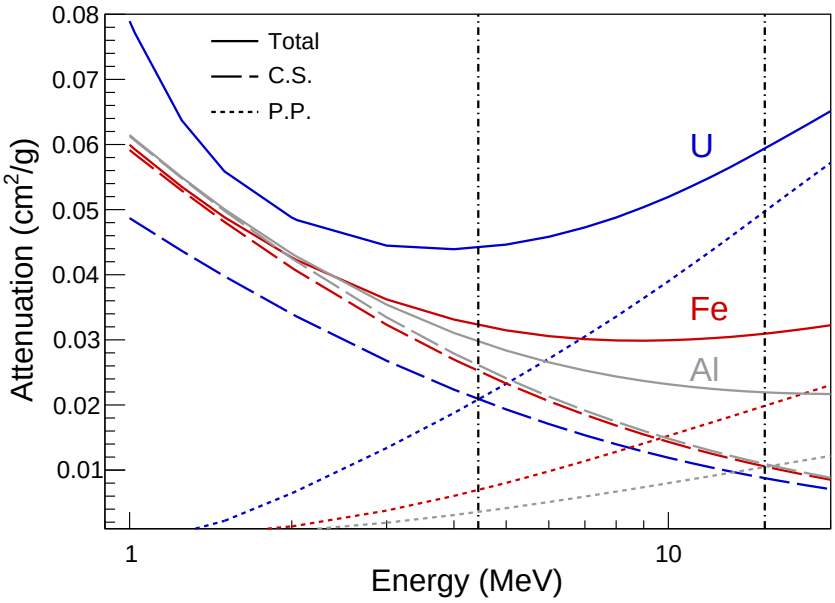

Figure 2.9: Values for μ/ρ in the energy domain of cargo radiography. The dotted vertical lines are the energies of the prominent γ-ray lines coming from $^{11}B(d,n\gamma)^{12}C$; note the increase in the pair production cross section at higher energies. This will yield bigger differences in radiography measurements of μ as a function of Z and energy, and can dictate the success of a dual-energy material reconstruction.

where I_0 is the intensity incident upon the cargo, I is the measured intensity after transport through the cargo, $\mu(E)$ is the energy-dependent linear attenuation coefficient, and x is the path length of the γ-ray through the cargo.

For bremsstrahlung beams, the measurement of $\mu(E)$ can employ either energy-integrating or spectroscopic detectors since the acquisitions can be taken separately. Due to the large amount of spectral overlap between the 6-MV and 9-MV beams, energy-integrating detectors degrade the separation of $\mu(E)$. However, to utilize the energy information of an LENR beam, spectroscopic detectors must be used. Transmission due to the separate energies is measured individually. Taking the logarithm of the transmission drops the dependence on x

$$R = \frac{ln(T(H))}{ln(T(L))} = \frac{\mu(H)}{\mu(L)} \tag{2.3}$$

where H and L represent high and low energy, respectively. This measured R-value will

allow for mapping from transmission measurement to a single variable which is a function of Z. The use of other lines in the γ-ray spectrum, 1.67 MeV, for example, could yield larger differences in R as a function of material. However, no analysis on this was done due to low penetration through thick cargoes. In this work, this formalism is extended to a dual-energy bremsstrahlung acquisition, assuming that spectroscopic detectors are used. Since radiography is projection-based imaging, Z_{eff}, a weighted combination of the various materials along a given ray, is measured rather than true material atomic number.

A series of transmission simulations was designed to study the effects of cargo thickness on measurement of R-value. A target of variable material and thickness was placed in between a source and a virtual detector, 31 materials at 6 different thicknesses were tested. In the calculation of R, specific regions of each spectrum were integrated. The integration technique had to be developed separately for each beam based on the acquisition system. All integration techniques assumed the detector had some capability of spectroscopy. This is not the case in all systems on the market today, and different vendors have other material reconstruction techniques based on energy-integrating detectors. No full detector response was modeled but counts per bin were adjusted based on the detector efficiencies discussed in the next chapter. This adjustment method likely over-represents the detector's efficiency at all energies, but it provides an approximation of detection efficiency.

Since the LENR beam produces both low and high energy photons in the same beam, there is only one resulting spectrum per detector. The 4.4 MeV and 15.1 MeV peaks in this spectrum were integrated separately. For the bremsstrahlung acquisitions, low and high-energy data were taken separately. Specific integration regions of the detected spectra were determined based on empirical tuning. Original integration of the 6-MV and 9-MV spectra from 0 to maximum energy yielded poor results. Through trial and error, the integration regions were tuned to yield the highest change in R-value as a function of Z. The final energy regions are 1-5 MeV for the 6-MV bremsstrahlung beam and 5-9 MeV for the 9-MV bremsstrahlung beam. The mean energy of each integration region is shown in Table.

Table 2.5: Mean energies (in MeV) of the integration regions used for calculation of R-values.

Beam	Low Energy	High Energy
Brem.	2.17	6.27
LENR	4.44	15.10
MPS	3.00	9.00

Table 2.6: Fit parameters for the curves shown in Figure 2.10. The fit line is calculate according to the equation $f(x) = p0 + (p1 \times x) + (p2 \times x^2) + (p3 \times x^3) + (p4 \times x^4)$.

Value	Brem.	LENR	MPS
$\bar{\chi}^2$	4.89E-7	2.12E-7	1.11E-7
p0	5.12E-1 $\pm$ 7.69E-4	4.43E-1 $\pm$ 5.05E-4	4.87E-1 $\pm$ 3.66E-4
p1	9.28E-3 $\pm$ 1.14E-4	2.59E-2 $\pm$ 7.47E-5	1.49E-2 $\pm$ 5.41E-5
p2	-1.15E-5 $\pm$ 4.71E-6	-2.56E-4 $\pm$ 3.10E-6	-6.75E-5 $\pm$ 2.25E-6
p3	-4.00E-7 $\pm$ 7.18E-8	1.08E-6 $\pm$ 4.72E-8	-3.19E-7 $\pm$ 3.42E-8
p4	2.02E-10 $\pm$ 3.61E-10	-2.14E-9 $\pm$ 2.37E-10	1.29E-9 $\pm$ 1.72E-10

2.5. This mean energy was calculated for the incident beam. It should be noted that the energy spectrum of a bremsstrahlung beam varies with cargo density, and this will further impact the R-value measurement[30, 32]. For the MPS beams, the low- and high-energy beams could be acquired separately or simultaneously. To keep the results consistent with bremsstrahlung beams, it was assumed that the detector readout would correspond only to one acquisition at a time. In other words, the detector has separate spectra for a 3-MeV acquisition and a 9-MeV acquisition, and these were integrated separately.

Figure 2.10(a) shows the achievable R-value curve based on the mean energies of each integration region. These curves were created by looking up the μ/ρ values on NIST's XCOM database[52]. The energies were determined by the mean energies shown in Table 2.5, and 27 materials were used, ranging in Z from 3 to 95. The lines shown on the plot are fourth-order polynomial fits to the data, and the fit parameters can be found in Table 2.6.

Figure 2.10 (b)-(d) show the R-value curve for each beam along with the fit line to the NIST data. The LENR and MPS beams produces the same R-value for a given material at all target thicknesses tested, while the bremsstrahlung acquisition produces an increasing

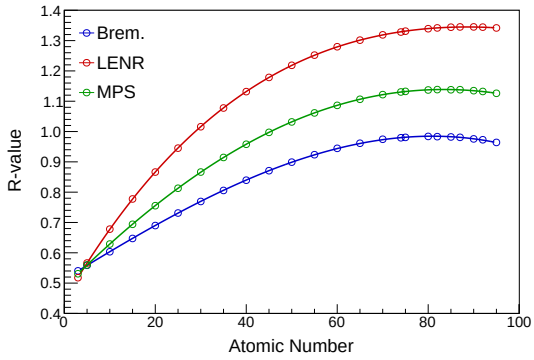

(a) NIST Data

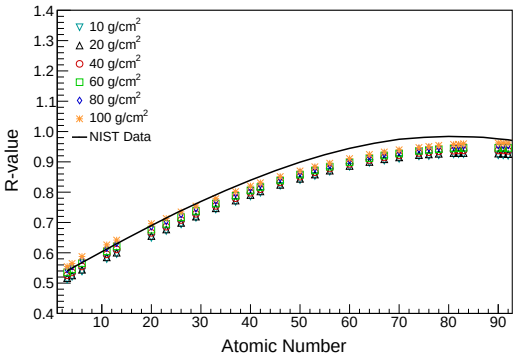

(b) Bremsstrahlung

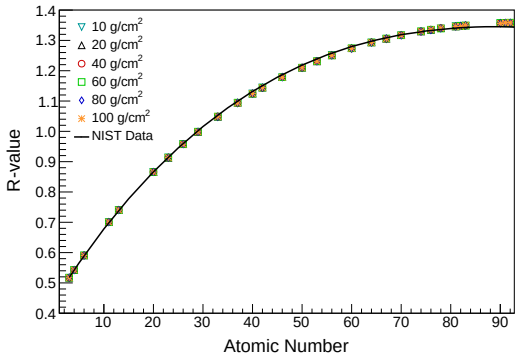

(c) LENR

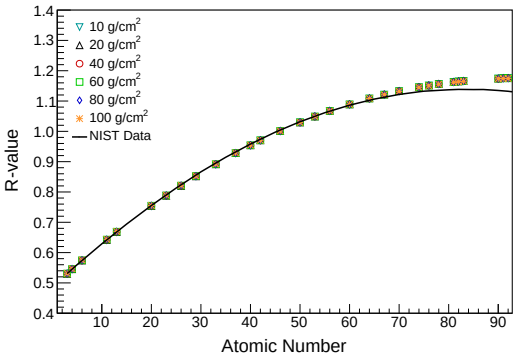

(d) MPS

Figure 2.10: Output R-values from the transmission simulation for the three types of imaging beams. A fit to the values on NIST XCOM for the mean beam energies is also shown on each plot. The range of R-values is highest for the LENR beam, and the simulated values are more accurate to the NIST data. Additionally, the R-values from the LENR and MPS beams are independent of cargo thickness, while they tend to increase with thicker cargo for the bremsstrahlung beams. Error bars are shown on the plot though they may be smaller than the data markers.

R-value with cargo areal density. This highlights a key advantage of monoenergetic beams; as cargo thickness is increased, the effective energy of the high and low energy regions does not change. However, for continuous spectra, the low energy photons are preferentially filtered out by the cargo, and thus the mean beam energy increases with cargo thickness, changing the effective linear attenuation coefficient, μ_{eff}. Additionally, the R-value varies over a wider domain when measured with the LENR beam than with the bremsstrahlung beams. This is due to the larger pair production interaction probability at 15.1 MeV than at 6.3 MeV, the average energy of the bremsstrahlung high energy region. The MPS source has slight disagreement from the NIST data at high Z. It is unclear why there is the divergence, however the disagreement seems to work to the advantage of the MPS source, leading to better material discrimination at high Z. In a working system, the R-value curve would be measured per system, so this error would be accounted for in a system calibration.

The differences in R-value curves arise mostly from differences in the energy spectra, and Figure 2.10(c) and (d) could equivalently be labeled 4/15 MeV and 3/9 MeV. The LENR beam energies were chosen based on the reaction used in this work. It is important to note that bremsstrahlung systems are typically limited to maximum energies of 10 MeV to limit photoneutron production. In previous studies, MPS sources have also been limited to this threshold, which is why the MPS sources in this work are at 3 and 9 MeV. If the 10 MeV limit could be exceeded, MPS sources could replicate the results shown in Figure 2.10(c) since the energies are tunable. Likewise, if the bremsstrahlung beams were allowed to go higher in energy, the R-value curve could be improved. On the other hand, if a LENR with lower-energy γ-rays were used, for example $^{16}O(p, p\gamma)^{16}O$, was used, the curve would not have as high of a range.

Beam Penetration

Image noise is inherently dependent on the number of information carriers which produce signal in the detector, and thus is partially a function of the beam penetration. Geant4

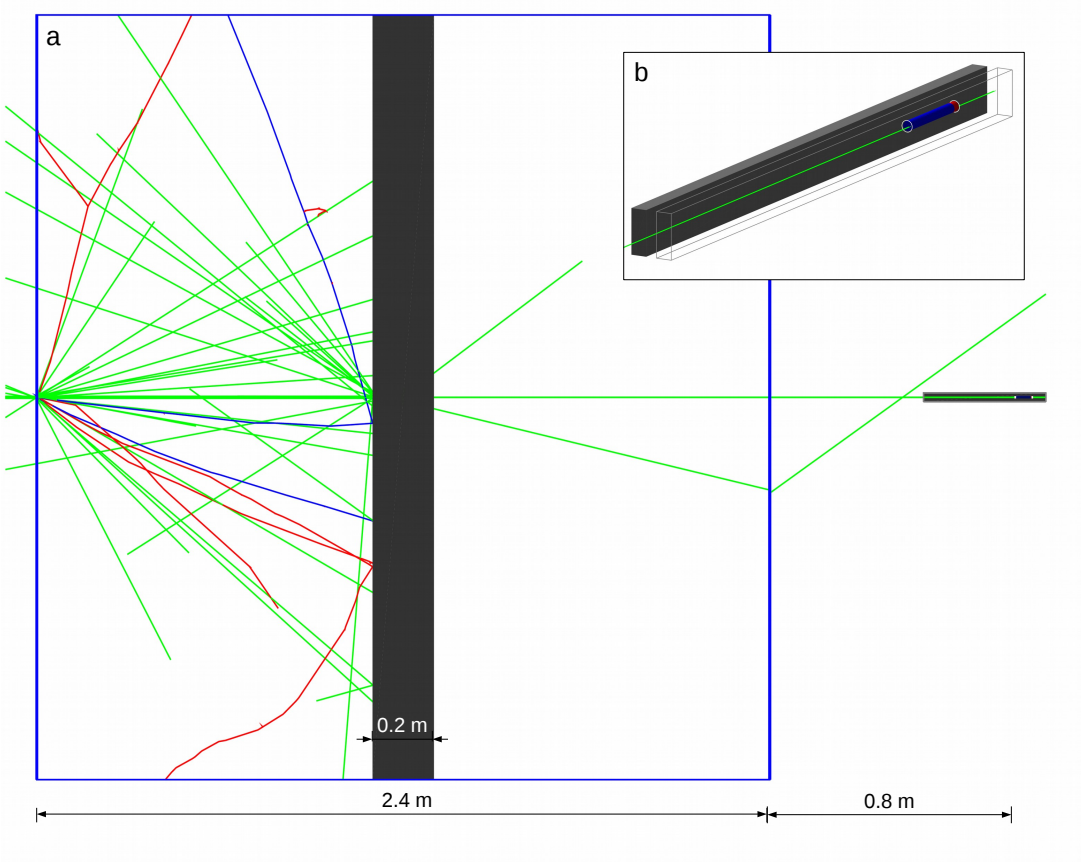

Figure 2.11: Geant4 geometry used for beam penetration simulations, (b) shows the detector volume. Collimators were placed around the detector to ensure that no photons scattered in to the detector from anywhere in the external volume. The source is a parallel planar source equal in size to the area of the detector face. Here the steel plate is 20 cm thick, a 40 cm thick plate was also used.

simulation is used to characterize the penetration of the radiography beams, the geometry of which can be seen in Figure 2.11. Photons are directly incident upon a steel plate either 20 cm or 40 cm thick. This plate is placed directly in the middle of a cargo container with 5 mm stainless steel walls. A sensing volume is placed opposite the source. The air volume tallies every photon which reaches it, measuring the detector-independent beam penetration. This geometry is exactly the same as that presented in similar simulations in [15].

The results of the penetration simulations are summarized in Table 2.7. Penetration is calculated as number of photons in the sensing volume divided by the number of incident

Table 2.7: Penetration for the various imaging beams. Relative penetration values are normalized to the 6-MV bremsstrahlung beam data. The mean energy (in MeV) for each beam after penetration through the cargo is also shown.

	20 cm steel			40 cm steel		
	Penetration		Mean	Penetration		Mean
	Absolute	Relative	Energy	Absolute	Relative	Energy
6-MV Brem	1.06E-3	1.00	3.50	4.14E-6	1.00	4.08
9-MV Brem	1.65E-3	1.55	4.55	8.65E-6	2.10	5.30
3-MeV MPS	2.20E-3	2.07	3.01	6.60E-6	1.61	3.02
6-MeV MPS	5.51E-3	5.18	6.01	3.90E-5	10.61	6.01
9-MeV MPS	6.28E-3	5.91	9.00	5.07E-5	13.93	9.00
LENR Total	1.96E-3	1.85	6.05	1.15E-5	6.13	6.54

photons. When imaging with the bremsstrahlung beams, the entire spectrum will not be used, as described above, and only the 4.4 MeV and 15.1 MeV portions of the LENR spectrum are used. Figure 2.12 shows the energy spectra of the beams before and after penetration through the 20 cm steel plate. These spectra show that the overall spectral shape of the MPS beams is not largely effected by the presence of the steel. On the other hand, bremsstrahlung spectra have a large energy shift after penetration. This change in energy as the beam traverses the cargo leads to degraded accuracy in measurement of the attenuation coefficient and imparts unnecessary dose to the cargo.

In imaging, it may be beneficial to adjust the ratios of low and high energy photons when possible. Specifically for the bremsstrahlung beams, the 9-MV provides higher quality information than the 6-MV beam. To account for this, vendors have developed uneven dose sharing mechanisms between the two beams. The Linatron Mi, from Varex Imaging, has a 1:3 dose sharing proportion between low and high energy beams[17, 32]. If this acquisition is considered as using one interlaced imaging beam, this will effect the beam penetration. Table 2.8 shows the modified penetration values and average beam energy using a 1:3 dose sharing mechanism. The MPS beams have also been combined in a similar manner in this table. While the relative yields of the 4.4 MeV and 15.1 MeV γ-rays can be altered with deuteron energy, $^{11}B(d, n\gamma)^{12}C$ is not regarded as a tunable source, so the

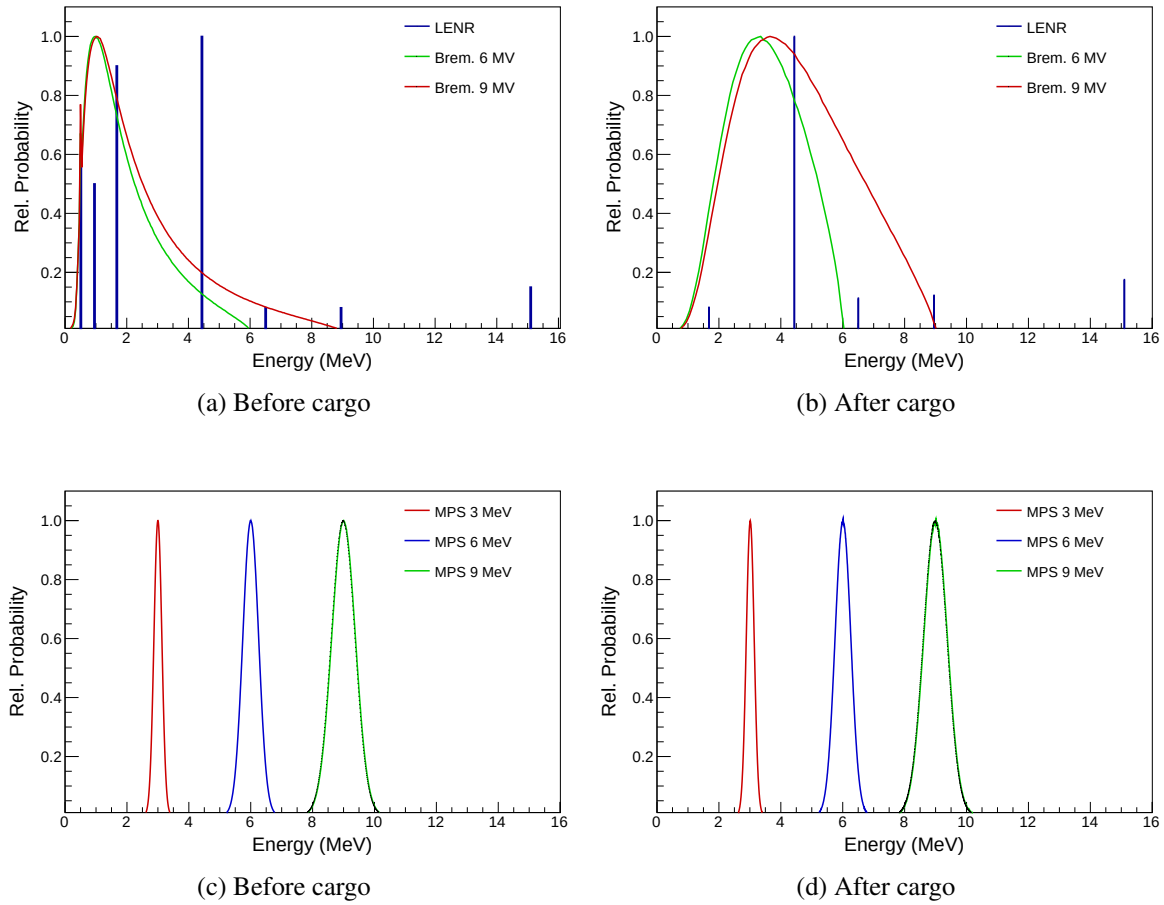

(a) Before cargo

(b) After cargo

(c) Before cargo

(d) After cargo

Figure 2.12: Energy distributions for the various imaging beams before and after transmission through 20 cm of steel. The monoenergetic beams show little change in mean energy after the cargo, leading to more accurate image reconstruction in an active interrogation imaging system.

Table 2.8: Beam penetration for the various combined imaging beams. The bremsstrahlung and MPS combinations account for the 1:3 ratio between the doses delivered by the low- and high-energy beams.

	20 cm steel			40 cm steel		
	Penetration		Mean	Penetration		Mean
	Absolute	Relative	Energy	Absolute	Relative	Energy
Brem	1.47E-3	1.00	5.17	7.30E-6	1.00	5.85
MPS	4.06E-3	2.76	7.36	2.84E-5	3.89	8.36
LENR	1.96E-3	1.33	6.05	1.15E-5	1.58	6.13

penetration values shown in Table 2.8 are the same as those shown in Table 2.7. The dose scaling values are based on the dose to the steel plate as described in the dose section of this chapter.

Conclusions

In this chapter three types of beam sources which could be used for cargo radiography have been discussed. Bremsstrahlung beams are the industry standard for imaging, in large part because of their relative ease of production and the high photon fluxes available. However, bremsstrahlung beams exhibit a low-energy peaked continuous energy distribution. This leads to potentially higher dose to the cargo and more scattering within the cargo, which could degrade image quality. Additionally, when dual-energy acquisition is necessary for material identification, bremsstrahlung beams perform relatively poorly due to little difference in effective beam energies.

Monoenergetic photon sources, on the other hand, can increase beam penetration, decrease scatter, and better sample the attenuation coefficient μ, for material identification. The monoenergetic sources considered are driven by low-energy nuclear reactions, namely $^{11}B(d, n\gamma)^{12}C$, and inverse Compton scattering. Reaction-based sources produce near-isotropic radiation beams which have to be collimated down to a fan beam, tossing away much of the flux. It is possible that collimation of these beams into multiple views could yield near-tomographic images, and that will be discussed later in this thesis. Reaction-

based sources can produce multiple monoenergetic γ-rays simultaneously, leading to perfect image registration and improved material discrimination, given the γ-ray lines are well separated in energy. Some reactions, specifically $^{11}B(d, n\gamma)^{12}C$, produce neutrons, which could be problematic from a dose standpoint, though the neutrons can be theoretically be moderated with shielding. Another approach to decreasing neutron generation is to use reactions that don't produce neutrons, for example $^{12}C(p, p\gamma)^{12}C$. It should be noted that improvements to accelerator design are necessary before reaction-driven sources could be implemented. The accelerator used in the experiment described above was run at various currents varying from 1 to 24 μA. Based on the flux measurements previously reported, the accelerator would need to be run at a beam current of roughly 50 mA in order to scan a 40-foot container in less than two minutes. Not only would this high current be a strain on existing accelerators, a field-deployable system would need to be more compact than the accelerator previously used.

ICS sources can produce nearly monoenergetic photons in a pulse-type mode which would allow for greatly reduced scatter if the accelerator and detectors if the detectors only read out signal after pulses from the accelerator. Additionally, these sources offer a tunable source in energy and output, which could be ideal for modulating dose based on cargo density. However, like LENR sources, these sources are still in a developmental stage and further research is needed for imaging applications.

CHAPTER 3
DETECTOR ARRAY

A complete understanding of the detectors used in the imaging array is needed to accurately model an imaging system. The imaging array used in this work will consist mostly of quartz Cherenkov detectors. These detectors are well-suited for this application, in large part because of their inherent energy threshold which removes much of the background present in an active interrogation environment. In this chapter, the reasoning behind choosing the two final detectors used, as well as the array dimensions are summarized from previous work; further details can be found in references [53, 44]. The detectors in the final imaging array are 6 mm in diameter and 50 mm long, although different-sized detectors have been investigated and used in experiments as a part of this work. The final detectors used are quartz, a Cherenkov detector, and LYSO, a scintillator.

In this chapter, quartz detectors are compared to sodium iodide, another detector of interest for active interrogation applications due to its relatively low cost, high intrinsic efficiency, and spectroscopic capabilities. A computational detector model is developed in Geant4 and validated against an experimentally-measured spectra of a plutonium beryllium (PuBe) monoenergetic γ-ray source[54]. After validation of the detector model, quartz is compared to sodium iodide detectors for performance in high-flux fields. In particular, pulse pileup is evaluated by studying the spectral changes in each detector as a function of source strength. Signal cross talk between neighboring detectors is studied via simulation and experiment. All measurements and initial simulations employed a PuBe source to mimic the high-energy application of these detectors. Cross talk simulations were verified with experimental data to inform design decisions of the imaging array. In addition to modeling the detectors used in the experiment, cross talk in the quartz detectors as a function of crystal diameter, studying a range from 5 to 50 mm, is characterized. After verification

of the detector model, cross talk induced in the quartz detectors by both the imaging beams described in Chapter 2 is simulated. To account for hardening of the bremsstrahlung beam after penetration through cargo, a 20 cm steel plate is placed between the source and the detector in these simulations. All cross talk simulations are modeled with parallel planar beam sources for simplicity. Finally, dose to the quartz and LYSO detectors are related as a function of imaging beam.

Detectors For Active Interrogation

In an active interrogation imaging system, an array of several detectors is typically placed opposite the beam source, and either the source/detector are translated or the cargo container will be translated across the imaging area. Fundamental to active interrogation techniques is the use of high-intensity beams of radiation, generally photons. These high-energy, high-intensity interrogating beams are challenging from a detection standpoint, but are necessary to minimize the data acquisition time required to yield a satisfactory image. The detection system must be able to process each pulse quickly in order to minimize pulse pileup or dead-time losses. In order to fully utilize dual-energy acquisition schemes, a detector must also have spectroscopic capabilities. Finally, in order to optimize spatial resolution, the ideal detector would be small, no more than a few millimeters in diameter. These considerations made two detectors stand out as candidates for this imaging array: quartz and LYSO. This work will focus in large part on quartz, but LYSO will be used in some scenarios so it is included in discussion of the detector and simulation framework as well.

Quartz

Cherenkov-based detectors, although not conventionally used in imaging applications, are becoming more popular in recent years due to a multitude of reasons. The speed of Cherenkov detectors and their energy threshold are both properties of the physics of de-

tection in the crystal. While in inorganic scintillators, the scintillation time is a property of the lattice structure and dopant concentration in the material, Cherenkov radiation emission time relies only on the amount of time it takes for a relativistic electron to slow down in the medium. If the velocity of a charged particle exceeds the speed of light in a given dielectric medium, it polarizes the medium and leaves it in an excited state. Upon de-excitation, photons of ultraviolet and visible wavelengths are released along a conical wavefront behind the particle. In order for an incident photon to be detected, it must be able to impart enough kinetic energy to an electron, so that its velocity is greater than the speed of light in the crystal. This induces the inherent energy threshold on the crystal. Since emission of Cherenkov radiation is an electromagnetic process it is nearly instantaneous, and thus the quartz detectors remove a large contribution to pulse pileup, scintillation decay time. The inherent energy threshold of Cherenkov radiation further reduces the probability of pulse pileup because low energy γ- or x-rays cannot be seen by the detector. The quartz detectors used in this work (GE 214) are only sensitive to photons with energies above 550 keV (electron threshold of 336 keV), eliminating contributions to the spectrum by scattered and background radiation.

While quartz detectors are low cost, fast, and robust to scattered radiation, they have relatively low light output. Where most inorganic scintillators produce several thousand optical photons per MeV deposited in the detector, quartz may produce just a few hundred optical photons per MeV deposited. This leads to relatively poor spectroscopic performance, and means that the entire imaging array should include some detectors other than quartz.

LYSO

Inorganic scintillators are widely used in radiation detection because of their high light output and relatively high density. In order to complement the poor energy resolution of quartz, LYSO detectors will also be incorporated into the final imaging array. Some

Table 3.1: Characteristics of various inorganic scintillators used in active interrogation. Data taken Saint Gobain's material data sheets for each scintillator[55, 56, 57, 58, 59, 60].

Material	Density (g/cm^3)	Primary Decay Time (μs)	Light Yield (Photons/MeV)	Hygroscopic
NaI(Tl)	3.67	0.250	38,000	yes
CsI(Tl)	4.51	1.000	54,000	slightly
LaBr(Ce)	5.08	0.016	63,000	yes
LYSO(Ce)	7.1	0.045	27,600	no
BGO	7.13	0.300	8,000-10,000	no
$CdWO_4$	7.9	14.000	12,000-15,000	no

of the important characteristics of LYSO and other scintillators considered for use in the imaging array are shown in Table. 3.1. Although NaI, CsI, and $CdWO_4$ are all widely used throughout the active interrogation community, LYSO was chosen because of the combination of high density and low decay time. Additionally, it is non-hygroscopic, which is desirable since a cargo radiography system will likely be exposed to the elements.

Detector Modeling and Validation

Quartz

The physics of Cherenkov radiation detectors are different from scintillators, and thus pose a more computationally challenging task. The energy threshold is difficult to account for in a simulation naively, and because of this, full optical model of the quartz detectors in Geant4 is necessary. This optical model fully accounts for the generation and propagation of optical photons throughout the crystal. The optical physics included in the model are G4Cerenkov, G4OpAbsorption, G4OpRayleigh, G4OpMieHG, and G4OpBoundaryProcess. The absorption length and index of refraction of the custom-made crystals were supplied by the manufacturer (Technical Glass Products, Painesville, Ohio), and the reflective surface properties were empirically adjusted to match the general shape of the experimental spectra obtained for a variety of sources. Finally, the wavelength-dependent quantum efficiency of the PMT's photo-cathode was factored into the calculations.

For model validation, simulated a PuBe spectrum is compared to experimental measurement. This source was chosen so that the energy would be well above the Cherenkov threshold in the detector, and it also mimics the high-energy application of these detectors. It should be noted that the neutrons given off by the source will create background signal in the laboratory, but will not be seen be seen by the quartz detectors at all.

The input spectrum for the PuBe source in the Geant4 model was calculated by implementation of a uniformly distributed α-particle source within a PuBe cylinder and recording the resulting γ-ray spectrum outside the cylinder. By simulating the α-particle transport, reaction with beryllium, and decay of the resulting carbon atom in Geant4, the broadening of the prominent γ-ray peak at 4.438 MeV is properly broadened. For comparison of simulated and experimentally measured spectra of PuBe, the lower part of the experimental spectrum was cut off below 500 keV because of the Cherenkov threshold. The spectra were then normalized such that they had the same area under the "shoulder" and the same x-intercept. It should be noted that a typical spectrum measured with a Cherenkov detector does not have the photopeaks characteristic of other spectroscopic detectors; rather, the detector's response forms a plateau, which falls off near the maximum energy deposition of a given photon. Regions of this shoulder and the trailing plateau can be regarded similarly to the photopeak of a typical spectroscopic detector, and fitting the tail of the shoulder has been shown as a method of energy calibration for these detectors[22, 61].

Weighted Chi-square distance is used to compare to the experimental and simulated data. This metric accounts for the uncertainty associated with counting experiments, and is typically used for comparisons of histogram data[62, 63]. The reduced chi-square distance metric is calculated using ROOT's Chi2Test function, which implements the method outlined by Gagunashvili[64].

Figure 3.1 shows the simulated and measured spectra. For comparison, each spectrum is normalized such that the area under the curve between 1.5 MeV and 4 MeV is the same. The reduced chi-square distance, $\bar{\chi}^2$, between the two spectra was calculated as 0.10. Gen-

erally, $\bar{\chi}^2 \leq 1$ indicates that the two spectra are drawn from the same distribution. Thus, the detector model simulates the light output of the quartz crystal accurately.

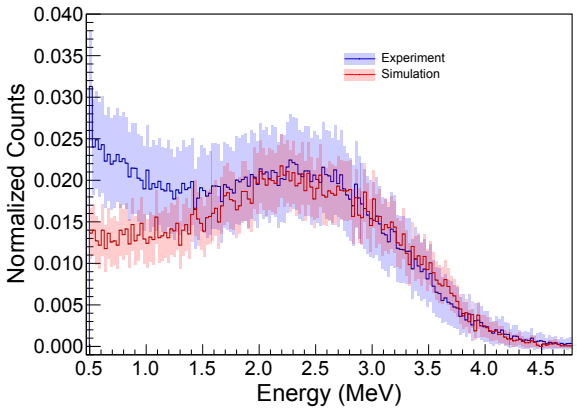

Figure 3.1: The experimentally measured and simulated Cherenkov spectra of a PuBe source, with the low energy portion of the spectrum cut off. Each curve is normalized such that the total area under the "photopeak" (1.5-4 MeV) is 1. The differences in the low energy region can be attributed to the low-energy plutonium decay lines and the effects of in-room scatter and activation, which were not accounted for in the simulation.

Rather than simulating the entire optical process with each simulation, a computationally intensive task, a 2D detector response function is pre-generated, the results can be seen in Figure 3.2. To generate the response function, photons with energies from 0.4 to 15.5 MeV are sent into the detector and the optical light output is measured. The wavelength-dependent quantum efficiency of the SiPM was factored into the simulations, and the incident photons were sampled from a source with the same width as the detector. After generation of the response function, subsequent simulations only need to tally photon energies in detector volumes composed of air. The optical process can be condensed to a process analogous to multiplication of the this energy distribution by the response function matrix. This can be implemented as a post-processing step, and it has reduced simulation time by multiple orders of magnitude. The response function shown in Figure 3.2 was generated with 200 independent runs of 50 million incident photons, each run takes an average of 30 hours of wall time, with 8 threads per run.

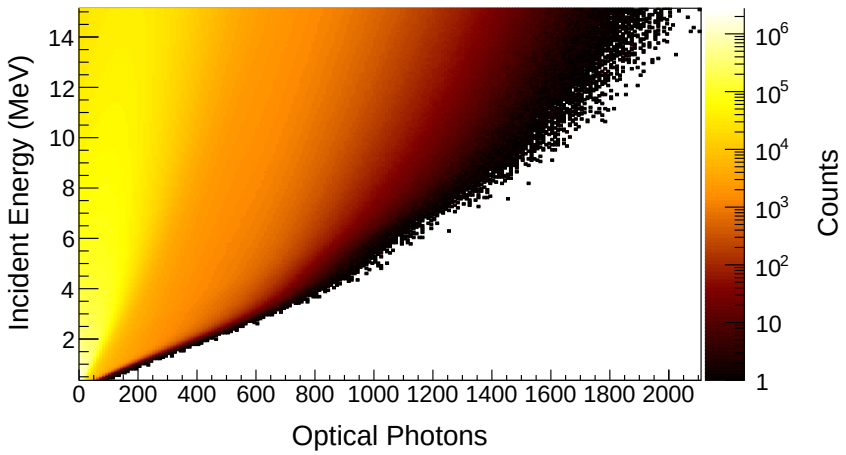

Figure 3.2: The full optical response function for the 6-mm quartz detector model, calculated in Geant4, with the heat-map shown in log scale. Photons from 0.4 to 15.5 MeV were fired into the detector, and the light output due to each incident energy was recorded.

Implementation of Response Function

As mentioned above, pre-generation of the response function allows the optical process to be reduced to a process that is analogous to matrix multiplication. However, strict matrix multiplication of the values does not preserve the Poisson statistics on the detected spectrum, so an algorithm had to be written to carry out this process. First, the 2D response function is converted to a cumulative distribution function (CDF), as shown in Figure 3.3a. The CDF is normalized such that the maximum value corresponds to the detector's efficiency at that energy. The blacked out line corresponds to the detector response at 5 MeV, which is shown in Figure 3.3b. Then, in the Geant4 simulation, only the photon energies which cross a detector volume need to be tallied. It is important that the sensitive detector in the simulation is air because the response function accounts for the intrinsic efficiency of the quartz. This energy data are collected and compiled into a histogram. For the convolution process, this histogram is then iterated through. At a given incident energy, 5 MeV for example, the CDF shown in Figure 3.3b is sampled n times, where n is the number of counts in the 5 MeV bin from the Geant4 simulation. If the random number is less than the detector's efficiency at that energy, the CDF is iterated through until the number is less than

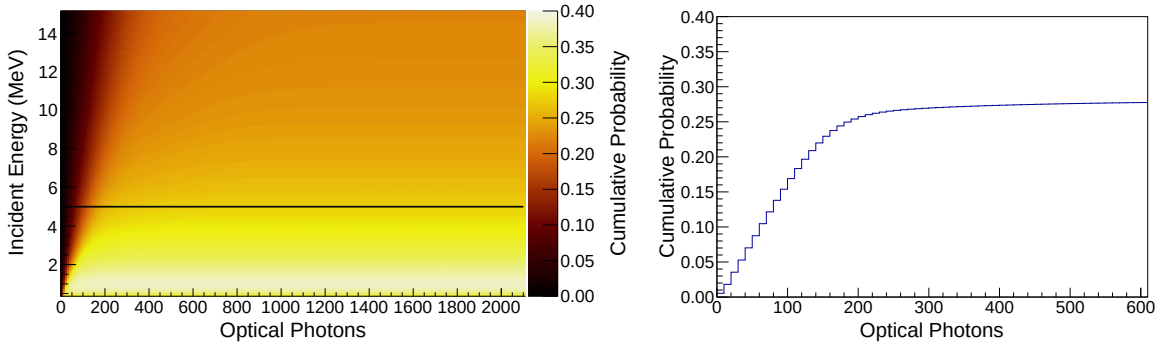

(a) (b)

Figure 3.3: 2D detector response, transformed into a CDF (a), and a projection of the 2D CDF at 5 MeV (b). By randomly sampling this CDF in detector post-processing the optical transport can be condensed to a process analogous to matrix multiplication.

the evaluated value of the CDF. A count is then added to that bin. As an example, the blue spectrum on Figure 3.6 shows the convolved detector response to the LENR beam shown in Figure 2.4.

Energy Calibration

This method of calculating the response function also allows for full characterization of the transformation from light output to energy deposited, i.e. the energy calibration. Rather than manually fitting each of the 302 calculated histograms, an automated calibration algorithm was written. Starting from the end of a given 1-D histogram, for example the detector response to a 5-MeV photon, the algorithm iterates backwards until a bin with at least 5 counts is found. From here, the bin contents and centers are stored, further iterating back until a bin with 100 counts is found. This data are compiled into a separate graph and fit with an exponential function

$$R(E) = e^{(C+S\times E)} \tag{3.1}$$

where $R(E)$ is the fit function, E is the number of optical photons (i.e. position on the x-axis), C represents a constant and S is the slope. Using ROOT's fit values for C and S this line was extrapolated down to a value of 1 and solved for the corresponding optical

photon bin:

$$R(E) = 1 = e^{(C+S\times E)}$$

$$ln(1) = 0 = C + S \times E$$

$$E = -C/S \tag{3.2}$$

This value was determined as the maximum energy deposition in the detector due to the incident photon energy (4.5 MeV in this case). This algorithm performs the same Cherenkov detector calibration described in [61], but in a fully automated manner. Starting from a bin with 5 counts reduces the effects of statistical fluctuations, though it was chosen rather empirically. Starting bin counts ranging from 1-10 were tested, and 1-3 produced very different curves. Using more than 4 counts as the starting point produced relatively stable results, while moving up towards 10 counts increases the fit uncertainty. Finally, 5 counts was chosen as a medium of these effects. The error induced by the fit is propagated through the calculation, and the resulting energy calibration curve can be see in Figure 3.4(a). Note that the curve is nonlinear, fitting to a 4th-order polynomial. The full energy-calibrated 2D response function can be seen in Figure 3.5.

Detection Efficiency

Detection efficiency is simultaneously measured when generating the response function. While the scaling of this efficiency is likely not the same as would be seen in an experiment, the shape of the curve should be constant, and this can help understanding of detector response at higher energies. Total detection efficiency (or intrinsic efficiency), $\epsilon(E)$, is calculated as

$$\epsilon(E) = \frac{total\ counts}{incident\ particles} \tag{3.3}$$

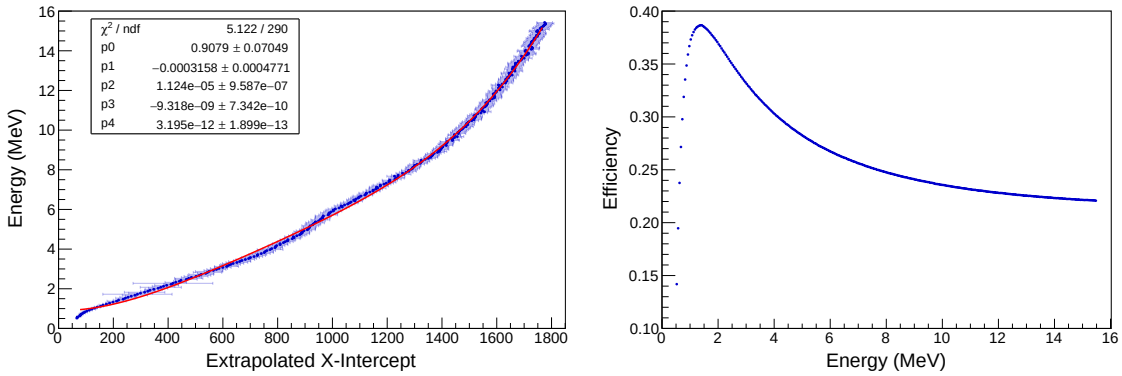

(a) Energy calibration

(b) Intrinsic detection efficiency

Figure 3.4: (a) Energy calibration curve and (b) detection efficiency calculated from the 6-mm quartz detector response function. (a) has the error drawn as a shaded region and (b) has error drawn for each data point, though error bars may be smaller than the data markers.

The calculated efficiency curve can be seen in Figure 3.4(b). Note that the efficiency grows rapidly as the Cherenkov threshold is overcome, and then dies off slowly after about 2 MeV, as interaction probability becomes less likely.

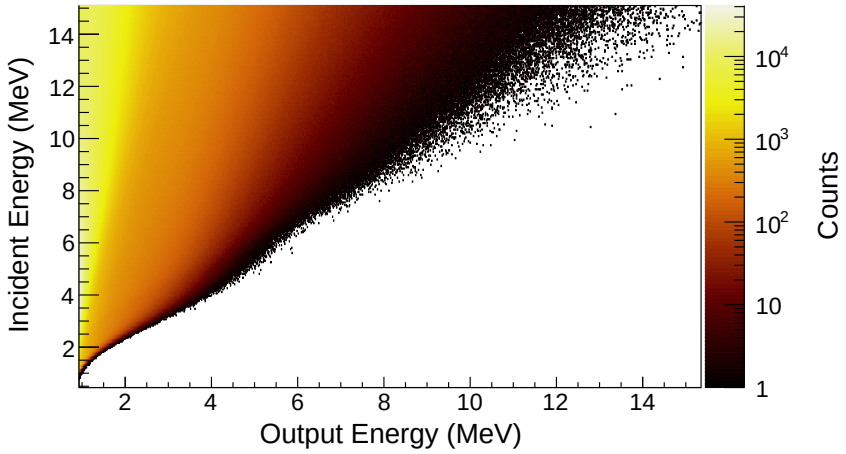

Figure 3.5: Energy calibrated quartz response function. The rare probability of full energy deposition can be seen at higher energies.

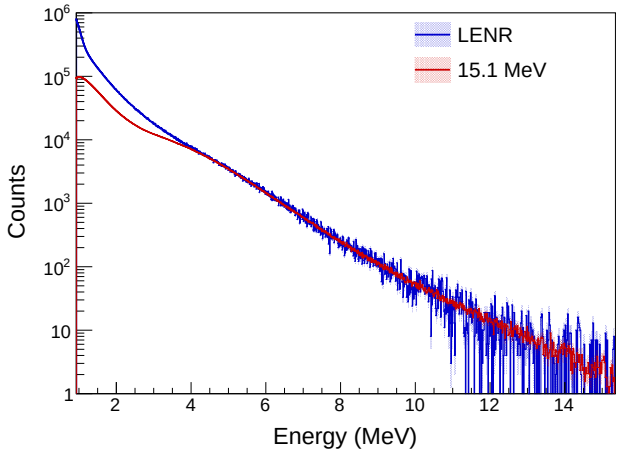

Figure 3.6: Quartz detector response (6-mm) to the LENR beam and a monoenergetic 15 MeV photon. Note that the 15.1 MeV signal contributes to the entire detected spectrum, leading to error in transmission measurements at the lower energies.

Spectrum Stripping

One of the goals of this work is design a detector array with 5 mm or better spatial resolution. This means that the detector crystals must be small, which decreases the overall detection efficiency, which will be especially poor at high energies. Full energy deposition at 15 MeV in the quartz crystals is highly improbable, so analysis methods must be able to account for these partial energy depositions in post-processing. Further complicating the quartz spectrum is the continuous nature of a Cherenkov spectrum. Figure 3.6 shows an example of the problem at hand. The blue spectrum is the 6-mm quartz detector's response to a monoenergetic 15.1 MeV photon while the red spectrum is the response to the LENR beam (the spectral heights are scaled so they match). The total spectral shapes are similar, and the 15.1 MeV photon from the LENR beam will impact transmission measurements for the lower energy photons.

To correct for this problem, a spectral stripping method which removes signal contributions from the 15.1 MeV photon was developed. This is possible because the full detector response function gives an indication of the entire detector response to a monoenergetic photon. The high-energy detector response is taken from the full detector response func-

tion. It is then scaled to the LENR histogram such that the area at the end of the histograms (i.e. the exponential portion) is equal. The monoenergetic response is then subtracted away from the LENR histogram. Figure 3.7 demonstrates this process for 3 different spectra. Each spectrum is tallied after transmission though a material. A low-Z, mid-Z, and high-Z material are tested so that the ratio between the 4.4 and 15.1 MeV γ-rays will be different on each spectrum. It should be noted that this method degrades the spectrum at higher energies. From an implementation standpoint, relevant data should be measured from the high-energy portion of the spectrum before the stripping is carried out.

This method was developed to increase the accuracy of the R-value calculations for finding material dependencies in transmission data. To evaluate the method, R-value curves for the LENR beam after convolution and stripping were reproduced, and these results are shown in Figure 3.8. Unlike the R-value measurements presented in the previous chapter, which were presented without a full detector response, the detected signal is rather continuous, even though the incident LENR spectrum is discrete. The R-value is measured based on wide integration regions to account for the continuous spectrum. The low-energy integration regions goes from 2.5 to 4.0 MeV, and the high-energy region spans from 9.0 to 15.2 MeV. Without the stripping method, the data produces a poorer curve as a function of Z, and the errors with respect to the raw data are large. After implementation of the stripping method, the curve is reproduced with lower error, especially for low-Z materials.

This stripping method works well for the enhancing measurement material-dependent R-values, although it would need to be improved if it were to be used in other applications. It also relies on an accurate measurement of the detector response to a monoenergetic photon input. For this method to be implemented on experimental data, either a truly monoenergetic source would have to be available, or the computational detector model must be validated at higher energies.

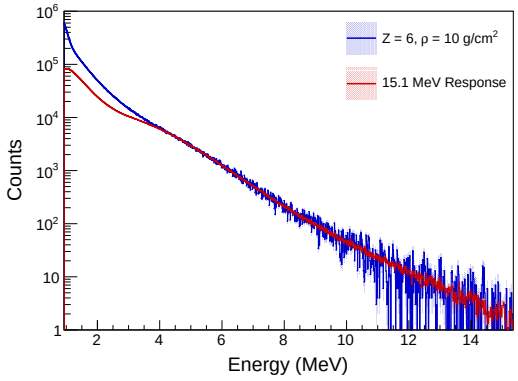

(a) Carbon, 10 g/cm^2, raw output

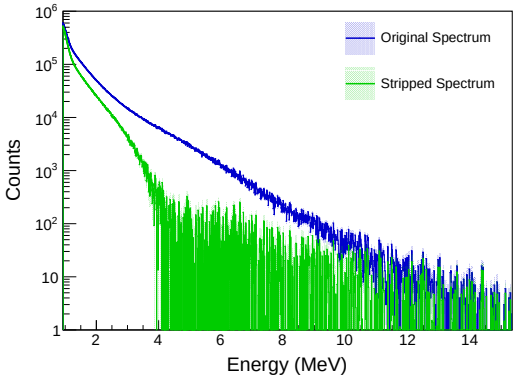

(b) Carbon, 10 g/cm^2, stripped spectrum

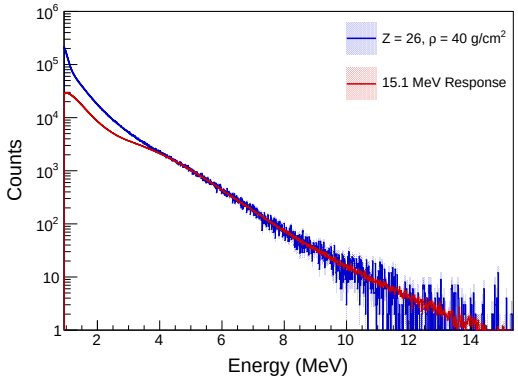

(c) Iron, 40 g/cm^2, raw output

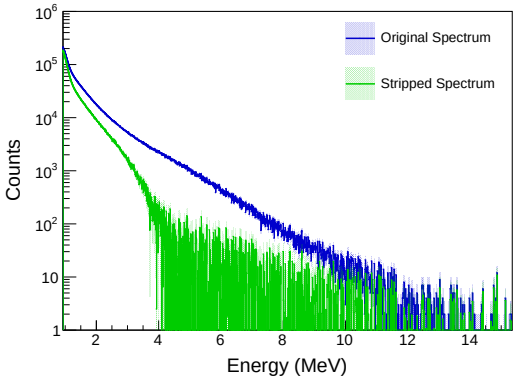

(d) Iron, 40 g/cm^2, stripped spectrum

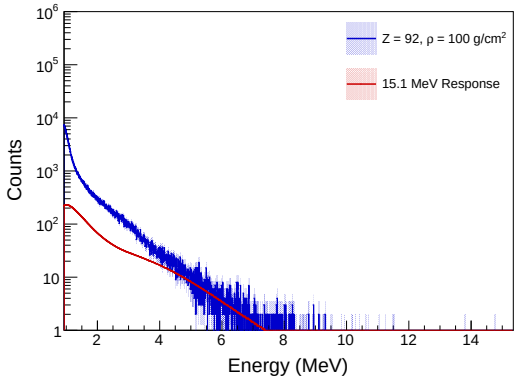

(e) Uranium, 100 g/cm^2, raw output

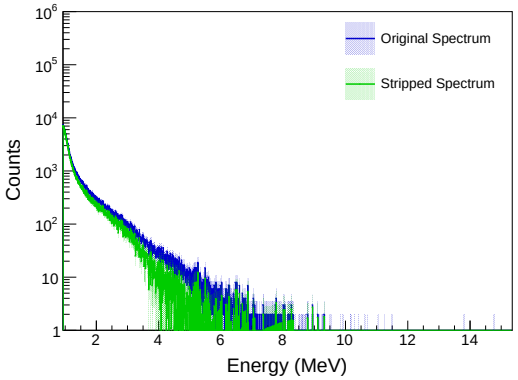

(f) Uranium, 100 g/cm^2, stripped spectrum

Figure 3.7: Demonstration of the spectral stripping method. In each figure, the LENR beam is transmitted through a different material to show the spectral stripping with different ratios of the transmitted 4.4 and 15.1 MeV photons. (a) and (b) show the method on a low-Z, low areal density material, where the 15.1 MeV γ-ray has a larger impact on the spectrum. (c) and (d) show a mid-Z, mid areal density material, and (e) and (f) show a high-Z, high areal density material.

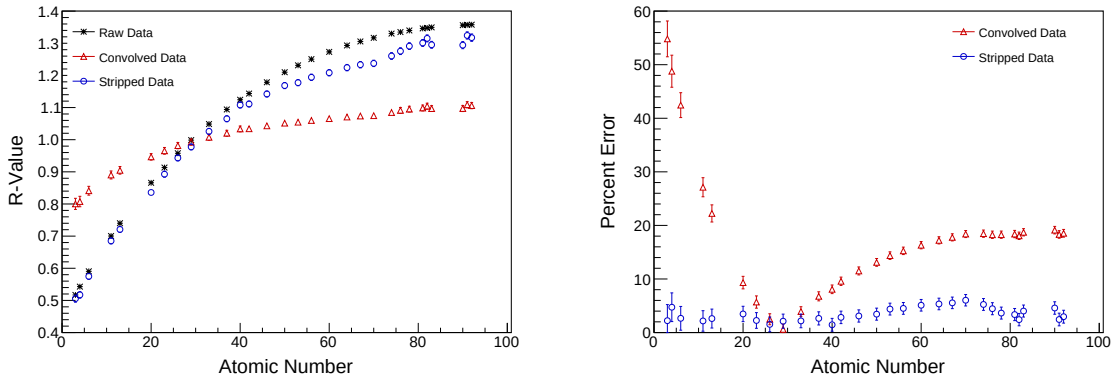

(a) (b)

Figure 3.8: Demonstration of the stripping method impact on R-value calculation. (a) shows the measured R-values of the convolved spectra before and after stripping. Raw data corresponds to the R-value measured before any detector post-processing. (b) shows the percent error of each dataset as a function of Z, using the raw data points as the ground truth.

Scintillators

Scintillators have considerably higher light yield than Cherenkov detectors, making simulation of optical processes prohibitively expensive. Rather than modeling the light output, energy deposition in the scintillators is tallied in simulation, and broadening is applied as post-processing based on known energy resolution. This process is commonly done for scintillators since the transformation from energy deposition to light output is strongly linear[27, 41]. The broadening function is based on the experimentally measured energy resolution of a given scintillator. Specifically, it creates an energy resolution fit according to Eq. 1:

$$R(E) = \frac{(p0 + p1 \times E)^{1/2}}{E} \tag{3.4}$$

where $p0$ and $p1$ are empirical constants, and E is the energy of the charged particle. The constants α and β are defined in units such that resolution is a unit-less quantity. This function is meant as an empirical adjustment to the theoretical energy resolution attainable in a scintillator. The energy deposition is spread according to a Gaussian function with σ

set based on Eq. 3.4, where $R = 2.35\sigma$; this fitting function is taken from Knoll[65]. This approach approximates scintillation; it does not completely account for the scintillation process and is reliant on accurate experimental measurements of energy resolution.

For the pileup and cross talk experiments which will be described below, the quartz detectors are compared to NaI to have a benchmark. In order to compare simulation results, a computational model on NaI was needed. The material properties of the sodium iodide detector were imported through Geant4's material database, and broadening was implemented as described above. Figure 3.9 shows the measured energy resolution curve for the sodium iodide. While the fit is not very good, it is adequate for comparison between simulated and experimental data as needed for this project. Figure 3.10 shows an example of two broadened spectra using this code. The curves are normalized such that the total area under each peak matches (both peaks were included in the normalization for the ^{60}Co data). The broadening does well for the ^{137}Cs spectra, and more poorly on the ^{60}Co data. The performance of the broadening at a given energy can be predicted by how close the fit shown in Figure 3.9 is to the data point at a particular energy. The data point for ^{137}Cs lies directly on the curve while the ^{60}Co points (1.17 and 1.33 MeV) sit well below the curve. While the agreement is not strong, it will serve for our evaluation of detector cross talk. Better characterization would be needed if the detector model were to be used for imaging or spectroscopy.

LYSO is also modeled in Geant4, but data for the energy resolution broadening function was not taken for the LYSO. It was noticed that although the broadening helped the NaI, it did not make a tremendous impact on final results. Additionally, although LYSO is included in the final imaging array, it is not included in the imaging simulations presented in this work. This decision was made to keep all imaging results consistent with the quartz, which has a validated detector model. That being said, LYSO is evaluated for crosstalk.

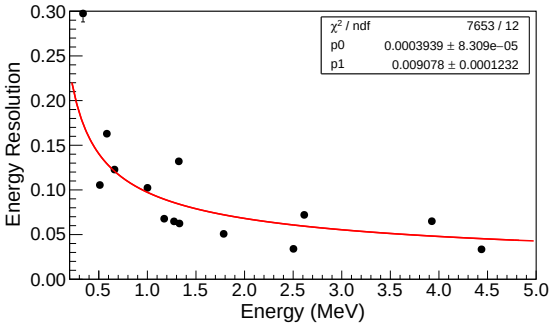

Figure 3.9: Measured energy resolution for the 50.8 mm × 101.6 mm × 406.4 mm sodium iodide detector. The fit line is calculated according to Equation 3.4. Though the fit quality is poor, it will serve for a simple broadening of the simulated NaI spectra.

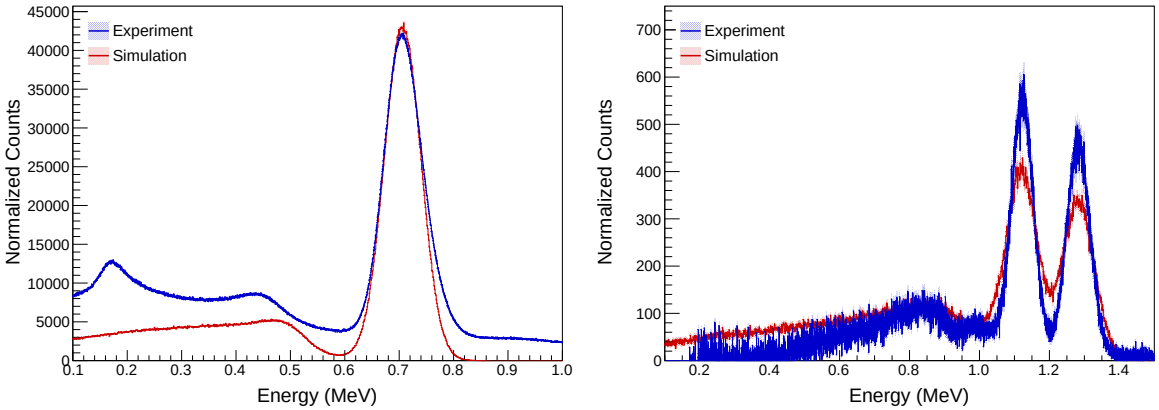

(a) ^{137}Cs (b) ^{60}Co

Figure 3.10: Broadened spectra plotted against experimentally measured spectra. Disagreement below the photopeaks can be attributed to the simplicity of the computational model. Additionally a backscatter peak can be seen on the low-energy end of the ^{137}Cs experimental spectrum. This was not accounted for in the simulation. The broadening function performs better at energies which lie close to the fit line shown in Figure 3.9.

Pileup

Pulse pileup can be defined as two or more radiation interactions occurring within the detector in less time than it takes the photo-sensing device and electronics to process the pulse produced from a single event. Pileup can occur in any radiation field and it is dependent on the detection system processing time, relative to the incident radiation flux. Processing time is dependent on the mechanisms of a given detector. In scintillators, it is determined by the characteristic decay time of excited atomic electrons which release optical photons upon de-excitation. The decay time is generally reported as the time necessary for the light output to reach 37%, or $1/e$, of the maximum light emission. To avoid complications due to pileup, some processing electronics attempt to separate pileup events, but most either simply reject the event chain or integrate it as one event[66].

While these methods can reduce pileup, rejecting the entire event chain leads to wasted time, or dead-time, in the counting process. Extended dead time increases the necessary measurement times and dose delivered to everything in the vicinity of an experiment. On the other hand, integrating multiple events as one destroys the spectroscopic information of an event and pollutes the overall spectrum[67]. This method can lead to spectral counts above the maximum known energy from a source. Summation peaks can also be introduced and photo-peaks can be broadened if a low energy event is combined with an event in a photo-peak[68, 69]. This loss of energy resolution increases uncertainty and decreases the effectiveness of a detector, especially when coupled with the other sources of energy resolution degradation, such as fluctuations in the PMT[70, 71]. Pileup effects have previously been shown to induce error in measurement of the linear attenuation coefficient, degrading the accuracy and usefulness of imaging[72].

In order to characterize the pulse pileup in the Cherenkov detectors, a 5 Ci PuBe source was placed at various distances from the detector. The quartz data was compared to data taken with a sodium iodide detector. The NaI detector used for these experiments was

2”×4”×16” (50.8 mm × 101.6 mm × 406.4 mm), a considerably larger volume than the 25-mm diameter quartz detectors used in this experiment. To account for the larger solid angle covered by the sodium iodide detector, a lower activity (1 Ci PuBe) source was used. In addition to changing the source strength, the distances from source to detector were adjusted for the sodium iodide experiment such that the total γ-ray flux incident on each detector face was kept constant. The flux-normalized distance for the sodium iodide detector was calculated using Eq. 3.5:

$$D_{NaI} = \sqrt{5\ C_{\Omega} D_Q^2} \tag{3.5}$$

where C_Ω is a correction factor for the difference in detector surface areas, the factor of 5 accounts for the different source strengths used between experiments (5 Ci vs 1 Ci), and D_Q is the distance used for measurements in the quartz experiments.

In experiments to measure pulse pileup, it is typical to integrate spectra as a function of increasing flux and measure the change in count rate. This method of pileup measurement would show that as pileup begins to take effect, the measured count rate will deviate from the increased count rate. However, because of the low-energy threshold of the Cherenkov detectors, the quartz detector will not be effected by the low-energy γ rays emitted by plutonium in the PuBe source. Thus, the effective flux on each detector would be different, and the results would exhibit a systematic bias towards the quartz detector. Instead, events registered above the theoretical maximum energy deposited in each detector were tallied as pileup counts. Since the maximum γ-ray energy is 4.4 MeV, any deposition registered above this energy must have occurred as a result of pileup.

For the sodium iodide, a Gaussian fit was applied to the 4.4 MeV photopeak. This fit was then extrapolated out past the centroid of the peak and evaluated at the center of each histogram bin. If a given bin held more events than predicted by the fit line plus one σ, the excess events were tallied as pileup events. This same order of events was applied to the quartz spectrum, except the fit was exponential rather than Gaussian, due to the

typical shape of a Cherenkov energy spectrum. In order to minimize fluctuations due to the PMT, the detectors were kept in a climate controlled room overnight before the experiment and both sets of experiments were done on the same day. All pileup measurements were calculated on energy-calibrated and background-subtracted data.

As an additional metric to characterize the pulse pileup in the sodium iodide detector, the changes in the peak center and full-width at half the maximum (FWHM) of the photopeak for the 4.438 MeV γ ray were measured. In a scintillator, the center of the photopeak will shift as incident radiation flux increases. As the time between events in the detector decreases, if the scintillator has not had enough time to decay, the baseline signal will elevate, a phenomenon known as afterglow. As this process happens repeatedly during the experiment, the total spectrum will drift upward leading to a photopeak which moves up in channel number and broadens. Another phenomenon that occurs in high flux situations is light or voltage hysteresis, a fluctuation in the voltage across the PMT as the frequency at which light hits the photocathode increases[73], further broadening the photopeak. For the analysis of sodium iodide spectra, all fits were calculated using ROOT's fitting toolkit[74]. Comparable quantities could not be calculated for the quartz spectra as they exhibit no true photopeak.

Figs. 3.11a and 3.11b illustrate the effect of pileup on the experimentally measured PuBe spectra as the incident flux increased (source-to-detector distance decreased) for the quartz and the sodium iodide detectors, respectively. A small change in the location and the slope of the Cherenkov spectral shoulders is observed. The end points of the Cherenkov spectra are shown in Figure 3.11a including the insert which highlights the shift in the extrapolated x-intercept of the shoulder and its uncertainty. On the other hand, as the sodium iodide detector moves closer to the source, for example at 5 and 10 cm, the spectral information begins to degrade due to pileup. In particular, the center of the photopeak shifts towards higher ADC channel number, the energy resolution decreases, and the ratio of the escape peak to the full energy peak changes.

The changes to the center of the photopeak for the sodium iodide spectra at different distances is highlighted as the insert of Figure 3.11b. Both x-intercept for quartz and photopeak center for sodium iodide correlate with the change in energy deposition as a function of pileup. The extrapolated quartz endpoint fluctuates by approximately 500 channels in the pileup experiment, while the centroid of the sodium iodide photopeak changes by roughly 1000 channels. However, the process of exponentially fitting a curve down to an x-intercept is relatively unstable, especially with few counts per bin, as was the case for the 25 cm and 50 cm measurements. This error is reflected in the insert of Figure 3.11a. On the other hand, fitting the Gaussian peaks on the sodium iodide shows very little error, and the greater change in these values in the sodium iodide show that the quartz detectors are less susceptible to pileup. These results are further quantified in Table 3.2.

The total counts due to pileup, calculated as described in above, are shown in Figure 3.12. As indicated from the spectra in Figure 3.11 sodium iodide pileup is consistently higher than that of the quartz by nearly a factor of four, and both detectors see some effects of pileup at close distances to the source. The energy resolution of the sodium iodide degrades under high fluxes. In active interrogation imaging applications, the detectors are often placed in an accelerator beam, either bremsstrahlung or other, and the flux is maximized so that scan time may be decreased. In a transmission measurement, this effect would not have a significant impact as the total spectrum is integrated. However spectral information may be desirable in some applications. One example is calculation of material atomic number, or Z_{eff}, which can be helpful when trying to identify special nuclear material. This is typically done via attenuation measurements at two different energies[30, 75], making accurate spectral information necessary for measurement of Z_{eff}. As the energy information of the sodium iodide detector changes more than quartz with increasing radiation flux, the quartz is better-suited for high flux applications.

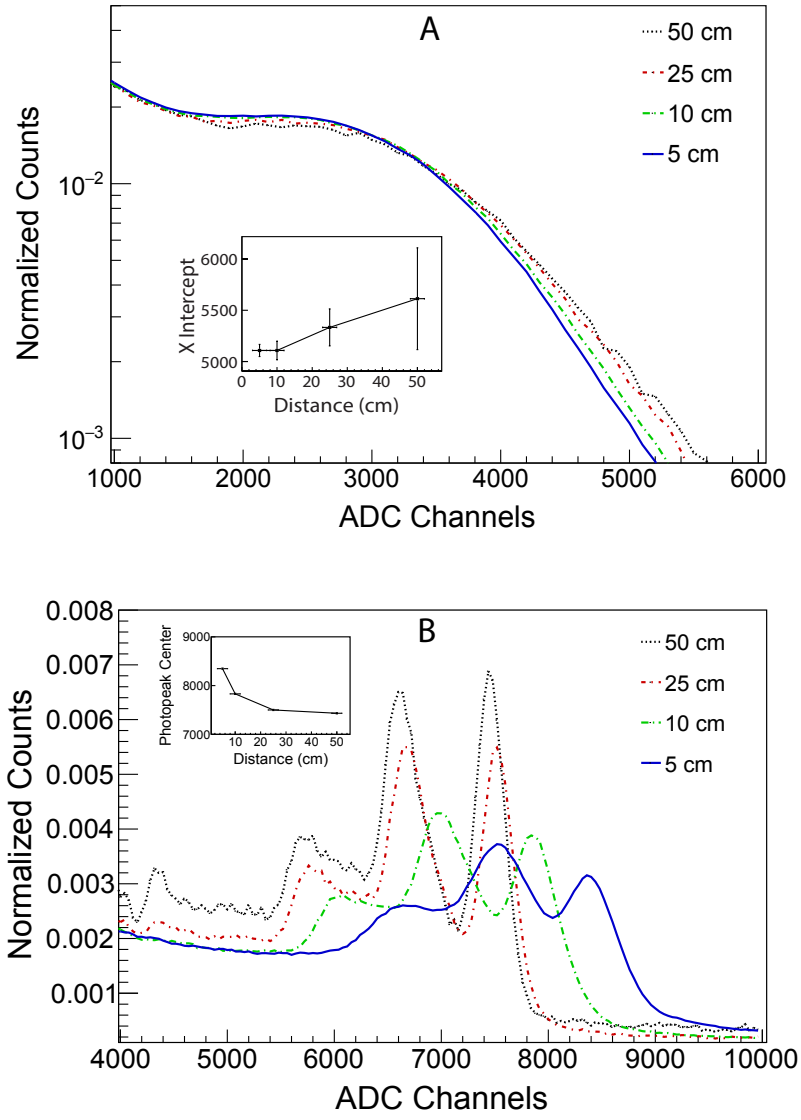

Figure 3.11: The measured spectra for the pileup experiment in quartz (A) and sodium iodide (B). As the source-to-detector distance decreases, the effects of pulse pileup become clear in the sodium iodide detector, while the quartz detector's measured spectra change little. The distances were adjusted according to Equation 3.5 to account for the differences in solid angle covered by each detector. Additionally, a 5 Ci PuBe source was used for the quartz while a 1 Ci PuBe source was used for the sodium iodide detector. Counts for all spectra are normalized such that the total area under the curve is one. The inserts on each plot show the relative change in the photopeak as a function of source strength.

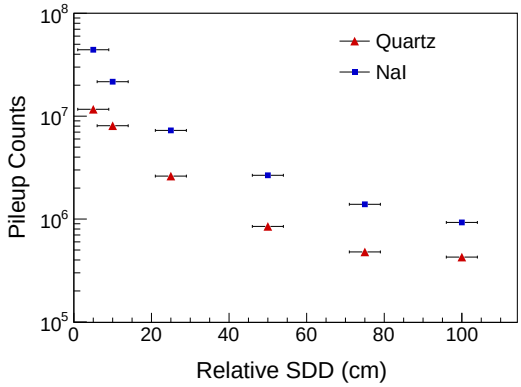

Figure 3.12: The calculated pileup for both the quartz and sodium iodide detectors. Pileup events are counts in bins beyond the photopeak. The source-to-detector distance was adjusted from one experiment to the other to account for the different detector sizes. Although both detectors see some effects of pileup, the quartz has fewer counts by a factor of about 4 at all distances.

Table 3.2: Photopeak data from the pileup experiments in sodium iodide. Each photopeak was fit to a Gaussian function using ROOT's fitting toolkit.

Distance (cm)	Peak Center (channel)	FWHM (channel)
5	8348 ± 2	676 ± 14
10	7830 ± 1	573 ± 7
25	7500 ± 1	365 ± 5
50	7432 ± 2	348 ± 7
75	7430 ± 3	356 ± 16
100	7423 ± 4	346 ± 15

Cross Talk

An important element of this thesis is simulating a full detector array and optimizing detector spacing, such that the array maximizes sensor density (improving spatial resolution) without sacrificing spectral information. In general, the effect of detector-to-detector scatter, or cross talk, increases as detectors are placed closer together. The increase in cross talk stems from both increase in solid angle and the angular dependence of Compton scattering, which is described by the Klein-Nishina cross sections[65, 76]. Multiple aspects of sensor cross talk have been previously studied. Other groups have studied neutron cross talk in scatter-based arrays[77, 78], low-energy x-ray cross talk in pixelated detectors for medical imaging applications[79, 80], and electronic cross talk, or charge sharing between adjacent pixels in flat-panel detectors[81, 82]. Radiative cross talk has been shown to cause loss of spatial resolution and energy information in cases where spectral information is desired[83]. Cross talk also leads to image noise which decreases contrast. Radiative cross talk, at energies relevant to active interrogation, has not yet been fully characterized. Comprehensive understanding of cross talk behavior is vital in development of an imaging array because of an inherent trade-off between spatial resolution (sensor packing) and image quality.

One way to alleviate the effects of cross talk is to apply a low-energy threshold as a post-processing technique[16]. Another approach is to reject coincident events in nearest neighbor detectors. While these methods decrease the effect of scatter, they also lead to wasted processing by the detection system because the detector must process an interaction which will later be discarded. Another approach to decrease cross talk is to use a radiation detector which is insensitive to low-energy photons, for example, a Cherenkov-based detector. This insensitivity is caused by the physics of the Cherenkov process rather than some threshold in software or electronics. This threshold will decrease the effects of cross talk on spectral information, as this means most scattered radiation will not be energetic

enough to produce a signal in a quartz detectors.

Radiative cross talk occurs when an incident photon undergoes Compton scattering in one detector, creating a photon which deposits its energy in a neighboring detector. While the scattering is relatively isotropic at low energies (below 100 keV), it is forward peaked at the regions of interest for active interrogation (up to 10 MeV). As with pileup, cross talk in quartz will be measured via experiment and compared to sodium iodide. A simulation framework for the study of cross talk in Cherenkov detectors of arbitrary size will also be developed. Geant4 and experimental measurements employing a PuBe source are used for benchmarking, then cross talk simulations are run with the LENR and bremsstrahlung beams to see how beam energy effects cross talk in these specific detectors.

For quartz, the entire Cherenkov process was simulated in Geant4. To allow for a comparison between the experimental data, which was acquired in conventional coincidence mode, and the simulated data, a "coincidence" mode simulation was designed. In Geant4, an event is a component of the simulation that can consist of one or multiple radiative emissions. Each event is processed independently. In the cross-talk simulations, each event contained only one γ ray emission, and only one detector was irradiated. If both detectors had energy deposition in a given event, that event was registered as "coincident".

The experimental cross talk data was acquired with a time gate of 8 ns to define true coincident events. The out-of-beam detector was shielded using lead bricks, while the in-beam detector was exposed to a PuBe source with 1 Ci of total activity, as shown in Figure 3.13. Both detectors were placed on aluminum rails to allow the out-of-beam detector to move back and forth. Figure 3.13a shows the experimental setup with the quartz detectors in place. The source-to-detector distance for the sodium iodide detectors was altered such that the detector saw the same number of γ rays. The detectors and source were raised 100 cm off the ground and placed in the center of a large room to decrease the effects of scatter and neutron activation within the room. For the sodium iodide, measurements were made with edge-to-edge detector distances (separation a in Figure 3.13) of 32, 50, 68, 84,

and 100 mm, and each measurement was conducted for 60 minutes. The smallest edge-to-edge separation for the NaI detectors was 32 mm due to a lip protruding at the back of the crystal. Lower efficiency and smaller solid angle of the quartz detectors required longer experimental measurements, on the order of 2 to 4 hours each in order to build up enough statistics. Additionally, fewer data points were taken, measuring edge-to-edge separations of 22, 32, 50, and 100 mm. Normalization factors were applied to account for differences in measurement times.

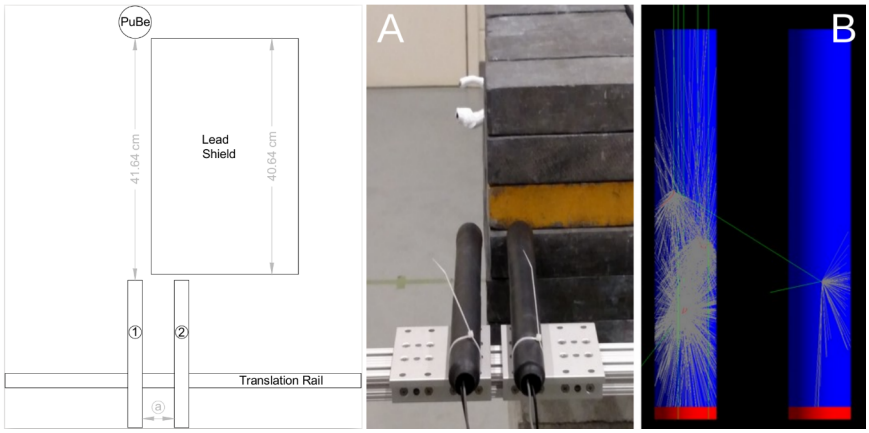

Figure 3.13: The experimental setup for quartz cross talk measurements is shown on the left. The distance *a* was changed in between experimental runs. Inset A is photograph of the experiment, with the quartz detectors in place. Inset B is a Geant4 screen shot from the crosstalk simulations, showing a cross talk event. The green tracks are γ rays and the gray tracks are optical photons. The red circle at the back of the detector is the PMT, and the particles are incident from the top of the image.

For both detectors, overnight background measurements with no source in place were taken in coincidence mode to account for random coincidences. The count rate for quartz was so low (700 total counts in 2 hours) that only one measurement was taken, with the detectors 22 mm apart. However, for the sodium iodide, two separate coincident background measurements were taken, one with 32 mm edge-to-edge separation and one with 100 mm edge-to-edge separation. As the raw number of coincident counts fell off at a linear rate, it was assumed that the background would die off similarly. An interpolation method based on the two background data points was used to calculated a position-dependent random coincidence rate.

The experimentally measured cross talk is compared to simulation for both detectors as illustrated in Figure 3.14. Error bars associated with the count rate are shown on both plots, though they are smaller than the markers for some data points. While the overall agreement between simulation and experiment for both detectors was strong, the agreement in sodium iodide diverged as the edge-to-edge separation increased, leading to simulation over-estimating the cross talk in sodium iodide by 10% at 100 cm. Disagreement like this is to be expected as not all environmental factors present in the experiment are accounted for in the simulations, and scintillation in the crystal was not simulated.

There is little discrepancy between the simulation and experiment for the quartz detectors because the full emission process of Cherenkov radiation is simulated. The complete optical processes in Cherenkov detectors typically yield a few hundred photons per MeV deposited, as opposed to approximately 38,000 photons per MeV in sodium iodide, making full simulation of Cherenkov radiation possible and the model more realistic. Higher-order cross talk, cross talk from the primary detector to a detector two pixels away, was originally studied via simulation. However, it was found that this effect was roughly two orders of magnitude below the nearest-neighbor cross talk, so these results have not been included.

The Geant4 models were next used to evaluate the cross talk in sodium iodide and quartz detectors with the same geometric configurations, both in the block and cylindrical geometries. Evidently, the cross talk effects on the energy deposition in quartz are less pronounced than in sodium iodide even for the same size detectors. Figure 3.15 shows the results of simulations with various edge-to-edge separations between the detectors, holding the number of particles incident on the primary detector constant between simulations. Coincidence probability is defined as the number of coincident counts divided by the total number of counts in the primary detector in order to alleviate effects of intrinsic efficiency. Note that when quartz is simulated in the same geometry as the sodium iodide, the associated cross talk is still smaller by a factor of two. Figure 3.15 also shows that for a small quartz detector at edge-to-edge distance of 4 mm, the probability of a photon scattering

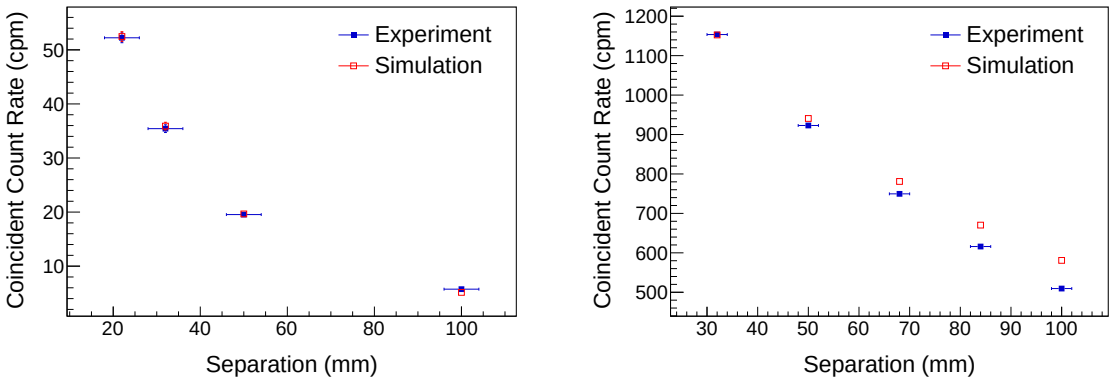

(a) Quartz (b) Sodium Iodide

Figure 3.14: Measured and simulated coincident count rates for the cross talk studies in quartz (a) sodium iodide (b). The differences between the simulation and experiment in the sodium iodide can be attributed to the fact that the scintillation process was not simulated and not all environmental factors were accounted for in the simulations. Error bars are drawn for all data points, though they may be smaller than the markers themselves. Note that the Y-axis between the two plots is on a different scale.

Table 3.3: Exponential fit parameters for data shown in Figure 3.15.

Dataset	Constant	Slope
NaI Block	-1.63	-1.11×10^{-2}
NaI Cylinder	-2.55	-3.73×10^{-2}
Quartz Cylinder	-4.07	-3.75×10^{-2}
Quartz Block	-2.35	-1.29×10^{-2}

from one detector to another is less than 2%.

Exponential fits have been applied to the simulated cross talk datasets according to Equation. The fit parameters can be seen in Table 3.3. Both the experimental and simulated results show that the cross talk decreases with increasing separation; however, the trends are different between the sodium iodide and quartz. There are two underlying causes of the change in cross talk with increasing distance: separation distance and scattered photon energy. The geometric $1/r^2$ effect of separation is coupled with the angular distribution of the Klein-Nishina cross sections for Compton scattering and the photon attenuation in each detector, both of which are energy dependent.

A previous study by Shin et al on neutron scattering and cross talk found a similar qual-

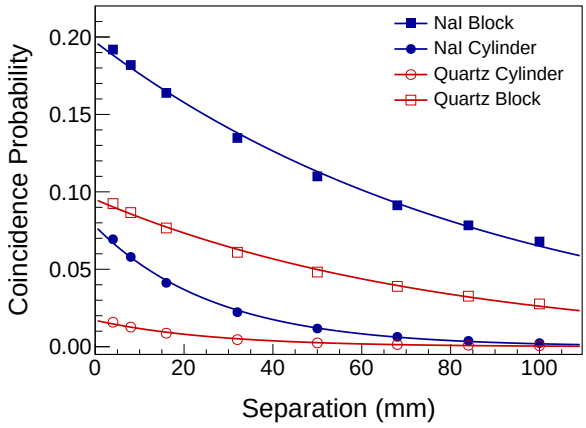

Figure 3.15: The simulated cross talk contributions to both the sodium iodide and quartz detectors, represented as coincident probability. These data were normalized to the total number of detected γ-rays by the primary detector, accounting for differences in detector efficiencies. To alleviate geometric effects of the smaller quartz crystal, additional simulation geometries were tested with the quartz physical properties in the sodium iodide's block geometry and vice versa. The total number of simulated particles which crossed each detector's surface was the same in all simulations. Additionally, exponential fits have been applied to all data sets; fit parameters can be found in table 3.3.

itative shape in the fall off of cross talk as a function of angle[77]. The authors concluded that higher cross talk at smaller angles was largely due to proximity between the detectors. In order to further understand the consequence of the combined energy-distance effect in photon cross talk, additional Geant4 simulations which mapped the position of photon interactions within each detector were run. To allow for a fair comparison, each detector was simulated in the sodium iodide block geometry, as described above. The results, shown in Figure 3.16, feature hit frequency data. As in previous cross talk simulations, only hits which led to events in both the primary and out-of-beam detectors were tallied.

The plots show that underlying physics of interaction in the different detector types has a significant impact on the position-dependent energy deposition. This is influenced by the energy threshold of the quartz detector. The photons which side-scatter in the primary detector are below 550 keV and thus cannot be detected in the quartz, leading to the decreased hit density at the front end of the crystal. However, the sodium iodide has no energy threshold, so it detects most photons which result from scatter in the primary detector. Pho-

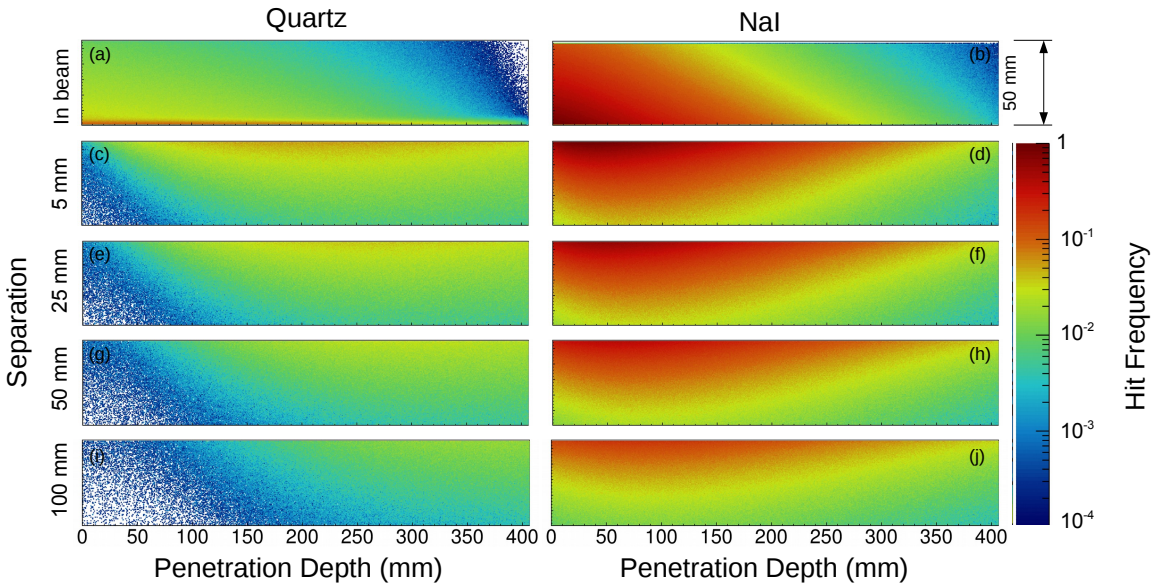

Figure 3.16: Results of cross talk simulations where the position of each γ-ray interaction was tallied. Inserts (a) and (b) represent the irradiated detector for each simulation. The inserts (c)-(j) show the hit maps with increasing detector separation. Note the different behavior of the hit maps for each detector reflect the difference in the underlying physical processes. Both simulations were run in the sodium iodide block geometry. Only hits which led to events in both the irradiated and out-of-beam detector were tallied. The hit maps are projections onto the YZ plane such that each detector element is 50 mm tall and 400 mm wide. All plots are normalized to the maximum value in the primary sodium iodide detector hit map. The same number of photons were fired onto both primary detectors.

ton attenuation in each detector further complicates the description of detector-to-detector cross talk. The higher density of the sodium iodide means that most of the incident γ-rays are stopped towards the front end of the detector, while γ-rays can penetrate further into the quartz. These effects combine to make the change in cross talk a function of energy in addition to the purely geometric $1/r^2$ fall off.

Finally, for optimization in the imaging array, cross talk in quartz as a function of spacing and detector diameter was evaluated. Figure 3.17 shows the results of the simulations where both detector diameter and inter-detector spacing were varied for the quartz detectors. Results show that cross talk is low for all considered configurations, with a maximum at 2%. The cross talk fraction, defined the same as above, fell off rapidly with both detector size and spacing, dropping to 0.5% for a 10 mm detector, even with small separation of

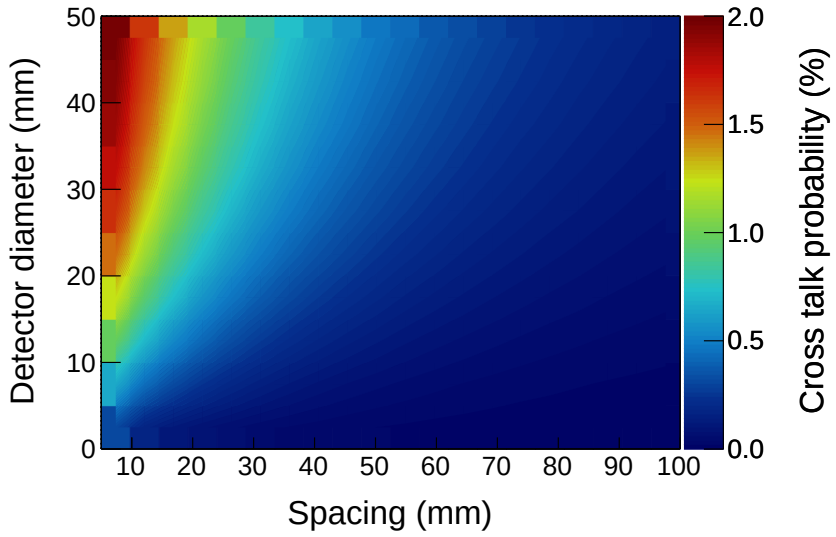

Figure 3.17: The cross talk fraction as a function of both detector diameter and distance between quartz detectors. This figure shows that even for a 50 mm detector with 5 mm between detectors, fewer than 2% of counts in a given detector will be attributable to the scatter from a nearby detector.

5-10 mm between detectors. This shows that a detectors under 20 mm in diameter can be placed 5 mm away from each other with little degradation of the final image quality due to scattering effects.

Final Design

As mentioned above, LYSO crystals will be included in the detector array. The final design was not a goal of this project, but it is discussed here as it will be used in all imaging simulations included in this work. Two imaging arrays will be mounted on a circuit board as shown in Figure 3.18. The detector-to-detector spacing within the sub-arrays is 5 mm (edge-to-edge) and the inter-array spacing is 11 mm. All detectors are coupled to silicon photomultipliers.

Although the LYSO detector model is not fully validated like the quartz model, cross talk between the two detector types is still simulated. Figure 3.19 shows the crosstalk between LYSO and quartz, and vice versa. The spacings used in the final imaging array are

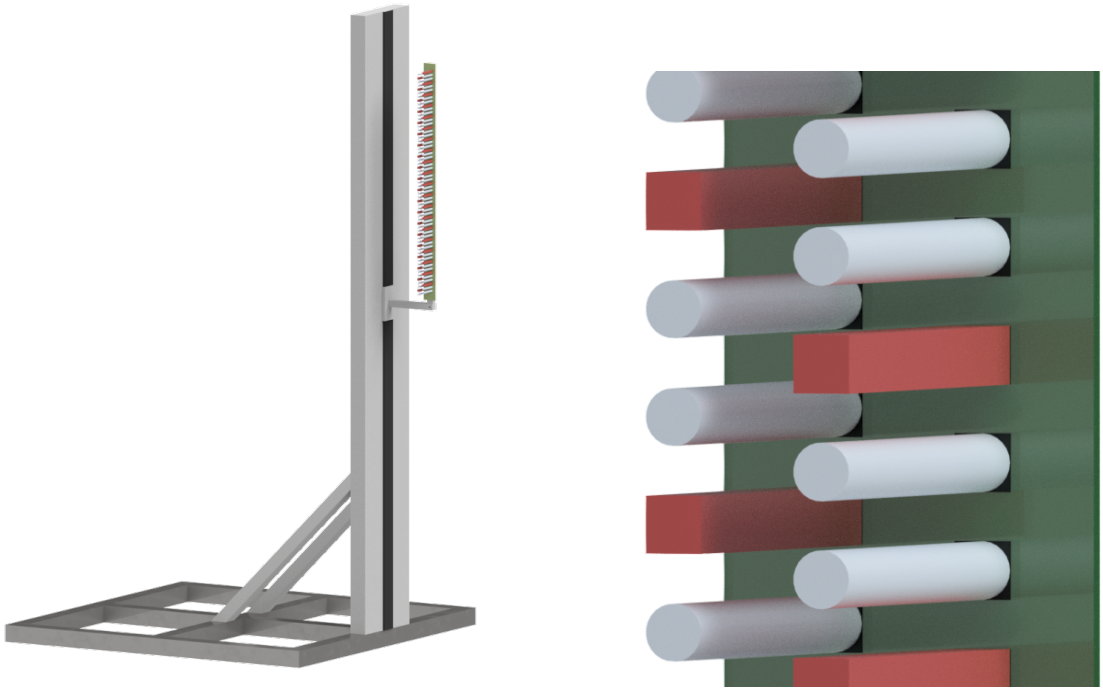

(a) (b)

Figure 3.18: Configuration for the final imaging array. (a) shows the full system and (b) is zoomed in on the detectors. The white detectors are quartz and red are LYSO. All detectors are 50 mm long in the direction of the beam and the faces are 6-mm squares (LYSO) and 6-mm diameter circles (quartz). The detector-to-detector spacing within the sub-arrays is 5 mm (edge-to-edge) and the inter-array spacing is 11 mm. The values on this plot account for crosstalk from the two nearest neighbor detectors. Image courtesy of Paul Rose[84].

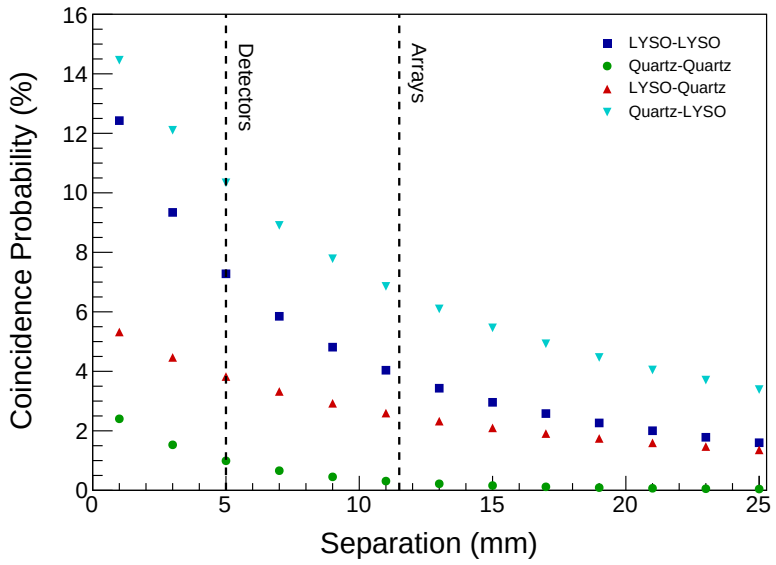

Figure 3.19: The cross talk fraction as a function of both detector diameter and distance between quartz and LYSO detectors. The dotted lines indicate detector-to-detector spacings in the imaging array shown in Figure 3.18.

highlighted on the plot. It is worth noting that the Quartz-LYSO and LYSO-LYSO crosstalk will not be negligible in the final array. However, the detector array will be mostly made up of quartz, which will partially mitigate the problem. Spectral post-processing methods could be applied to LYSO spectra if necessary, although this would not be ideal. The cross talk between the sub-arrays is not anticipated to be a problem, and quartz-to-quartz crosstalk is negligible.

The final evaluation of cross talk was to compare monoenergetic beams and the bremsstrahlung beams to be used for imaging. To make this cross talk model more realistic to a cargo scanning scenario, a 20 cm thick steel block was placed between the detectors and the planar imaging source. Figure 3.20 shows the Geant4 cross talk model with the LYSO detectors. Quartz was also tested, and simulations were done at detector-to-detector distances for 5 mm and 11 mm. Each simulation was run with 1×10^{10} incident particles. The results are summarized in Table 3.4. In general, the bremsstrahlung beams created less cross talk in the detectors, although all cross talk was relatively low. As anticipated the quartz exhibited

Figure 3.20: LYSO cross talk simulation with 5-mm detector-to-detector separation and a 20 cm steel block between the source and detector. In this image, 100 photons are incident upon the block and 1 makes it through the detector. This photon deposits energy in the primary detector but scatters away from the secondary detector.

Table 3.4: Cross talk probabilities (listed in percent) for the imaging beams used in this project. Each beam was filtered by 20 cm of steel to approximate a realistic cargo imaging scenario. The separations, 5 mm and 11 mm, are the distances between detectors in the final imaging array.

	No Threshold				1 MeV Threshold	
	Quartz		LYSO		LYSO	
Beam	5 mm	11 mm	5 mm	11 mm	5 mm	11 mm
6-MV Brem.	0.068	0.020	5.089	2.776	1.149	1.206
9-MV Brem.	0.181	0.029	6.155	3.380	1.648	0.825
3-MeV MPS	0.052	0.020	4.600	2.500	0.876	0.402
6-MeV MPS	0.213	0.023	7.822	4.331	2.251	1.152
9-MeV MPS	0.986	0.167	10.387	5.781	3.678	1.915
LENR	0.523	0.142	7.441	4.120	2.351	0.549

less cross talk than the LYSO. Figures 3.21 and 3.22 shows each detector's response to the the six imaging beams tested. Note that in the LYSO, most of the crosstalk events are 511 keV photons resulting from positron annihilation in the primary detector. Implementation of a 1 MeV energy threshold can eliminate the 511 signal and reduce the overall cross talk contribution in the LYSO detectors. Due to the inherent energy threshold of the Cherenkov detectors, this post-processing threshold has little effect on the cross talk signal.

Detector Dose

The geometry shown in Figure 2.11 was used to measure detector dose as well as beam penetration. For these simulations, the full optical process was modeled to ensure the Cherenkov process was accounted for properly. Both quartz and LYSO were used, the steel plate was kept at a constant thickness of 20 cm, and 4×10^{10} particle histories were run.

The results are shown in Table 3.5. Energy deposition is measured in the detector per

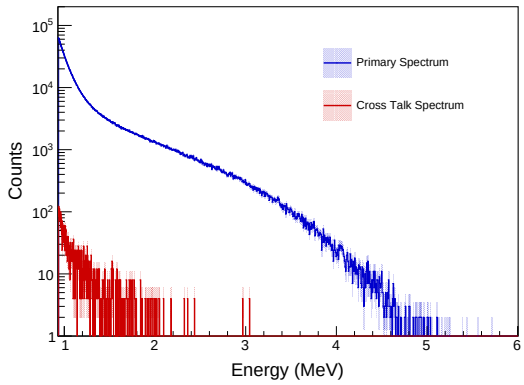

(a) Quartz response to 6-MV bremsstrahlung beam

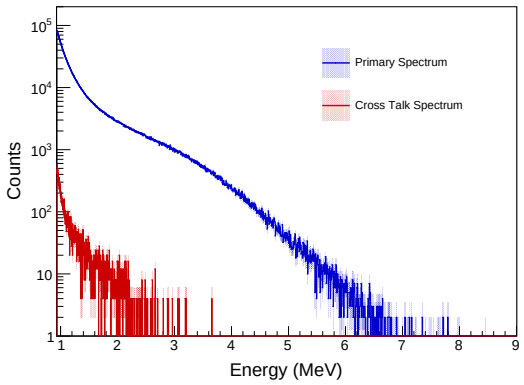

(b) Quartz response to 9-MV bremsstrahlung beam

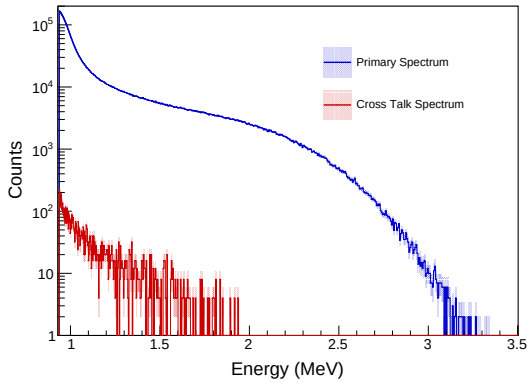

(c) Quartz response to 3-MeV MPS beam

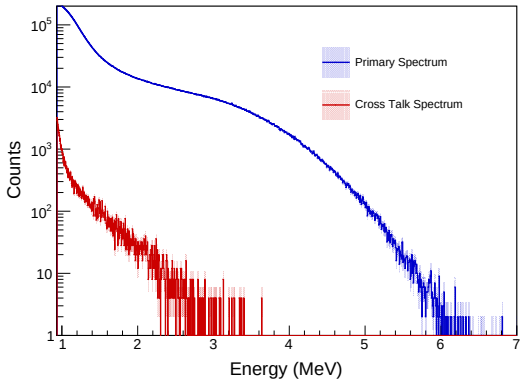

(d) Quartz response to 6-MeV MPS beam

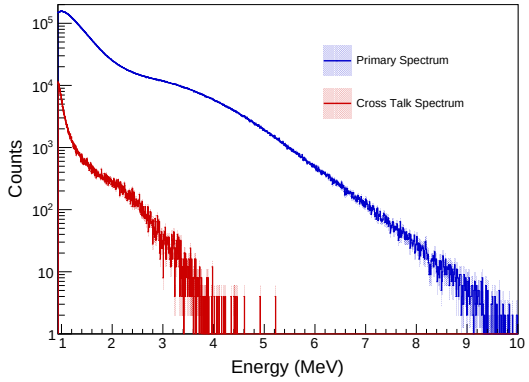

(e) Quartz response to 9-MeV MPS beam

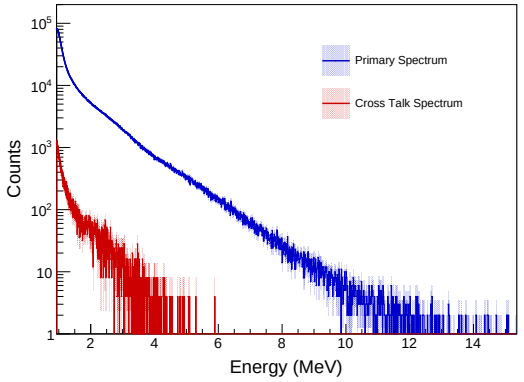

(f) Quartz response to LENR beam

Figure 3.21: Quartz detector cross talk for the imaging beams tested including full optical modeling. The relatively low contributions of cross talk to the overall signal mean that cross talk will not be an issue for these detectors.

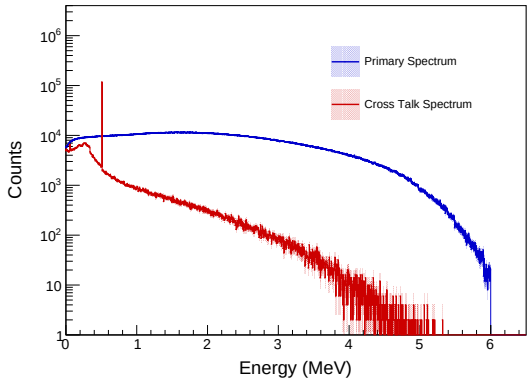

(a) Energy deposition in LYSO from the 6-MV brem-sstrahlung beam

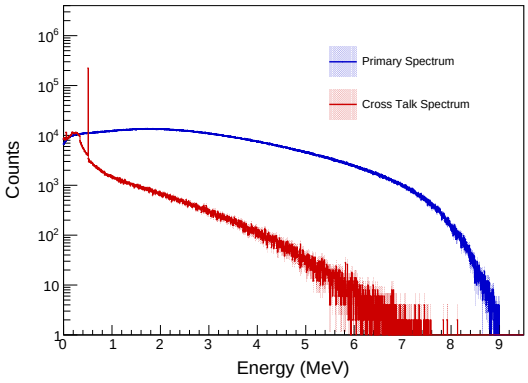

(b) Energy deposition in LYSO from the 9-MV brem-sstrahlung beam

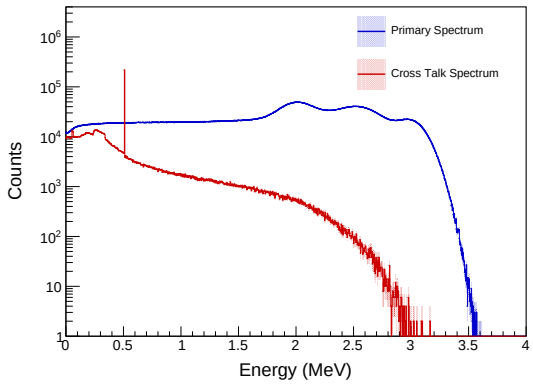

(c) Energy deposition in LYSO from the 3-MeV MPS beam

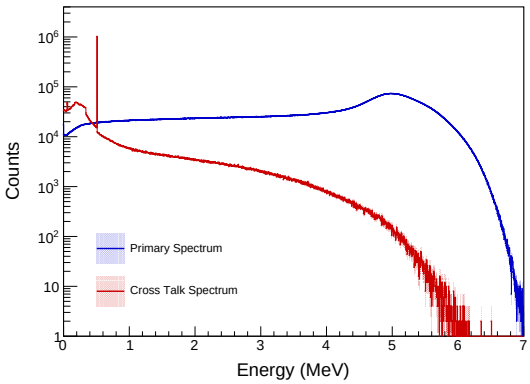

(d) Energy deposition in LYSO from the 6-MeV MPS beam

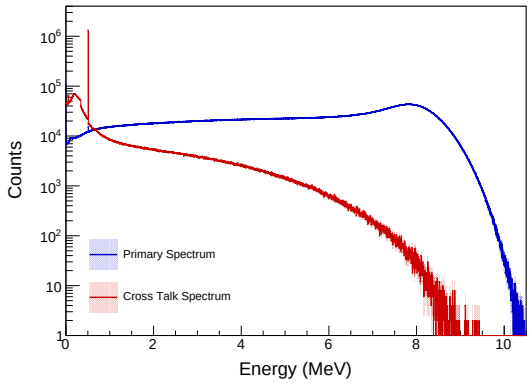

(e) Energy deposition in LYSO from the 9-MeV MPS beam

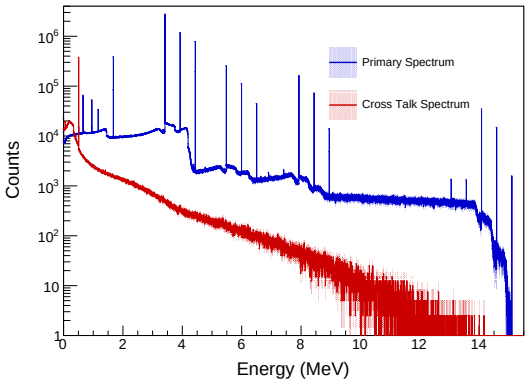

(f) Energy deposition in LYSO from the LENR beam

Figure 3.22: LYSO cross talk for the imaging beams tested. Note that the full optical process was modeled in the quartz while energy deposition was tallied in the LYSO, leading to nearly perfect energy resolution. Most of the cross talk photons in the LYSO fall in the 511 keV peak, which is cut off on all figures. An energy threshold of 1 MeV can greatly reduce the contributions of cross talk to these spectra. The LENR source was modeled as truly discrete, so there are sharp peaks present in that spectrum while the MPS sources are modeled with a 10% energy spread.

Table 3.5: Detector dose after penetration through 20 cm of steel by each beam. Doses are given in Gy per source photon in the second and third columns and Gy per penetrating photon in the fourth and fifth columns.

Beam	Per Source Photon		Per Penetrating Photon	
	Quartz	LYSO	Quartz	LYSO
6-MV Brem	2.94E-15	2.73E-14	1.42E-11	2.53E-11
9-MV Brem	5.56E-15	5.38E-14	1.51E-11	3.29E-11
3-MeV MPS	5.67E-15	4.91E-14	1.35E-11	2.20E-11
6-MeV MPS	2.49E-14	2.47E-13	1.59E-11	4.49E-11
9-MeV MPS	3.48E-14	4.12E-13	1.85E-11	6.43E-11
LENR	8.24E-15	7.24E-14	1.64E-11	4.18E-11

source photon as well as per penetrating photon (using the penetration values previously calculated). The monoenergetic beams are much more penetrating, so they deposit a higher dose per source photon. Normalizing for the amount of penetrating photons reduces the efficiency as compared to a bremsstrahlung beam.

These detector dose results alone do not tell the whole picture of the dose reduction possible with monoenergetic beams. Because the beams are more penetrating, they deliver less dose to the cargo while getting more photons through the container. Table 3.6 shows dose that would be delivered to the cargo (or the human phantom in the container) to get equal dose in the quartz and LYSO detectors, normalized to the bremsstrahlung beam. All doses are normalized to the 6-MV brem. dose. All of the monoenergetic sources except the 3-MeV MPS offer reductions in the dose to the cargo as compared to the 6-MV brem. source, with the 9-MeV MPS source offering up to an 80% dose reduction for the human phantom. As mentioned above, in a dual-energy imaging acquisition, bremsstrahlung systems typically share the dose between low and high energy in a 1:3 ratio. Table 3.7 shows the effects of a combined bremsstrahlung acquisition. In the table, the MPS sources have been combined in the same manner. Both discrete-energy sources offer reductions in the human phantom dose as compared to bremsstrahlung, with the MPS source offering almost a 40% decrease to the human phantom.

Table 3.6: Adjusted dose values for the cargo and human phantoms using the imaging beams as described in the previous chapter.

Beam	Human Phantom		Steel Plate	
	Quartz	LYSO	Quartz	LYSO
6-MV Brem	1.00	1.00	1.00	1.00
9-MV Brem	0.63	0.60	0.68	0.65
3-MeV MPS	0.68	0.73	0.81	0.87
6-MeV MPS	0.23	0.22	0.37	0.35
9-MeV MPS	0.21	0.17	0.40	0.32
LENR	0.48	0.51	0.57	0.60

Table 3.7: Adjusted dose values for the cargo and human phantoms using a 1:3 dose sharing ratio between low- and high-energy beams for the bremsstrahlung and MPS sources.

Beam	Human Phantom		Steel Plate	
	Quartz	LYSO	Quartz	LYSO
Brem	1.00	1.00	1.00	1.00
MPS	0.61	0.62	0.78	0.79
LENR	0.65	0.70	0.74	0.80

Conclusions

The results presented in this chapter have shown that quartz Cherenkov-based radiation detectors are well suited for the high flux environments typical of active interrogation imaging applications. Due to the electromagnetic nature of Cherenkov emission, these detectors are more resistant to the effects of pulse pileup than sodium iodide detectors. The inherent energy threshold of the Cherenkov process also makes these detectors robust to scatter, especially detector-to-detector scatter, or cross talk. In experimental cross talk studies, the coincident count rate in the small diameter quartz detectors was over an order of magnitude lower than in large block sodium iodide detectors. While cross talk signal may induce little error in the neighboring detectors, quartz detectors still suffer from energy loss due to escaping photons or electrons. One way to mitigate this effect would be to use larger detectors, however this would inhibit spatial resolution. Rather, using the wide integration regions for R-value measurement partially compensates for incomplete energy deposition.

The results presented in this chapter show that quartz detectors can be packed tightly into an imaging array and detector cross talk will not degrade the spectra. This is crucial to the success of an active interrogation system as scatter from detector to detector can inhibit image contrast and detectability of potential SNM. LYSO crystals will also be integrated in to the final imaging array. These suffer more greatly from cross talk than the quartz, but these effects can be mitigated by reduced numbers of LYSO crystals, and post-processing if necessary.

In addition to studying the effects of edge-to-edge separation on detected spectra, the effects of changing crystal diameter were also investigated. The simulation results show with a crystal diameter of 50 mm, even at 5 mm edge-to-edge separation, only 2% of registered counts will be attributed to cross talk. When simulated in the same geometry, quartz showed a lower coincidence probability than sodium iodide by a factor of 2-4 at small detector separations. This shows that, from a cross talk perspective, the quartz detectors can be made essentially as small as possible.

It should be noted that though pileup was studied experimentally in this chapter, the effects of pileup are not included in any of the simulation work in this thesis. While this may lead to some inaccuracies, the pileup in quartz detectors is low, and it was not deemed worth the computational cost to include pileup effects in the simulations for this work.

Finally, cross talk in LYSO and quartz for imaging beams used in active interrogation was evaluated. It was found that the higher energy beams led to greater cross talk, though the probability of cross talk is relatively low, maximally around 0.5% and 10% in the quartz and LYSO, respectively. Implementation of a 1 MeV threshold can reduce the LYSO cross talk to around 4%.

CHAPTER 4
RADIOGRAPHIC IMAGING

When describing the capabilities of an imaging system, there is no clear metric which says one imaging system is better than another. This is especially true in cargo radiography, where the problem and application space are not as clear as, for example, medical imaging. There are multiple beam sources, ranging from relatively simple radioisotope sources and electron linear accelerators to heavy ion accelerators. Radiation dose can be measured to the cargo, to the detectors, or to the system operators. The ANSI standard N42.46-2008 outlines imaging tests for beam penetration, contrast sensitivity, and spatial resolution[85]. While these tests may be simple to implement in the field, they can be subjective, and are not appropriate for a thorough comparison of different imaging sources. DNDO has laid out other tests for imaging systems, and previous investigators have used multiple phantoms to evaluate various aspects such as contrast and spatial resolution.

The goal of this work is to provide a broad and thorough comparison between bremsstrahlung beams and monoenergetic beams for use in imaging. While some of the work included in this thesis has included the use of inverse Compton scattering sources, image evaluation will not include these sources for brevity. The parameters that will be tested include spatial resolution, imaging accuracy (with regard to Z_{eff} imaging), contrast, image noise, and contrast-to-noise ratio (CNR). All images presented below are cargo-dose matched using the 20-cm steel plate calculations presented in Chapter 2. In all cases below, the source geometries for the LENR and bremsstrahlung beams were exactly the same. All simulations assumed an infinitesimal emission spot size, while any practical accelerator will have some emission spot. In bremsstrahlung and LENR sources, this is due to the spreading of the electron or ion beam. In the experiments discussed in previous chapters, the LENR emission spot was about 1 cm, corresponding to the diameter of the deuteron

beam. One spatial resolution simulation was run with a 1 cm emission spot in place and the differences in spatial resolution with and without the focal spot were found to be negligible.

In this chapter, the results of application of a noise suppression algorithm to reconstructed images are also shown[86]. The algorithm relies on the full data measured in transmission to suppress noise on R-value (material-dependent) images. Coupling this algorithm with the LENR imaging beam may lead to further reductions in the imaging dose.

Imaging Simulation in Geant4

Geant4 allows for adjustable physics models, allowing the user to only model physical processes that are relevant to a given simulations. This allows for optimization of the code based on the physics processes that are necessary for the application. Additionally, Geant4 is capable of multi-threading which will allow for great decreases in simulation time. In order to characterize the threading capabilities of Geant4, cross talk simulations in the LYSO crystals were timed. These simulations included no optical modeling and used the standard physics list `FTFP_BERT`. Both strong scaling and weak scaling of Geant4 were tested. For strong scaling tests, the job size was held constant as the number of processors is increased from 1 to 64. Strong scaling efficiency is calculated as

$$\epsilon_{strong} = \frac{t_1}{(N * t_N)} * 100 \tag{4.1}$$

where t_1 is the time one processor to run the simulation, and t_N is the time for multiple processors to run the simulation. Weak scaling tests increase the job size in accordance with increased use in processors such that each processor does the same amount of work. Weak scaling efficiency is calculated as

$$\epsilon_{weak} = \frac{t_1}{t_N} * 100 \tag{4.2}$$

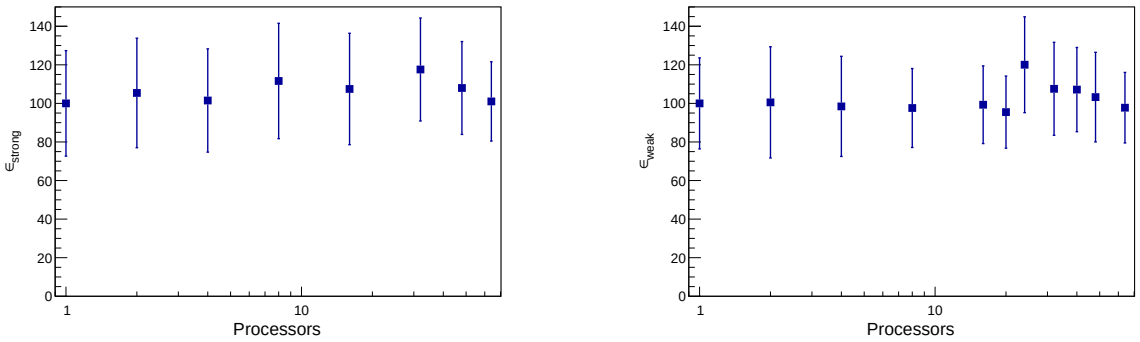

(a) Strong scaling

(b) Weak scaling

Figure 4.1: Strong and weak scaling efficiency for Geant4 particle transport simulation. It is important to note that this scaling is only relevant for the physics processes used in the simulation, as other processes can have different memory footprints or computational efficiencies. For the physics list `FTFP_BERT`, Geant4 is nearly 100% efficient by both measures.

Geant4 implements event-level parallelism, so the job per processor correlates directly with the number of primary events. In this work, one event constitutes one primary particle. For the characterization, 10 simulations per scaling were submitted. Figure 4.1 shows the results of these simulations as the number of processors is increased. Inset (a) shows the strong scaling efficiency and (b) shows the weak scaling efficiency. The large error bars stem from the different compute nodes used on our cluster. The cluster has 16 nodes with 64 cores each, and half the nodes have different architectures. When submitting jobs to the system, the specific nodes cannot selected, so there can be sizable fluctuations in computational times. All of the data shown in the figure were run as jobs on a single node, i.e. on a shared memory system.

All imaging simulations are run on a 15-node CPU cluster, and each node has 64 processors. All simulations are carried out in the same workflow. The simulations are broken up into slices, which generally correspond to 3 mm steps of the beam/detectors. The slices are submitted to the cluster as separate jobs. Figure 4.1 shows that the number of processors can be scaled up each for each simulation to as many as 64 cores without performance penalties. The cluster used, Critcel, is run and managed by Georgia Tech's Partnership for

Advanced Computing Environment (PACE) and is run by a central scheduling system. To minimize wait times due to the scheduler, jobs are typically submitted requesting 16 cores. Using all of the compute nodes, the simulations can run up to 60 slices simultaneously. In the simulations, the "detector" is a sensitive volume of air which stops all particles that enter it. This data can be adjusted for efficiency in post-processing or convolved with the quartz response function which inherently accounts for detection efficiency. Applying detector response after the simulation greatly reduces the simulation time. All image reconstruction is done in ROOT[74]. Transmission images are calculated by normalizing a given slice to a "flatfield" slice which has no cargo between the source and detector. This is equivalent to applying Equation 2.2 to every detector in the simulation. Using multiple flatfield slices can help to reduce image noise by establishing a more stable I_0, and every simulation below will use at least two flatfield slices. R-value images are calculated using the integration method described in Chapter 2 applied to every detector in the simulation. The data for the 6-MV brem and 9-MV brem images are combined in post-processing, similar to any dual-energy acquisition system with separate bremsstrahlung imaging beams. As mentioned in previous Chapters, the dose ratio between the low and high energy acquisitions is 1:3.

ANSI Spatial Resolution

The ANSI standard N42.46-2008 test for spatial resolution consists of imaging a series of steel line-pair gauges. This simulation geometry was created in Geant4 for simulation and can be seen in Figure 4.2. The line pairs are to be made of carbon steel, and C1008 was used in these simulations. The distance d is changed between tests, and the spatial resolution is determined when the line pairs can no longer be distinguished. The test is to be done with objects in front of or behind the line pairs. Values of d ranging from 1 mm to 10 mm in steps of 1 mm were tested, and these results were combined into one image in post-processing for visualization. The imaging source was a fan beam vertically, with the angle set so that the detector array was fully irradiated. The detector array geometry was

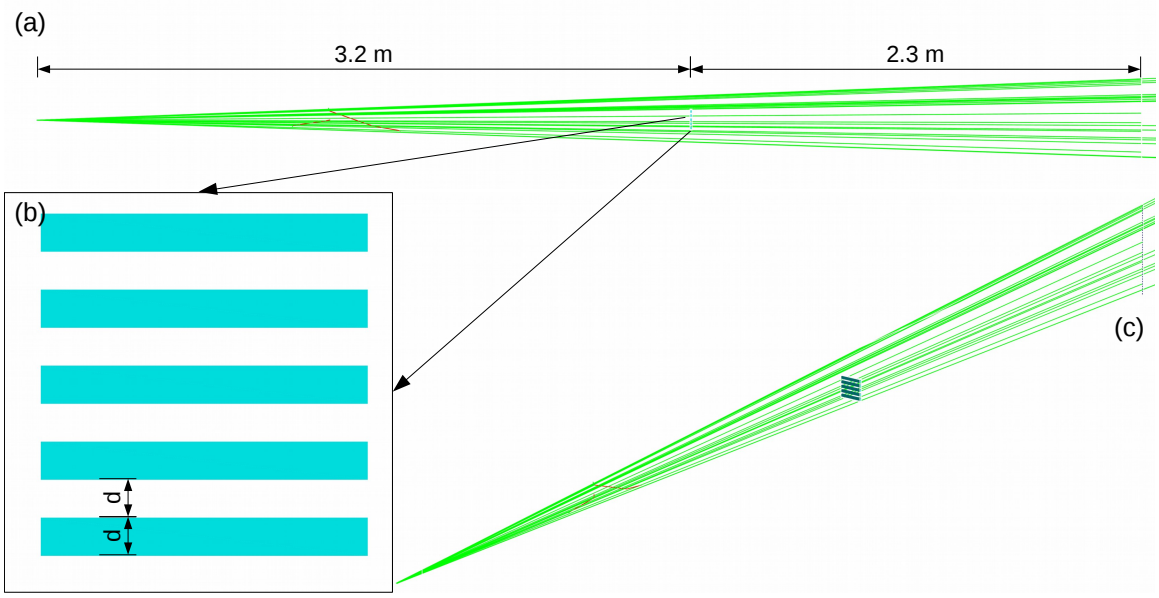

Figure 4.2: Simulation geometry for the spatial resolution phantom. (a) shows the whole geometry from the side, includeing the source-to-object distance and object-to-detector distance. (b) shows the line pairs in detail, where the distance d is adjustable in the simulation. (c) shows a view from behind the source for better visualization. The source is a fan beam with the fan-angle set to fully irradiate the detector array. The imaging source is 6 mm wide. The line pairs are made of carbon-steel according to the ANSI standard N42.46-2008.

the same as presented in the previous chapter using only quartz. The edge-to-edge detector spacing was 5 mm, and two sub-arrays that were evenly offset (such that the center of a detector in sub-array a would be exactly in between two detects in sub-array b) were used. The source-to-object distance was 3.2 m, and the source-to-detector distance was 5.5 m. The resulting images can be seen in Figure 4.3. The transmission data was normalized such that both beams would show transmission on the same scale. The data from separate simulations were combined to show all results in one image. The beam source has very little effect on the spatial resolution for this data, and both beams can clearly distinguish line pairs down to 5 mm. At 4 mm, there are still 5 distinctive line pairs, but the intensity values are non-uniform, so they cannot be truly resolved. Figure 4.4 shows this difference by taking projections through slices of the 3 mm and 4 mm data.

In addition to testing the spatial resolution as outlined in the standard, spatial resolution

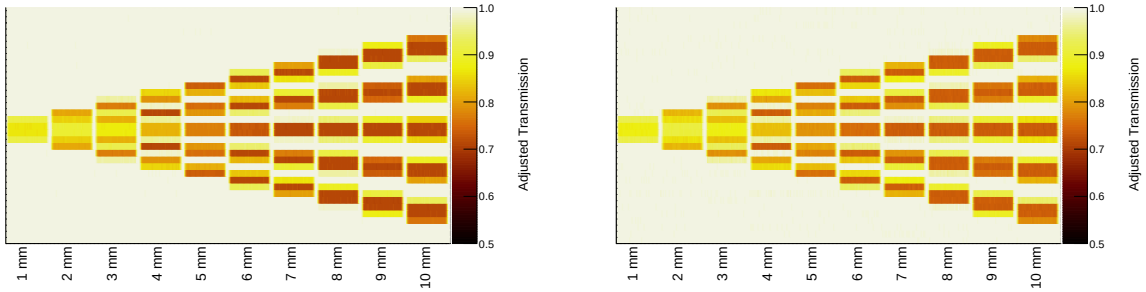

(a) Brem. (b) LENR

Figure 4.3: ANSI spatial resolution test for line pairs ranging from 1 mm on the left side of each image to 10 mm on the right in steps of 1 mm. The simulations for each of these geometries were run separately and the results were combined in post-processing. The beam source had little impact on the spatial resolution, and line pairs down to 4 mm can be discerned. Each pixel is 3 mm (horizontally) by 3.2 mm (vertically).

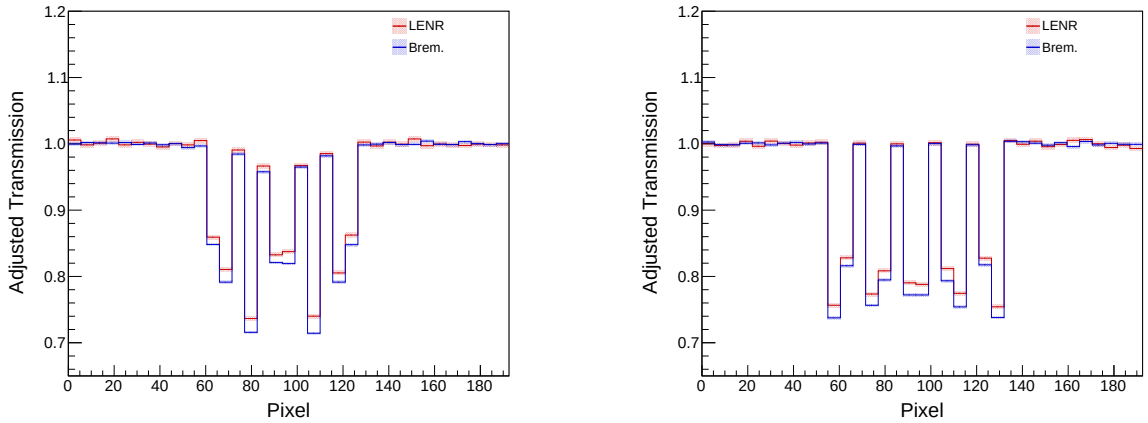

(a) 3 mm (b) 4 mm

Figure 4.4: Line profiles through the 3 mm and 4 mm line pairs. At 3 mm, the full information of each line is lost while signal levels are preserved at 4 mm. The pixel size is 5.5 mm at the detector and 3.2 mm at the line pairs.

was tested with steel plates in front of and behind the line pairs. Cumulative steel thicknesses of 1 cm, 10 cm, and 20 cm were used. The plates were as placed though they made up the walls of a cargo container in the beamline. The results of the simulations for both beam sources can be seen in Figure 4.5. Adding the steel plates induces more scattering (especially at 20 cm), making a more strenuous test of spatial resolution. The results shown here are also largely independent of beam source. The image noise grows as the steel thickness increases, strongly effecting the image quality at 20 cm. The noise effect is strongly seen on the line profiles in Figure 4.6, and the 4 mm line pairs are fairly indistinguishable at 20 cm with either beam. The loss of contrast combined with the increased noise effectively reduce the spatial resolution. These tests show that while the spatial resolution of the system may be 4 mm according to the standard, actual spatial resolution is dependent on the composition of the cargo. In these simulations, the steel plate effectively served to decrease the signal-to-noise ratio. A similar effect could have been observed by decreasing the imaging dose, and in this way spatial resolution can be partially related to dose.

Material Discrimination Phantom

A phantom containing 6 different materials to test the imaging capability of each beam; the geometry can be seen in Figure 4.7. Each cylinder is 10 cm thick, and the phantom is placed inside a mock cargo container with 5 mm stainless steel walls. The imaging source is a plane with width equivalent to the detector diameter (6 mm) and height equal to the detector array (700 mm), which is described in Chapter 3. The cargo is stepped in 3 mm increments for a total of 220 steps. The final image size is then 660 mm (horizontal) by 700 mm (vertical). The phantom is imaged with the each beam separately.

The NCRP has set an upper dose limit of 500 mrem for a cargo image acquisition[11]. Since the cargo being imaged in this study is smaller than a typical container, set a limit of 5 mrem was set for these simulations. This limit roughly corresponds to the difference in area between the simulated container and a 20 foot ISO container. All full dose results

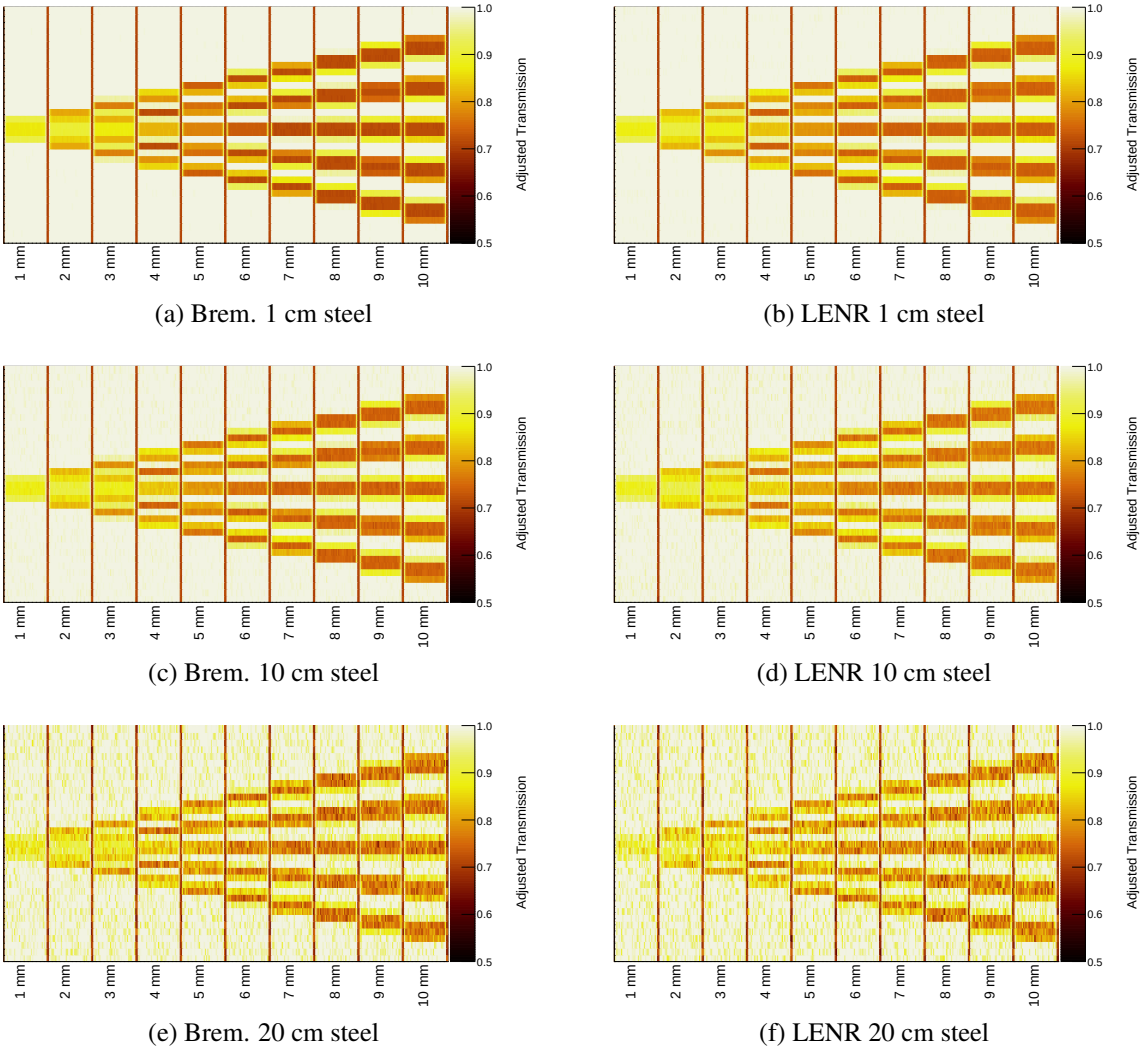

(a) Brem. 1 cm steel

(b) LENR 1 cm steel

(c) Brem. 10 cm steel

(d) LENR 10 cm steel

(e) Brem. 20 cm steel

(f) LENR 20 cm steel

Figure 4.5: ANSI spatial resolution test for line pairs ranging from 1 mm to 10 mm with steel plates placed around the line pairs. As the steel thickness increases, the image noise increases and the spatial resolution can be effected. Each pixel is 3 mm (horizontally) by 3.2 mm (vertically).

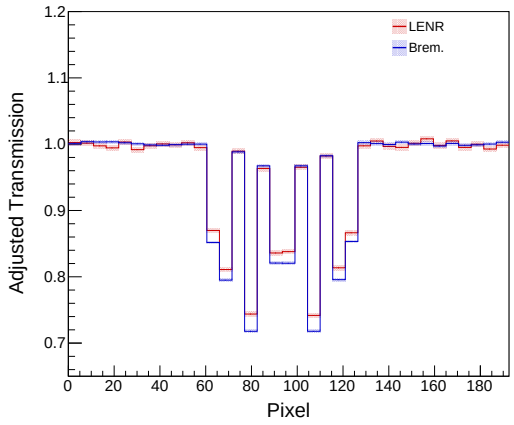

(a) 3 mm, 1 cm steel

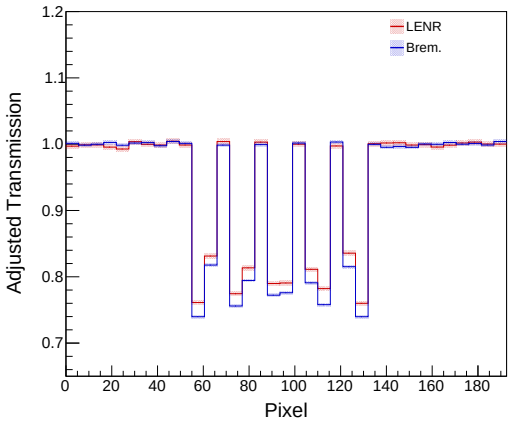

(b) 4 mm, 1 cm steel

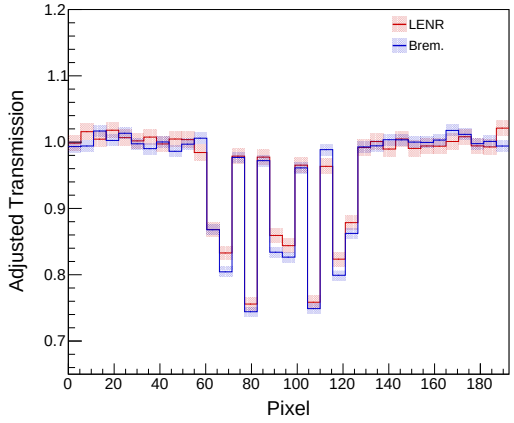

(c) 3 mm, 10 cm steel

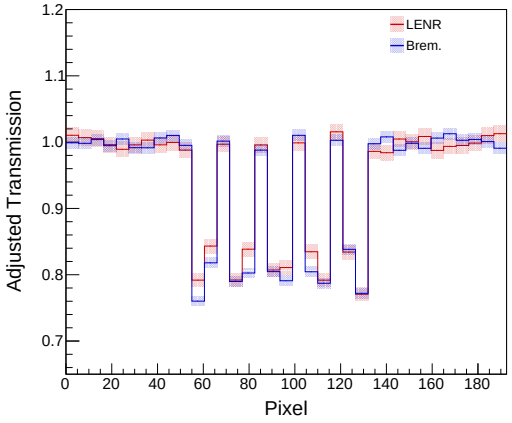

(d) 4 mm, 10 cm steel

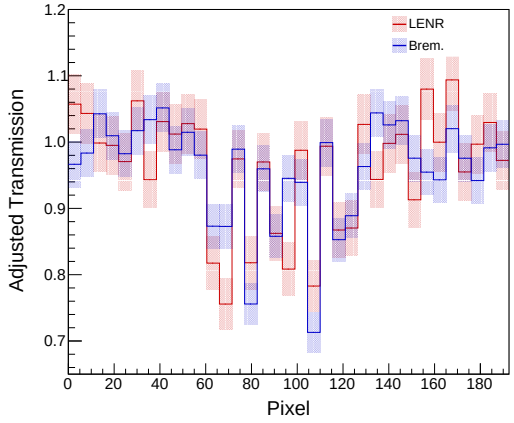

(e) 3 mm, 20 cm steel

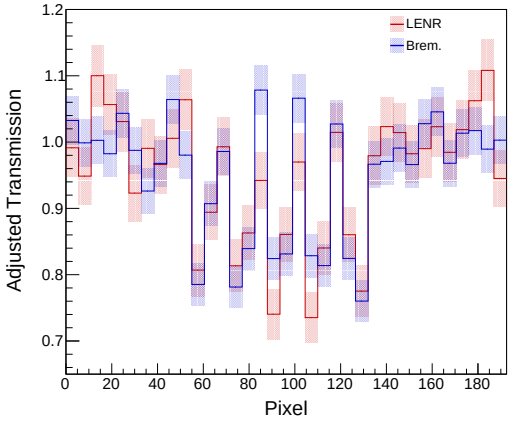

(f) 4 mm, 20 cm steel

Figure 4.6: Line profiles through the 3 mm and 4 mm line pairs with steel plates in front of and behind the line pairs. At 20 cm of steel, the noise greatly effects the separation line pairs. The pixel size is 5.5 mm at the detector and 3.2 mm at the line pairs.

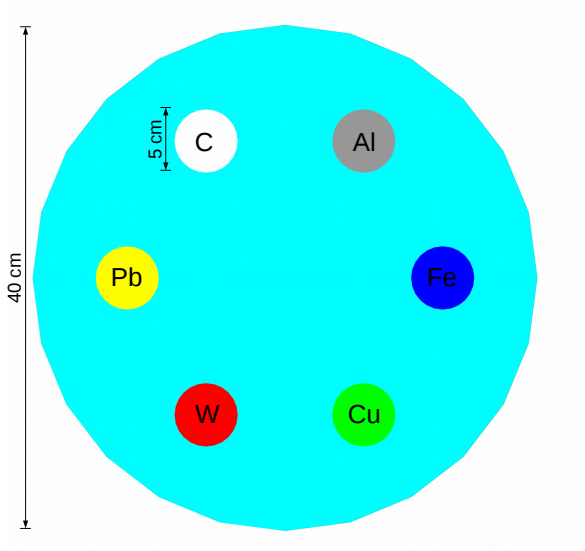

Figure 4.7: Geant4 phantom used for material identification. All rods and the water cylinder are 10 cm thick. The elements of each material are shown on the image, and the phantom is suspended in a small-scale cargo container with 5 mm stainless steel walls. The source is modeled as a parallel-beam plane source, and the phantom is imaged in 3 mm steps horizontally. Two detector arrays are used behind the container with a total of 140 quartz detectors with 5.5 mm effective pixel size.

shown below correspond to a dose to the cargo of 5 mrem. A post-processing algorithm for reducing the detection statistics, i.e. simulating decreased imaging dose, was written to study the effects on image quality. This allows for characterization of contrast, image noise, and accuracy as a function of dose.

The quantitative metrics used to evaluate the performance of each imaging beam are pixel error, contrast-to-noise ratio (CNR), and image noise. Pixel error is measured as

$$E_{mat} = \frac{|R_{mat} - R_{NIST}|}{R_{NIST}} \tag{4.3}$$

where R_{mat} is the measured R-value of a given material, R_{NIST} is the expected R-value based on data from NIST's XCOM database[52]. CNR is measured as

$$CNR_{mat} = \frac{|R_{mat} - R_{water}|}{\sigma_{water}} \tag{4.4}$$

where σ_{water} is the noise standard deviation (STD) of 1650 pixels in a central region of the water cylinder. For all imaging simulations, the dose to the cargo between the combined bremsstrahlung acquisition and the LENR acquisition is matched.

Figure 4.8 shows the total transmission images of the material discrimination phantom. In addition to the full dose acquistion (5 mrem), images at lower dose are also shown to display the effects of dose on image quality. The lower dose images show a higher noise STD, i.e. pixel-to-pixel variation. Overall, all six materials stand out in the images. The white pixels in the images correspond to a zero pixel, and the dense tungsten, with an areal density of 193 g/cm^2, proved to be a problem for both methods at low dose.

Figure 4.9 shows the R-value reconstructed images of the contrast evaluation phantom with both beams. At full dose, all six rods can be seen in both figures, however the difference between the rods stands out more with the LENR image. This is because of the larger range of R-values achievable with the LENR beam, as shown by Figure 2.10. As the dose is reduced, higher contrast present on the LENR image allows the rods to stand out stronger against the noise as compared to the bremsstrahlung image. Figure 4.10 shows cross-sectional line profiles of the full dose images. Figure 4.10a shows the horizontal profile through lead and iron rods, and Figure 4.10b shows vertical profile through the tungsten and carbon rods. Inserts (c) and (d) show the same profiles through the low dose images. As the dose is reduced, the noise becomes high in both the LENR and bremsstrahlung images, and only the lead rod is clearly distinguishable above the background. Table 4.1 summarizes the CNR present for each of the materials in each image. The LENR image shows higher or equivalent CNR for every rod, averaging 50% and 56% higher contrast on the high and low dose images, respectively.

As mentioned above, the dose to the cargo for each acquisition was matched, and a post-processing algorithm was written to study the effects of decreasing the dose. Figure 4.11 shows the noise standard deviation as a function of imaging dose in both of the transmission images and the R-value images. The noise present on R-value images is the result of

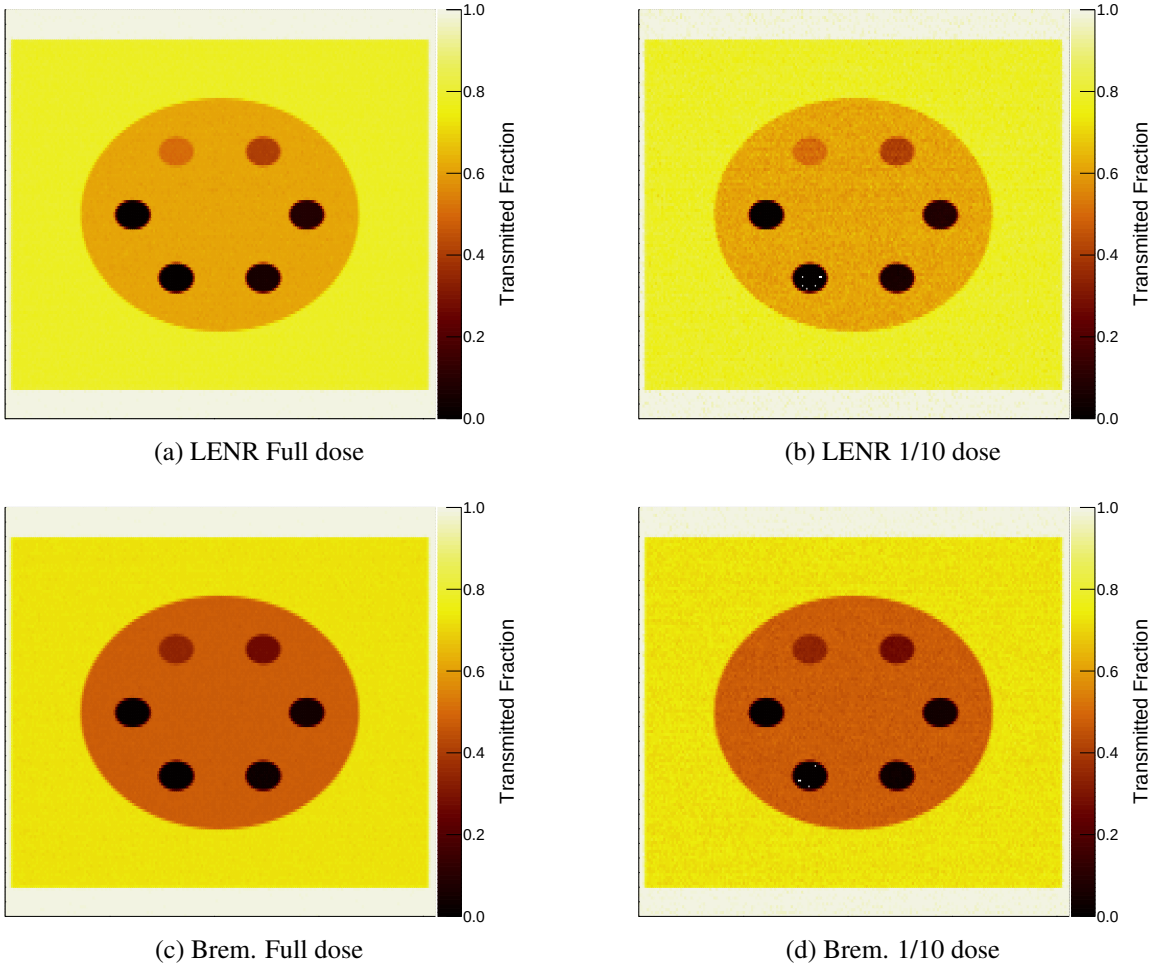

(a) LENR Full dose

(b) LENR 1/10 dose

(c) Brem. Full dose

(d) Brem. 1/10 dose

Figure 4.8: Transmission images for the phantom shown in Figure 4.7. The full dose acquisition corresponds to 5 mrem for the whole acquisition. Note the larger noise levels present on the low dose images. The image size is 660 mm (horizontal) by 700 mm (vertical).

Table 4.1: Contrast-to-noise ratio for each material in the images shown in Figure 4.9.

	LENR		Brem.	
Z	5 mrem	0.5 mrem	5 mrem	0.5 mrem
6	1.64 ± 0.10	0.67 ± 0.11	0.41 ± 0.11	0.10 ± 0.11
13	0.78 ± 0.09	0.22 ± 0.10	0.79 ± 0.10	0.13 ± 0.10
26	5.64 ± 0.08	1.64 ± 0.08	3.37 ± 0.08	1.11 ± 0.08
29	7.03 ± 0.09	2.11 ± 0.09	4.08 ± 0.09	1.41 ± 0.09
74	13.68 ± 0.42	2.36 ± 0.21	11.97 ± 0.39	1.89 ± 0.19
82	17.75 ± 0.22	5.41 ± 0.23	10.35 ± 0.16	3.21 ± 0.18
Mean	7.75 ± 0.08	2.07 ± 0.06	5.16 ± 0.08	1.31 ± 0.05

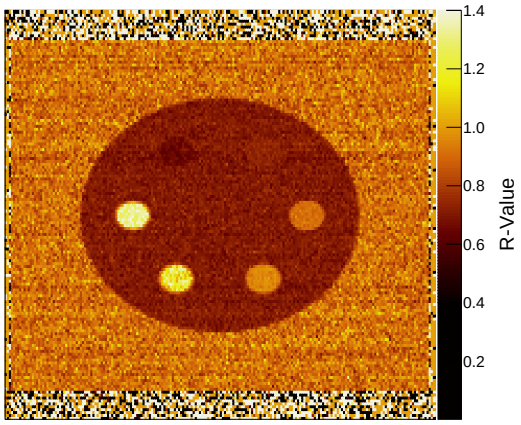

(a) LENR Full dose

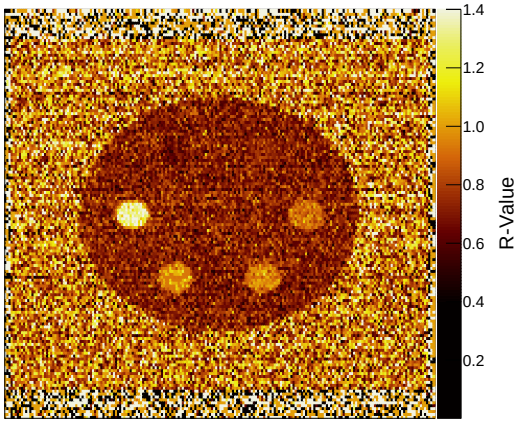

(b) LENR 1/10 dose

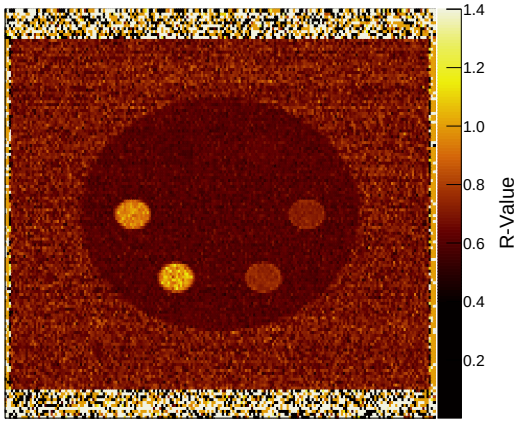

(c) Brem. Full dose

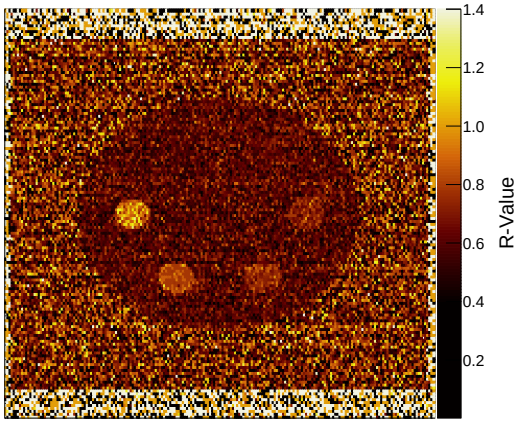

(d) Brem. 1/10 dose

Figure 4.9: R-images for the phantom geometry shown in Figure 4.7. The images acquired with the LENR beam show a higher range of R-values and thus higher contrast. This effect is exacerbated as the imaging dose is decreased. Full dose acquisitions impart 5 mrem to the cargo. The image size is 660 mm (horizontal) by 700 mm (vertical).

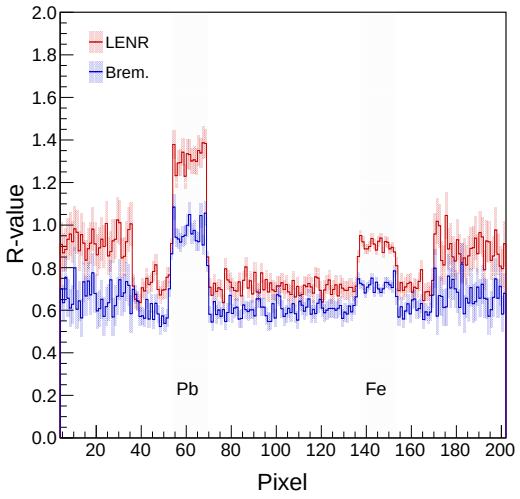

(a) Horizontal profile for the full dose images.

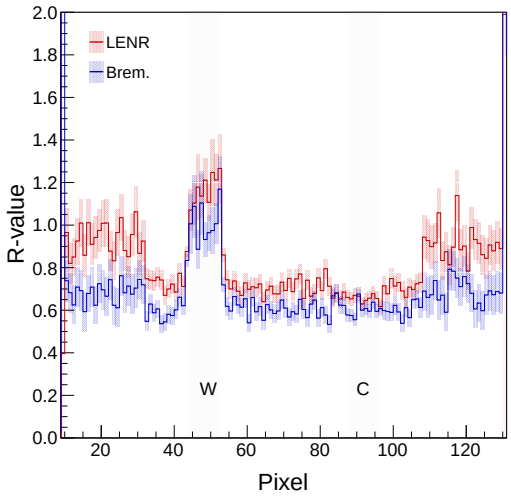

(b) Vertical profile for the full dose images.

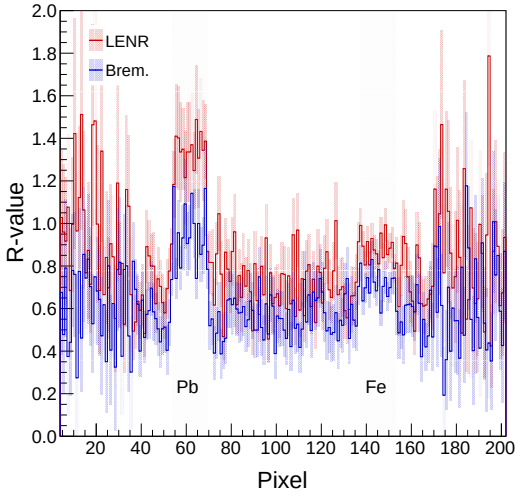

(c) Horizontal profile for the 1/10 dose images.

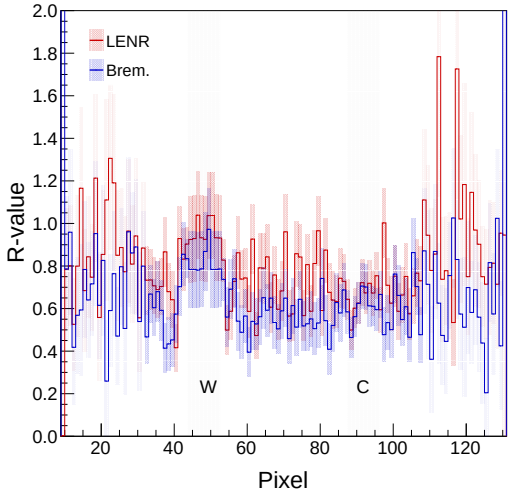

(d) Vertical profile for the 1/10 dose images.

Figure 4.10: Cross-line profiles for the full dose bremsstrahlung and LENR images shown in Figure 4.9; (a) corresponds to a horizontal line through the lead and iron rods and (b) corresponds to a vertical line through the tungsten and carbon rods. The higher inherent contrast of the LENR image is clear in both profiles, although the carbon rod cannot be discerned from the background in (b) with either beam. Pixels in horizontal profiles are 3 mm, and pixels in vertical profiles are 5.5 mm

propagation of noise on the low and high energy images, and thus is higher. The LENR method proves lower noise on the resulting R-value image for all doses.

Figure 4.12 shows the mean CNR for all six rods as the dose is changed. The LENR method outperforms the bremsstrahlung method by an average of 63% ($\pm$ 1%) for the same cargo dose. CNR is an important metric as it can dictate how detectable an object is in both human and computer vision[87, 88, 89]. A higher CNR means that a given object will stand out against the background stronger. In the context of cargo scanning, this is important because potential threats which stand out above the background level are more likely to be detected, increasing the true positive rate. Additionally, if an image has higher inherent CNR, the false positive rate can be reduced because the error margin on the threshold for a threatening object can be reduced. Effectively, this increases that threshold, leading to fewer objects being flagged as threatening.

Finally, error on the R-value for each material is measured relative to theoretical values pulled from NIST XCOM, and the results are summarized in Table 4.2. With the exception of tungsten, the two beams behaved similarly. The LENR image had 2.59 and 2.06 times as much error as the bremsstrahlung image for the high and low dose acquisitions, respectively. As shown in Table 4.2, most of the error in the LENR method arises in the high-Z rods. This stems from a much higher pair production probability for the 15.1 MeV γ-ray than with the bremsstrahlung beams. The relatively high areal densities, 193 g/cm^2 and 114 g/cm^2 for the tungsten and lead, respectively, meant that very few 15.1 MeV photons penetrated through the materials.

Pixel Similarity Based Non-Local Filtration

One advantage of using a nuclear-reaction based beam is that the high and low energy images are acquired simultaneously and the images will be perfectly registered. Although the pixel values between the low and high energy images are different, their structures are constant. This redundant structural information can be utilized to reduce noise on the

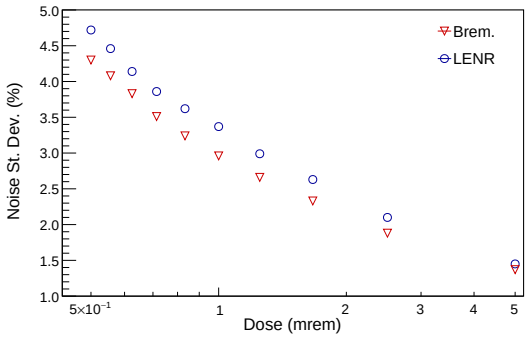

(a) Low energy transmission images.

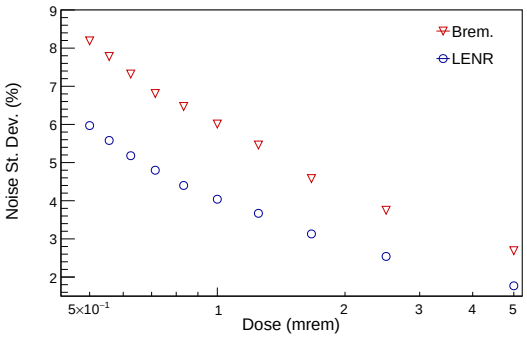

(b) High energy transmission images.

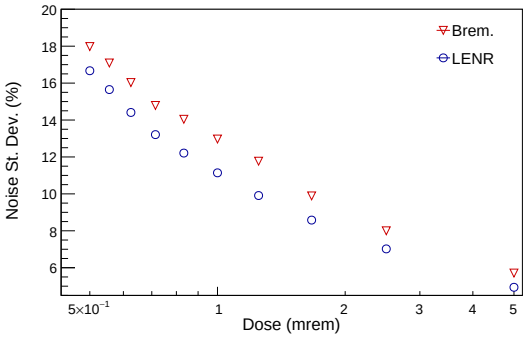

(c) R-value images.

Figure 4.11: Noise standard deviation for the material discrimination phantom as a function of dose. The noise on the low-energy transmission (a), high-energy transmission (b), and R-value image (c) are shown. As the dose is decreased, the image noise increases. The R-value image noise reflects the propagation of noise from both transmission images, and thus has the highest noise values.

Table 4.2: Material percent error for each material for each image shown in Figure 4.9. Percent error is calculated relative to predicted R-values using NIST's XCOM database for attenuation coefficients. The final row shows the root-mean-square error.

	LENR		Brem.	
Z	5 mrem	0.5 mrem	5 mrem	0.5 mrem
6	1.91 ± 0.54	2.06 ± 1.71	3.69 ± 0.57	3.28 ± 1.83
13	1.75 ± 0.42	0.02 ± 1.35	2.89 ± 0.48	5.09 ± 1.51
26	1.37 ± 0.28	1.46 ± 0.89	1.74 ± 0.35	0.94 ± 1.14
29	0.47 ± 0.30	0.27 ± 0.94	1.28 ± 0.37	0.56 ± 1.20
74	10.61 ± 1.12	33.77 ± 1.76	4.77 ± 1.35	18.85 ± 2.13
82	0.98 ± 0.57	0.22 ± 1.91	0.37 ± 0.57	0.75 ± 1.96
RMSE	4.52 ± 0.44	13.82 ± 0.72	2.87 ± 0.40	8.10 ± 0.85

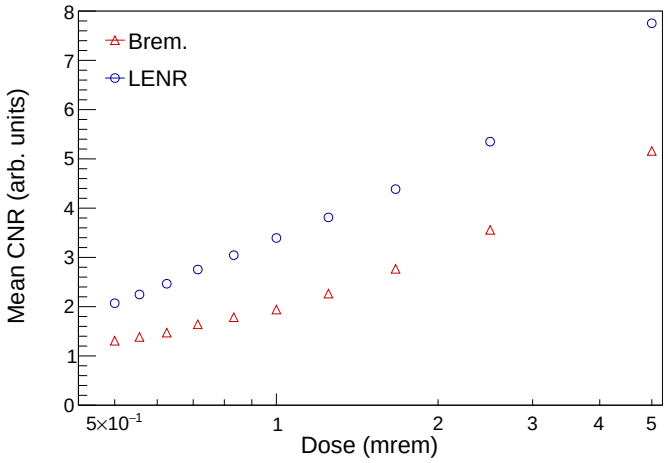

Figure 4.12: Average contrast-to-noise ratio (CNR) of all six material rods seen in Figure 4.7 as a function of dose. As dose is decreased to a minimum, the LENR beam consistently outperforms the bremsstrahlung beams. Error bars are drawn on the plot though they are smaller than the data markers.

reconstructed material images, further enhancing the usefulness of the LENR beam. Reducing final image noise allows for a potentially larger reduction in dose as the imaging noise and dose are correlated. This kind of noise suppression is also possible on interlaced bremsstrahlung images given that the low and high energy acquisitions can be spatially registered.

The R-value images shown in Figure 4.9 suffer from poor statistics, leading to high levels of pixel-to-pixel variation. This is because when the R-value images are constructed, only photons which are detected in specific energy levels are counted. Any photons outside of these energy windows are thrown out, and the dose they impart to the cargo and surroundings is essentially wasted. The information that these photons provide, however, is valuable. While the pixel values between the transmission images (energy-dependent or integrated) and R-value images may change, their structures remain constant. Thus, the integrated transmission image, which has lower noise levels than the R-value image, can be used to build a material map. An algorithm leveraging this information is presented below, and the original algorithm development can be found in References [86, 90].

The true value of an image pixel, $\vec{x}_i$, can be estimated via weighted averaging of pixels

of the same or similar materials $\vec{x}(k)$

$$\langle \vec{x}_i \rangle = \sum_{k \in N_i} w_{ik} \vec{x}_k \tag{4.5}$$

where N_i are the pixels are the same or similar materials compared to the i'th pixel and w_{ik} is the normalized weight (i.e., $\sum_{k \in N_i} w_{ik}$ = 1) quantifying the similarity between the materials of the i'th and the k'th pixels. Equation 4.5 can be written in a matrix form

$$\langle \vec{x} \rangle = W \vec{x} \tag{4.6}$$

where w_{ik} is an element of the similarity matrix W at the i'th row and the k'th column. Equation 4.6 indicates the multiplying the image vector by the similarity matrix reduces the image noise.

The similarity between two given pixels i and k in a given search window Ω_i is calculated using an empirical Gaussian model

$$s_{ik} = \begin{cases} exp(-\frac{(x_i - x_k)^2}{h^2}) & if\ |x_i - x_k| < 3h\ and\ k \in \Omega_i \\ 0 & otherwise \end{cases} \tag{4.7}$$

where s_{ik} is the similarity between pixels i and k, x_i and x_k are the measured transmission values at pixels i and k, and h is a user-determined parameter. This form of non-local filtration has been used in image processing, and can be especially useful for noise suppression when prior information is known about the structures within an image[91, 90, 92].

The strength of the noise suppression is ultimately controlled by two parameters: h and the size of Ω_i. A small value of h will lead to a tighter similarity window, and may lead to fewer pixels being included in the similarity calculation, while a larger value of h may lead to misclassification of materials. A larger Ω_i will make the noise suppression more non-local, possibly enhancing accuracy at the expense of larger computational times. In this

work, h is set as the 0.001, and Ω_i is set to a 31×31 patch, centered about pixel i. Below, this filtration technique will be applied to the images presented in the previous section. The noise suppression algorithm was implemented in Matlab.

Figure 4.13 shows the noise suppressed R-value images and Figure 4.14 shows the corresponding cross line profiles. The noise suppression method is effective for both bremsstrahlung and LENR acquisitions. At low dose, the noise suppression is stronger for the LENR image. Additionally, because of the lower inherent contrast in the bremsstrahlung images, the carbon rod is largely missed in the pixel similarity calculation, as shown specifically by insets (b) and (d) of Figure 4.14. At lower dose, an artifact can be seen on the tungsten and lead rods. The pixel values are pulled closely together as the spacing between given pixels decreases, and this leads to the slanting line profiles on the rods seen in Figure 4.14 (c) and (d).

Figure 4.15 shows the noise reduction and mean CNR on the noise suppressed images as a function of imaging dose. Noise reduction factor is simply $\sigma_{noisy}/\sigma_{suppressed}$. The noise suppression gets stronger for the LENR image as dose is decreased, leading to similar levels of noise on the final image. The bremsstrahlung, however, is relatively constant, leading to reduced efficacy of the noise suppression algorithm at lower dose. This is due to the higher inherent contrast levels of the LENR imaging source. As dose gets low, image noise grows, and low contrast objects are lost in the noise, as shown in Figure 4.10. Tables 4.3 and 4.4 show the same metrics shown in Tables 4.1 and 4.2 but on the noise suppressed images. After noise reduction, the LENR images show improvement in CNR over the bremsstrahlung images by factors of 3.58 and 9.41 while adding little error to the original image. This improvement in CNR can lead to better detection of small objects and potential threats in the context of cargo scanning, making the LENR source more reliable for imaging.

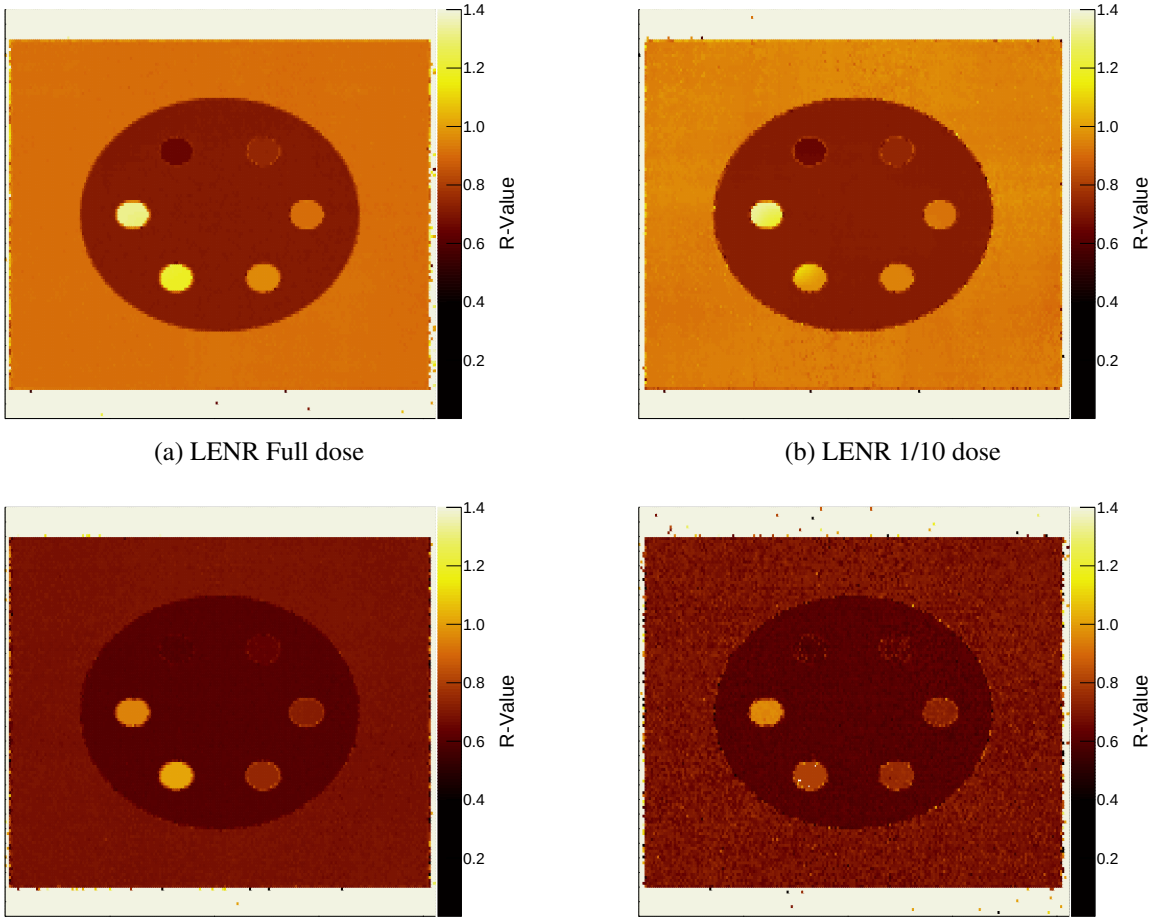

(a) LENR Full dose

(b) LENR 1/10 dose

(c) Brem. Full dose

(d) Brem. 1/10 dose

Figure 4.13: R-images for the phantom geometry shown in Figure 4.7 after noise suppression. At low dose, the noise suppression is stronger on the LENR image, shown by the lower noise STD in the background of the image. All six rods clearly stand out on the LENR image, while the carbon rod is very similar to the water region in the bremsstrahlung images. An artifact can be seen on the low-dose LENR image where the tungsten and lead pixels that are close spatially both get included in the similarity calculation. The image size is 660 mm (horizontal) by 700 mm (vertical).

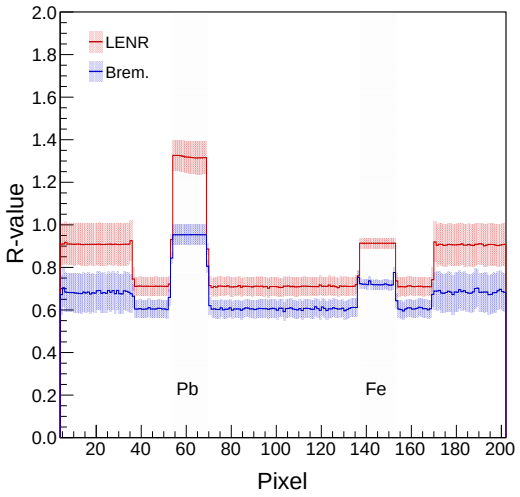

(a) Horzontal profile for the full dose images.

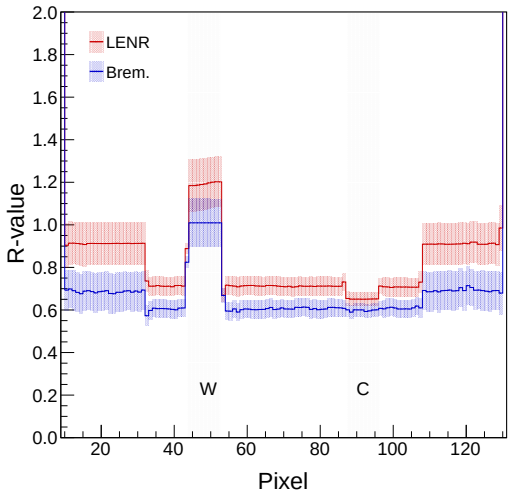

(b) Vertical profile for the full dose images.

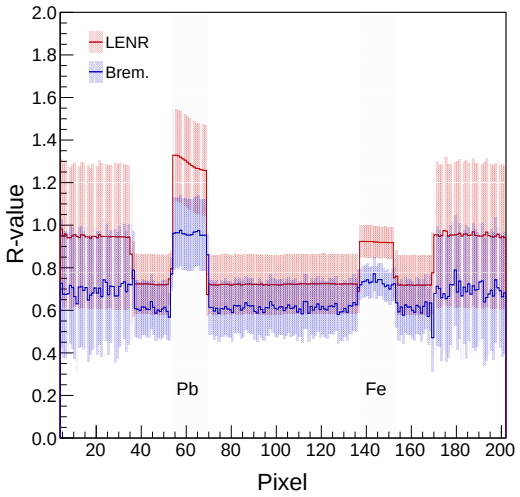

(c) Horzontal profile for the 1/10 dose images.

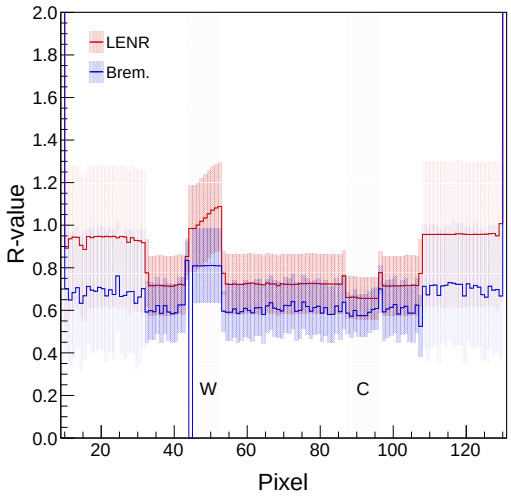

(d) Vertical profile for the 1/10 dose images.

Figure 4.14: Cross-line profiles for the full dose bremsstrahlung and LENR images shown in Figure 4.13. The noise suppression greatly improves the noise features of the profiles, and all materials stand out better than in Figure 4.10. The carbon rod is still mostly on the bremsstrahlung images. Note that the noise suppression method reduces the noise standard deviation but does not greatly impact the measurement uncertainty. At low dose, one pixel in the tungsten rod profile has an R-value of zero, due to no high-energy transmission. Pixels in horizontal profiles are 3 mm, and pixels in vertical profiles are 5.5 mm.

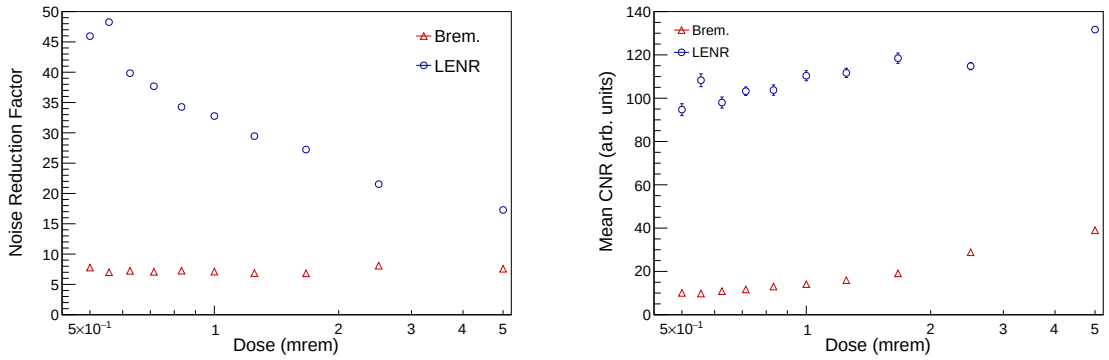

(a) (b)

Figure 4.15: (a) shows the noise reduction factor for both bremsstrahlung and LENR generated images as a function of dose is shown in the left. As the dose gets lower, noise suppression gets stronger for the LENR beam, keeping the image noise level relatively constant. (b) shows the mean contrast-to-noise ratio for the six rods in each noise-suppressed image, as function of dose. Although the CNR for the LENR does decrease with dose, it remains around a factor of 10 higher than the CNR achieved with the bremsstrahlung imaging source.

Table 4.3: CNR for each material in the images shown in Figure 4.13.

	LENR		Brem.	
Z	5 mrem	0.5 mrem	5 mrem	0.5 mrem
6	29.12 ± 1.80	26.63 ± 4.87	2.24 ± 0.83	0.03 ± 0.85
13	14.58 ± 1.61	10.40 ± 4.37	6.51 ± 0.74	1.83 ± 0.76
26	97.97 ± 1.36	81.41 ± 3.73	25.64 ± 0.62	8.91 ± 0.65
29	121.63 ± 1.47	93.83 ± 3.90	30.73 ± 0.66	10.84 ± 0.70
74	232.95 ± 6.73	124.24 ± 9.68	90.73 ± 2.92	13.16 ± 1.50
82	293.85 ± 4.21	231.77 ± 10.20	78.12 ± 1.24	25.66 ± 1.41
Mean	131.68 ± 1.42	94.71 ± 2.74	39.00 ± 0.58	10.07 ± 0.42

Table 4.4: Material percent error for each material for each image shown in Figure 4.13. The final row shows the root-mean-square error.

	LENR		Brem.	
Z	5 mrem	0.5 mrem	5 mrem	0.5 mrem
6	2.27 ± 0.58	1.24 ± 1.71	2.99 ± 0.57	1.25 ± 1.84
13	1.55 ± 0.49	0.63 ± 1.34	2.46 ± 0.48	3.07 ± 1.53
26	1.32 ± 0.36	0.45 ± 0.91	1.61 ± 0.35	0.36 ± 1.15
29	0.53 ± 0.38	1.65 ± 0.92	1.35 ± 0.37	0.39 ± 1.21
74	11.35 ± 1.44	29.39 ± 1.76	4.81 ± 1.35	21.97 ± 2.13
82	1.07 ± 0.90	3.37 ± 1.85	0.47 ± 0.57	0.62 ± 2.00
RMSE	4.82 ± 0.57	12.11 ± 0.71	2.67 ± 0.43	9.07 ± 0.86

Full-Scale Cargo Simulation

The final imaging test in this work is simulation of a full-scale cargo container which can be seen in Figure 4.16. The data are taken with a fan-beam with a half-fan angle of 30° (the same geomtery shown in 2.6). Rather than simulating a beam that is divergent horizontally, the source was approximated as planar in the horizontal dimension, with a width of 6 mm. The container walls are 5 mm of stainless steel. The container is stepped through the imaging system in 6-mm steps, and 580 detectors are used. Due to limited computational time, only one detector array is simulated, as opposed to the staggered sub-array approach used in previous simulations. Vertical tungsten collimators are placed on both sides of the detector array. The collimators extend 30 cm from the detector face. The dose to the cargo, based on the average cargo used in Chapter 2 is set to 500 mrem for this simulation. There are various objects placed inside the container to be used for characterizing the beams, and Figure 4.17 shows some more details of each of this objects. The reasons for including each of these objects will explained below, starting from the left and moving right.

The molybdenum and aluminum hollow rods are in place to provide a qualitative comparison of spatial resolution between the two imaging beams. Molybdenum should be a high-contrast material in both the transmission and R-value images. The aluminum should be low contrast in the transmission image. The rods of varying material will characterize

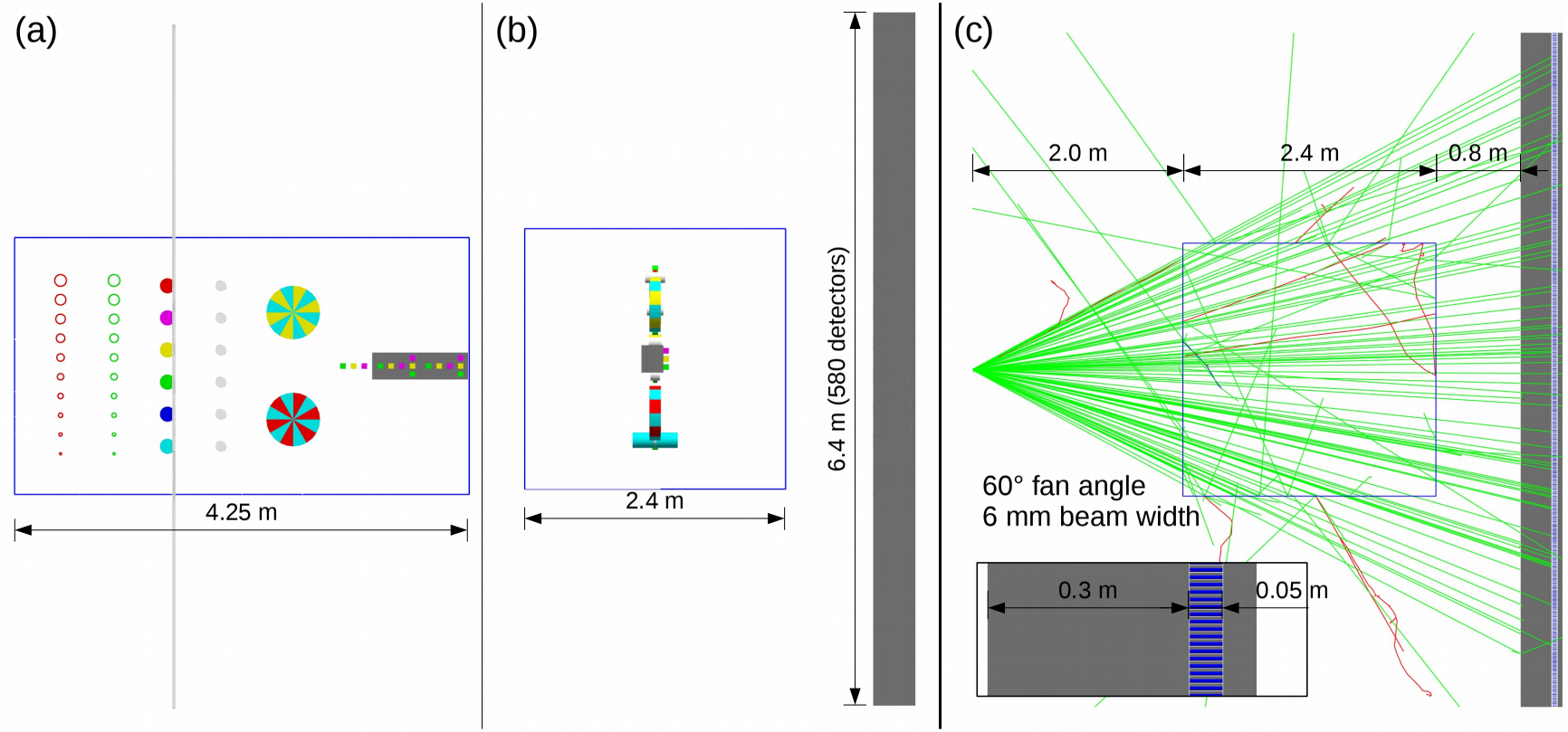

Figure 4.16: Geant4 geometry for the full-scale cargo container simulation. (a) shows a straight-on view of the container, where the beam would be coming out of the paper. The gray line behind the container is the detector array. (b) shows a side-view where the beam would be incident from the top of the screen. (c) shows a view perpindicular to the fan-beam without the contents of the container for clarity. One of the tungsten collimators is not drawn so that the detectors can be seen, and the insert highlights the detector array. The various colors represent different materials in the phantom.

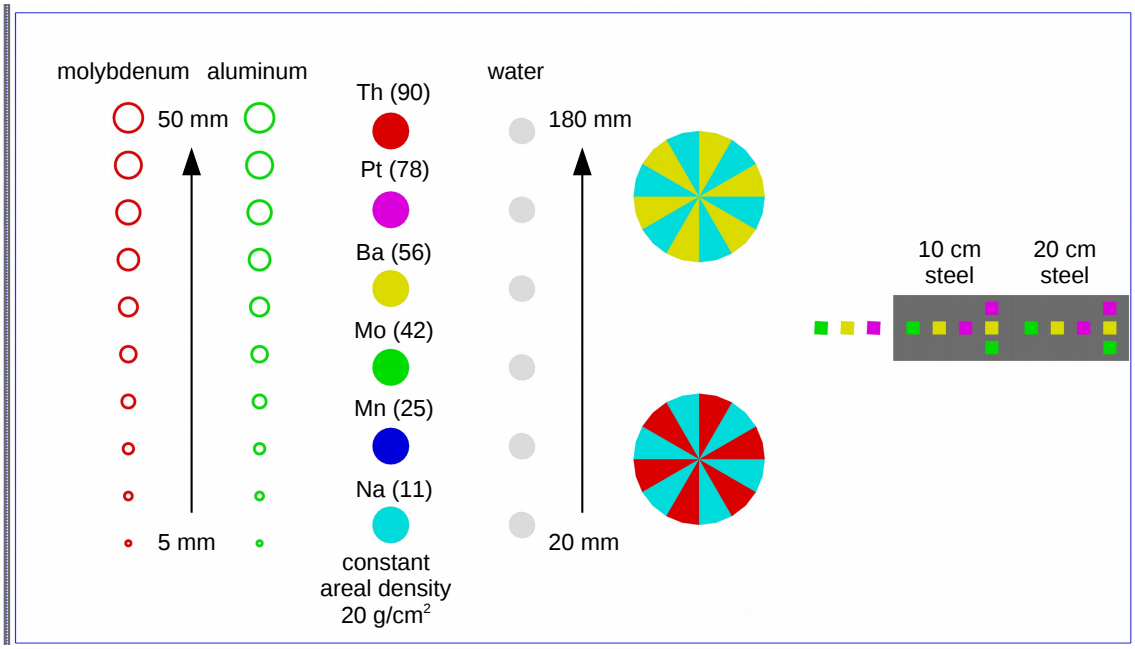

Figure 4.17: Annotated Geant4 geometry for the full-scale container simulation. The circles on the left will show spatial resolution for the system, as will the alternating-color cylinders. The rods of varying materials will help to characterize the performance of the R-value reconstruction. The silver rods are actually air pockets in a "water" tank which will test the sensitivity of the imaging system. The multi-color blocks to the right of the image show the effects that beam attenuation has on contrast and R-value calculation.

the material discrimination of each beam, much like the results presented in the previous section. These rods have a constant areal density, so they should all look similar on the transmission image. The gray cylinders next to the material rods are air pockets inside a 50 cm thick water tank (not shown here). These will test the beams for sensitivity to different areal densities. They increase in thickness from 2 cm to 18 cm moving from bottom to top. The two phantoms next to the air pockets are another qualitative spatial resolution test. The cyan material in both wheels is stainless steel. Similar to the hollow circles one of the materials, tungsten (red), is meant to be high-contrast, and the other, copper (yellow), is meant to be low contrast. Finally, the three repeated blocks to the right are low-Z, mid-Z, and high-Z materials. This series of tests is meant to show the effects that cargo thickness has on material accuracy, as well as contrast and spatial resolution. The blocks are situated behind the 10 cm and 20 cm steel plates are arranged horizontally and vertically to test the effects of in-beam scattering.

Full Results

Figure 4.18 shows the transmission images of the full cargo container, Figure 4.19 shows the raw R-value images, and Figure 4.20 shows the noise suppressed R-value images, using the noise suppression method outlined in the previous section. The regions of the image containing the floor and ceiling of the container have been clipped for visualization. Immediately, the higher contrast of the LENR beam can be seen on the transmission and R-value images. Additionally, the stainless steel plates on the right side of the R-value images appear to have different values although they are the same material as the background, an effect of beam hardening. The sodium rod is also distorted, an effect of the fan-beam acquisition. The full simulation corresponds to an image size of 6.4 m vertically by 4.2 m horizontally at the detectors. In sum, 580 detectors were used, with a diameter of 6 mm each and a detector-to-detector spacing of 5 mm, and the cargo was stepped through the system in 6-mm increments. The zoomed-in images in Figs. 4.18, 4.19, and 4.20 are 272

Table 4.5: Run times for each slice of the full-scale container simulation. Each slice was run with 16 threads.

Beam	Average Time (hr)
6 MV Brem.	11.01 ± 6.29
9 MV Brem.	11.40 ± 4.52
LENR	25.16 ± 4.58

pixels vertically by 694 pixels horizontally, corresponding to an image height and width of 1.81 m (at the center of the container) and 4.16 m. 716 image slices were generated (including 16 for flatfield measurements), and the average run time per slice for each beam is listed in Table 4.5.

Hollow Circles

Figure 4.21 shows the vertical line profile through the center of the molybdenum and aluminum hollow cylinders. This provides a similar measure of spatial resolution to that presented above. The 5 mm holes cannot be resolved for either material by either beam. Both beams can discern the molybdenum rods for every cylinder larger than 1 mm, but the LENR provides a higher inherent contrast, and thus it is easier to pick out the rods against the background. The bremsstrahlung beam can barely discern any of the aluminum rods due to the low CNR. Figure 4.22 shows the line profile through the hollow circles for the noise suppressed R-value image. By suppressing the background noise, the aluminum rods stand out stronger with both beams, effectively enhancing the low-contrast spatial resolution.

Contrast Rods

Figure 4.23 shows the vertical projection through the center of the contrast rods for the transmission images and Figure 4.24 shows the original and noise suppressed R-value projections. The six materials can all be discerned from the background. There is no contrast present for the manganese circle (Z of 25) on the R-value image, but an object can be seen there due to the lower pixel variance within the rod. The sodium rod is very blurred because

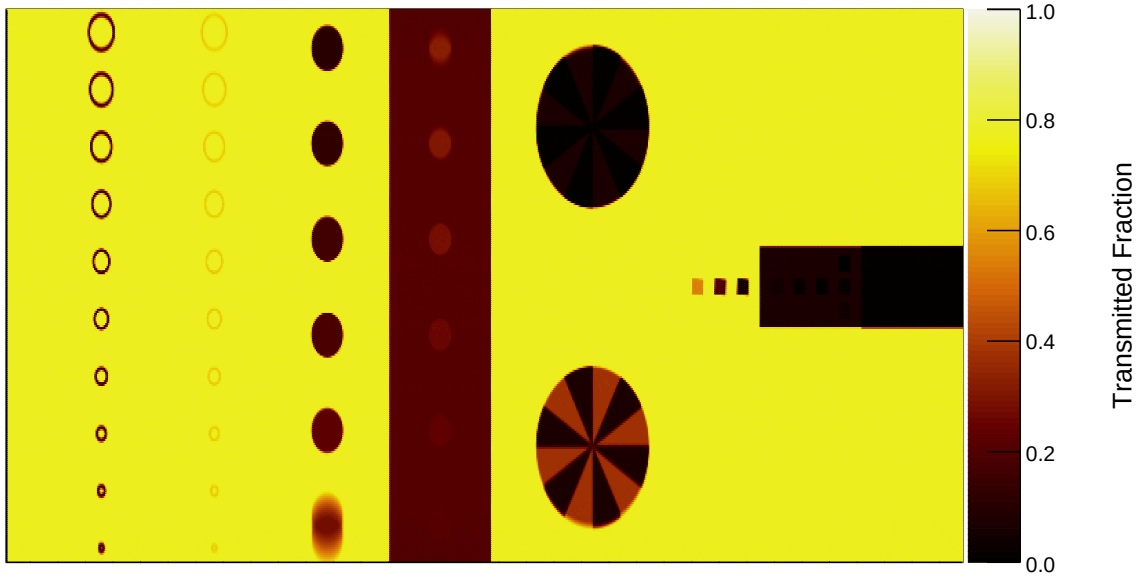

(a) LENR total transmission

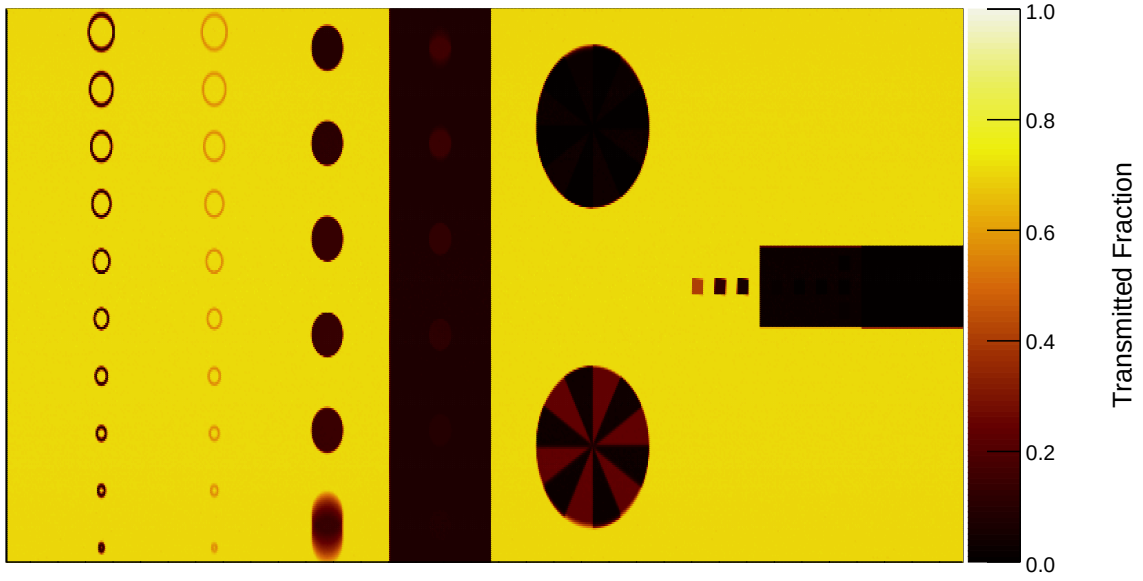

(b) Brem total transmission

Figure 4.18: Transmission images for the full-scale cargo container simulation. The structural information in these images will be used for noise suppression on the R-value images. The image size is 4.16 m (horizontally) by 1.81 m (vertically) at the center of the container.

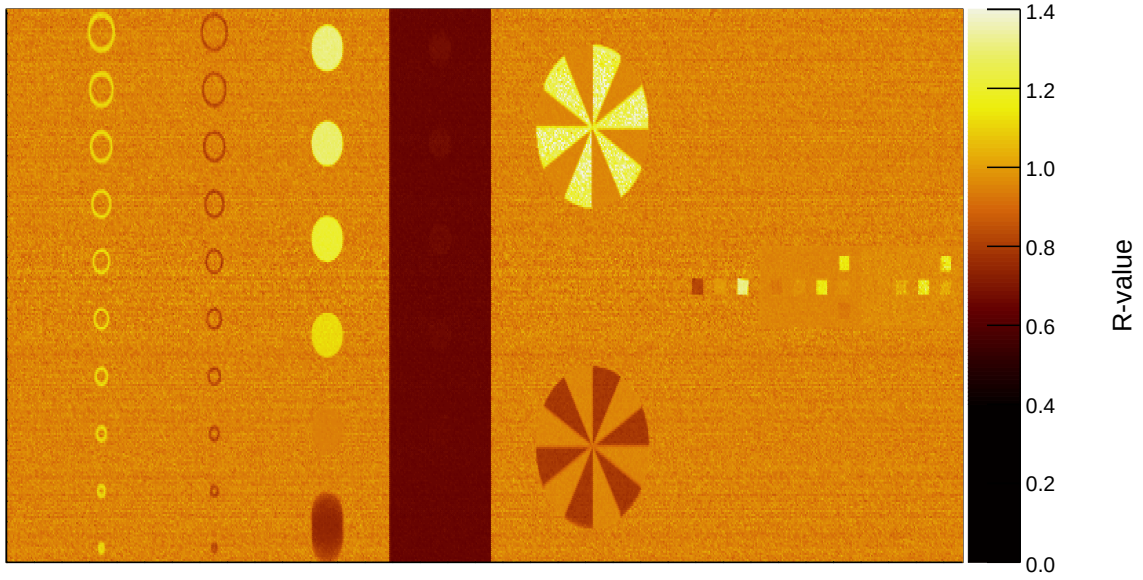

(a) LENR R-value

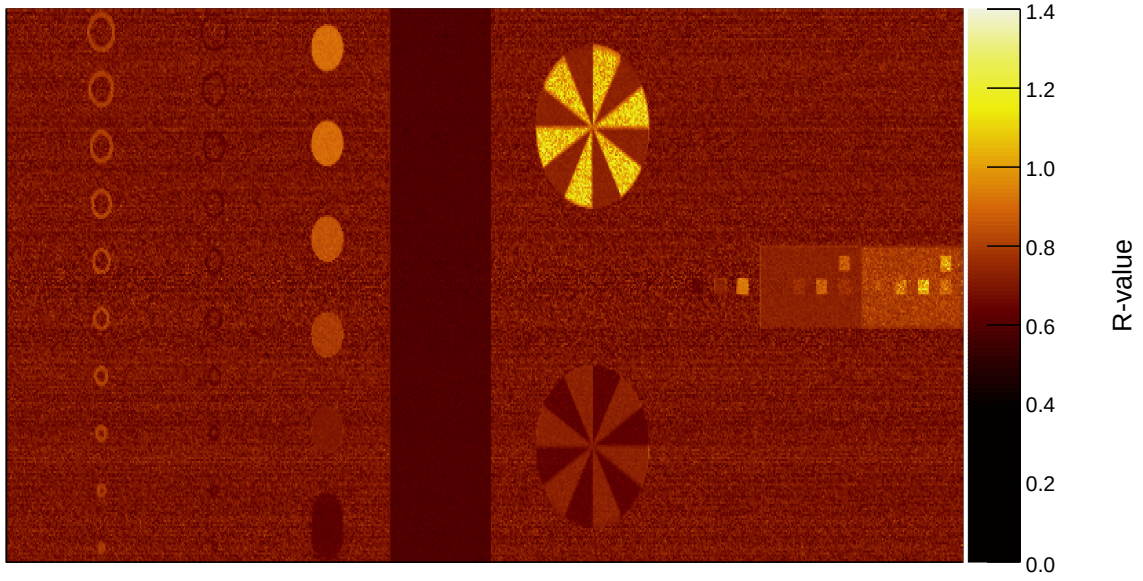

(b) Brem R-value

Figure 4.19: Raw R-value images of the full-scale container simulation. As with the small-scale container, the LENR beam provides higher contrast and lower noise levels. The image size is 4.16 m (horizontally) by 1.81 m (vertically) at the center of the container.

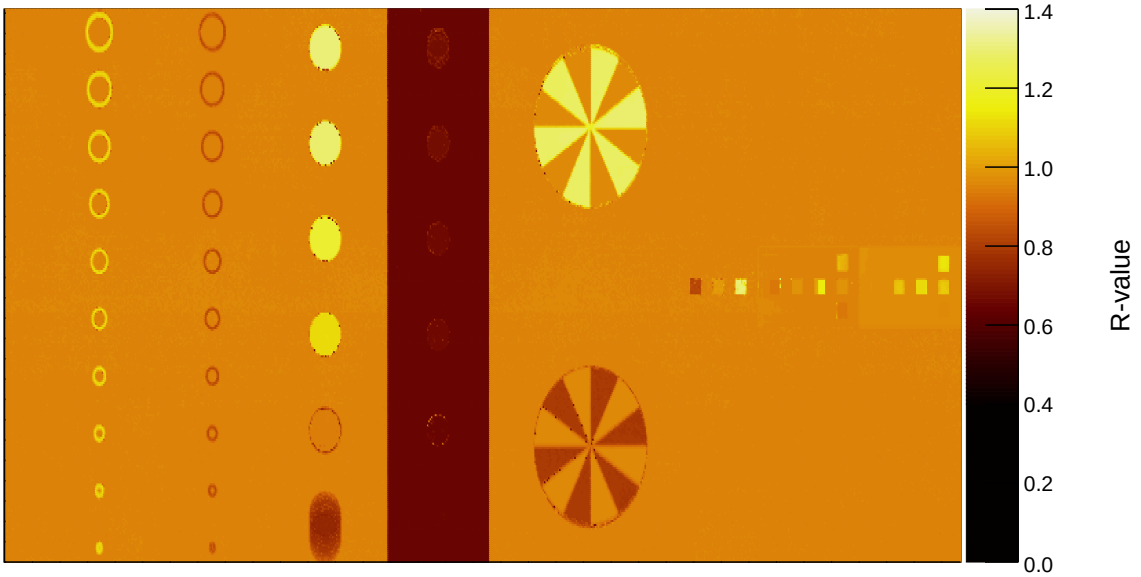

(a) LENR R-value

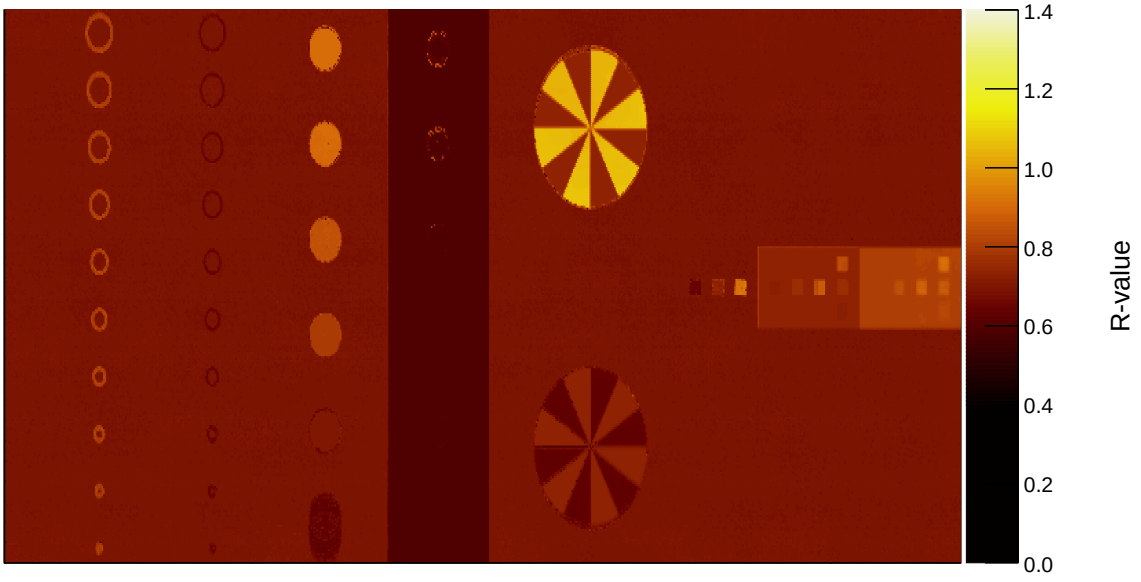

(b) Brem R-value

Figure 4.20: Noise suppressed R-value images. The noise suppression algorithm works well for this container with the exception of a few misclassifications at material interfaces, especially for the air pockets in the center of the image. The image size is 4.16 m (horizontally) by 1.81 m (vertically) at the center of the container.

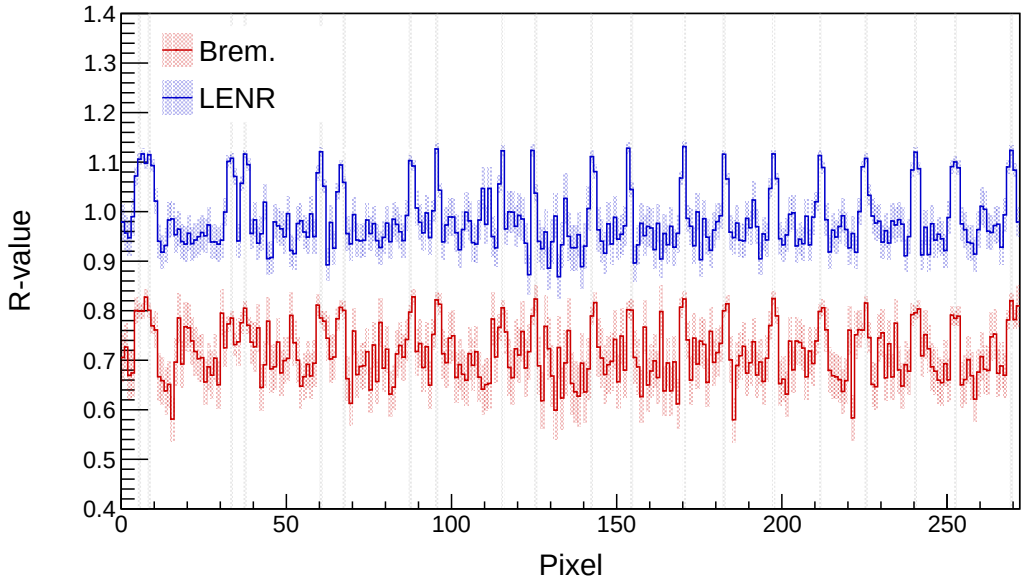

(a) Molybdenum Circles

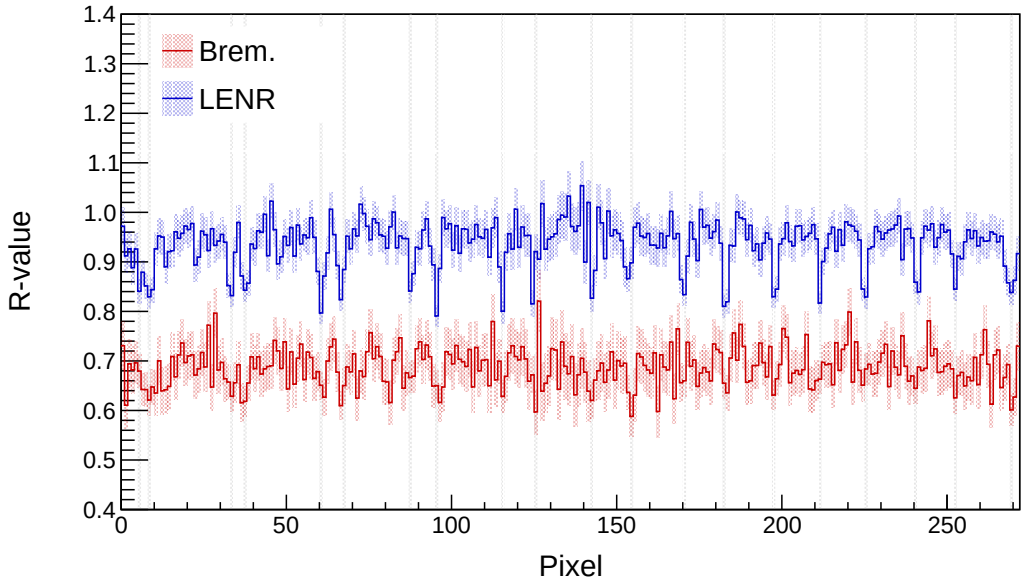

(b) Aluminum Circles

Figure 4.21: Vertical projections through the hollow circles of the cargo container image. (a) shows the projection through the molybdenum circles, where both beams can distinguish all of the circles except for the smallest one. (b) shows the projection through the aluminum circles, where the bremsstrahlung beam can hardly distinguish any of the circles due to the low contrast and high noise present in the image. The grey lines show the true location of the edges of the hollow circles. Each pixel is 6.64 mm.

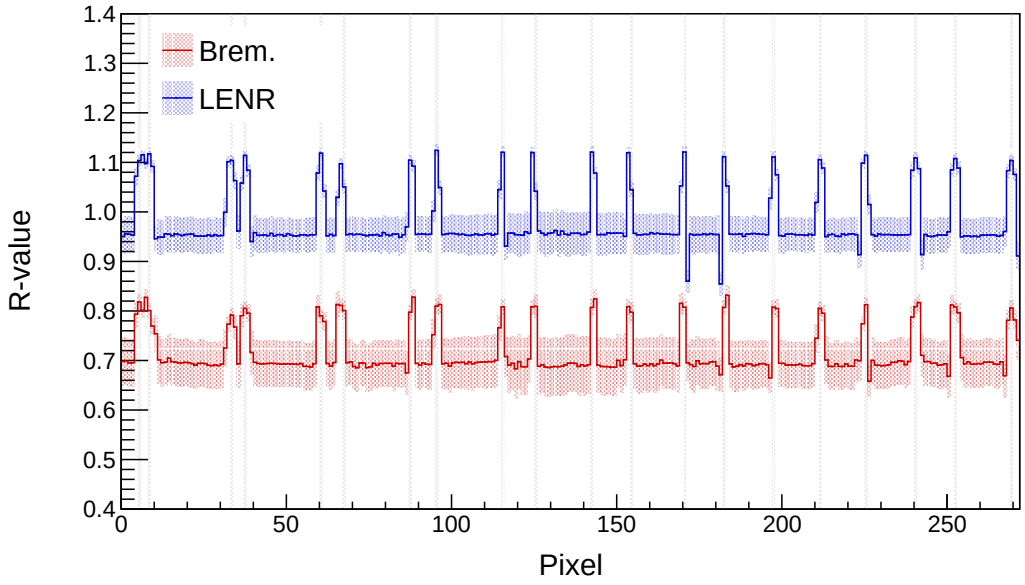

(a) Molybdenum Circles

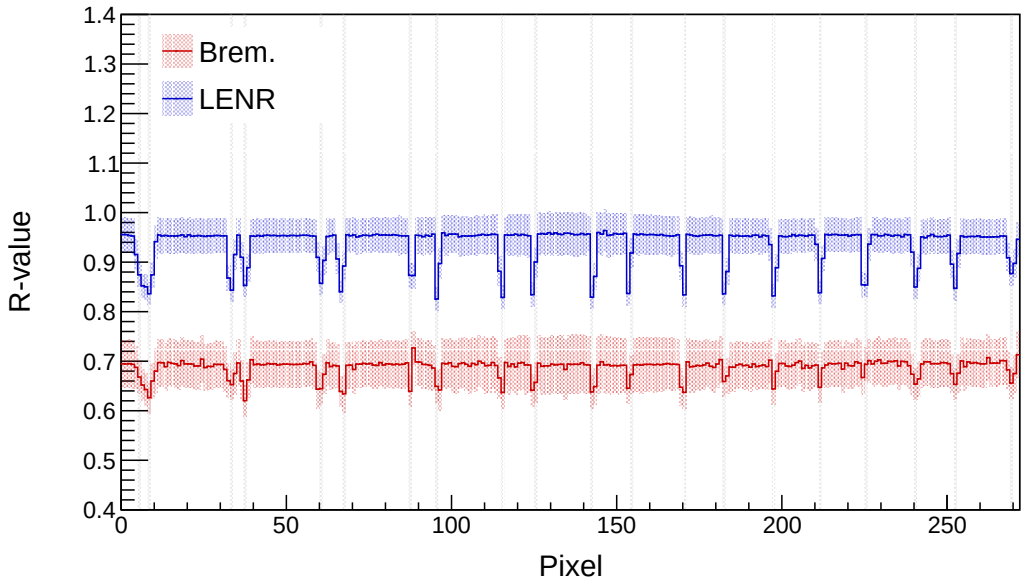

(b) Aluminum Circles

Figure 4.22: Vertical projections through the hollow circles of the cargo container image. (a) shows the projection through the molybdenum circles and (b) shows the projection through the aluminum circles. The lower background noise levels allows all of the circles to stand out in this projection, effectively enhancing the spatial resolution, especially for lower contrast materials such as the aluminum. Each pixel is 6.64 mm.

Table 4.6: CNR for the contrast rods in the full-container image.

Material (Z)	Original		Noise Suppressed	
	Brem.	LENR	Brem.	LENR
Na (11)	2.70 ± 0.02	7.01 ± 0.21	23.46 ± 0.02	104.76 ± 0.29
Mn (25)	0.42 ± 0.02	0.18 ± 0.20	4.76 ± 0.02	4.49 ± 0.27
Mo (42)	2.00 ± 0.02	5.88 ± 0.25	21.40 ± 0.02	89.41 ± 0.35
Ba (56)	3.47 ± 0.02	9.20 ± 0.26	37.16 ± 0.02	141.74 ± 0.37
Pt (78)	4.83 ± 0.02	12.07 ± 0.23	50.85 ± 0.02	184.88 ± 0.34
Th (90)	4.98 ± 0.02	12.72 ± 0.25	52.58 ± 0.02	196.55 ± 0.37
Mean	3.07 ± 0.01	7.84 ± 0.01	31.70 ± 0.10	120.31 ± 0.14

Table 4.7: Mean values and percent error for the contrast rods in the full-container image.

Material (Z)	Mean		Percent Error	
	Brem.	LENR	Brem.	LENR
Na (11)	0.62 ± 0.00	0.76 ± 0.00	4.11 ± 0.11	3.27 ± 0.06
Mn (25)	0.71 ± 0.00	0.95 ± 0.00	1.89 ± 0.09	0.02 ± 0.05
Mo (42)	0.80 ± 0.00	1.11 ± 0.00	0.16 ± 0.11	1.65 ± 0.06
Ba (56)	0.85 ± 0.00	1.21 ± 0.00	0.43 ± 0.11	1.56 ± 0.06
Pt (78)	0.90 ± 0.00	1.29 ± 0.00	0.88 ± 0.09	0.00 ± 0.05
Th (90)	0.91 ± 0.00	1.31 ± 0.00	2.69 ± 0.09	1.24 ± 0.05
RMSE			2.19 ± 0.05	1.70 ± 0.02

of its length and because it is at the bottom of the container, so the photons pass through it obliquely. This is not observed on the thorium rod because it is much thinner than the sodium rod (1.7 cm vs 20.3 cm). The corresponding CNR for each rod in the R-value images can be seen in Table. 4.6. For this CNR, the background was taken over 104,000 pixels throughout various portions of the image. The large amount of pixels involved in the calculation leads to a very stable estimate of the mean and noise STD. With the exception of the manganese, the LENR beam outperformed the bremsstrahlung beams on all rods, averaging 3.12 times higher CNR across all rods on the raw data and 3.80 times higher on the noise suppressed data. The two methods perform similarly with respect to error, with the LENR having a slightly lower RMSE for all rods, as shown by Tables 4.7 and 4.8.

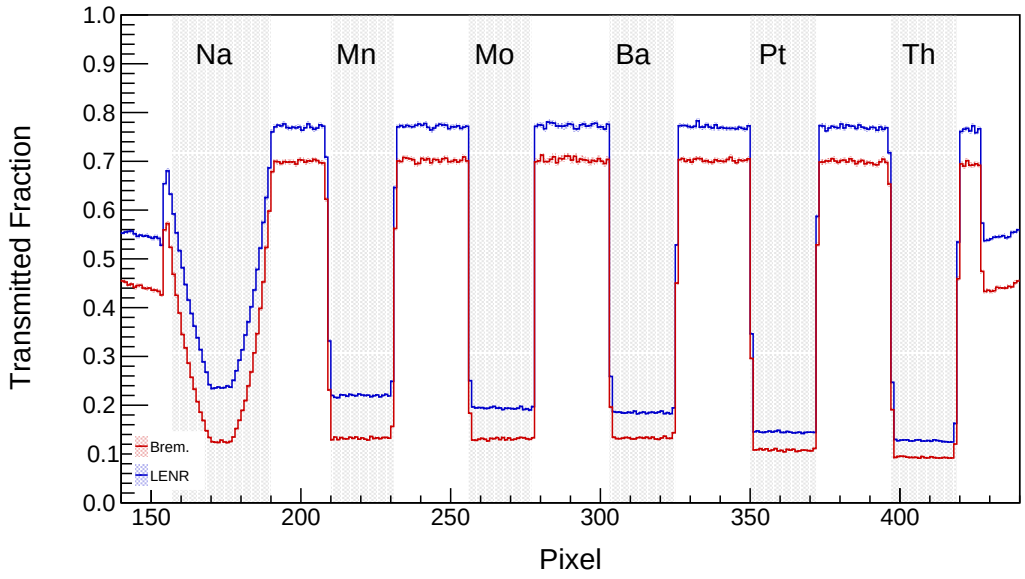

(a) Low Energy Transmission

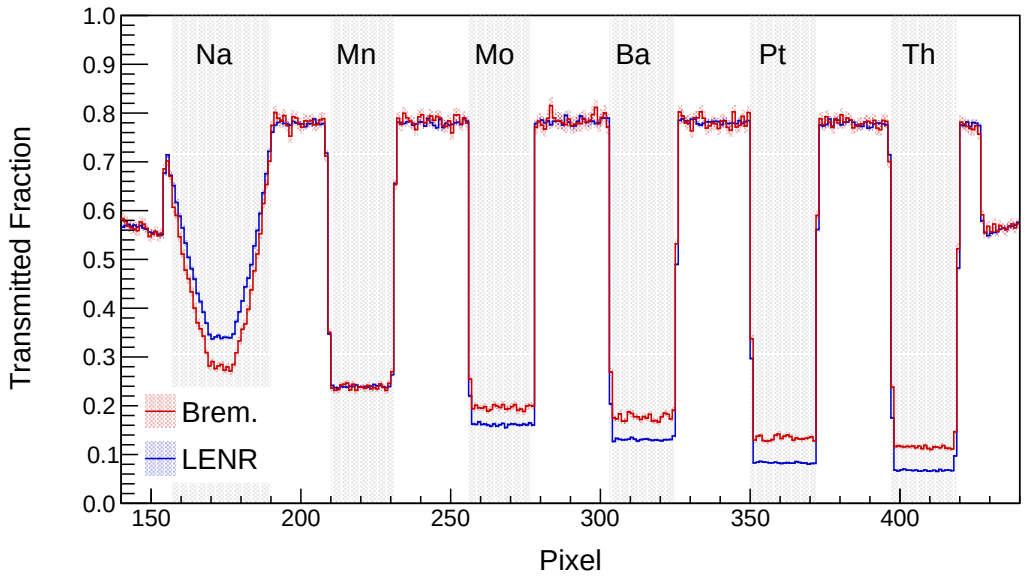

(b) High Energy Transmission

Figure 4.23: Vertical projections through the contrast rods for the (a) low-energy transmission and (b) high-energy transmission. All six rods easily stand out on all images, although there is significant blurring for the sodium rod. Each pixel is 6.64 mm.

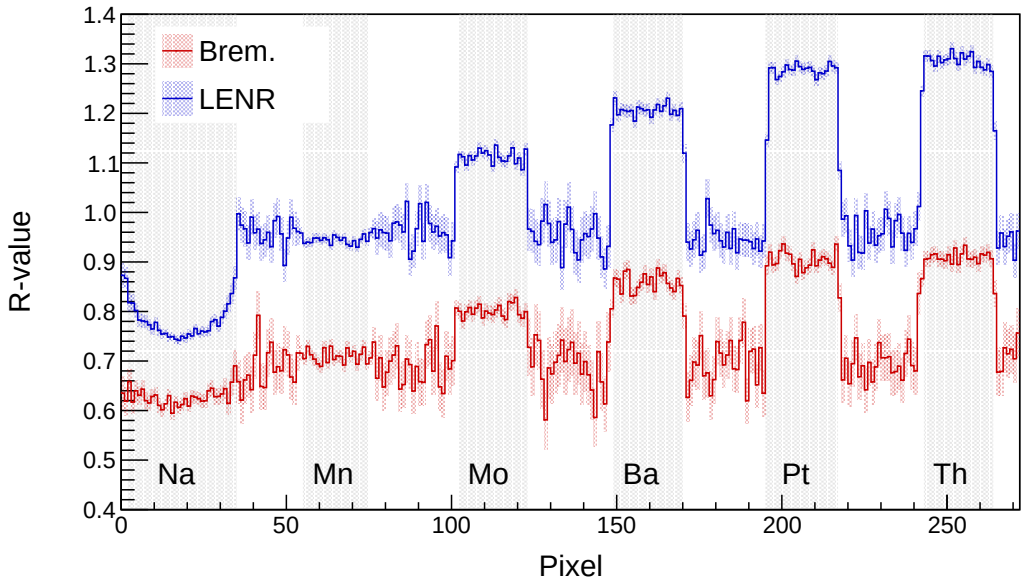

(a) Original

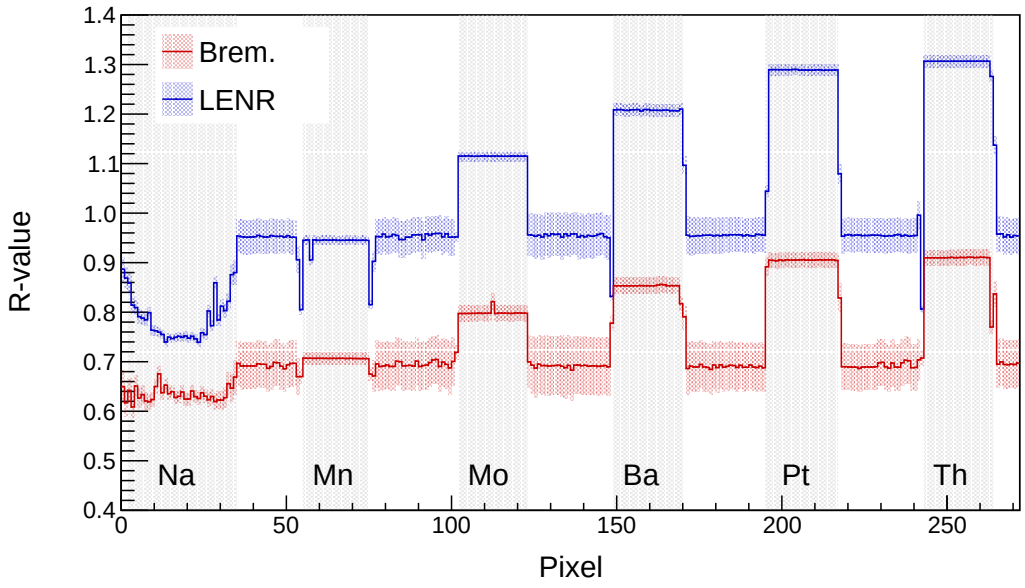

(b) Noise Suppressed

Figure 4.24: Vertical projections through the contrast rods for the (a) original and (b) noise suppressed R-value images. All six rods easily stand out on all images, although the LENR rods have higher contrast on the R-value image. Each pixel is 6.64 mm.

Table 4.8: Mean values and percent error for the contrast rods in the full-container image after noise suppression.

Material (Z)	Mean		Percent Error	
	Brem.	LENR	Brem.	LENR
Na (11)	0.64 ± 0.00	0.76 ± 0.00	1.06 ± 0.11	2.44 ± 0.06
Mn (25)	0.71 ± 0.00	0.94 ± 0.00	1.97 ± 0.09	0.31 ± 0.05
Mo (42)	0.80 ± 0.00	1.11 ± 0.00	0.07 ± 0.11	1.40 ± 0.06
Ba (56)	0.85 ± 0.00	1.21 ± 0.00	0.31 ± 0.11	1.49 ± 0.06
Pt (78)	0.90 ± 0.00	1.28 ± 0.00	1.37 ± 0.09	0.24 ± 0.05
Th (90)	0.91 ± 0.00	1.31 ± 0.00	3.11 ± 0.09	1.24 ± 0.05
RMSE			1.67 ± 0.04	1.41 ± 0.02

Air Pockets

Figure 4.25 shows the vertical projection through the center of the air pockets in the water portion of the container. This slice tests the sensitivity of each imaging beam to small perturbations in Z_{eff} of the material. All of the pockets can be seen in the transmission projections, but most are not seen in the R-value image. The thickest two rods can be seen on the LENR image before noise suppression. After noise suppression, more of the pockets are seen on the LENR image, although the mislcassification rate is higher for this data than for the previous data shown. The small contrast present on this slice proves a challenge for the noise suppression algorithm. Table 4.9 shows the mean R-value in each rod, as well as the percent error using the expected R-value based on data from NIST XCOM. Table 4.10 shows the same data for the noise suppressed images. Both methods perform consistently with respect to error, but the LENR image does show a change in mean R-value at the thickest two pockets, while the bremsstrahlung image produces the same R-value for all pockets. Noise suppression produces a slight decrease in error and slightly enhances the R-value for the longer rods.

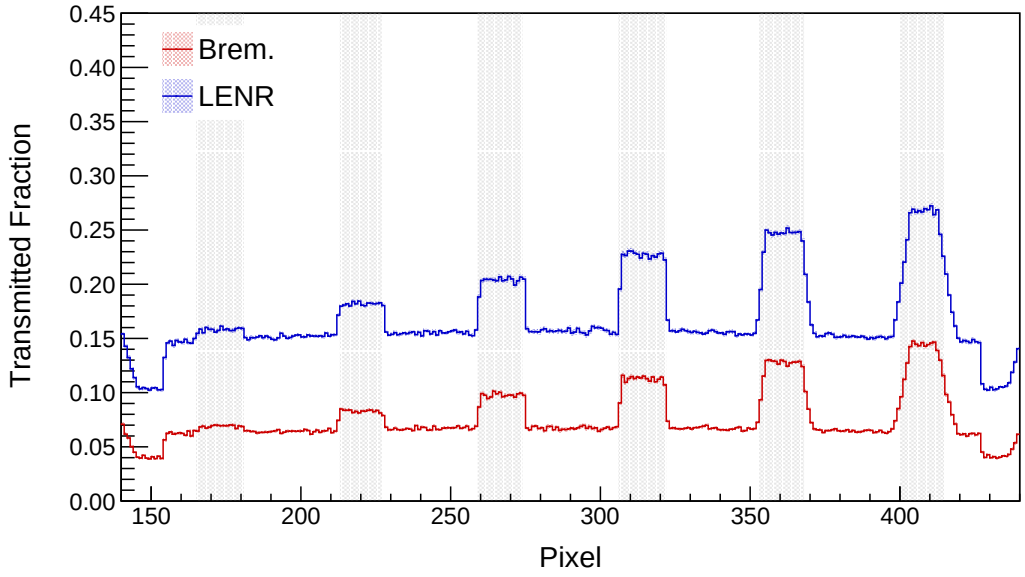

(a) Low Energy Transmission

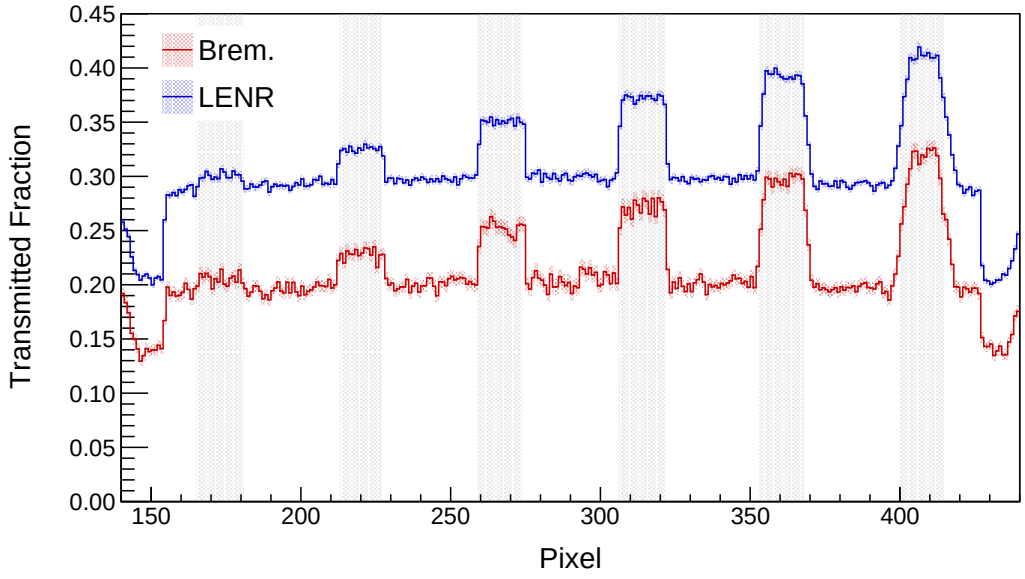

(b) High Energy Transmission

Figure 4.25: Vertical projections through the air pockets in the water tank for the (a) low-energy transmission and (b) high-energy transmission. Each pixel is 6.64 mm.

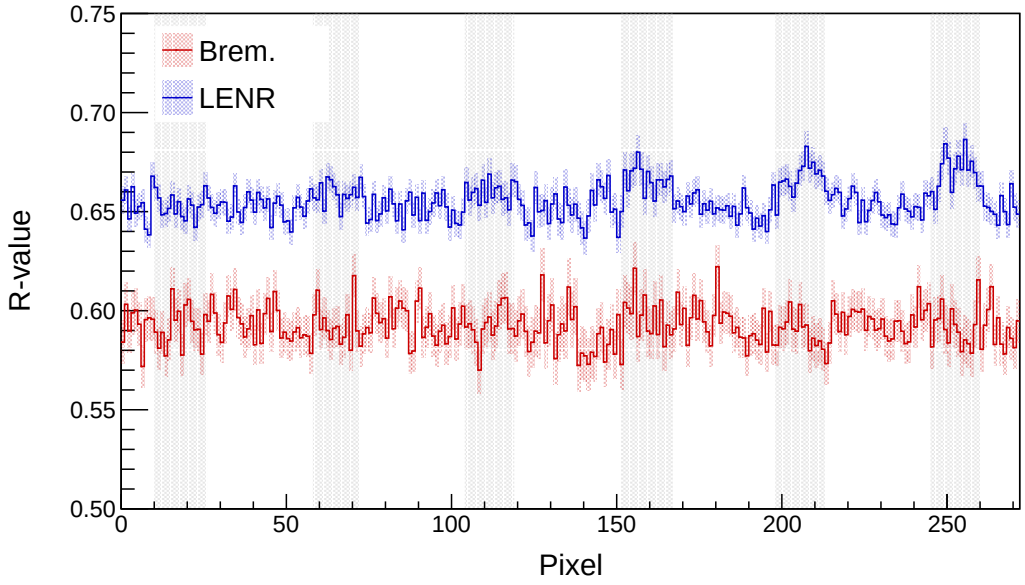

(a) Original

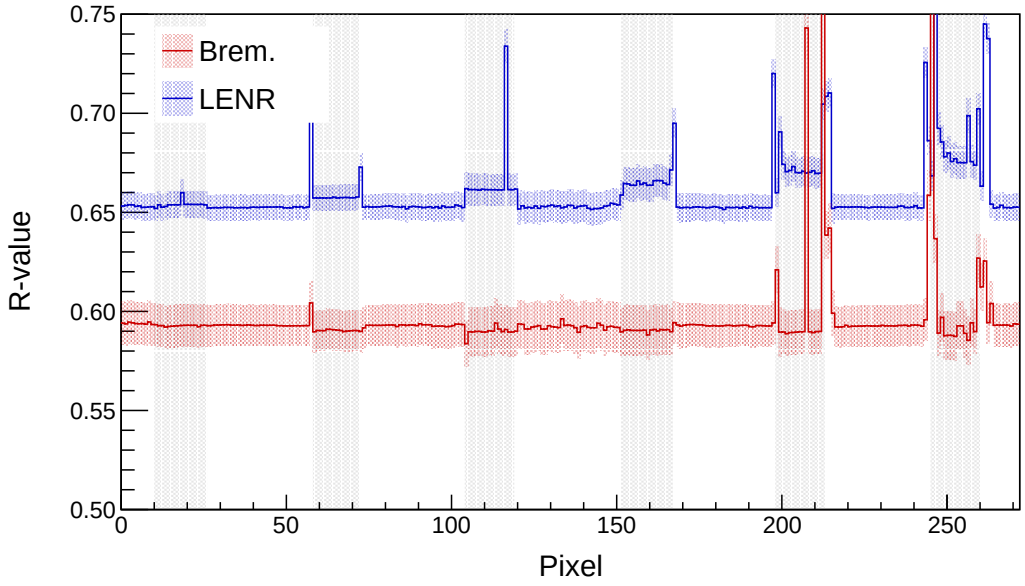

(b) Noise Suppressed

Figure 4.26: Vertical projections through the air pockets for the (a) original and (b) noise suppressed R-value images. Although all of the pockets stand out on the transmission images, only the thickest ones stand out on the R-value LENR images. After noise suppression, more of the pockets are visible on the projection, but the misclassification rate is high for this data, shown by the very high valued pixels within each pocket and on the edges of the pockets. Each pixel is 6.64 mm.

Table 4.9: Mean values and percent error for the air pockets in the full-container image.

Pocket Thickness (cm)	Mean		Percent Error	
	Brem.	LENR	Brem.	LENR
2.0	0.59 ± 0.00	0.65 ± 0.00	2.30 ± 0.19	3.62 ± 0.10
5.2	0.59 ± 0.00	0.66 ± 0.00	2.79 ± 0.18	3.73 ± 0.10
8.4	0.59 ± 0.00	0.66 ± 0.00	3.06 ± 0.21	3.59 ± 0.12
11.6	0.59 ± 0.00	0.66 ± 0.00	3.45 ± 0.22	3.82 ± 0.13
14.8	0.59 ± 0.00	0.67 ± 0.00	3.55 ± 0.19	3.72 ± 0.11
18.0	0.59 ± 0.00	0.67 ± 0.00	4.06 ± 0.21	4.03 ± 0.12
RMSE			3.25 ± 0.08	3.76 ± 0.05

Table 4.10: Mean values and percent error for the air pockets in the full-container image after noise suppression.

Pocket Thickness (cm)	Mean		Percent Error	
	Brem.	LENR	Brem.	LENR
2.0	0.59 ± 0.00	0.65 ± 0.00	2.28 ± 0.19	3.71 ± 0.10
5.2	0.59 ± 0.00	0.66 ± 0.00	2.82 ± 0.18	3.53 ± 0.10
8.4	0.59 ± 0.00	0.66 ± 0.00	2.93 ± 0.21	3.25 ± 0.12
11.6	0.59 ± 0.00	0.67 ± 0.00	3.30 ± 0.22	3.38 ± 0.13
14.8	0.60 ± 0.00	0.67 ± 0.00	2.78 ± 0.20	3.11 ± 0.11
18.0	0.60 ± 0.00	0.68 ± 0.00	2.91 ± 0.21	2.78 ± 0.12
RMSE			2.85 ± 0.08	3.31 ± 0.05

Aliasing Phantom

The circular phantoms to the right of the air pockets in Figs. 4.19 and 4.20 are meant to test the spatial resolution in another way. As the pinwheels get closer to the center, the pixels will start to bleed together as spatial resolution is lost. Similar to the other spatial resolution test in the full-scale container, both high-contrast and low-contrast materials were tested. Figure 4.27 shows a zoomed in image of the tungsten and steel phantom for both beams. On the noise suppressed image, the two materials perform similarly with regards to resolution, with the bremsstrahlung beam doing slightly better by preserving separation between the steel and tungsten at a smaller radius. Figure 4.28 shows the results for the more challenging separation between aluminum and steel. There is stronger blurring for both beams, as compared to the tungsten phantom, and there are more erroneous pixels on the noise suppressed images.

Contrast Blocks

The final portion of the container image contains blocks of aluminum, copper, and lead behind varying thicknesses of steel. Figure 4.29 shows a zoomed in image of the blocks. The blocks are in multiple sets of three. Starting from the left, the order is aluminum, copper, lead. Then the pattern repeats behind a 10 cm thick steel plate. Immediately to the right of these blocks is a vertical array of the same three blocks (with aluminum at the bottom). The vertical array was added to test whether the presence of the other blocks in the beam-line would increase the in-beam scattering and effect R-value measurements. The pattern repeats again to the right behind 20 cm of steel.

The LENR beam again has higher contrast than the bremsstrahlung beam, and it better preserves the aluminum block behind the 10 cm steel plate. Neither beam can preserve the aluminum behind the 20 cm steel plate, but the other blocks are all preserved. Table 4.11 shows the mean value and percent error for each of the horizontally arranged blocks in the original image, and table 4.12 shows the same data for the noise suppressed image. Tables

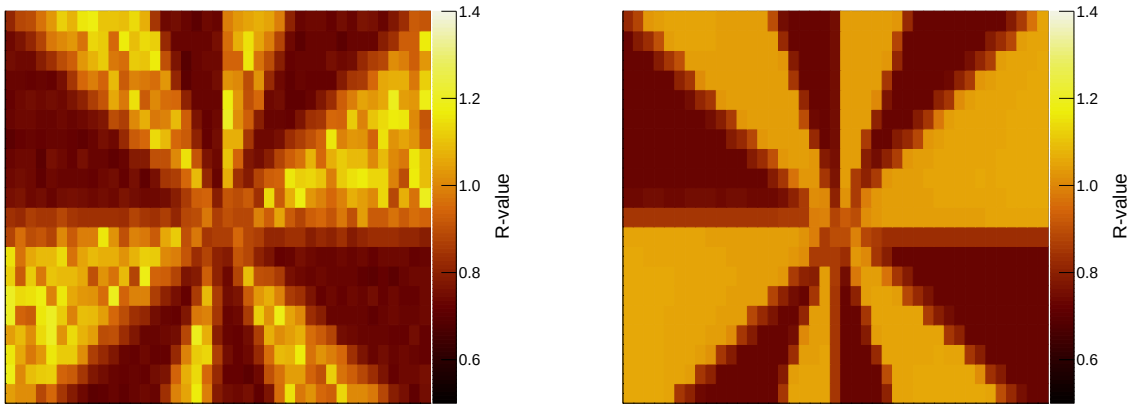

(a) Original bremsstrahlung image

(b) Noise suppressed bremsstrahlung image

(c) Original LENR image

(d) Noise suppressed LENR image

Figure 4.27: Zoomed-in images of the tungsten and steel phantom for qualitative evaluation of spatial resolution. Each image is 0.61 m (horizontally) by 0.66 m (vertically).

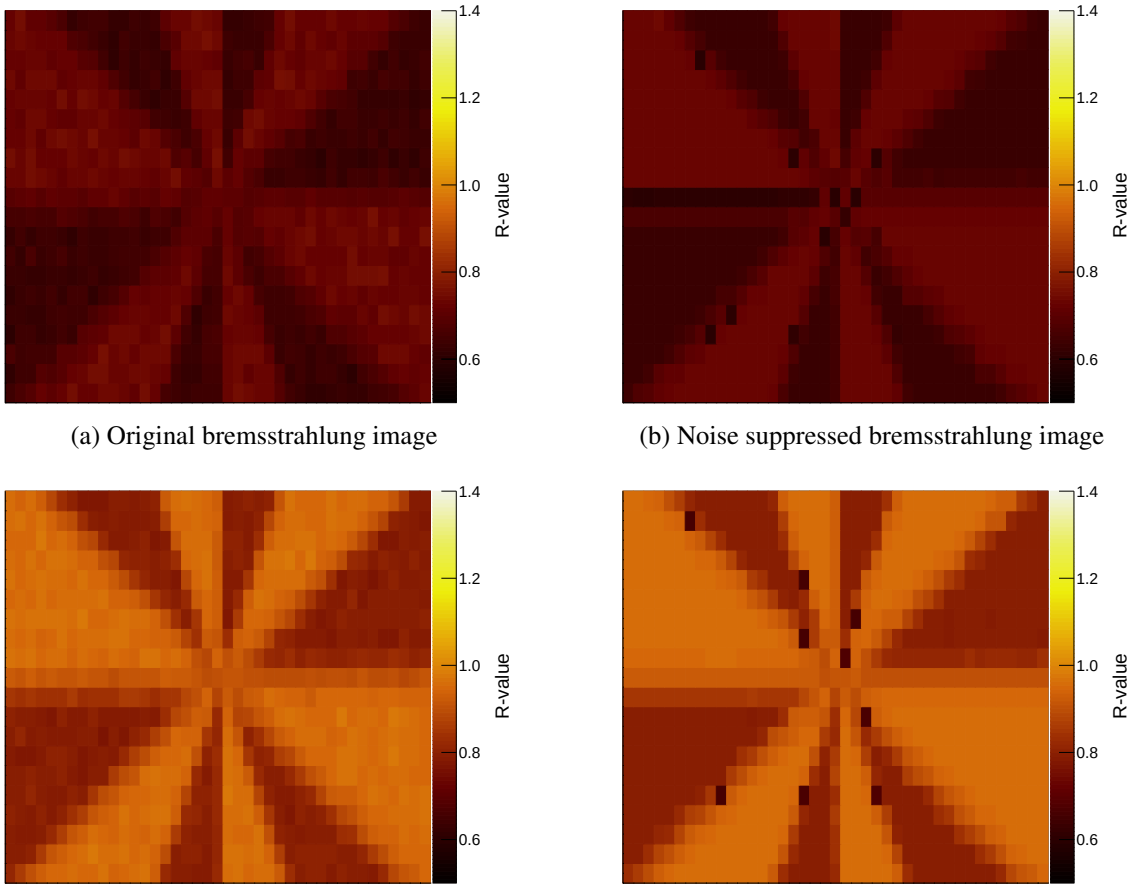

(a) Original bremsstrahlung image

(b) Noise suppressed bremsstrahlung image

(c) Original LENR image

(d) Noise suppressed LENR image

Figure 4.28: Zoomed-in images of the aluminum and steel phantom for qualitative evaluation of spatial resolution. The beams perform similarly here. The noise suppression algorithm classifies multiple pixels incorrectly, especially at the material interface. Each image is 0.61 m (horizontally) by 0.66 m (vertically).

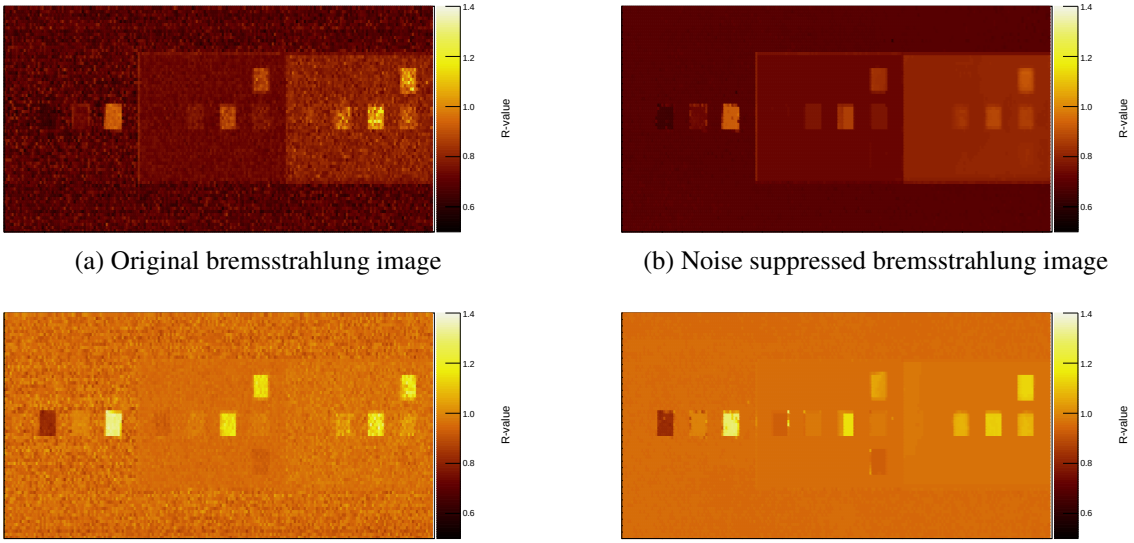

(a) Original bremsstrahlung image

(b) Noise suppressed bremsstrahlung image

(c) Original LENR image

(d) Noise suppressed LENR image

Figure 4.29: Zoomed-in images of the small blocks used to test the effect of increased steel in the beamline. The bremsstrahlung beam reads the differing steel thicknesses as different materials, an effect of beam hardening. Each image is 1.32 m (horizontally) by 0.46 m (vertically).

4.13 and 4.14 show the means and errors for the vertical blocks. There is little difference between the horizontal and vertical blocks. For these small blocks, the noise suppression induces error because it classifies different materials as the same. This stems from the low transmission values behind the steel plates. Finally, Table 4.15 shows the mean values for regions of the steel plates for both the bremsstrahlung and LENR beams.

Noise Levels

As a final comparison between the imaging beams on the cargo container data, the noise STD levels of different materials before and after noise suppression are shown in Table 4.16. For the average noise levels, the various regions were given weights according to the number of pixels used for the noise STD calculation. This accounts for the fact that of 104,000 pixels were used in the background calculation while only 79 pixels were used for the steel plates. The LENR beam had 27% and 39% lower noise STD than the bremsstrahlung before and after noise suppression. This again reflects the higher penetra-

Table 4.11: Mean values and percent error for the horizontal blocks with steel plates.

Steel Thickness (cm)	Material (Z)	Mean		Percent Error	
		Brem.	LENR	Brem.	LENR
0	Al (13)	0.65 ± 0.10	0.85 ± 0.12	1.87 ± 15.17	3.25 ± 13.97
	Cu (29)	0.73 ± 0.11	0.99 ± 0.12	1.14 ± 14.42	0.27 ± 12.53
	Pb (82)	0.89 ± 0.12	1.24 ± 0.14	5.37 ± 12.53	6.98 ± 10.44
	RMSE			3.35 ± 7.45	4.45 ± 6.44
10	Al (13)	0.73 ± 0.11	0.94 ± 0.12	2.14 ± 14.98	1.19 ± 13.06
	Cu (29)	0.76 ± 0.11	0.97 ± 0.12	4.25 ± 14.93	0.73 ± 12.75
	Pb (82)	0.86 ± 0.12	1.12 ± 0.13	0.53 ± 13.58	5.76 ± 11.12
	RMSE			2.76 ± 8.62	3.42 ± 6.48
20	Al (13)	0.82 ± 0.11	0.96 ± 0.12	14.55 ± 15.81	2.83 ± 13.09
	Cu (29)	0.90 ± 0.12	1.02 ± 0.13	24.17 ± 16.33	5.88 ± 13.12
	Pb (82)	0.99 ± 0.12	1.12 ± 0.13	22.41 ± 15.36	0.17 ± 11.81
	RMSE			20.80 ± 9.17	3.77 ± 7.57

Table 4.12: Mean values and percent error for the horizontal blocks with steel plates after noise suppression.

Steel Thickness (cm)	Material (Z)	Mean		Percent Error	
		Brem.	LENR	Brem.	LENR
0	Al (13)	0.66 ± 0.10	0.86 ± 0.12	1.36 ± 15.21	4.00 ± 14.02
	Cu (29)	0.73 ± 0.11	0.99 ± 0.12	1.40 ± 14.41	0.57 ± 12.51
	Pb (82)	0.88 ± 0.12	1.21 ± 0.14	6.28 ± 12.47	9.43 ± 10.30
	RMSE			3.80 ± 7.33	5.92 ± 6.33
10	Al (13)	0.73 ± 0.11	0.94 ± 0.12	2.59 ± 15.01	1.10 ± 13.06
	Cu (29)	0.76 ± 0.11	0.97 ± 0.12	4.28 ± 14.93	0.55 ± 12.74
	Pb (82)	0.84 ± 0.11	1.08 ± 0.13	0.96 ± 13.48	9.52 ± 10.89
	RMSE			2.94 ± 8.61	5.54 ± 6.31
20	Al (13)	0.81 ± 0.11	0.97 ± 0.12	12.62 ± 15.67	3.61 ± 13.14
	Cu (29)	0.83 ± 0.11	1.04 ± 0.13	14.23 ± 15.66	8.55 ± 13.28
	Pb (82)	0.86 ± 0.12	1.08 ± 0.13	6.22 ± 14.31	3.48 ± 11.60
	RMSE			11.55 ± 8.97	5.73 ± 7.54

Table 4.13: Mean values and percent error for the vertical blocks with steel plates.

Steel Thickness (cm)	Material (Z)	Mean		Percent Error	
		Brem.	LENR	Brem.	LENR
10	Al (13)	0.73 ± 0.14	0.94 ± 0.15	2.62 ± 18.99	0.98 ± 16.51
	Cu (29)	0.77 ± 0.14	0.98 ± 0.16	4.98 ± 18.95	0.79 ± 16.14
	Pb (82)	0.86 ± 0.15	1.13 ± 0.17	1.27 ± 17.24	5.46 ± 14.09
	RMSE			3.33 ± 10.90	3.23 ± 8.20
20	Al (13)	0.81 ± 0.12	0.96 ± 0.13	12.82 ± 16.77	2.11 ± 13.95
	Cu (29)	0.89 ± 0.13	1.02 ± 0.13	21.71 ± 17.28	5.68 ± 14.01
	Pb (82)	0.99 ± 0.13	1.13 ± 0.14	21.84 ± 16.38	1.02 ± 12.68
	RMSE			19.26 ± 9.72	3.55 ± 8.06

Table 4.14: Mean values and percent error for the vertical blocks with steel plates after noise suppression.

Steel Thickness (cm)	Material (Z)	Mean		Percent Error	
		Brem.	LENR	Brem.	LENR
10	Al (13)	0.73 ± 0.14	0.94 ± 0.15	2.58 ± 18.99	0.95 ± 16.50
	Cu (29)	0.77 ± 0.14	0.98 ± 0.16	4.78 ± 18.94	0.84 ± 16.14
	Pb (82)	0.83 ± 0.14	1.03 ± 0.16	2.97 ± 16.88	13.42 ± 13.48
	RMSE			3.57 ± 10.68	7.78 ± 7.80
20	Al (13)	0.82 ± 0.12	0.97 ± 0.13	14.79 ± 16.92	3.06 ± 14.01
	Cu (29)	0.85 ± 0.12	1.06 ± 0.14	17.21 ± 16.96	10.25 ± 14.31
	Pb (82)	0.89 ± 0.13	1.12 ± 0.14	10.39 ± 15.59	0.24 ± 12.63
	RMSE			14.41 ± 9.65	6.18 ± 8.25

Table 4.15: Mean values and percent error for the steel plates.

Steel Thickness (cm)	Mean		Percent Error	
	Brem.	LENR	Brem.	LENR
Original				
10.0	0.73 ± 0.02	0.96 ± 0.03	1.52 ± 3.19	0.52 ± 2.77
20.0	0.80 ± 0.02	0.97 ± 0.03	10.96 ± 3.34	1.89 ± 2.79
Noise Suppressed				
10.0	0.73 ± 0.02	0.96 ± 0.03	1.52 ± 3.19	0.58 ± 2.77
20.0	0.81 ± 0.02	0.97 ± 0.03	10.96 ± 3.34	1.99 ± 2.79

Table 4.16: Noise levels across various regions of the full container image before and after noise suppression.

Region		Original		Noise Suppressed	
		Brem.	LENR	Brem.	LENR
Background		3.77E-2	2.79E-2	3.50E-3	1.80E-3
Water		7.23E-3	4.33E-3	3.99E-4	4.21E-4
Contrast Rods	Na	1.16E-2	1.13E-2	3.50E-3	1.80E-3
	Mn	1.12E-2	7.81E-3	3.99E-4	4.21E-4
	Mo	1.44E-2	1.11E-2	1.95E-2	2.06E-2
	Ba	1.55E-2	1.30E-2	6.96E-3	9.05E-3
	Pt	1.38E-2	1.75E-2	3.24E-4	4.77E-2
	Th	1.47E-2	1.48E-2	2.83E-2	1.11E-2
Air Pockets	2.0 cm	9.26E-3	6.27E-3	3.58E-4	1.06E-3
	5.2 cm	9.62E-3	5.33E-3	1.80E-3	7.23E-3
	8.4 cm	1.07E-2	6.97E-3	3.85E-3	1.26E-2
	11.6 cm	1.11E-2	7.03E-3	2.40E-3	1.03E-2
	14.8 cm	1.03E-2	7.77E-3	2.55E-2	1.21E-2
	18.0 cm	1.10E-2	8.02E-3	2.52E-2	1.94E-2
Steel Plates	10 cm	1.02E-2	7.18E-3	2.54E-4	2.11E-4
	20 cm	2.25E-2	1.33E-2	1.91E-3	1.36E-3
Weighted Mean		4.71E-2	2.53E-2	5.63E-3	2.09E-3

tion values of the LENR beam and shows that monoenergetic beams can provide higher quality images at equivalent cargo doses.

Conclusions

In this chapter some of the advantages of a monoenergetic imaging system as compared to a bremsstrahlung-based imaging system have been highlighted. There is little difference in spatial resolution, which is largely determined by the detector array. The monoenergetic beam allows for higher-contrast material reconstruction, which can be especially helpful in the presence of noise. Using a full-scale simulation of a cargo container, it was shown that the monoenergetic beam provides an average increase in contrast-to-noise ratio of 2.55 for 6 materials spanning from 11-90 in atomic number.

All images were acquired with the same dose to the cargo. Without noise suppression,

the LENR beam produced consistently lower noise levels on R-value images. Typically, the LENR beam had lower noise levels at lower dose levels, meaning the LENR beam at 1.75 mrem had similar performance to the bremsstrahlung beams at 2.5 mrem.

Additionally, noise suppression using the transmission image as prior knowledge can increase performance of both imaging beams. When tested on the cargo container, noise suppression yielded an increase in contrast-to-noise ratio by a factor of 10.33 and 15.35 for the bremsstrahlung and monoenergetic images, respectively, while introducing little error. The noise suppression was more effective on the LENR images, consistently reducing noise to the same levels even as the dose was decreased. This could be extrapolated to show that similar or superior image quality with the LENR beam can be achieved at lower doses when noise suppression is used.

The monoenergetic beam showed slightly higher contrast sensitivity, accurately finding small air pockets in a water container while they were largely missed by the bremsstrahlung beam. The monoenergetic beam shows little bias as cargo thickness is increased while the bremsstrahlung beam hardens as cargo thickens, leading to errors in the measurement of the attenuation coefficient.

As mentioned in previous chapters, the R-value reconstruction is energy-dependent. If the high-energy bremsstrahlung beam instead had an end point of 15 MeV, it would achieve a higher contrast R-value curve, although it would not be as strong as the LENR beam. Additionally, if a LENR with lower energies were used, the R-value contrast would not be as high as what is shown here. If an ICS beam were used for imaging, it could provide decreased scatter as compared to the LENR beam used in these simulations. This is because ICS sources produce pencil beams which are rastered across the cargo container. The detection system could be synchronized with the source such that only the detector that was currently being irradiated would read out signal. This would effectively eliminate scattering from the measurement and lead to more accurate R-value reconstructions. Additionally, the divergence of the MPS beam can be tightly controlled, further decreasing the scatter per

pixel.

CHAPTER 5
TOMOGRAPHIC IMAGING

The advent of computerized tomography (CT) in the 1970s brought about a way to study three-dimensional anatomy in humans without the need for surgery. CT alleviated the x-ray contrast problems induced by projecting a 3D human onto a 2D space, and greatly expanded medical diagnostic capabilities. Similarly, incorporation of CT technology into the application space of cargo scanning could alleviate the need to open potentially threatening containers. In cases when a container must be manually investigated, a 3D distribution of the objects within would allow an operator to know exactly what object in the container needs further screening. Knowing exactly where he or she needs to look could reduce radiation exposure to the inspector when SNM is present as well as decrease the inspection time.

In medical CT, an x-ray source (bremsstrahlung driven) and corresponding radiation array of radiation detectors are rotated around a patient. This would be unfeasible in cargo scanning due to the large size of the containers. Additionally, rotating the cargo while holding the source and detector positions constant would require a large footprint for the imaging system. If, however, the radiation source is isotropic, or nearly isotropic, it could be collimated to produce multiple views of the container. Over the last 40 years, there has been a tremendous amount of research into the improvement of tomographic reconstruction algorithms, although there has been very little carry-over from medical CT to security applications, though previous authors have extended few-view tomography to scanning for air cargo containers[93].

In this chapter, the theory behind iterative image reconstruction will be discussed. The reconstruction algorithm used for reconstructing cargo data, called ASD-POCS (adaptive steepest descent method for projection onto convex sets), will then be discussed in detail.

Multiple modifications to this algorithm were made for implementation, and these will be discussed in detail, after the pseudocode for ASD-POCS is laid out. Finally, reconstructed datasets on numerical phantoms and simulated data will be shown. The algorithm and testing were all carried out in Matlab. Simulation was carried out in Geant4.

Image Reconstruction

Complete tomographic image reconstruction relies on full angular sampling of an object; typically a radiation source and a detector are rotated around an imaged object over 360°. This allows for oversampling of the imaged object and analytical reconstruction via filtered backprojection (FBP). If radiation dose is a concern, or if full angular sampling is not possible, the minimum rotation angle for accurate reconstruction via FBP is 180° for parallel beams, or 180° + α for fan-beams, where α is the fan angle. This requirement on angular sampling makes full FBP impractical for a cargo scanning situation. However, iterative approaches to image reconstruction have shown promise for multiple scenarios where FBP is not possible. Iterative methods have also been around since the 1970s but have garnered more interest in the last decade due to increasing computational power and algorithm efficiency. Iterative reconstruction algorithms are ideal for cases where there is "missing" data or where statistical models can be employed. The task of transmission imaging for cargo containers fits both of these cases. Rather than truly missing data, these datasets are undersampled, with few projections, or views, and those views are taken over a limited angle.

Many iterative algorithms exist in the literature for medical CT and emission tomography. However CT still relies on several projections, typically at least 50, but in more cases well over 360 projections. Emission tomography algorithms, such as those used for SPECT or PET reconstruction, are more under-sampled than CT. Typically, however the nature of their datasets is different than what is expected with cargo scanning. Emission tomography typically has full angular coverage, but with noisy measurements, and possibly sparse

views. In cargo scanning, full angular coverage is not possible, but it is possible that the data will be less noisy. Additionally, the constraints on spatial resolution in 3D are less for cargo applications than in medical applications. The algorithm discussed below is intended to give a general location of a potential threat, so the desired spatial precision is lower.

Reconstruction Algorithm

Iterative Image Reconstruction

As mentioned above, FBP provides an analytical formulation for CT image reconstruction. However, for many cases, the criteria for full FBP reconstruction cannot be satisfied. For example, full rotation around the object is impossible in the context of cargo scanning. Instead, image reconstruction can be seen as solving the system of linear equations

$$M\vec{f} = \tilde{g} \tag{5.1}$$

where M is a system matrix composed of N_{data} row vectors $\vec{M}_i$ which describe the path length of a ray through the imaging volume, $\vec{f}$ is the desired reconstructed image, and $\tilde{g}$ is the measured transmission data (through the imaged object). This equation can, in general, be overdetermined or underdetermined. For this application, which will be few-view and limited-angle, this will be an underdetermined system. Directly solving this inverse problem is not tractable due to the large size of the system matrix, so iterative matrix inversion techniques are typically carried out. Solving Eqn. 5.1 without any data constraints can be slow, if not impossible, and can lead to artifacts. Instead, data constraints relying on *a priori* information are usually imposed, the most common of these is data non-negativity. There are various ways to implement this knowledge. Commonly, they come in the form of regularization, where the solution of Equation 5.1 is constrained in some way.

System Matrix Generation

The system matrix, M (also called the forward projection matrix), can be calculated via ray-tracing algorithms or Monte Carlo, and this has been done in Geant4 for the results presented below. As mentioned above, this matrix holds the path lengths for a given view (which is dictated by angle between the source and the detector array) through every pixel in the reconstructed imaging space. Figure 5.1 shows an example of how the system matrix will be built. In this system for cargo scanning, the source will be collimated down to a few views, 3 in this example. The container will then be driven through the imaging space, as shown in Figure 5.1a, tracing over a gridded area which will correspond to pixel positions in the reconstructed image. Rather than physically moving the imaging space (i.e. the grid in Figure 5.1b), the source and detector are translated in 3 mm steps from right to left. The source is simulated as a point, and slices are taken through the entire imaging space for a given view. This means that the most oblique views have more slices than perpendicular views. Figure 5.1b shows 3 projections at 3 views.

The matrix M is organized such that each row corresponds to a specific slice within a view. Every column element represents the mean path length through a given image pixel. For example, Figure 5.1b shows a 32 pixel $\times$ 32 pixel imaging space. This grid will be transformed into a row vector which is 1024 elements long. There are 9 total slices in this example, so the matrix size would then be 9×1024. With more views or slices, this problem becomes less underdetermined. Likewise, with more pixels in the reconstructed image, the problem becomes more underdetermined. Two separate data acquisition schemes will be used in this work. The first will have 11 views and 2494 total projections, and the second will have 5 views and 1198 total projections. Table 5.1 shows the number of slices per view for the 11-view matrix as well as the angle of the view (where 0° is perpindicular to the cargo). There is symmetry in view-angle, so only positive angles are shown in the table. For the 5-view system matrix, views at -60°, -24°, 0°, 24°, and 60° were used. The sparsity patterns of the two matrices can be seen in Figure 5.2.

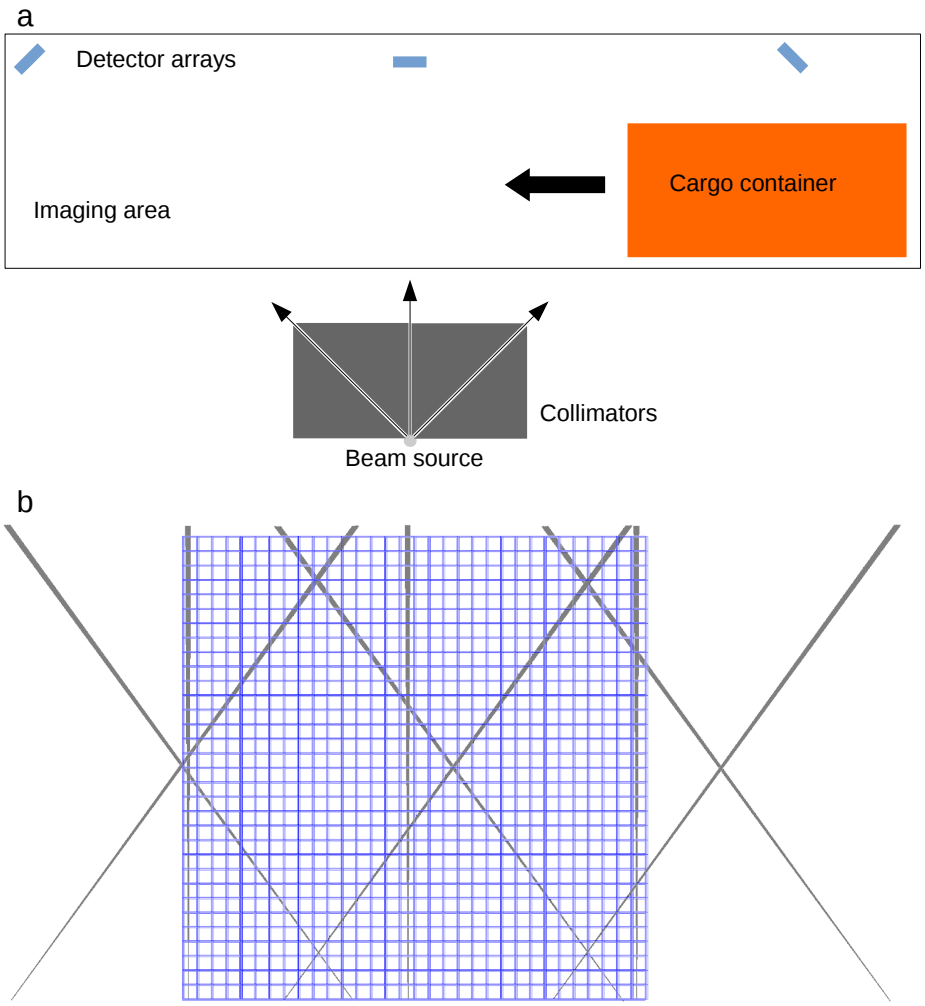

Figure 5.1: Inset (a) shows a simplified acquisition system for tomographic imaging. An isotropic beam source is collimated down to a few views, 3 in this example. A cargo container is then driven through the imaging area, and transmission measurements of the container are taken at multiple angles. Inset (b) shows a discretization of the imaging area into pixels for reconstruction. The angle of the gray rays determine the "view", and multiple slices are taken per view. Inset (b) is output from the simulation used to generate the system matrix for image reconstruction.

Table 5.1: Number of slices per view for the tomographic imaging system. Each slice is separated by 3 mm, and every view fully covers the imaging grid.

Angle	Slices
0°	128
12°	156
24°	185
36°	221
48°	271
60°	350

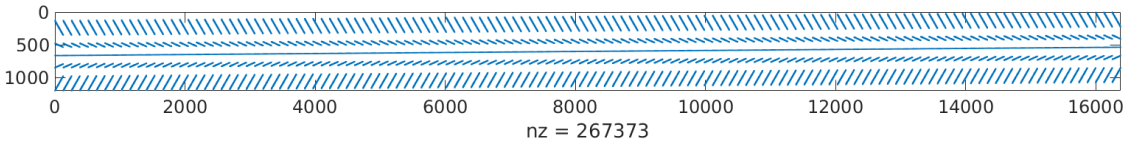

(a) 5 views

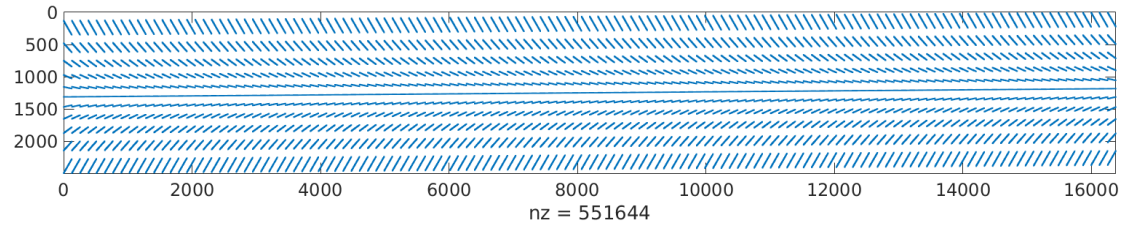

(b) 11 views

Figure 5.2: Sparsity patterns of the two system matrices used in this work. The 5-view matrix is more underdetermined than the 11-view matrix. *nz* corresponds to the number of non-zeros in each matrix.

ASD-POCS

The reconstruction algorithm is an adaptive steepest-descent method for projection onto convex sets (ASD-POCS). It was first implemented by Sidky et al for cone-beam CT in [94], and then modified for digital breast tomosynthesis (DBT) in [95]. The algorithm relies on the theory of compressed sensing, a data extraction technique first proposed by Candes, Romberg, and Tao in 2006[96]. Compressed sensing allows for reconstruction of a continuous signal by sparsely sampling the discrete Fourier transform of an object. This is typically carried out through minimization of the total variation (TV) of the object. Constrained TV minimization is effective when the reconstructed image is sparse in some sense. While this constraint can be difficult to meet for image reconstruction, if the image is piecewise constant, the gradient magnitude image (GMI) will be sparse, so TV minimization effectively minimizes the GMI. A rule of thumb for TV minimization is that the more sparse the signal, the faster and more accurate the reconstruction. If an image has N nonzeroes, only $2N$ samples in the Fourier domain are needed. In the case of image reconstruction, FBP already relies on sampling in the Fourier domain, so CT is a natural

application of compressed sensing theory.

The ASD-POCS algorithm seeks to minimize the image TV

$$\vec{f}^* = argmin||\vec{f}||_{TV} \tag{5.2}$$

where $||\vec{f}||_{TV}$ is typically defined is

$$||\vec{f}||_{TV} = \sum_{i,j} \sqrt{(f_{i,j} - f_{i-1,j})^2 + (f_{i,j} - f_{i,j-1})^2} \tag{5.3}$$

over all image pixels i, j. Eqn. 5.2 is minimized subject to the constraints

$$|M\vec{f} - \tilde{g}| \leq \epsilon \tag{5.4}$$

and

$$\vec{f}_i \geq 0 \tag{5.5}$$

where ϵ is a nonzero term which accounts for the measurement noise in $\tilde{g}$. The pseudocode, as presented in [95], is shown in Alg. 1. In implementation, the algorithm first does the POCS step (also called algebraic reconstruction technique, ART) step, solving eqn. 5.1. It then carries out the total variation minimization steps for ng iterations per outer loop iteration. The magnitude of the TV reduction step is calculated via a line-search method, ensuring an optimal step size in the optimization space.

Algorithm 1 will be explained line-by-line below. First, all input variables are set, β controls the speed for the algebraic reconstruction update, N_{iter} is the number of total iterations, ng is the number of TV minimization iterations per outer iteration, r_{max} is the called the ratio parameter by the original authors, and γ_{red} controls the coarseness of the line search. The ART step performs algebraic reconstruction, the operator P enforces positivity. The variable dp measures the magnitude of the change brought about by ART.

Algorithm 1 Pseudocode for original ASD-POCS algorithm. Reproduced from [95].

$\beta = 1.0, N_{iter} = 10, ng = 5, r_{max} = 1.0, \gamma_{red} = 0.8, \vec{f} = 0$
for $i = 1, N_{iter}$ **do**
  for $j = 1, N_{data}$ **do**
    $\vec{f} = \vec{f} + \beta \vec{M}_j * \frac{g_j - \vec{M}_j * \vec{f}}{\vec{M}_j * \vec{M}_j}$ ▷ ART step
  end for
  $\vec{f} = P(\vec{f})$ ▷ enforce positivity
  $\vec{f}_{res} = \vec{f}$
  $dp = |\vec{f} - \vec{f}_0|$
  $\vec{f}_0 = \vec{f}$
  for $j = 1, ng$ **do** ▷ steepest descent loop (TV steps)
    $R_0 = R(\vec{f})$
    $\vec{df} = \nabla_{\vec{f}} R(\vec{f})$
    $\hat{df} = \vec{df}/|\vec{df}|$
    $\vec{f'} = \vec{f} - dp * \hat{df}$
    $\vec{f'} = P(\vec{f'})$
    $\gamma = 1.0$
    while $R(\vec{f'}) > R_0$ **do** ▷ line search
      $\gamma = \gamma * \gamma_{red}$
      $\vec{f'} = \vec{f} - \gamma dp * \hat{df}$
      $\vec{f'} = P(\vec{f})$
    end while
    $\vec{f} = \vec{f'}$
  end for
  $dg = |\vec{f'} - \vec{f}_0|$
  if $dg > r_{max} * dp$ **then**
    $\vec{f} = r_{max} \frac{dp}{dg} (\vec{f'} - \vec{f}_0) + \vec{f}_0$
  end if
end for
return $\vec{f}_{res}$

In the steepest descent loop, R represents the TV regularization

$$R(\vec{f}) = ||\vec{f}||_{TpV} = \sum_{i,j} \Delta_{i,j}^{p}, \tag{5.6}$$

where

$$\Delta_{i,j} = \sqrt{(f_{i,j} - f_{i-1,j})^2 + (f_{i,j} - f_{i,j-1})^2 + \sigma}. \tag{5.7}$$

$\Delta_{i,j}$ represents the gradient magnitude image. The small constant σ is added to ensure differentiability. The exponent p allows for control of the minimization. ASD-POCS is unique in the fact that it changes the norm in which the TV is measured. Ideally, TV regularization would result in minimization of the ℓ_0-norm of the gradient magnitude image (i.e. p = 0). However, this problem is not solvable in polynomial time due to its non-convex nature. Instead, the ℓ_0 norm can be approximated by the ℓ_p norm where $0 < p \leq 2$, this is called the TpV norm, $||\cdot||_{TpV}$. In line 12, the gradient of the TpV norm, with respect to the each image element is calculated

$$\begin{aligned} \frac{\partial ||\vec{f}||_{TpV}}{\partial f_{i,j}} = & \, p\Delta_{i,j}^{p-2}(2f_{i,j} - f_{i-1,j} - f_{i,j-1}) \\ & + p\Delta_{i+1,j}^{p-2}(f_{i,j} - f_{i+1,j}) \\ & + p\Delta_{i,j+1}^{p-2}(f_{i,j} - f_{i,j+1}) \end{aligned} \tag{5.8}$$

Lines 14 is the gradient descent step, with magnitude dp and direction $d\vec{f}$. The line search is carried out in lines 17-20. This is implemented to ensure that the gradient descent step is truly the steepest descent step in the direction of $d\vec{f}$. If the algorithm has overstepped an optimal point, the line search will reduce the step size until that optimal point is reached. Line 25 balances the minimization problem between the POCS step (ART) and steepest descent steps (TV). Initially, when the change due to ART is large, the TV steps are allowed to make large progress. Later in the iteration, when the object structures come into clearer view, the steepest descent is adaptively reduced according to the reduction in the ART step.

This reduces the over-smoothing and edge blurring artifacts typical of TV-based image reconstructions.

Modifications to the algorithm

In pursuit of a successful image reconstruction algorithm, modifications were made .to Alg. 1. The first modification will be to modify the ART step. ART is a naturally ill-posed problem, and proceeding through the ART step by reconstructing orthogonal projections sequentially can improve the conditioning of the system matrix M. Additionally, ART is known to amplify noise along certain projections as the number of iterations is increased[95]. Stemming from these ideas, we carry out the ART steps in a random order, which is different for every iteration. By separating projections throughout the system matrix, we can make the system better conditioned, and randomizing the order we solve the problem prevents the noise along certain projections from being amplified.

Alg. 1 uses an isotropic image gradient for the TV regularization, i.e. the gradient is given the same weight in all directions. Several authors have proposed the use anisotropic gradients to reflect the data acquisition scheme[97, 98, 99]. In the case of limited angle CT, the anisotropic gradient would weight the gradient stronger in a path perpendicular to the acquisition scheme[100], reflecting that the measurements reveal more information between adjacent rays than within a ray. In other words, if $\hat{x}$ is in the direction of cargo movement and $\hat{y}$ is into and out of the cargo container, then more is known about the pixel-to-pixel variation in $\hat{x}$ than in $\hat{y}$, and the gradient is modified to reflect this. To introduce this anisotropy to the formulation, directional coefficients are introduced to Equation 5.7

$$\Delta_{i,j,aniso} = \sqrt{A * (f_{i,j} - f_{i-1,j})^2 + B * (f_{i,j} - f_{i,j-1})^2 + \sigma}. \tag{5.9}$$

where A and B are values between 0 and 1. These coefficients will then be integrated into

the derivative of Equation 5.9

$$\begin{aligned}\frac{\partial||\vec{f}||_{TpV}}{\partial f_{i,j}} = p\Delta_{i,j,aniso}^{p-2}(A*(f_{i,j}-f_{i-1,j})+B*(f_{i,j}-f_{i,j-1})) \\ + p\Delta_{i+1,j,aniso}^{p-2}(A*f_{i,j}-f_{i+1,j}) \\ + p\Delta_{i,j+1,aniso}^{p-2}(B*f_{i,j}-f_{i,j+1})\end{aligned} \tag{5.10}$$

Other authors have proposed re-weighting the TV norm to reflect a higher weight where the gradient is small (i.e. where the image is constant)[101, 102, 103]. Including these weights modifies Eqn. 5.6

$$R_w(\vec{f}) = ||W\vec{f}||_{TpV} = \sum_{i,j} w_{i,j}\Delta_{i,j}^{p} \tag{5.11}$$

where W is the weighting matrix, and $w_{i,j}$ are the individual pixel weights, calculated as

$$w_{i,j}^{(k+1)} = \frac{1}{\Delta_{i,j}^{(k),p=1}+\sigma} \tag{5.12}$$

where (k) corresponds to iteration number and σ is introduced to avoid division by 0. These modifications are incorporated into the algorithm below as an attempt to increase the efficacy of ASD-POCS for this problem.

Evaluation

Numerical Phantom Studies

The Shepp-Logan numerical phantom will be used for evaluation of the ASD-POCS algorithm[104]. The geometry of the phantom is shown in Figure 5.3b. Rather than simulating an image acquisition in Geant4 or another simulation toolkit, initial testing will be carried out on forward-projected phantom data. That is, $\tilde{g}$ is generated by multiplying the phantom (in vector form) by M. This allows for fair comparisons between methods and will allow for quick switching between phantoms and adjustment of noise levels when evaluating the

Figure 5.3: The Shepp-Logan phantom shown in Matlab. The pixel size is 128×128 and the image is shown on the window [0.0 1.0].

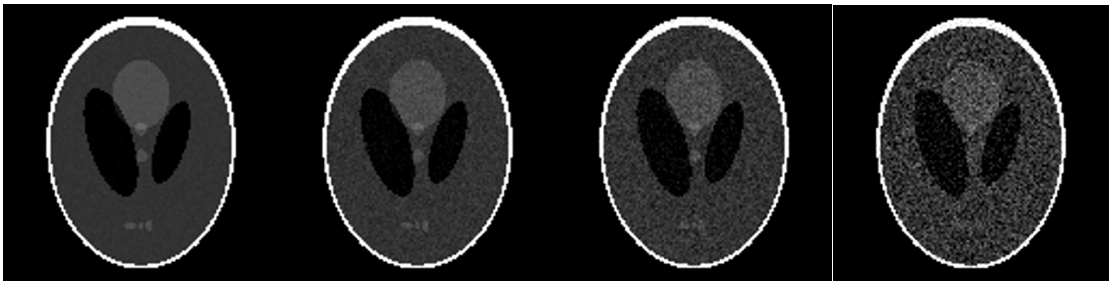

(a) $\sigma = 0.01$ (b) $\sigma = 0.03$ (c) $\sigma = 0.05$ (d) $\sigma = 0.10$

Figure 5.4: The Shepp-Logan phantom with different levels of Gaussian noise.

reconstructions. Forward projecting the data also gives a perfectly known image so image error can be measured as the algorithm proceeds.

The Shepp-Logan phantom will be used to test all of the modifications listed above. Zero-mean Gaussian noise will be added to the image data to simulate more realistic imaging scenarios. Sigma values of 0.01, 0.03, 0.05, and 0.10 will be used. Figure 5.4 shows the noisy Shepp-Logan Phantoms. All images in Figure 5.4 and below are shown on the window [0.0 1.0].

For quantitative evaluation of algorithm performance, the ℓ_2-norm of the image error and the structural similarity are measured. Structural similarity (SSIM) accounts for the

Table 5.2: Parameters used for iterative reconstruction algorithm These parameters were chosen independently based on values which provided the lowest-error reconstruction on the noiseless Shepp-Logan phantom.

Parameter	Value
ART steps	1
TV steps	5
β	0.9
r_{max}	0.8
γ_{red}	0.8
p	0.8
σ	1E-6
A	1
B	0.01

difference between the a reference image and the reconstructed image by evaluating luminance (brightness), contrast, and correlation. It was originally developed to provide a fully objective comparison between different images which compares the contrast, feature shape, and brightness of the two images[105]. A SSIM of 1 corresponds to two images that are exactly the same.

All image reconstruction and comparisons are implemented in Matlab. The algorithm has several parameters which impact performance. A wide range of each of these components were initially tested independently to determine which produced an image with the lowest error. After this initial testing, all components were held constant throughout all evaluations. The final parameter space is shown in Table 5.2. There are countless ways to determine the optimal parameters to be used in an image reconstruction algorithm, and the method we use does not necessarily find the optimal value for each parameter, but it provides a good first approximation.

To test each of the modifications, as well as the products of multiple multiplications, 8 different images were reconstructed from Shepp-Logan data with varying levels of noise. Reconstructions were allowed to run for 200 iterations, there was no significant difference in computational time between each algorithm (around 3 minutes per reconstruction).

Figure 5.5 shows the error and SSIM as a function of iteration number for all 8 tests. ASD-POCS is the original algorithm, ASD-Rand-POCS is ASD-POCS, but carrying out the ART (POCS) step in random projection order, RWTV is the re-weighted TV modification, ATV is anisotropic TV, and RWATV is re-weighted and isotropic TV. The reconstructed images are 128×128 pixels and 11 views were used. From this data, we can see the the random POCS is the only modification which improves over ASD-POCS on the noiseless image. As the noise gets higher, this parity decreases, and at a σ value of 0.10 multiple methods perform equivalently to ASD-POCS in SSIM. In fact, using all three modifications, the random ART, anisotropic TV, and re-weighted TV yielded one of the poorer results at low noise levels. Figure 5.6 shows the reconstructed images with no noise, Figure 5.7 shows the reconstructed images with $\sigma = 0.01$, Figure 5.8 shows the reconstructed images with $\sigma = 0.05$, and Figure 5.9 shows the reconstructed images with $\sigma = 0.10$. With no noise added, the random modification to the POCS step clearly helps the algorithm. The smoothness of the original image is preserved and the lesions at the bottom of the phantom are better preserved. The other modifications make no improvement over the original algorithm. The random POCS algorithm leads to the lowest noise standard deviation among all 8 algorithms at all noise levels. As noise is increased, the random ART leads to speckling artifacts. At the highest noise level (Figure 5.9) the three modifications together perform nearly as well as the original algorithm.

Tomography with 11 views is likely unfeasible. To keep space and dose to a minimum, as few as 3 views would be desirable. In testing the algorithm, it was found that 5 views was the fewest that could be used reconstruction. Using a down-sampled forward-projection matrix, reconstructions were run with 5 views, and the results are shown below. The resulting error and SSIM plots can be seen in Figure 5.10. As could be expected, the reconstruction qualities are poorer. The minimum error is 0.8 for all methods and the maximum SSIM is around 0.7. The reconstructed images can be seen in Figs. 5.11, 5.12, 5.13, and 5.14. This acquisition scheme loses the round shape of the original phantom and

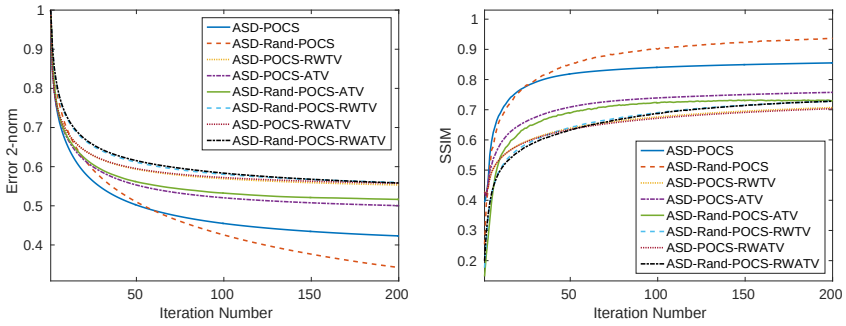

(a) noiseless

(b) noiseless

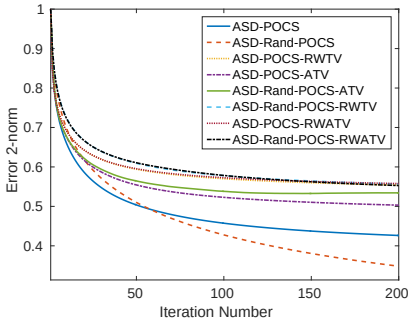

(c) $\sigma = 0.01$

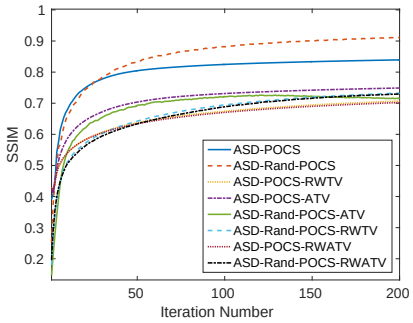

(d) $\sigma = 0.01$

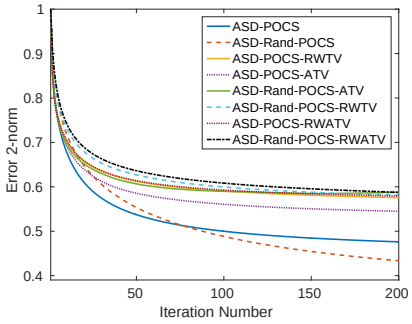

(e) $\sigma = 0.05$

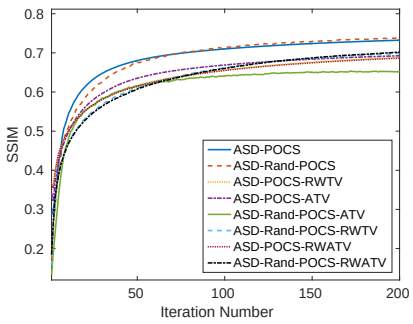

(f) $\sigma = 0.05$

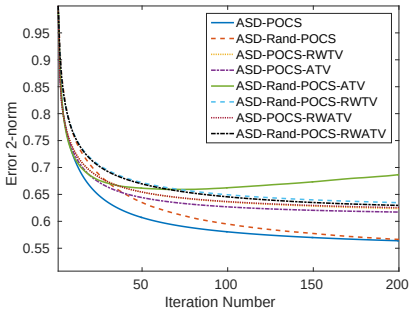

(g) $\sigma = 0.10$

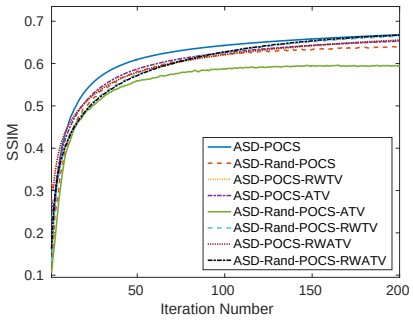

(h) $\sigma = 0.10$

Figure 5.5: Error 2-norm and structural similarity for the modified versions of the ASD-POCS algorithm. In general, the only modification which improves algorithm performance is randomizing the ART step. As the noise level increases, the overall performance decreases, and the majority of the modifications lead to equivalent performance of the original algorithm.

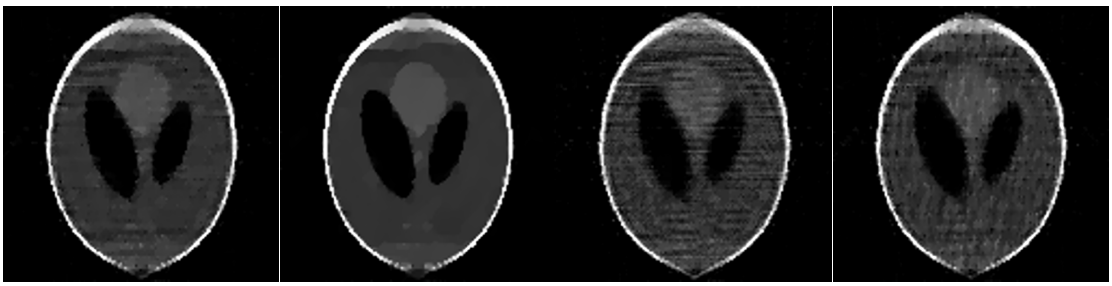

(a) ASD-POCS (b) Rand-POCS (c) POCS-RWTV (d) POCS-ATV

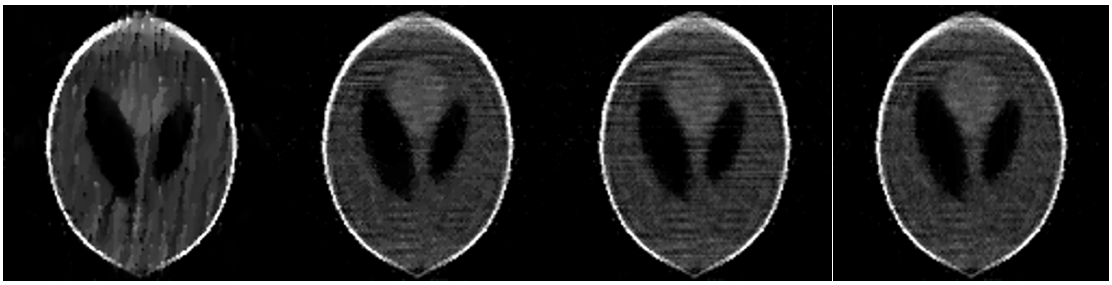

(e) Rand-POCS-ATV (f) Rand-POCS-RWTV (g) POCS-RWATV (h) Rand-POCS-RWATV

Figure 5.6: Reconstructions of the noiseless Shepp-Logan phantom.

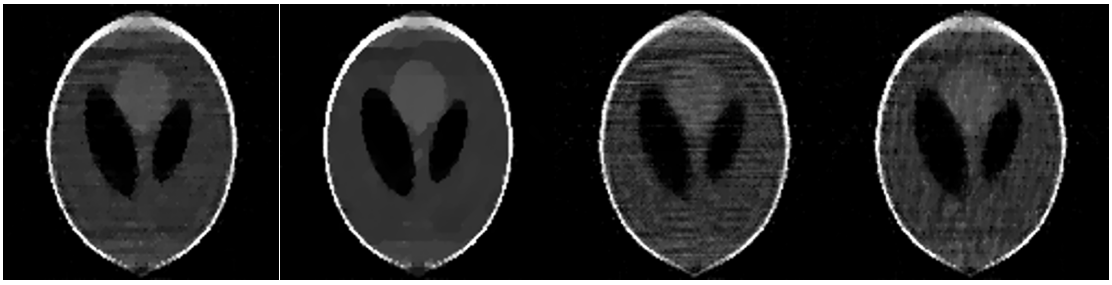

(a) ASD-POCS (b) Rand-POCS (c) POCS-RWTV (d) POCS-ATV

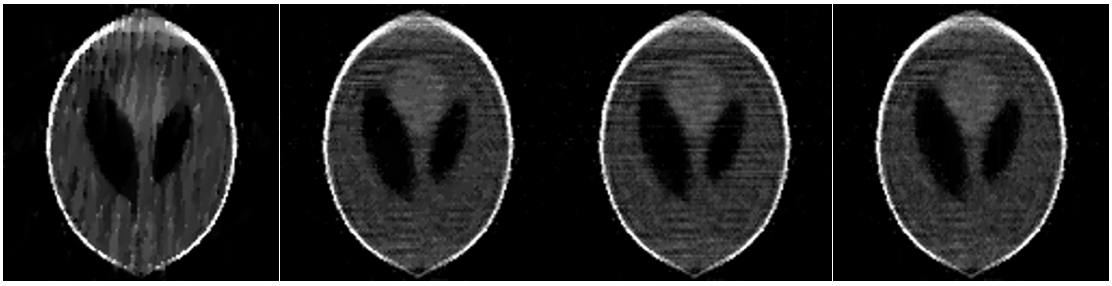

(e) Rand-POCS-ATV (f) Rand-POCS-RWTV (g) POCS-RWATV (h) Rand-POCS-RWATV

Figure 5.7: Reconstructions of the Shepp-Logan phantom with Gaussian noise ($\sigma = 0.01$)

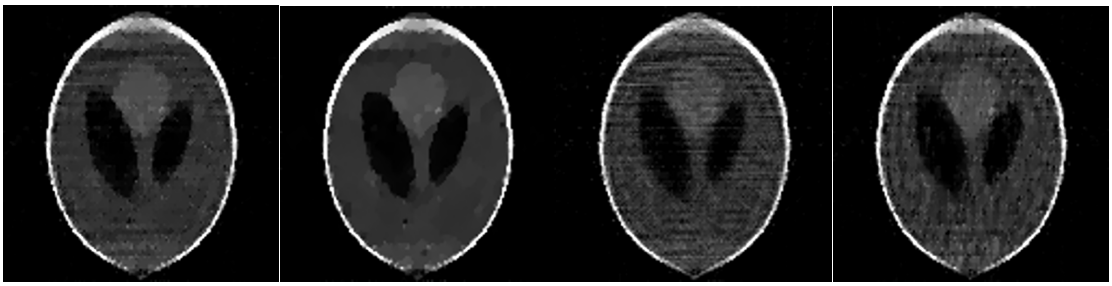

(a) ASD-POCS (b) Rand-POCS (c) POCS-RWTV (d) POCS-ATV

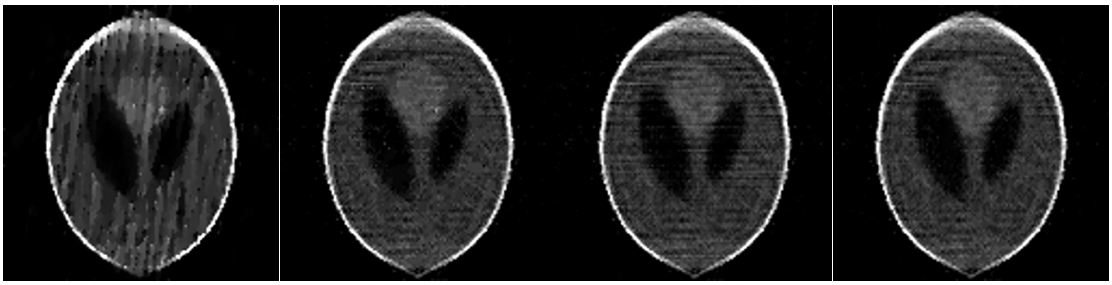

(e) Rand-POCS-ATV (f) Rand-POCS-RWTV (g) POCS-RWATV (h) Rand-POCS-RWATV

Figure 5.8: Reconstructions of the Shepp-Logan phantom with Gaussian noise ($\sigma = 0.05$).

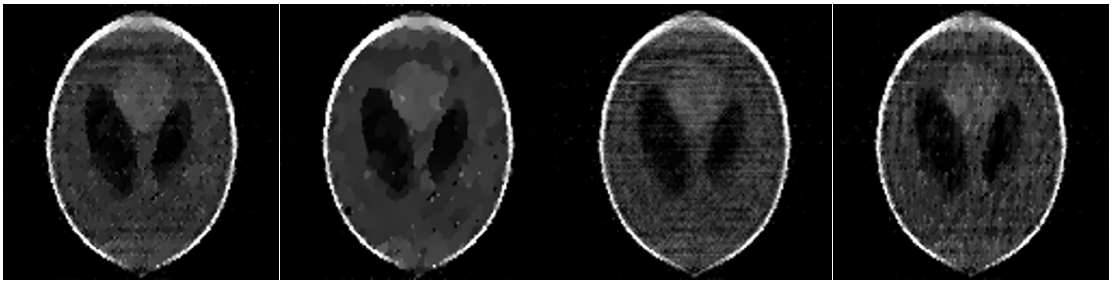

(a) ASD-POCS (b) Rand-POCS (c) POCS-RWTV (d) POCS-ATV

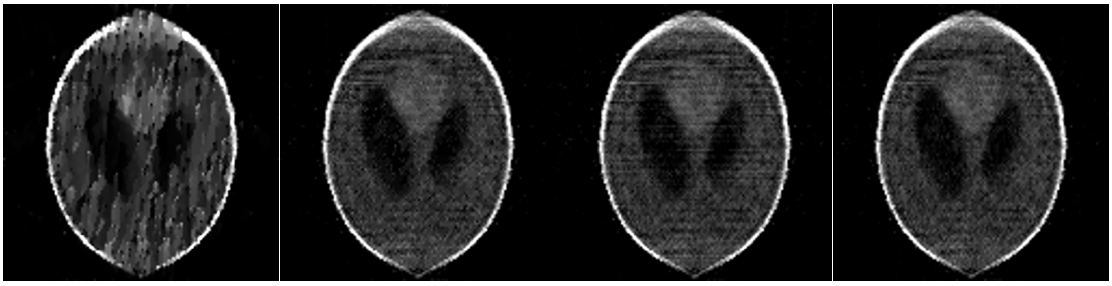

(e) Rand-POCS-ATV (f) Rand-POCS-RWTV (g) POCS-RWATV (h) Rand-POCS-RWATV

Figure 5.9: Reconstructions of the Shepp-Logan phantom with Gaussian noise ($\sigma = 0.10$).

elongates the structures. The image reconstruction with random ART and re-weighted TV (inset f) performs marginally better than the other modifications. It has the lowest error and highest SSIM when noise is added. Additionally, it can partially separate the air cavities while ASD-POCS and ASD-Rand-POCS blur them together.

Figure 5.15 shows the integral of each image column for the best-performing algorithms as well as the phantom values. If a planar radiographic imaging scheme were used, this would be all of the information provided by the one-detector tall imaging system. The reconstructions preserve the integral values of the original phantom with 11 views, but cannot reach the high values in the center of the profile with only 5 views. This can be seen in the figures above as the two air pockets tend to blend together with only 5 views. Figure 5.16 shows a vertical line profile through the center of the phantom. At low noise levels, the ASD-Rand-POCS algorithm does the best, preserving a piece-wise constant signal. As the noise is increased, the performance of ASD-Rand-POCS drops to equivalent levels to the other methods. With only 5 views, the images are elongated, clearly shown by the edge values in Figure 5.16. This is an artifact of the limited angle-sampling, and it is exacerbated with fewer views.

The above results showed that the ASD-POCS and ASD-Rand-POCS algorithms performed better than the others. To further evaluate these methods, reconstructions were run for 10,000 iterations on the Shepp-Logan phantom. The error norm and SSIM for the two methods as a noise is increased can be seen in Figure 5.17. Both 5 views and 11 views were tested, but only reconstructions with 11 views are shown because those with five views showed little difference from the reconstructions after 200 iterations. With relatively low levels of noise, the ASD-Rand-POCS method significantly outperforms ASD-POCS in both error and SSIM. As the noise is increased, the benefits of the random ART step are decreased, and ASD-POCS outperforms ASD-Rand-POCS in both metrics at the highest noise level. Figure 5.18 shows the reconstructed images for the two algorithms and Figure 5.19 shows the vertical line profiles through the center of the phantom. ASD-Rand-

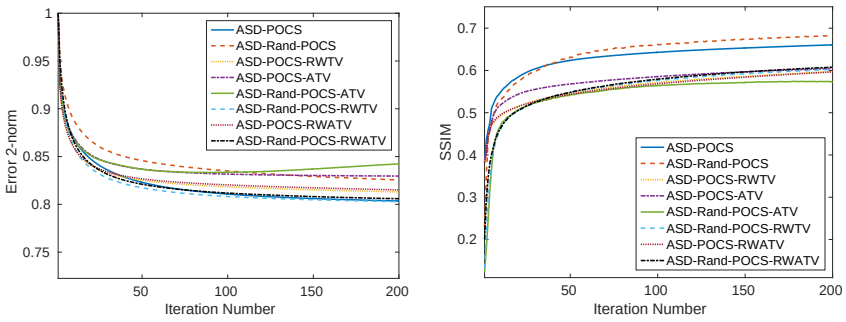

(a) noiseless

(b) noiseless

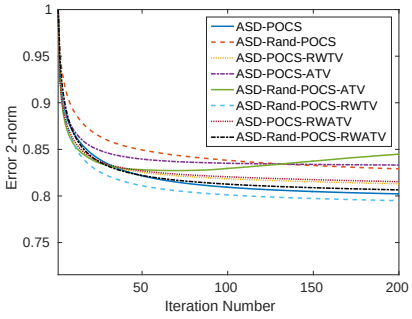

(c) $\sigma = 0.01$

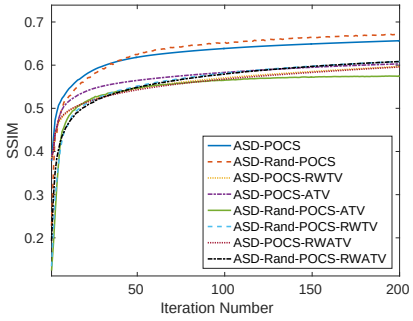

(d) $\sigma = 0.01$

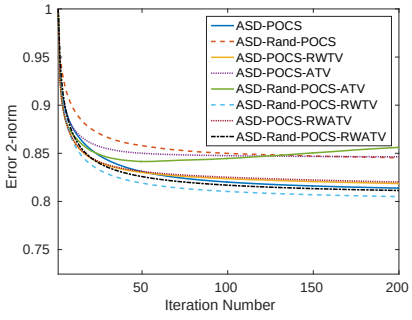

(e) $\sigma = 0.05$

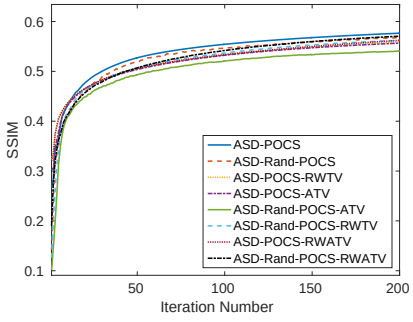

(f) $\sigma = 0.05$

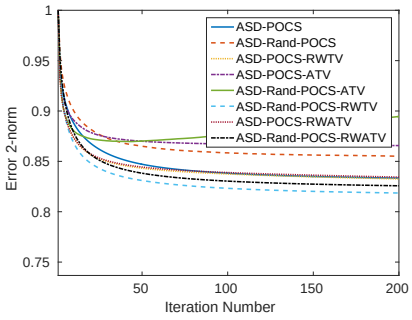

(g) $\sigma = 0.10$

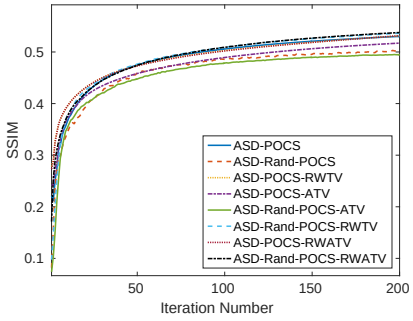

(h) $\sigma = 0.10$

Figure 5.10: Error 2-norm and structural similarity for the modified versions of the ASD-POCS algorithm. In general, the only modification which improves algorithm performance is randomizing the ART step. As the noise level increases, the overall performance decreases, and the majority of the modifications lead to equivalent performance of the original algorithm.

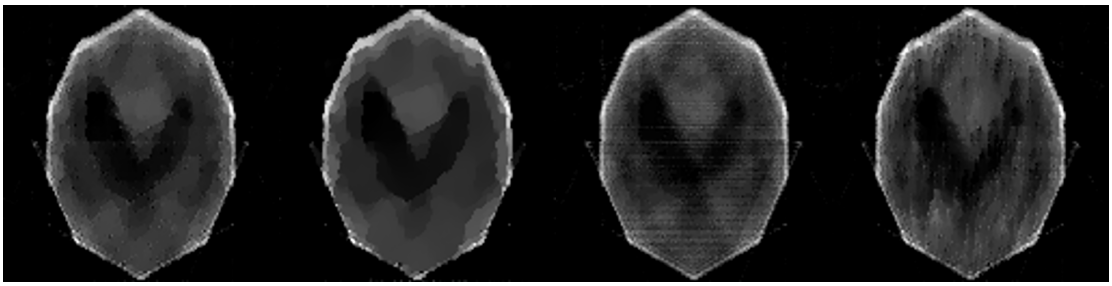

(a) ASD-POCS (b) Rand-POCS (c) POCS-RWTV (d) POCS-ATV

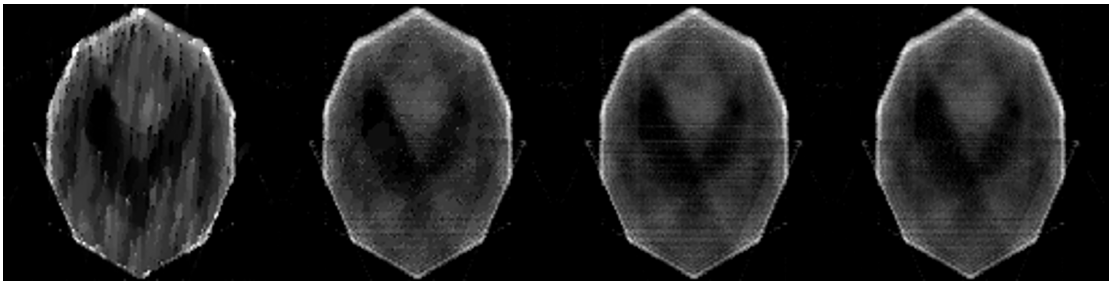

(e) Rand-POCS-ATV (f) Rand-POCS-RWTV (g) POCS-RWATV (h) Rand-POCS-RWATV

Figure 5.11: Reconstructions of the noiseless Shepp-Logan phantom.

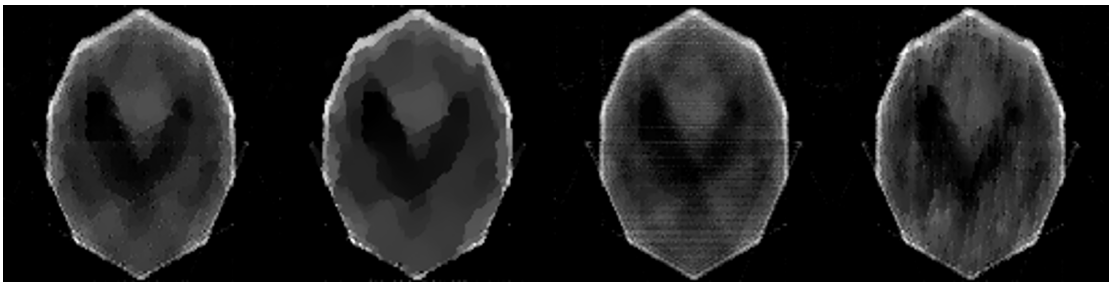

(a) ASD-POCS (b) Rand-POCS (c) POCS-RWTV (d) POCS-ATV

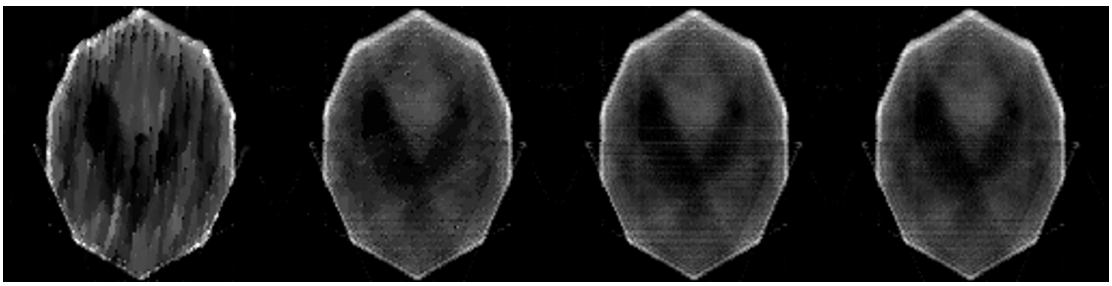

(e) Rand-POCS-ATV (f) Rand-POCS-RWTV (g) POCS-RWATV (h) Rand-POCS-RWATV

Figure 5.12: Reconstructions of the Shepp-Logan phantom with Gaussian noise ($\sigma = 0.01$).

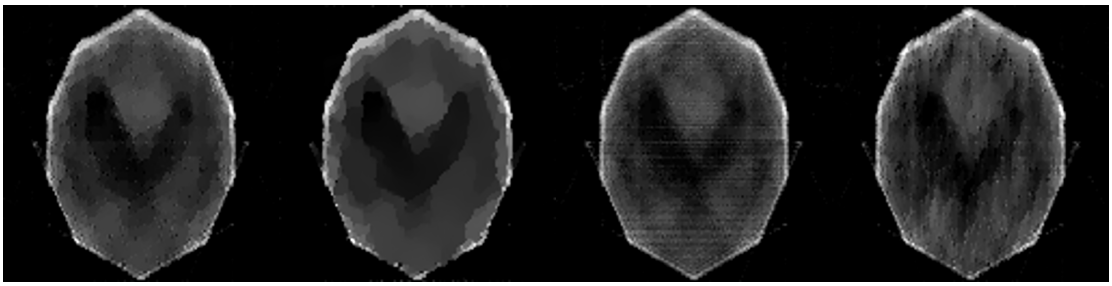

(a) ASD-POCS (b) Rand-POCS (c) POCS-RWTV (d) POCS-ATV

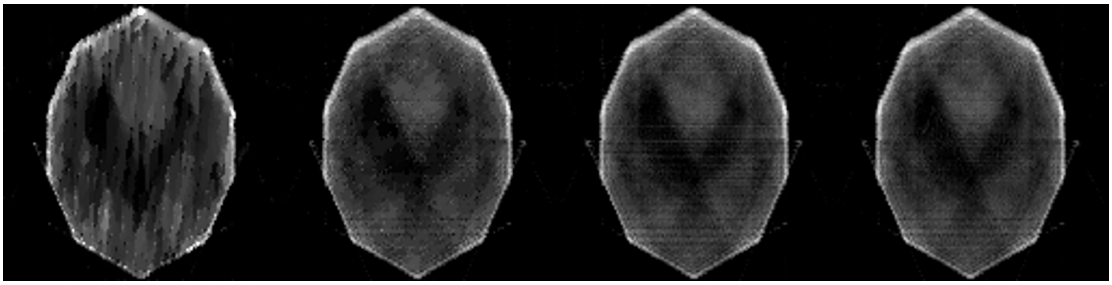

(e) Rand-POCS-ATV (f) Rand-POCS-RWTV (g) POCS-RWATV (h) Rand-POCS-RWATV

Figure 5.13: Reconstructions of the Shepp-Logan phantom with Gaussian noise ($\sigma = 0.05$).

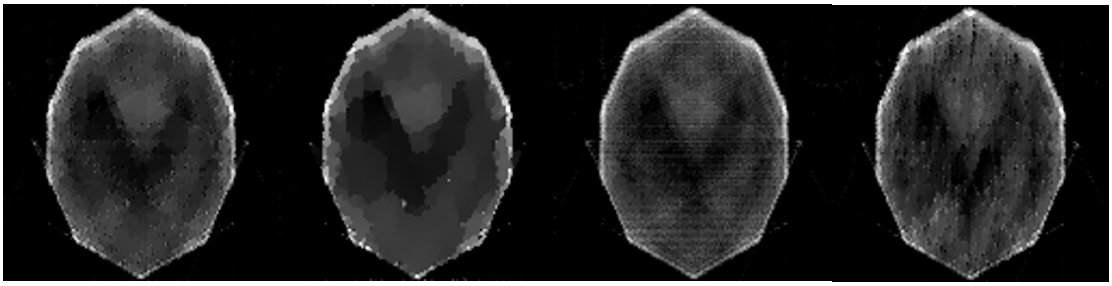

(a) ASD-POCS (b) Rand-POCS (c) POCS-RWTV (d) POCS-ATV

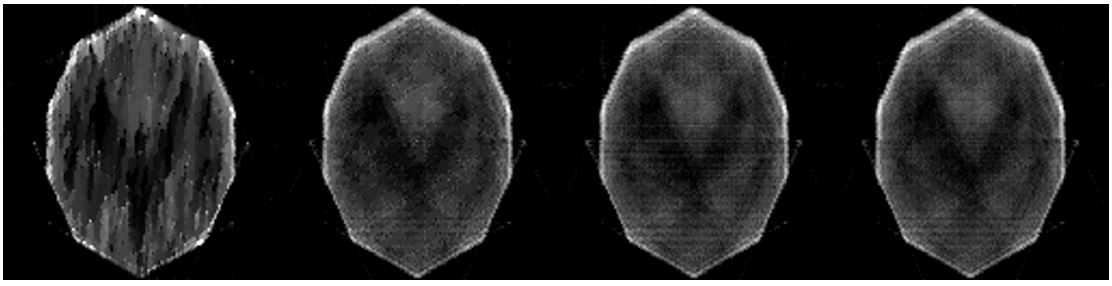

(e) Rand-POCS-ATV (f) Rand-POCS-RWTV (g) POCS-RWATV (h) Rand-POCS-RWATV

Figure 5.14: Reconstructions of the Shepp-Logan phantom with Gaussian noise ($\sigma = 0.10$).

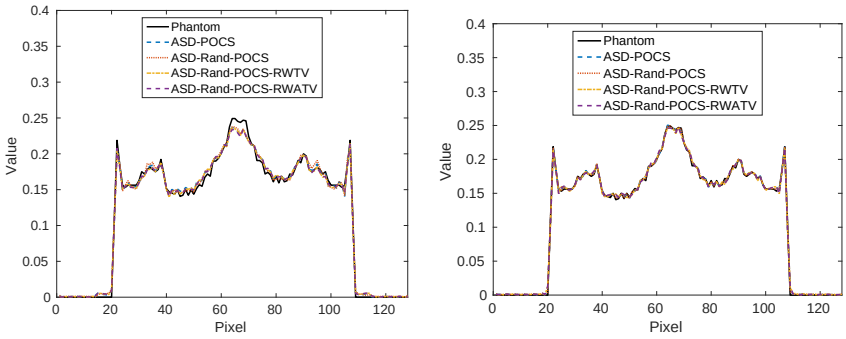

(a) noiseless, 5 views

(b) noiseless, 11 views

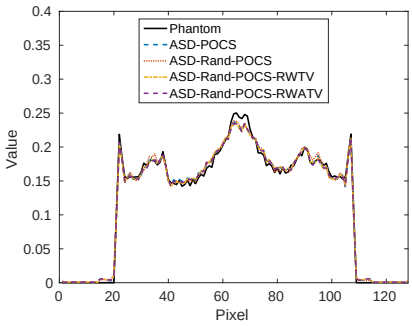

(c) $\sigma = 0.01$, 5 views

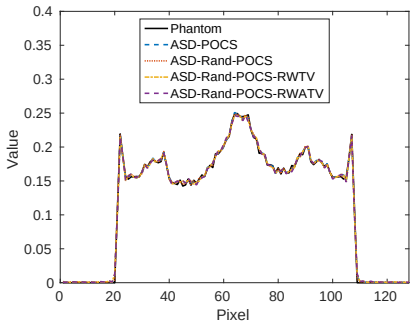

(d) $\sigma = 0.01$, 11 views

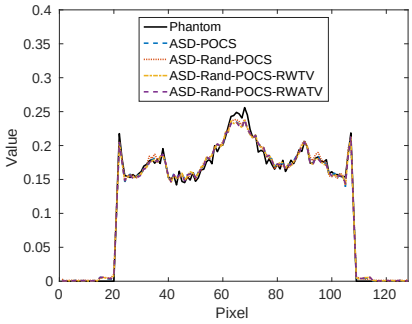

(e) $\sigma = 0.05$, 5 views

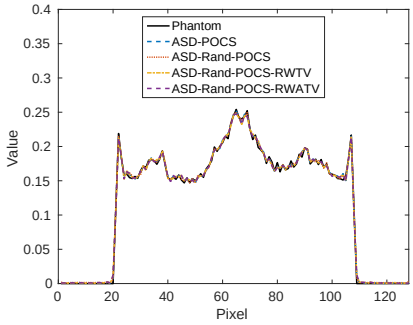

(f) $\sigma = 0.05$, 11 views

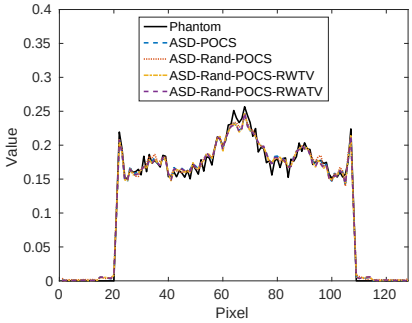

(g) $\sigma = 0.10$, 5 views

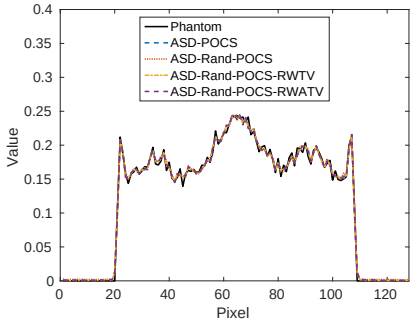

(h) $\sigma = 0.10$, 11 views

Figure 5.15: Integral profile for some of the images shown in the figures above. If simple projection radiography were used to image the cargo, this would be the only information provided. The 11-view scheme fully recovers the true phantom signal, while the 5-view scheme slightly dampens the signal in the center of the object.

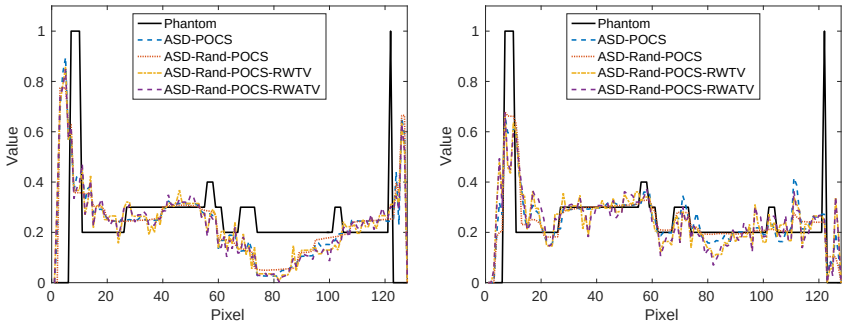

(a) noiseless, 5 views (b) noiseless, 11 views

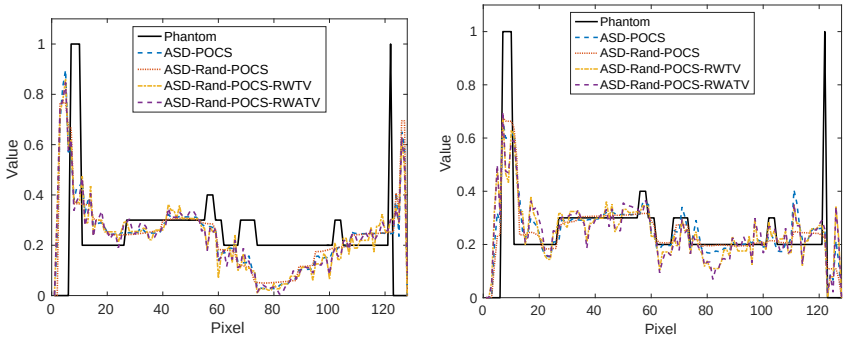

(c) $\sigma = 0.01$, 5 views (d) $\sigma = 0.01$, 11 views

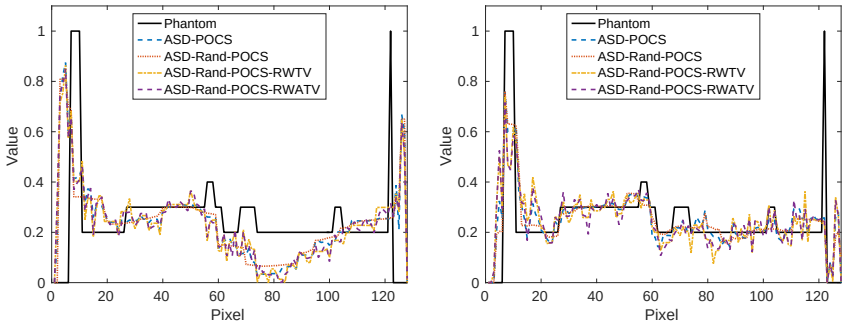

(e) $\sigma = 0.05$, 5 views (f) $\sigma = 0.05$, 11 views

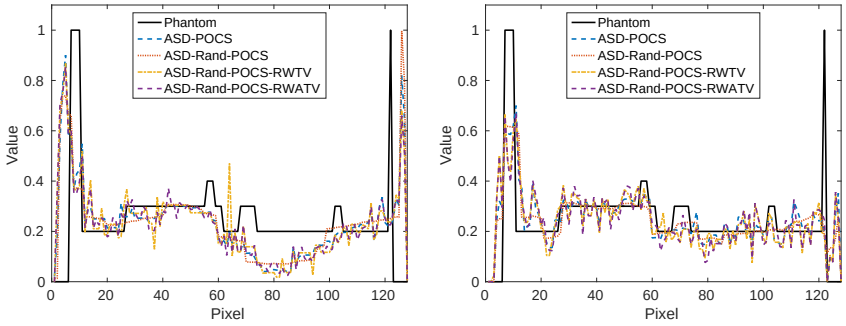

(g) $\sigma = 0.10$, 5 views (h) $\sigma = 0.10$, 11 views

Figure 5.16: Profile through a vertical slice of the images shown above. Limiting the acquisition scheme to only 5 views significantly impacts the reconstruction. At high noise levels the signal recovery is relatively poor for all methods.

POCS produces images with smoother textures and lower noise levels. Additionally, when the noise on the data is low, the three small lesions at the bottom of the phantom can be fully resolved. At the highest noise level the ASD-Rand-POCS method produces a salt-and-pepper artifact. In cases where this kind of artifact are produced, it could be easily removed by using a median filter on the image. Overall, ASD-Rand-POCS generally performs better with regards to error and SSIM, and the reconstructed images typically have better textures and spatial resolution.

Geant4 Phantom

After algorithmic comparison on numerical phantom data, a more realistic cargo simulation was run. The geometry, seen in Figure 5.20, is the same water phantom presented in Chapter 4, but flipped on its side. The figure shows γ-rays from a view at $36°$. This geometry is one detector height. The data was generated in a fan-beam, as opposed to a cone-beam, for decreased computational time. Tomographic data was taken with 11 views with both the LENR beam and the bremsstrahlung beams, and the dose to the cargo was matched for each acquisition. The flux per view was adjusted to account for the longer source-to-detector distance more oblique views. ASD-POCS and ASD-Rand-POCS algorithms were used for reconstructed. Each algorithm was carried out for 200 iterations. Some images shown below are converted to Hounsfield units (HU)

$$HU = \frac{\mu_{mat} - \mu_{water}}{\mu_{water}} * 1000 \tag{5.13}$$

where μ_{mat} and μ_{water} are the linear attenuation coefficients for a given material and water, respectively. Converting images to HU mitigates the differences in μ as a function of energy, allowing LENR and bremsstrahlung images to be shown on the same window.

Figure 5.21 shows the reconstructed low-energy images taken with 11 views, and Figure 5.22 shows the reconstructed high-energy images. In both figures, each image is shown on

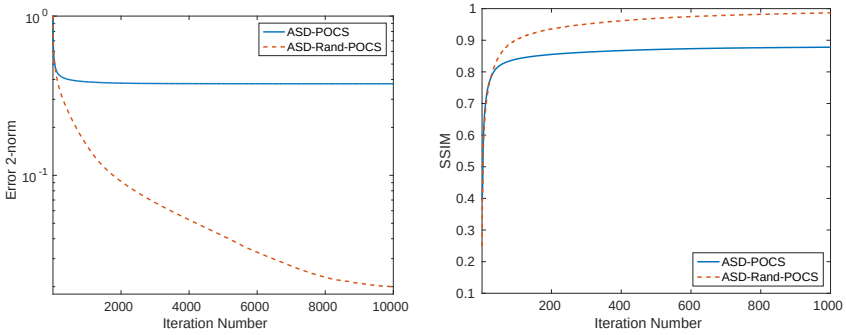

(a) noiseless

(b) noiseless

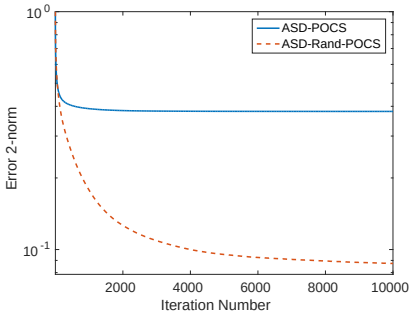

(c) $\sigma = 0.01$

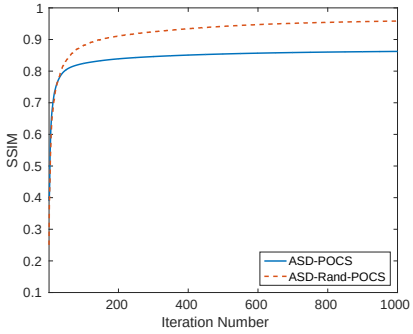

(d) $\sigma = 0.01$

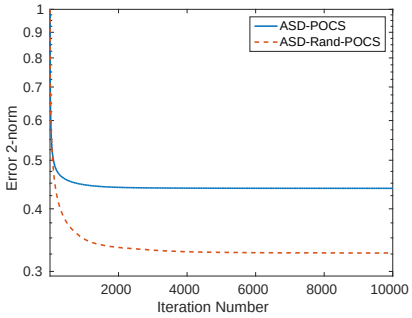

(e) $\sigma = 0.05$

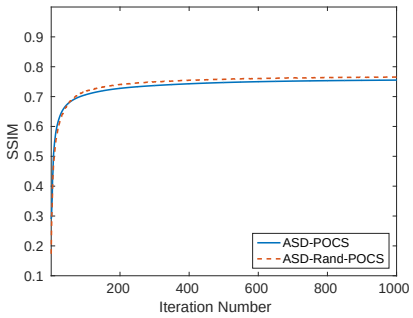

(f) $\sigma = 0.05$

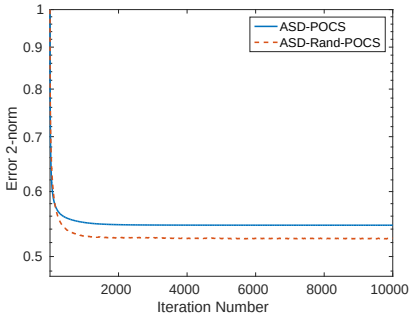

(g) $\sigma = 0.10$

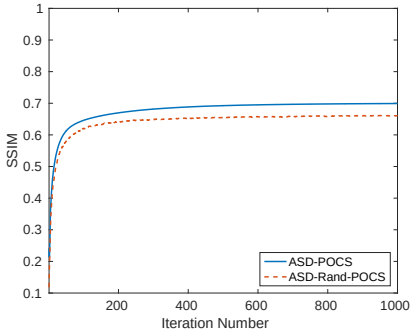

(h) $\sigma = 0.10$

Figure 5.17: Error 2-norm and structural similarity for ASD-POCS and ASD-Rand-POCS when the reconstruction was carried out for 10,000 iterations. With noiseless data, the ASD-Rand-POCS algorithm greatly outperforms ASD-POCS. As noise is increased, the improvement decreases.

(a) noiseless (b) $\sigma = 0.01$ (c) $\sigma = 0.05$ (d) $\sigma = 0.10$

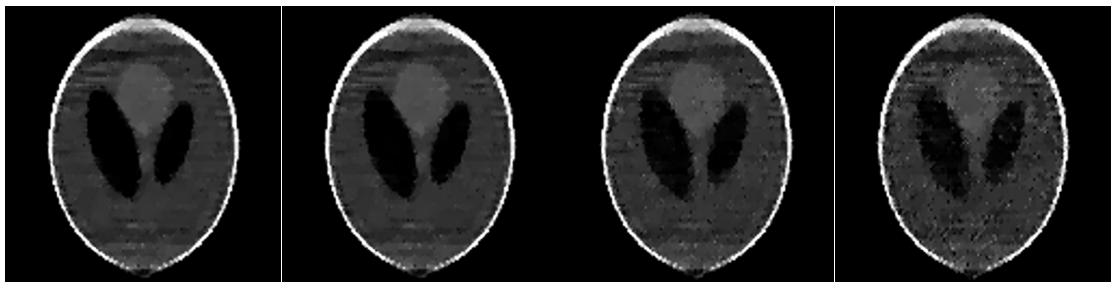

(e) noiseless (f) $\sigma = 0.01$ (g) $\sigma = 0.05$ (h) $\sigma = 0.10$

Figure 5.18: Reconstructions of the Shepp-Logan phantom after 10,000 iterations. (a)-(d) show reconstructions with ASD-Rand-POCS and (e)-(h) show reconstructions with ASD-POCS. The random algorithm better reduces image noise at all original noise levels and produces images with smoother textures.

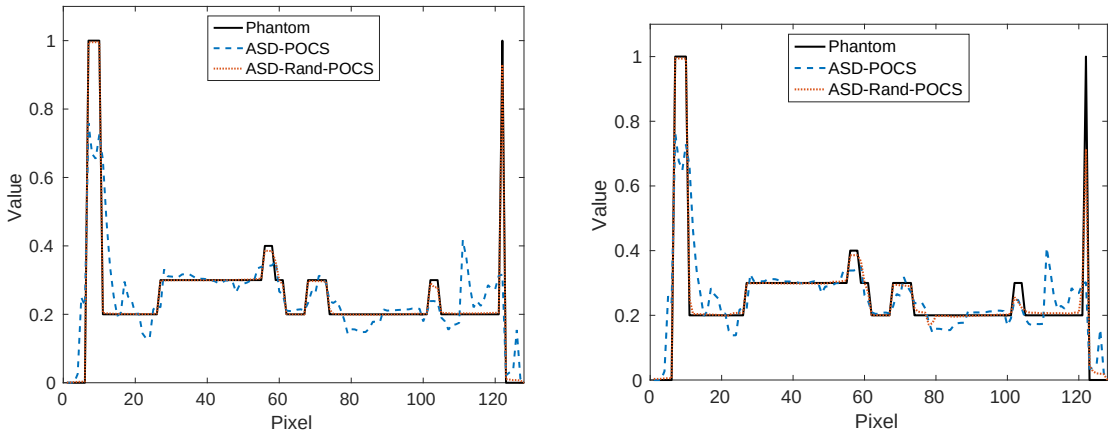

(a) noiseless (b) $\sigma = 0.01$

(c) $\sigma = 0.05$ (d) $\sigma = 0.10$

Figure 5.19: Vertical profiles through the images shown in Figure 5.18. At low noise levels, the ASD-Rand-POCS recovers the original signal nearly perfectly. As the noise gets stronger, both methods degrade.

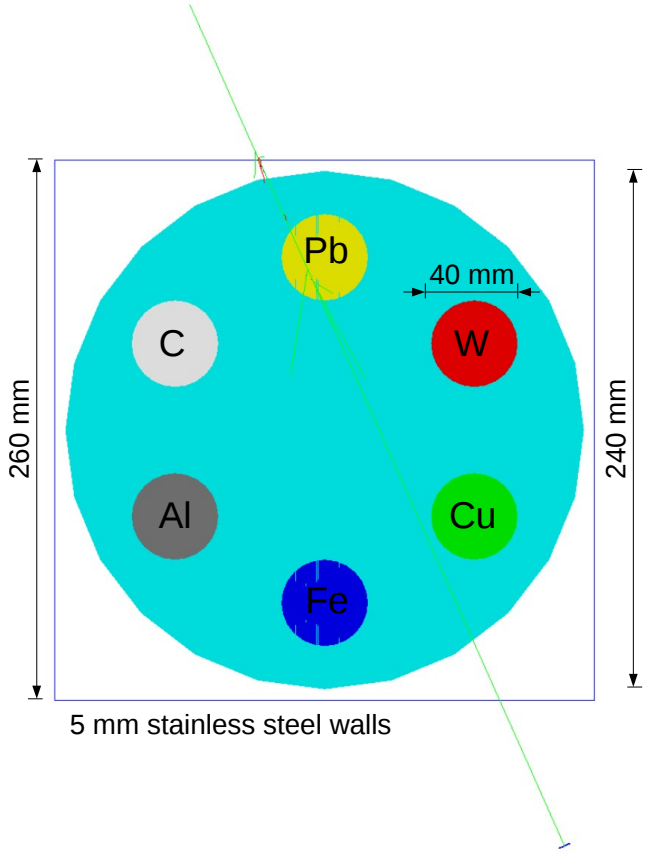

Figure 5.20: Geant4 simulation phantom for tomographic image reconstruction.

two windows, one in HU which shows the rods and one in μ which better shows the image background. On the simulated data, the ASD-Rand-POCS outperforms the ASD-POCS method. Four rods are seen on both images (a) and (b), but (c) and (d) show that the ASD-Rand-POCS method can reconstruct all six rods while ASD-POCS only sees four. ASD-Rand-POCS better preserves the background values, although both methods reconstruct several zero pixels within the phantom. The front and rear walls cannot be seen in any reconstruction, an artifact of the limited-angle acquisition scheme.

Figure 5.23 shows the reconstructed low-energy images taken with 5 views, and Figure 5.24 shows the reconstructed high-energy images. On this relatively simple phantom geometry, the 5-view reconstructions do better than they did for the Shepp-Logan phantoms. Both reconstruction techniques also find 5 rods where ASD-POCS only found 4 rods with 11 views. These images suffer more from under-sampling artifacts, shown as streaks across the water cylinder and above the container.

As with radiographic imaging, the advantage of acquisition at multiple photon energies is that material compositions can be back-calculated from multiple measurements of material coefficients. Basis material decomposition in CT is typically carried out via matrix inversion methods, but these lead to noise amplification[106]. Since the noise levels are already high and the image quality is poor on these reconstructed images, material identification will instead be calculated similarly to the methods presented in Chapter 4. A mean value for each rod in each transmission image was calculated, and the ratio of the high-energy value to the low-energy value (R-value) is calculated. Table 5.3 shows the error on the measured R-values for each rod on both the 5-view and 11-view images.

Conclusions

Tomography has been widely used in medical imaging because of its non-invasive capability to inside of patients. It has also been employed in some security scanning environments, but has previously been thought of as infeasible for cargo container imaging. By drawing on

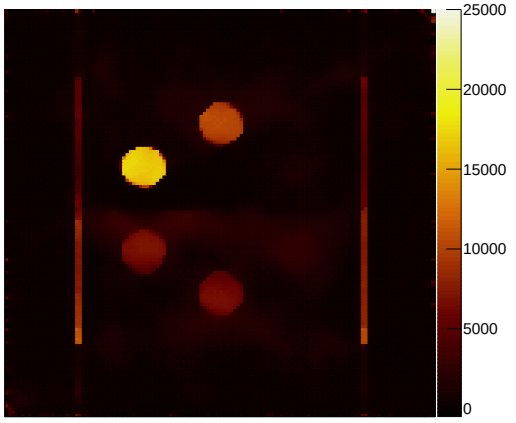

(a) LENR, ASD-Rand-POCS, HU

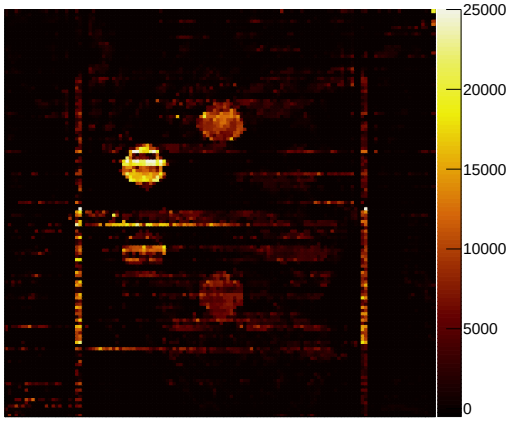

(b) LENR, ASD-POCS, HU

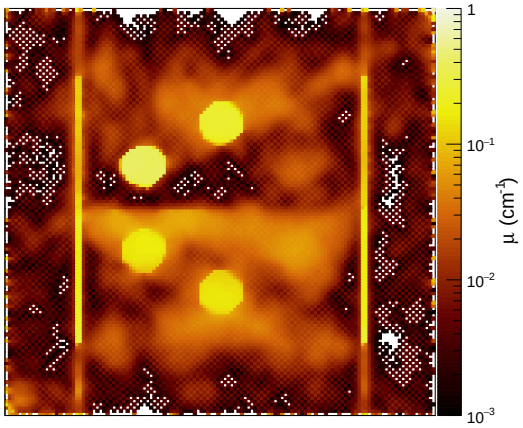

(c) LENR, ASD-Rand-POCS, μ

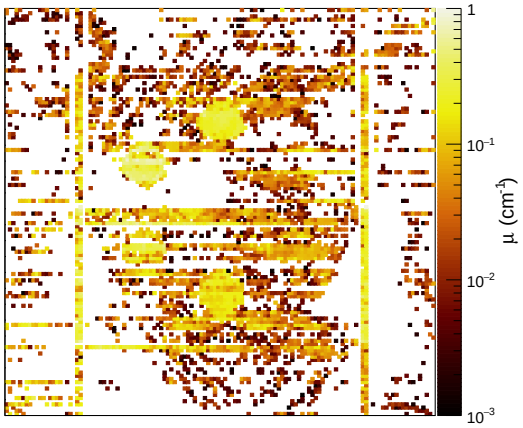

(d) LENR, ASD-POCS, μ

Figure 5.21: Low-energy CT images of the container phantom, reconstructed with ASD-Rand-POCS and ASD-POCS. The top row shows images in HU, highlighting the rods and container walls, and the bottom row shows images in μ on a logarithmic scale, highlighting the full water cylinder. Zero pixels are shown as white in the lower images. As with the Shepp-Logan phantom, the random algorithm suppresses noise and preserves smoother textures. Both methods reconstruct 4 of the rods adequately, and the fifth and sixth rods (copper and carbon) can faintly be seen on the ASD-Rand-POCS image in μ.

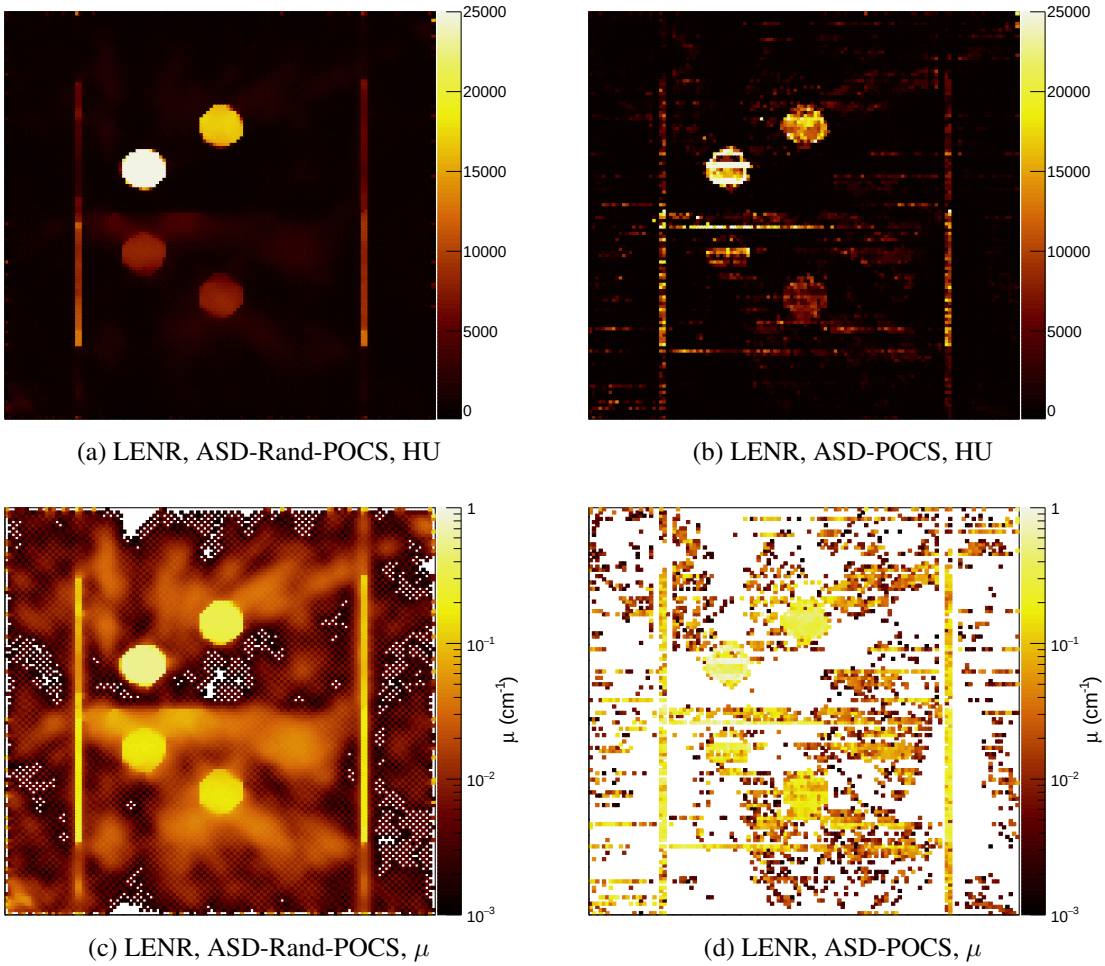

(a) LENR, ASD-Rand-POCS, HU

(b) LENR, ASD-POCS, HU

(c) LENR, ASD-Rand-POCS, μ

(d) LENR, ASD-POCS, μ

Figure 5.22: High-energy CT images of the container phantom, reconstructed with ASD-Rand-POCS and ASD-POCS. Note that the contrast is higher at higher energies, although the image quality for both methods is similar to that shown in Figure 5.21

Table 5.3: Percent error of the R-values for the images shown in Figures 5.21 - 5.24

	5 Views		11 Views	
Z	ASD-POCS	ASD-Rand-POCS	ASD-POCS	ASD-Rand-POCS
		LENR		
6	95.02 ± 11.11	64.56 ± 11.33	27.97 ± 68.86	0.10 ± 21.11
13	43.84 ± 27.93	28.92 ± 4.41	4.21 ± 66.09	18.04 ± 10.26
26	2.54 ± 22.19	5.72 ± 4.86	2.67 ± 50.98	2.94 ± 5.60
29	1.45 ± 91.88	7.58 ± 3.98	3.91 ± 84.64	1.88 ± 5.96
74	7.24 ± 27.70	6.96 ± 2.94	2.91 ± 95.93	4.13 ± 3.40
82	0.20 ± 23.47	2.17 ± 7.57	5.52 ± 67.20	0.37 ± 6.58
RMSE	42.84 ± 6.36	29.29 ± 4.23	11.98 ± 28.27	7.69 ± 4.05

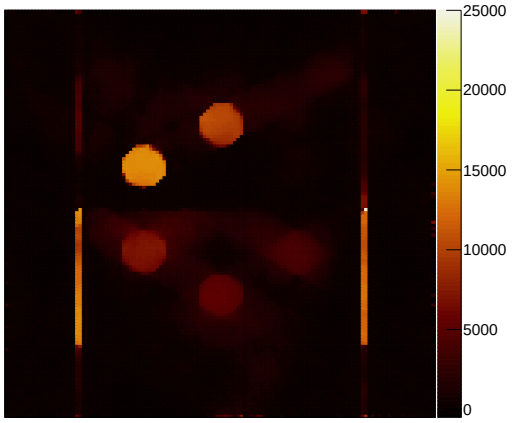

(a) LENR, ASD-Rand-POCS, HU

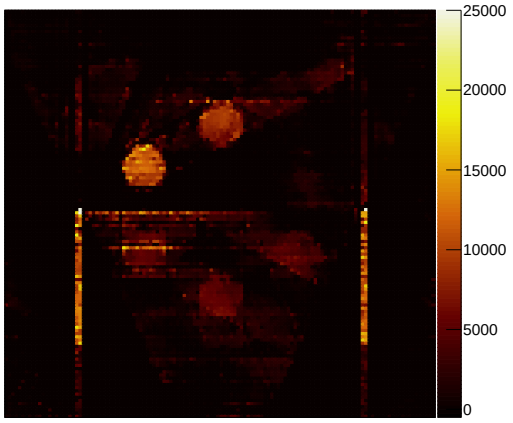

(b) LENR, ASD-POCS, HU

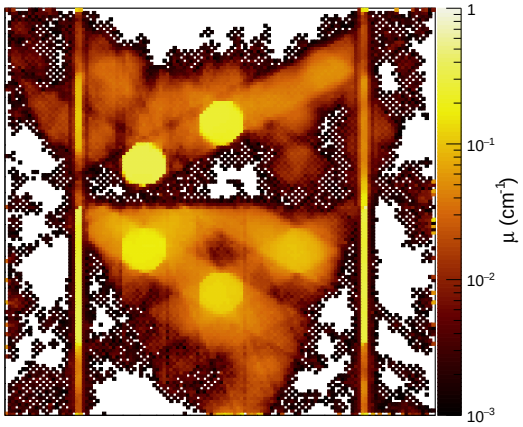

(c) LENR, ASD-Rand-POCS, μ

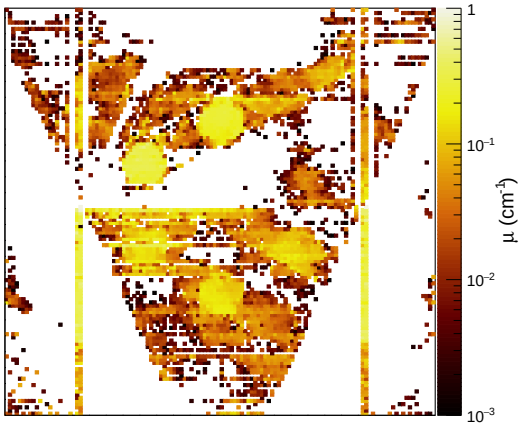

(d) LENR, ASD-POCS, μ

Figure 5.23: Low-energy CT images of the container phantom, reconstructed with ASD-Rand-POCS and ASD-POCS, taken with 5 views. Both reconstruction techniques preserve 5 rods on this dataset. The water cylinder is also more strongly preserved in this case, though under-sampling artifacts are more prevalent, especially on the μ images.

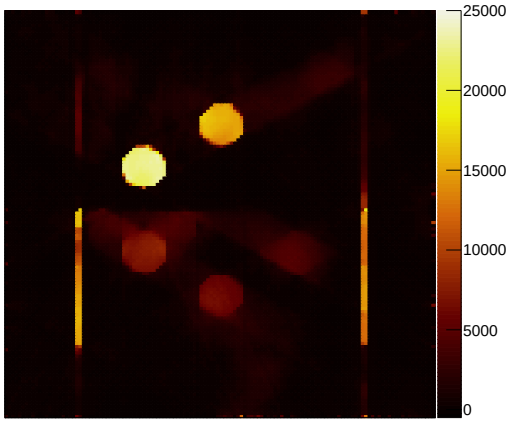

(a) LENR, ASD-Rand-POCS, HU

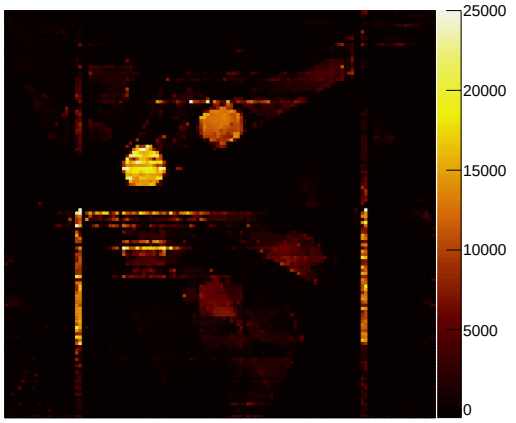

(b) LENR, ASD-POCS, HU

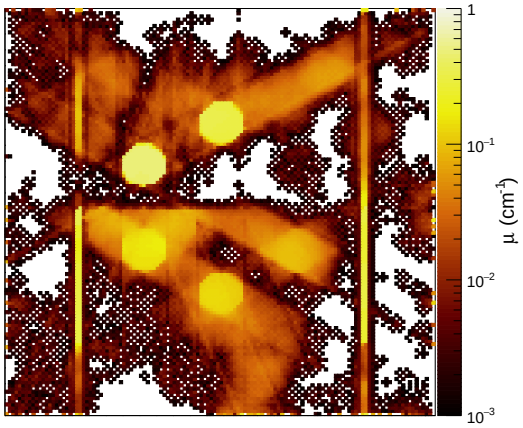

(c) LENR, ASD-Rand-POCS, μ

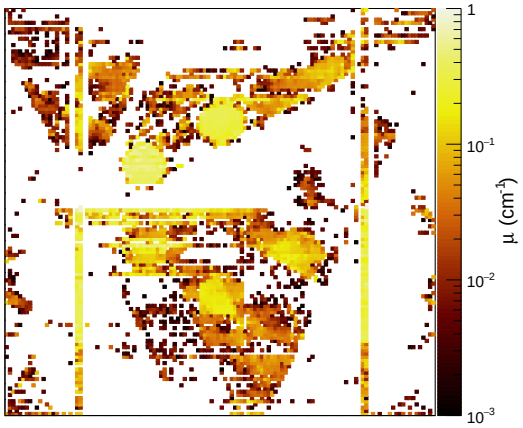

(d) LENR, ASD-POCS, μ

Figure 5.24: High-energy CT images of the container phantom, reconstructed with ASD-Rand-POCS and ASD-POCS. Note that the contrast is higher at higher energies, although the image quality for both methods is similar to that shown in Figure 5.23

the vast medical literature, this work has shown that some form of tomography may be possible for cargo container imaging. Rather than rotating the container or the source/detector, an isotropic (or nearly isotropic) radiation source can be collimated down to a few views of the container, and this data can be reconstructed via iterative algorithms.

An algorithm developed for limited-angle few-view CT, ASD-POCS, was employed for the cargo scenario. A small modification to the algorithm, namely randomizing the matrix multiplication process (termed ASD-Rand-POCS), allowed for larger error reduction and larger structural similarities when tested on a numerical phantom commonly used in medical CT. When tested on Geant4-generated data of a more realistic cargo scanning situation, ASD-Rand-POCS outperformed ASD-POCS in both image quality and reconstruction accuracy. Although the spatial resolution of the reconstructed images was not evaluated, 4 cm rods of varying-Z materials were easily identified as long as they had relatively high inherent contrast. Images acquired with as little as 5 views of the cargo were able to reconstruct material R-values with RMS-error of 6.85% ($\pm$ 2.15%) on 4 mid-Z and high-Z rods.

In this chapter, it was shown that reconstruction is possible for one specific phantom, but further testing is needed. The angles used for reconstruction spanned $\pm 60^{\circ}$, leading to a large footprint for a cargo scanning system. Ideally, this span would be decreased as much as possible for accurate reconstruction to reduce the size of the imaging system. It should also be noted that when scanning a realistic cargo container, the oblique views will have longer path lengths through the container. Although the simulation in this chapter accounted for the $1/r^2$ flux fall-off, attenuation through larger portions of the container were not tested because the phantom used was round. This higher attenuation will lead to noisier projections from the oblique views which could degrade image quality. This could be accounted for by weighting projections according to the signal-to-noise ratio in the ART step.

CHAPTER 6
CONCLUSIONS

This thesis characterized the imaging capabilities of a monoenergetic γ-ray imaging system. Two types of monoenergetic imaging beams were used, one driven by the low-energy nuclear reaction $^{11}B(d, n\gamma)^{12}C$ and another system driven by inverse Compton scattering. The goal of this work was to show that use of these beams can lead to improved cargo radiography. This was tested through characterization of beam penetration, scattering, and energy information. The LENR beam was compared to bremsstrahlung beam in both small-scale and full-scale imaging simulations. Additionally, some practical characteristics of the detector array were studied with simulation and experiment.

It was found that both monoenergetic imaging beams are more highly penetrating than bremsstrahlung beams, the industry standard for cargo radiography. Higher penetration can lead to decreased scan times as more photons make it through the cargo, given comparable fluxes can be produced. As more photons move through the container without interacting, comparable image quality can be attained with lower dose to the cargo. The LENR beam was found to be 33% more penetrating (through an average cargo container) than the combined bremsstrahlung imaging beams, while the combined MPS beam was 176% more penetrating than the bremsstrahlung beams. Through simulation, this work showed that within the cargo container, monoenergetic beams deliver more of their dose within the beamline, meaning total dose to the cargo is decreased. To investigate the penetration effects on a human stowaway in the container, the penetration results were integrated with detection efficiency. It was shown that the LENR beams provide around a 30% dose reduction to the human phantom and the MPS beams provide roughly a 40% dose reduction for the same signal in the detector.

Monoenergetic beams experience no spectral shift as they move through cargo so they

can more accurately reconstruct the material attenuation coefficient. These beams are also capable of achieving better material specificity when dual-energy images are acquired due to a larger separation between the beams in energy. For a range in atomic number from 3 to 92, the dynamic range of the R-value (which corresponds to Z) is around 0.4 for a bremsstrahlung beam and 0.9 for the LENR beam, yielding better separation especially at lower Z.

The imaging system used in this work is comprised of mainly quartz Cherenkov radiation detectors. These detectors were chosen because their inherent energy threshold rejects most scattered signal and they process pulses faster than other typical detectors such as scintillators. This leads to less system dead time, and the energy threshold blinds these detectors to most detector cross talk, which can become a problem as sensors are placed close together in imaging arrays. A complete detector response function for photons from 0.4 to 15.5 MeV was developed after the detector model was validated against experimental data. This allowed for a complete understanding of the detection efficiency and spectral quality over the entire energy space relevant to cargo imaging. Detector-to-detector cross talk for the imaging array has been characterized, and it was found that cross talk contributes less than 2% of the overall signal for the 25-mm quartz detectors for a 4.4 MeV beam. The higher energy imaging beams, such as the LENR beam, lead to higher cross talk than lower energy or bremsstrahlung beams, but in the worst case scenario, the cross talk probability is less than 1% for the 6-mm detectors with 5 mm edge-to-edge separation. Cross talk in LYSO is higher due to its higher efficiency and different detection mechanism. However, implementation of a 1 MeV energy threshold reduces the maximal cross talk to less than 4%. Finally, it is found that after penetration through 20 cm of steel, representing an average cargo container, monoenergetic beams can offer at least a 23% reduction in dose to the cargo for equivalent dose to the detectors. This is important because dose to the detectors is directly correlated with image quality. For the best case scenario, LYSO detectors with MPS beams, the dose reduction can be as great as 62%.

Bremsstrahlung and LENR imaging beams are evaluated for image quality on Geant4-generated data. The detector array is also tested for limits in spatial resolution. According to the test outlined in ANSI standard N42.46-2008, the spatial resolution of the detector array is 4 mm. This work has shown that the presence of cargo in the beam (specifically steel) can hinder this spatial resolution by reducing the image contrast and increasing image noise. R-value reconstructed images are used here to represent images in material atomic number (Z_{eff}). Due to the higher separation in energy of the LENR beam as compared to the bremsstrahlung beam, LENR images produce higher-contrast R-values, leading to enhanced detectability of high-Z materials and potentially smuggled SNM. Two radiography simulations were run to test the imaging beams, one small-scale container and one full-scale container. The two methods perform similarly with regards to error, but the LENR beam produces 50% and 155% higher CNR on the two tests.

A noise suppression technique, using the full transmission data to generate a true material map, was implemented to enhance CNR for both methods. While the noise suppression was stronger for the LENR method, it produced noise reduction by at least a factor of 5. At the lowest dose LENR image, noise STD was reduced by a factor of 45. By reducing the noise, the effective spatial resolution of each imaging system was increased, as shown on the full-scale cargo image. With noise suppression it is possible to reduce the dose necessary to image. It was found that similar image quality and accuracy were found when acquiring an image with 1/10 as much dose as had been previously used. It is possible that the dose could be reduced even further with optimiziation of the noise suppression algorithm.

Both the LENR and bremsstrahlung beams are produced relatively isotropically. Typically, these beams are collimated down to narrow fan beams, tossing away most of the flux produced. Instead, these could be collimated down to a few separate beams leaving the accelerator at multiple angles. If multiple detector arrays were placed downstream from the cargo, near tomographic data could be reconstructed using advanced reconstruction

algorithms. The final contribution of this work has shown that slight modifications to algorithms proposed for medical CT reconstruction can achieve some form of tomography in some sense. After initial testing and characterization on numerical phantoms, the reconstruction algorithm, ASD-Rand-POCS, was tested on Geant4-simulated data. While the spatial resolution of the image reconstruction was not tested, it was able to accurately reconstruct contrast rods of mid-Z and high-Z materials using only 5 views of the container. By reconstructing data in different energy domains, R-values were reconstructed in the same manner as radiographic images. For all six rods, including two low-Z materials, the reconstructions calculated R-value with 29% RMSE. Focusing on only the 4 mid-Z and high-Z rods, the RMSE was reduced to 7%.

REFERENCES

[1] C. Paris, "The state of global shipping in three charts," *The Wall Street Journal*, 2017.

[2] C. Paris and L. Llamas, "A brief history of shipping," *The Wall Street Journal*, 2018.

[3] E. Phillips, "Vibrant holiday sales spur late-season surge in imports," *The Wall Street Journal*, 2017.

[4] H. Gowadia, "FY17 research and development efforts at the U.S. Dept. of Homeland Security," United States Cong. Senate Subcommittee on Homeland Security, Tech. Rep., 2016.

[5] C. D. Clemett, P. N. Martin, C. Hill, J. R. Threadgold, R. C. Maddock, B. Campbell, J. OMalley, R. S. Woolf, B. F. Phlips, A. L. Hutcheson, *et al.*, "Active interrogation of depleted uranium using a single pulse, high-intensity photon and mixed photon-neutron source," *IEEE Trans. Nucl. Sci.*, vol. 62, no. 2, pp. 494–503, 2015.

[6] J. Jones, B. Blackburn, S. Watson, D. Norman, and A. Hunt, "High-energy photon interrogation for nonproliferation applications," *Nucl. Instrum. Meth. A*, vol. 261, no. 1, pp. 326–330, 2007.

[7] V. J. Orphan, E. Muenchau, J. Gormley, and R. Richardson, "Advanced gamma-ray technology for scanning cargo containers," *Appl. Radiat. Isot.*, vol. 63, no. 5, pp. 723–732, 2005.

[8] B. Sowerby and J. Tickner, "Recent advances in fast neutron radiography for cargo inspection," *Nucl. Instrum. Meth. A*, vol. 580, no. 1, pp. 799–802, 2007.

[9] R. C. Runkle, D. L. Chichester, and S. J. Thompson, "Rattling nucleons: New developments in active interrogation of special nuclear material," *Nucl. Instrum. Meth. A*, vol. 663, no. 1, pp. 75–95, 2012.

[10] C. Moss, C. Hollas, G. McKinney, and W. Myers, "Comparison of active interrogation techniques," in *IEEE NSS/MIC, 2005*, IEEE, vol. 1, 2005, pp. 329–332.

[11] H. Martz, S. Glenn, J. A. Smith, C Divin, and S. Azevedo, "Poly- versus mono-energetic dual-spectrum non-intrusive inspection of cargo containers," *IEEE Trans. Nucl. Sci.*, vol. 64, no. 7, pp. 1709–1718, 2017.

[12] B. Archambault, A. Hagen, K. Masuda, N. Yamakawa, and R. P. Taleyarkhan, "Threshold rejection mode active interrogation of SNMs using continuous beam DD neutrons with centrifugal and acoustic tensioned metastable fluid detectors," *IEEE Trans. Nucl. Sci.*, 2016.

[13] J. E. Goldsmith, J. S. Brennan, M. D. Gerling, P. A. Marleau, and M. Monterial, "Additional capabilities of a compact neutron scatter camera: Active interrogation, time-correlated pulse-height multiplication measurements, and gamma imaging," in *IEEE NSS/MIC, 2015*, IEEE, 2015, pp. 1–4.

[14] R. S. Woolf, B. F. Phlips, A. L. Hutcheson, E. A. Wulf, J. C. Zier, S. L. Jackson, D. P. Murphy, R. J. Commisso, J. W. Schumer, C. D. Clemett, *et al.*, "Pulsed power active interrogation of shielded fissionable material," *IEEE Trans. Nucl. Sci.*, vol. 62, no. 3, pp. 1278–1287, 2015.

[15] C. Geddes, B. Ludewigt, J. Valentine, B. Quiter, M. Descalle, G. Warren, M. Kinlaw, S. Thompson, D. Chichester, C. Miller, *et al.*, "Impact of monoenergetic photon sources on nonproliferation applications final report," Idaho National Laboratory (INL), Idaho Falls, ID (United States), Tech. Rep., 2017.

[16] E. A. Miller, J. A. Caggiano, R. C. Runkle, T. A. White, and A. M. Bevill, "Scatter in cargo radiography," *Appl. Radiat. Isot.*, vol. 69, no. 3, pp. 594–603, 2011.

[17] *Varex Imaging*, `https://www.vareximaging.com`, accessed March 1, 2018.

[18] *Rapiscan Systems*, `https://www.rapiscansystems.com`, accessed March 1, 2018.

[19] *Nuctech*, `https://www.nuctech.com`, accessed March 1, 2018.

[20] C. Geddes, S. Rykovanov, N. H. Matlis, S. Steinke, J.-L. Vay, E. H. Esarey, B. Ludewigt, K. Nakamura, B. J. Quiter, C. B. Schroeder, C. Toth, and W. P. Leemans, "Compact quasi-monoenergetic photon sources from laser-plasma accelerators for nuclear detection and characterization," *Nucl. Instrum. Meth. B*, vol. 350, pp. 116 –121, 2015.

[21] S. Banerjee, S. Chen, N. Powers, D. Haden, C. Liu, G. Golovin, J. Zhang, B. Zhao, S. Clarke, S. Pozzi, J. Silano, H. Karwowski, and D. Umstadter, "Compact source of narrowband and tunable x-rays for radiography," *Nucl. Instrum. Meth. B*, vol. 350, pp. 106 –111, 2015.

[22] P. Rose, A. Erickson, M Mayer, J Nattress, and I Jovanovic, "Uncovering special nuclear materials by low-energy nuclear reaction imaging," *Sci. Rep.*, vol. 6, p. 24 388, 2016.

[23] B. E. O'Day III, Z. S. Hartwig, R. C. Lanza, and A. Danagoulian, "Initial results from a multiple monoenergetic gamma radiography system for nuclear security," *Nucl. Instrum. Meth. A*, vol. 832, pp. 68–76, 2016.

[24] J. Nattress and I. Jovanovic, "Response and calibration of organic scintillators for gamma-ray spectroscopy up to 15-MeV range," *Nucl. Instrum. Meth. A*, vol. 871, pp. 1 –7, 2017.

[25] S. Agostinelli, J. Allison, K. a. Amako, J Apostolakis, H Araujo, P Arce, M Asai, D Axen, S Banerjee, G Barrand, *et al.*, "Geant4: A simulation toolkit," *Nucl. Instrum. Meth. A*, vol. 506, no. 3, pp. 250–303, 2003.

[26] C. Liu, G. Golovin, S. Chen, J. Zhang, B. Zhao, D. Haden, S. Banerjee, J. Silano, H. Karwowski, and D. Umstadter, "Generation of 9 MeV γ-rays by all-laser-driven Compton scattering with second-harmonic laser light," *Opt. Lett.*, vol. 39, no. 14, pp. 4132–4135, 2014.

[27] T. Taddeucci and R. Sheffield, "Neutron and gamma-ray production with low energy beams," LA-UR-07-2724, Los Alamos National Laboratory, Los Alamos NM, Tech. Rep., 2007.

[28] A. Antolak, B. Doyle, K.-N. Leung, D. Morse, and P. Provencio, "Active interrogation using low-energy nuclear reactions," in *Proc. SPIE*, Int. Soc. Opt. Photonics, vol. 5923, 2005, p. 592 303.

[29] T. J. Kwan, R. E. Morgado, T.-S. F. Wang, B Vodolaga, V Terekhin, L. Onischenko, S. Vorozhtsov, E. Samsonov, A. Vorozhtsov, Y. G. Alenitsky, *et al.*, "The development of enabling technologies for producing active interrogation beams," *Rev. Sci. Instrum.*, vol. 81, no. 10, p. 103 304, 2010.

[30] S Ogorodnikov and V Petrunin, "Processing of interlaced images in 4–10 MeV dual energy customs system for material recognition," *Phys. Rev. Accel. Beams*, vol. 5, no. 10, p. 104 701, 2002.

[31] R. E. Alvarez and A. Macovski, "Energy-selective reconstructions in x-ray computerised tomography," *Phys. Med. & Biol.*, vol. 21, no. 5, p. 733, 1976.

[32] P. M. Shikhaliev, "Megavoltage cargo radiography with dual energy material decomposition," *Nucl. Instrum. Meth. A*, vol. 882, pp. 158 –168, 2018.

[33] P. B. Rose Jr. and A. S. Erickson, "Cherenkov detectors for spatial imaging applications using discrete-energy photons," *J. Appl. Phys.*, vol. 120, no. 6, p. 064 903, 2016.

[34] *Passport Systems Inc*, `https://www.passportsystems.com`, accessed March 1, 2018.

[35] W. Bertozzi, R. Hasty, A. Klimenko, S. E. Korbly, R. J. Ledoux, and W. Park, "Imaging and radiography with nuclear resonance fluorescence and effective-z (EZ-3D™) determination; SNM detection using prompt neutrons from photon induced fission," in *AIP Conference Proceedings*, AIP, vol. 1099, 2009, pp. 559–564.

[36] S. Van Liew, W. Bertozzi, N. DOlympia, W. A. Franklin, S. E. Korbly, R. J. Ledoux, and C. M. Wilson, "Identification and imaging of special nuclear materials and contraband using active x-ray interrogation," *Physics Procedia*, vol. 90, pp. 313–322, 2017.

[37] J. E. Bakkali and T. E. Bardouni, "Validation of monte carlo geant4 code for a 6mv varian linac," *Journal of King Saud University-Science*, vol. 29, no. 1, pp. 106–113, 2017.

[38] P. Dyer, D. Bodansky, A. G. Seamster, E. B. Norman, and D. R. Maxson, "Cross sections relevant to gamma-ray astronomy: Proton induced reactions," *Phys. Rev. C*, vol. 23, pp. 1865–1882, 5 1981.

[39] J Kiener, M Berheide, N. Achouri, A Boughrara, A Coc, A Lefebvre, F de Oliveira Santos, and C. Vieu, "Gamma-ray production by inelastic proton scattering on ^{16}O and ^{12}C," *Phys. Rev. C*, vol. 58, no. 4, p. 2174, 1998.

[40] R. G. Herb, D. W. Kerst, and J. L. McKibben, "Gamma-rays from light elements due to proton bombardment," *Phys. Rev.*, vol. 51, pp. 691–698, 9 1937.

[41] A. Fessler, T. Massey, B. Micklich, and D. Smith, "Thick target photon yields and angular distributions for the ^{19}F(p,$\alpha\gamma$)^{16}O source reaction at incident proton energies between 1.5 and 4.0 MeV," *Nucl. Instrum. Meth. A*, vol. 450, no. 2, pp. 353 –359, 2000.

[42] S. Harissopulos, C. Chronidou, K. Spyrou, T. Paradellis, C. Rolfs, W. Schulte, and H. Becker, "The ^{27}Al (p,γ)^{28}Si reaction: Direct capture cross-section and resonance strengths at E_p = 0.2-1.12 MeV," *Eur. Phys. J. A*, vol. 9, no. 4, pp. 479–489, 2000.

[43] B. S. Henderson, H. Y. Lee, T. D. MacDonald, R. G. Nelson, and A. Danagoulian, "Experimental demonstration of multiple monoenergetic gamma radiography for effective atomic number identification in cargo inspection," *ArXiv preprint arXiv:1802.04225*, 2018.

[44] P. B. Rose, *Imaging of special nuclear materials using monochromatic gamma rays from low-energy nuclear reactions*, 2017.

[45] W. Gillis, "Method development and performance study of Geant4 and Gold's algorithm for gamma spectral unfolding," Master's thesis, Georgia Institute of Technology, 2018.

[46] K. T. Phuoc, S. Corde, C. Thaury, V. Malka, A Tafzi, J.-P. Goddet, R. Shah, S. Sebban, and A. Rousse, "All-optical Compton gamma-ray source," *Nat. Photonics*, vol. 6, no. 5, p. 308, 2012.

[47] S. Corde, K. T. Phuoc, G. Lambert, R Fitour, V. Malka, A. Rousse, A Beck, and E Lefebvre, "Femtosecond x rays from laser-plasma accelerators," *Rev. Mod. Phys.*, vol. 85, no. 1, p. 1, 2013.

[48] H. Chang, B Qiao, T. Huang, Z Xu, C. Zhou, Y. Gu, X. Yan, M Zepf, and X. He, "Brilliant petawatt gamma-ray pulse generation in quantum electrodynamic laser-plasma interaction," *Sci. Rep.*, vol. 7, p. 45 031, 2017.

[49] D. J. Stark, T. Toncian, and A. V. Arefiev, "Enhanced multi-MeV photon emission by a laser-driven electron beam in a self-generated magnetic field," *Phys. Rev. Lett.*, vol. 116, p. 185 003, 18 2016.

[50] G. Chen, "Understanding x-ray cargo imaging," *Nucl. Instrum. Meth. B*, vol. 241, no. 1, pp. 810 –815, 2005.

[51] W. Snyder *et al.*, "Report of the task group on reference man," Pergamon Press; Oxford, Tech. Rep., 1974.

[52] *NIST XCOM: Photon cross section database*, `https://physics.nist.gov/PhysRefData/Xcom/html/xcom1.html`, accessed April 18, 2018.

[53] P. B. Rose, "Cherenkov detectors for transmission studies of monoenergetic high-energy photons in active interrogation applications," Master's thesis, Georgia Institute of Technology, 2015.

[54] H. R. Vega-Carrillo, E. Manzanares-Acua, A. M. Becerra-Ferreiro, and A. Carrillo-Nuez, "Neutron and gamma-ray spectra of 239–PuBe and 241–AmBe," *Appl. Radiat. Isot*, vol. 57, no. 2, pp. 167 –170, 2002.

[55] *NaI(Tl) and Polyscin NaI(Tl) sodium iodide*, `https://www.crystals.saint-gobain.com/products/nai-sodium-iodide`, accessed April 17, 2018.

[56] *CsI(Tl) thallium activated cesium iodide*, `https://www.crystals.saint-gobain.com/products/csitl-cesium-iodide-thallium`, accessed April 17, 2018.

[57] *Lanthanum bromide*, https://www.crystals.saint-gobain.com/products/brillance-labr3-lanthanum-bromide, accessed April 17, 2018.

[58] *LYSO and engineered LYSO*, https://www.crystals.saint-gobain.com/products/prelude-420-LYSO, accessed April 17, 2018.

[59] *BGO bismuth germanate*, https://www.crystals.saint-gobain.com/products/bgo, accessed April 17, 2018.

[60] *$CdWO_4$ cadmium tungstate*, https://www.crystals.saint-gobain.com/products/cdwo4-cadmium-tungstate, accessed April 17, 2018.

[61] P. Rose and A. Erickson, "Calibration of cherenkov detectors for monoenergetic photon imaging in active interrogation applications," *Nucl. Instrum. Meth. A*, vol. 799, pp. 99–104, 2015.

[62] N. Gagunashvili, "Chi-square tests for comparing weighted histograms," *Nucl. Instrum. Meth. A*, vol. 614, no. 2, pp. 287–296, 2010.

[63] S. Bityukov, N. Krasnikov, A. Nikitenko, and V. Smirnova, "A method for statistical comparison of histograms," *ArXiv:1302.2651*, 2013.

[64] N. Gagunashvili, "Comparison of weighted and unweighted histograms," *ArXiv physics/0605123*, 2006.

[65] G. F. Knoll, *Radiation detection and measurement*, 3rd. John Wiley & Sons, 2000, ch. Radiation Spectroscopy with Scintillators, pp. 329–331.

[66] M. G. Strauss, "Solid-state pulse-height encoding system with pileup reduction for counting at high input rates," *Rev. Sci. Instrum.*, vol. 34, no. 4, pp. 335–345, 1963.

[67] L. Wielopolski and R. P. Gardner, "Prediction of the pulse-height spectral distortion caused by the peak pile-up effect," *Nucl. Instrum. Meth.*, vol. 133, no. 2, pp. 303–309, 1976.

[68] F. H. Tenney, "Idealized pulse pileup effects on energy spectra," *Nucl. Instrum. Meth.*, vol. 219, no. 1, pp. 165–172, 1984.

[69] K. Taguchi, E. C. Frey, X. Wang, J. S. Iwanczyk, and W. C. Barber, "An analytical model of the effects of pulse pileup on the energy spectrum recorded by energy resolved photon counting x-ray detectors," *Med. Phys.*, vol. 37, no. 8, pp. 3957–3969, 2010.

[70] R. Devanathan, L. Corrales, F. Gao, and W. Weber, "Signal variance in gamma-ray detectors: A review," *Nucl. Instrum. Meth. A*, vol. 565, no. 2, pp. 637 –649, 2006.

[71] A. N. Vasil'ev, "From luminescence non-linearity to scintillation non-proportionality," *IEEE Trans. Nucl. Sci.*, vol. 55, no. 3, pp. 1054–1061, 2008.

[72] "Correction of pulse-height spectra for peak pileup effects using periodic and random pulse generators," *Nucl. Instrum. Meth. A*, vol. 255, no. 3, pp. 559 –581, 1987.

[73] *PMT Handbook*, 3rd ed. Hamamatsu Photonics Inc., 2007.

[74] R. Brun and F. Rademakers, "Root: An object oriented data analysis framework," *Nucl. Instrum. Meth. A*, vol. 389, no. 1-2, pp. 81–86, 1997.

[75] Y. Xing, L. Zhang, X. Duan, J. Cheng, and Z. Chen, "A reconstruction method for dual high-energy CT with MeV x-rays," *IEEE Trans. Nucl. Sci.*, vol. 58, no. 2, pp. 537–546, 2011.

[76] F. H. Attix, *Introduction to radiological physics and radiation dosimetry*, 1st. John Wiley & Sons, 2004, pp. 161–162.

[77] T. H. Shin, M. J. Marcath, A. DiFulvio, S. D. Clarke, and S. A. Pozzi, "Neutron cross-talk characterization of liquid organic scintillators," in *IEEE NSS/MIC, 2015*, IEEE, 2015, pp. 1–4.

[78] T. H. Shin, A. Di Fulvio, T. Jordan, D. L. Chichester, S. D. Clarke, and S. A. Pozzi, "Fast neutron multiplicity counter based on Stilbene and EJ-309 scintillators for nuclear non-destructive assay," in *INMM 57th Annual Meeting, Atlanta GA*, 2016.

[79] K. Taguchi, C. Polster, O. Lee, K. Stierstorfer, and S. Kappler, "Spatio-energetic cross talk in photon counting detectors: Detector model and correlated Poisson data generator," *Med. Phys.*, vol. 43, no. 12, pp. 6386–6404, 2016.

[80] H. Bornefalk, C. Xu, C. Svensson, and M. Danielsson, "Design considerations to overcome cross talk in a photon counting silicon strip detector for computed tomography," *Nucl. Instr. Meth. A*, vol. 621, no. 1, pp. 371–378, 2010.

[81] H. Bornefalk and M. Danielsson, "Photon-counting spectral computed tomography using silicon strip detectors: A feasibility study," *Phys. Med. Biol.*, vol. 55, no. 7, p. 1999, 2010.

[82] S. Utrup, M. Chappo, B. Harwood, T. Krecic, R. P. Luhta, R. Mattson, D. Salk, and C. Vrettos, "Design and performance of a 32-slice CT detector system using back-illuminated photodiodes," in *Proc. SPIE*, Int. Soc. Opt. Photonics, vol. 5368, 2004, pp. 40–51.

[83] P. J. L. Riviere, J. Bian, and P. A. Vargas, "Penalized-likelihood sinogram restoration for computed tomography," *IEEE Trans. Med. Imag.*, vol. 25, no. 8, pp. 1022–1036, 2006.

[84] P. B. Rose, personal communication, Aug. 10, 2017.

[85] "American national standard for determination of the imaging performance of x-ray and gamma-ray systems for cargo and vehicle security screening," *ANSI N42.46-2008*, pp. 1–26, 2008.

[86] M. P. L. Z. Joe Harms Tonghe Wang, *Noise suppression for energy-resolved CT using similarity-based non-local filtration*, 2016.

[87] G. E. Legge and J. M. Foley, "Contrast masking in human vision," *J. Opt. Soc. Amer.*, vol. 70, no. 12, pp. 1458–1471, 1980.

[88] D. G. Pelli and P. Bex, "Measuring contrast sensitivity," *Vision Res.*, vol. 90, pp. 10 –14, 2013.

[89] F. Perazzi, P. Krähenbühl, Y. Pritch, and A. Hornung, "Saliency filters: Contrast based filtering for salient region detection," in *IEEE. Conf. Comput. Vision and Pattern Recognition*, IEEE, 2012, pp. 733–740.

[90] J. Harms, T. Wang, M. Petrongolo, T. Niu, and L. Zhu, "Noise suppression for dual-energy CT via penalized weighted least-square optimization with similarity-based regularization," *Med. Phys.*, vol. 43, no. 5, pp. 2676–2686, 2016.

[91] J.-S. Lee, "Digital image smoothing and the sigma filter," *Computer. Gr. Image Process.*, vol. 24, no. 2, pp. 255–269, 1983.

[92] T. Wang and L. Zhu, "Dual energy CT with one full scan and a second sparse-view scan using structure preserving iterative reconstruction (SPIR)," *Phys. Med. Biol.*, vol. 61, no. 18, p. 6684, 2016.

[93] X. Duan, J. Cheng, L. Zhang, Y. Xing, Z. Chen, and Z. Zhao, "X-ray cargo container inspection system with few-view projection imaging," *Nucl. Instrum. Meth. A*, vol. 598, no. 2, pp. 439–444, 2009.

[94] E. Y. Sidky and X. Pan, "Image reconstruction in circular cone-beam computed tomography by constrained, total-variation minimization," *Phys. Med. Biol.*, vol. 53, no. 17, p. 4777, 2008.

[95] E. Y. Sidky, X. Pan, I. S. Reiser, R. M. Nishikawa, R. H. Moore, and D. B. Kopans, "Enhanced imaging of microcalcifications in digital breast tomosynthesis through

improved image-reconstruction algorithms," *Med. Phys.*, vol. 36, no. 11, pp. 4920–4932, 2009.

[96] E. J. Candes, J. Romberg, and T. Tao, "Robust uncertainty principles: Exact signal reconstruction from highly incomplete frequency information," *IEEE Trans. Inf. Theory*, vol. 52, no. 2, pp. 489–509, 2006.

[97] T. Goldstein and S. Osher, "The split bregman method for L1-regularized problems," *SIAM J. Imaging Sci.*, vol. 2, no. 2, pp. 323–343, 2009.

[98] T. Chan, S. Esedoglu, F. Park, and A Yip, "Recent developments in total variation image restoration," *Math. Models Comput. Vision*, vol. 17, no. 2, 2005.

[99] Y. Huang, O. Taubmann, X. Huang, V. Haase, G. Lauritsch, and A. Maier, "Scale-space anisotropic total variation for limited angle tomography," *IEEE Trans. Radiat. Plasma Med. Sci.*, pp. 1–1, 2018.

[100] Z. Chen, X. Jin, L. Li, and G. Wang, "A limited-angle CT reconstruction method based on anisotropic TV minimization," *Phys. Med. Biol.*, vol. 58, no. 7, p. 2119, 2013.

[101] E. J. Candes, M. B. Wakin, and S. P. Boyd, "Enhancing sparsity by reweighted ℓ_1 minimization," *J. Fourier Anal. Appl.*, vol. 14, no. 5, pp. 877–905, 2008.

[102] T. Wang, K. Nakamoto, H. Zhang, and H. Liu, "Reweighted anisotropic total variation minimization for limited-angle CT reconstruction," *IEEE Trans. Nucl. Sci.*, vol. 64, no. 10, pp. 2742–2760, 2017.

[103] H. Kim, J. Chen, A. Wang, C. Chuang, M. Held, and J. Pouliot, "Non-local total-variation (NLTV) minimization combined with reweighted L1-norm for compressed sensing CT reconstruction," *Phys. Med. Biol.*, vol. 61, no. 18, p. 6878, 2016.

[104] L. A. Shepp and B. F. Logan, "The fourier reconstruction of a head section," *IEEE Trans. Nucl. Sci.*, vol. 21, no. 3, pp. 21–43, 1974.

[105] Z. Wang, A. C. Bovik, H. R. Sheikh, and E. P. Simoncelli, "Image quality assessment: From error visibility to structural similarity," *IEEE Trans. Image Process.*, vol. 13, no. 4, pp. 600–612, 2004.

[106] M. Petrongolo and L. Zhu, "Noise suppression for dual-energy CT through entropy minimization," *IEEE Trans. Med. Imaging*, vol. 34, no. 11, pp. 2286–2297, 2015.